THE UNIVERSITY OF HULL

Utilisation of CO$_2$ for the Preparation of Inorganic Solids

being a Thesis submitted for the Degree of PhD in the

University of Hull

by

Matthew John Bennett MChem (Hons)

March 2019

Abstract

The work in this project reports: (1) the preparation of the mixed oxide carbonates; $Sr_2CuO_2(CO_3)$, $Sr_{1.8}Ba_{0.2}CuO_2(CO_3)$ and $Sr_{1.75}Ca_{0.25}CuO_2(CO_3)$ via direct reaction of the parent oxides with CO_2, (2) the extraction of CO_2 to re-form the original oxides and (3) a Density Functional Theory (DFT) model for understanding the thermodynamics and structural changes of Sr_2CuO_3 reacting with CO_2, forming $Sr_2CuO_2(CO_3)$.

The one-dimensional structured series of $Sr_{2-x}A_xCuO_3$ (A = Ca, Ba and x = 0 − 2) was directly reacted with CO_2, forming oxide carbonates. An alternating gaseous approach was used so CO_2 would react within the anion vacancies of these compounds at specific temperatures. Identical reaction parameters were used for barium and strontium compounds, however calcium compounds required a longer residence time. This has been attributed to the smaller anion vacancies and lower CO_2 reaction affinity. In all cases CO_2 could be removed from the oxide carbonates to re-form the original oxides for consequent reactions. The structural changes as well as carbonate formation were studied using a DFT model. This showed how atomic positioning changes when forming $Sr_2CuO_2(CO_3)$ from the original oxide. An ΔH_{rxn} value was calculated which included the enthalpy of structural rearrangement, $\Delta H_{structure}$, and formation of the carbonates, $\Delta H_{carbonate}$. This provides an insight into the thermodynamics involved when forming mixed oxide carbonates from an oxide.

Ce_2MnN_3 and the $Sr_{2-x}Ba_xPdO_3$ (x = 0 − 2) series are both isostructural to Sr_2CuO_3 and were also investigated. $Sr_{2-x}Ba_xPdO_3$ compounds indicated only surface carbonates whilst Ba_2PdO_3 resulted in $Ba_{11}Pd_{11}O_{20}(CO_3)_2$, $BaCO_3$ and Pd metal. CO_2 splitting has been proposed to occur with Ce_2MnN_3, resulting in reactions with O_2 forming CeO_2 and MnO_2.

Acknowledgements

List of abbreviations

CCS	Carbon Capture and Storage
CCU	Carbon Capture and Utilisation
DFT	Density Functional Theory
ICSD	Inorganic Crystal Structural Database
IPCC	International Panel on Climate Change
FTIR	Fourier Transform Infrared
MOF	Metal Organic Framework
PES	Potential Energy Surface
PXRD	Powder X-ray Diffraction
RMSD	Root-Mean-Square Deviation
RP	Ruddlesden-Popper
TGA	Thermogravimetric Analysis
XRD	X-ray Diffraction

Contents

Chapter 1

Introduction

1.1   Carbon Capture and Storage (CCS)

As a result of mass global industrialisation, the amount of CO_2 released into our atmosphere is increasing on a global scale.[1–3] In 2017 it was reported that approximately 36.8 Gt of CO_2 was released into the atmosphere.[4] CO_2 adsorbs the heat from the Sun's radiation that is reflected off the Earth's surface. This "trapping" of heat causes the Earth's surface temperature to increase unnaturally, resulting in man made climate change. A report by the International Panel on Climate Change (IPCC) predicts a rise in global temperature of up to 1.9 °C by 2100.[5] As a result, global efforts have been made to either store or utilise CO_2 to prevent its release into the atmosphere.

Utilisation of CO_2 is an attractive approach as it redirects the greenhouse gas towards different chemical processes, such as preparing fuels and other chemicals.[6,7] This is an advantageous alternative compared to simple CO_2 storage, as not only is the gas removed from industrial emissions, but it can also be used towards preparing materials. Some of the common types of materials which can be prepared from utilising CO_2 include, carbonates MCO_3, ureas $(RHN)_2CO$ and polycarbonates.[8,9]

There are three primary approaches in which CO_2 can be captured from emissions within industry. These are post-combustion, pre-combustion and oxyfuel combustion.[10,11]

- Post-combustion capture: this involves dissolving the CO_2 in amine-based solutions. The CO_2 can then be removed from the liquid to be compressed and stored externally underground.

- Pre-Combustion capture: the fuel is pre-treated by being converted into a mix of hydrogen and CO_2. The gases are then separated so CO_2 can be stored separately.

- Oxyfuel combustion: this has the fuel source burned in pure oxygen instead of air to produce a more concentrated stream of CO_2. This will have less alternative gases within the steam which makes the separation process easier.

The current types of carbon capture and storage (CCS) materials used within industry are amine-based (NH_2R'), solvents.[12] However due to their limitations alternative materials have also been investigated such as metal organic frameworks (MOFs), zeolites (natural and synthetic) as well as alkaline earth metal oxides (Ca/MgO).[13, 14]

Amine solvents are used as the primary pre/post-combustion method for the absorption of CO_2. This type of CO_2 capture has been described as the "wet-scrubbing" approach and is carried out at high pressures and low temperatures.[13,15,16] When CO_2 is released from industrial emissions it is passed into a chamber containing an amine based solution. This solution acts to separate the CO_2 from the gas flow and have it stored as a bicarbonate. The CO_2 enriched amine solution is then piped into a separate vessel and heated in order to recover the amine solution. The regenerated solution is then piped back into the system for further reactions with the CO_2 collected and stored.[17] A schematic of how this process operates within an industrial environment is shown in Figure 1.1. The main type of amine solvent which is used is monoethanolamine (MEA) ($NH_2CH_2CH_2OH$).
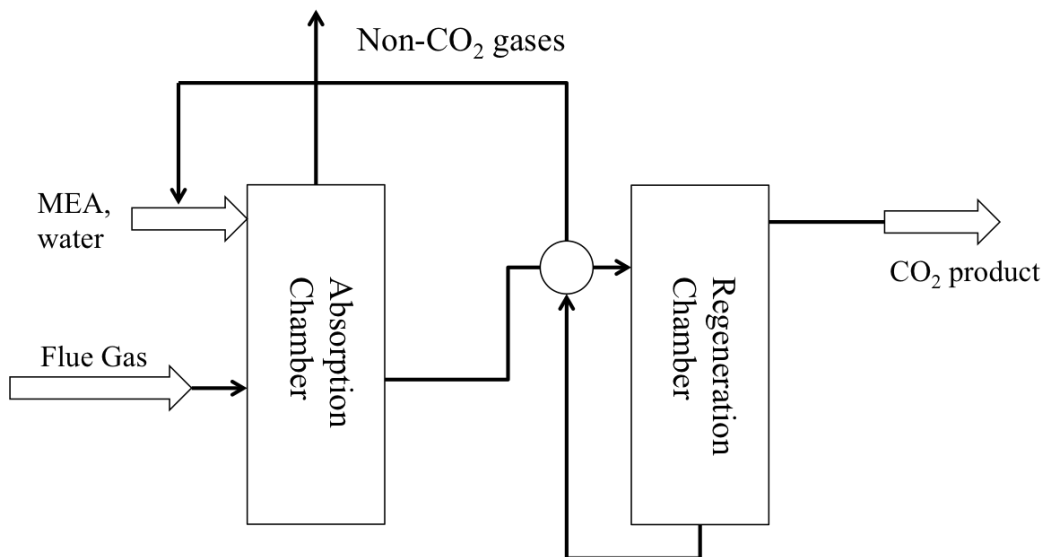
Figure 1.1: Schematic of the layout of the absorption of CO_2 from a monoethanolamine (MEA) solution in an industrial environment.

Currently MEA is used as the benchmark solvent for all CCS applications within industry.[12, 18] However different types of amines solvents have been developed, such as secondary and tertiary amine molecules for capturing CO_2 on an industrial scale.[19] The absorption process itself occurs when CO_2 reacts with H_2O within the solution to produce a carbonic acid.[20, 21] The amine group from the MEA then reacts to strip a H^+ producing a bicarbonate with a monoethanolammonium ion. The reaction mechanism between CO_2 and the amine solution is illustrated in Figure 1.2, to explain this process step by step.
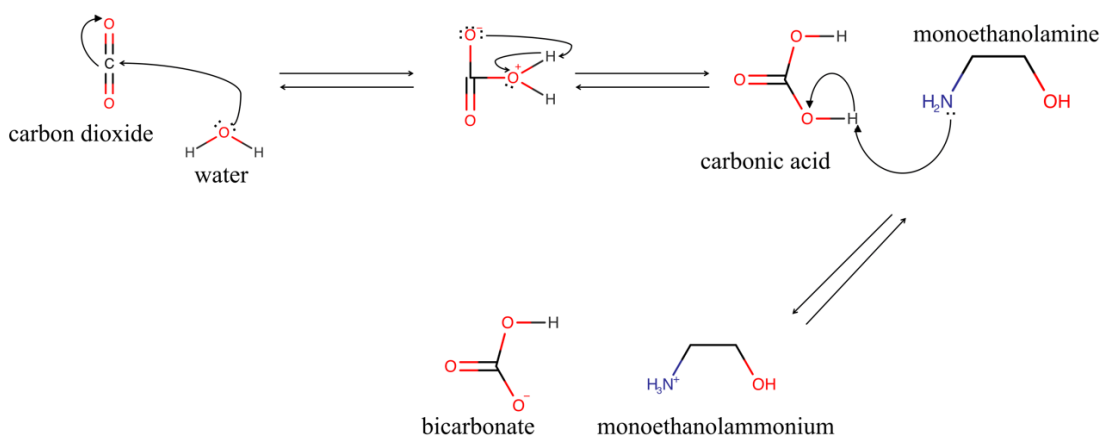
Figure 1.2: A reaction mechanism between CO_2, H_2O and monoethanolamine resulting in CO_2 being captured in the form of a bicarbonate

The benefit of using amine-solvents for CO_2 capture is that the initial molecules can be regenerated after use with the CO_2 removed and stored separately. However, these materials have limitations and various drawbacks. These include safety concerns when being used on a large industrial scale, as well as the chemical limitations of amine solvents as they can degrade in the presence of O_2, SO_x and NO_x which are also present in the emissions flow.[22, 23] Due to the limitations of this type of approach various solid based materials have been investigated as an alternative.

1.2 Solid Materials for CO_2 Capture and Utilisation type

1.2.1 Zeolite towards CO_2 storage

One of the most well researched class of materials in the field of CO_2 capture and storage, are porous, which are based on aluminosilicate minerals i.e zeolites.[24–26] These have been used for a variety of applications based upon their porous structure and ion-exchange properties.[27] Their crystalline framework is built from SiO_4 and AlO_4 tetrahedra that are interlinked and can form a regular array of pores varying from 0.5-1.2 nm in size.[28] In these structures Si^{4+} cations are partially substituted by Al^{3+}, which result in a negatively charged structure that is balanced from the insertion of exchangeable metal cations such as Na^+, K^+, Ca^{2+} and Mg^{2+}, inserted throughout the pores and framework of the structure.

Both naturally occurring (X and Y Faujasite) and synthetic, for example (5A and 13X) type zeolites have been investigated for the physisorption of CO_2 from an emissions flow.[29, 30] The chemical properties of zeolites can be readily changed by altering the Si:Al cation ratio. The adsorption process of CO_2 is via an ion-induced dipole interaction from the metal cations, present at the surface of the pores.[31] As CO_2 molecules enter into the zeolite pores it becomes attracted to the surface via attractive dispersion forces. Figure 1.3 shows the change in the electron densities resulting in a δ- charge on either side of a CO_2 molecule when attracted to a metal cation.

$$(\text{metal ion})^{x+} \ldots \quad ^{\delta-}O=\overset{\delta+}{C}=O^{\delta-}$$
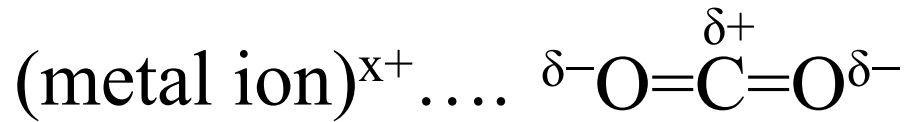
Figure 1.3: A representation of CO_2 being attracted to a metal ion via attractive dispersion forces in zeolites.

The strength of the attractive forces between the zeolite material to CO_2 depends on the type of metal cations present. These forces can be stronger when cations of high charge to density ratio are used. However, these types of forces are not as strong as covalent bonds, this allows CO_2 to be desorbed from the surfaces of the pores so the material can be used for further capturing cycles. The size of the pores is also important as the volume needs to be able to accommodate CO_2 molecules that have an average kinetic diameter of 3.3 Å.[32] Using the crystal structural information of the zeolite, Natrolite, (Figure 1.4) shows how a CO_2 molecules can be inserted into the pores of this type of material.[33, 34]
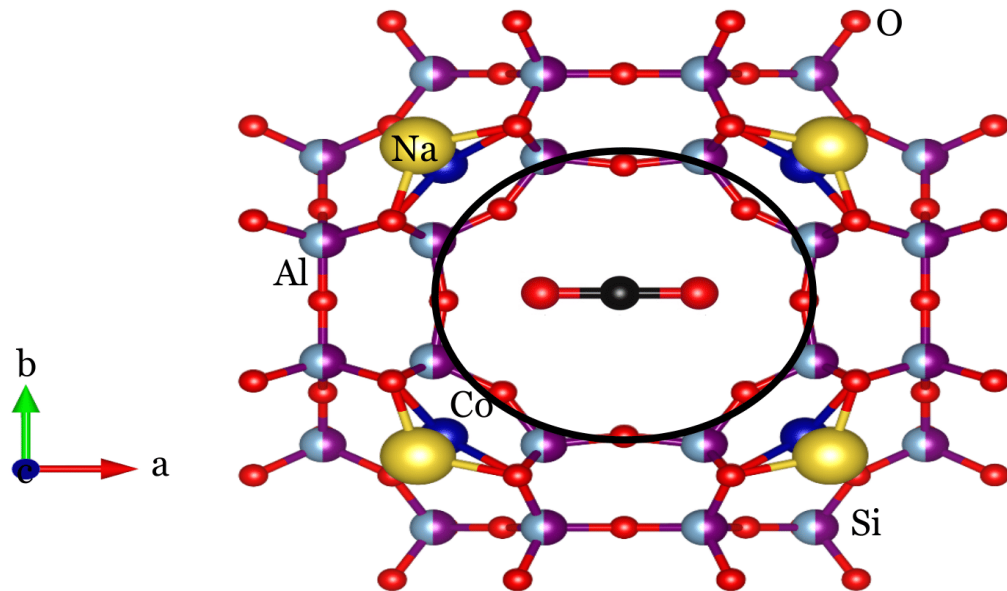
Figure 1.4: The crystal structure of Natrolite, with one of its pores highlighted using a black oval and the CO_2 at the centre. This figure shows the different metals present and their coordination which make up the overall structure. The half coloured sphere show atoms that can be either Al or Si that are in 1:1 ratio of each other. The red spheres represent the oxygen atoms.

Although a great deal of work has been committed into the adsorption capabilities of zeolites, these materials still have limitations when applied on a large industrial scale. Their selectivity for CO_2 starts to decline at temperatures as low as 30 °C and becomes negligible above 200 °C.[35] Furthermore, in order to desorb CO_2, temperatures of up to 500 °C are required resulting in high energy consumption.[36,37]

Although zeolites do have limitation for CCS applications, the concept of how they work is most useful. These compounds have pores within their structure which is large enough to accommodate multiple gaseous CO_2 molecules that are physisorbed through Van der Waals forces. By this principle various other compounds which have vacant voids, similar to the pores within zeolites can be used to store and even react with CO_2. As a result compounds which have vacancies within their crystal structure have been investigated for reacting with CO_2 in a similar way to zeolites as discussed within this project.

1.2.2 Alkaline Earth Oxides MO (M = Ca, Mg and Sr) towards Metal Carbonates

CO_2 is Lewis acidic in nature, in that it can receive electrons towards forming a carbonate $(CO_3)^{2-}$ ion. As such alkaline earth metal oxides (MO) are able to adsorb CO_2 via their basic M-O$^-$ sites on their surfaces.[38] This results in a chemisorption process the creates chemical bonds with CO_2 forming a metal carbonate, MCO_3. The exothermic carbonation and endothermic calcination type reactions for these materials are given in Equations 1.1 and 1.2 with M = alkaline earth metal.[39,40] Of these various types of materials, alkaline earth metal oxides (MgO and CaO) have been studied extensively for CO_2 capture.[41,42]

$$MO_{(s)} + CO_{2(g)} \rightarrow MCO_{3(s)} \tag{1.1}$$

$$MCO_{3(s)} \rightarrow MO_{(s)} + CO_{2(g)} \tag{1.2}$$

CaO acts to adsorb CO_2 at temperatures of over 700 °C, and operates via a chemical looping process. During chemical looping the CO_2 is passed over the metal oxide to form the

carbonate $CaCO_3$, then a desorption reaction occurs to remove CO_2. This allows CaO to be regenerated and reused over multiple cycles.[43] The sorption process of CO_2 to CaO has been found to occur both on the surface (adsorption) and throughout the bulk (absorption) of the material's structure.[44,45] However the limitations of CaO are with its low regenerability for desorbing CO_2. This is caused from the sintering of particles occurring during the sorption process. As a result this can reduce the CO_2 capturing capabilities. One of the ways designed to avoid sintering over calcination reactions, is through incorporating inert materials such as $Ca_{12}Al_{14}O_{33}$ and $MgAl_2O_4$ into the CaO crystallites resulting in a mixture of these phases. $Ca_{12}Al_{14}O_{33}$ and $MgAl_2O_4$ are inert to reacting with CO_2, and act to separate the CaO particles reducing the effects of sintering, but also still maintain high capturing capabilities.[46,47]

Alternatively MgO-based adsorbers can act as an attractive alternative due to their low temperature formation and regenerability properties (below 500 °C), compared to CaO. These materials can attract CO_2 via their basic O^{2-} sites at temperatures between 200-400 °C. This initially results in a carbonate being formed on the surface layers.[48] As a result of this however, MgO materials only have moderate adsorption capabilities, and the sorption is also slower when compared to that of CaO.[49] Attempts to improve the adsorption capabilities of MgO have been investigated. This has varied from having mesoporous structures to increase surface area, as well as using metal oxide supports.[50–53]

MgO and CaO react favourably to form metal carbonates, and due to their relative cheap cost, they are attractive as CO_2 capturing materials. However, their limitations lie in their regenerative abilities and loading capacities. The availability of surface sites for forming metal carbonates is a main factor to consider when using these types of materials. Different methods have been developed to increase the availability of these sites such as changing the morphology and particle size.[54]

Work by Miccio *et al.* also explored using SrO for high temperature CO_2 capture.[55] This study has looked into different capturing capabilities of particle types (coarse and fine) of SrO on different supports such as Al_2O_3 and hydrotalcites, $Mg_6Al_2CO_3(OH)_{16}.4(H_2O)$. It was found that of the different types of materials, coarse particles of SrO performed the best with regard to their CO_2 capturing abilities over repeated cycles. This is due to coarse particles being able to maintain their architecture compared to fine articles that collapse and

aggregate.

In summary, the alkaline earth metal oxide MO (M = Mg, Ca and Sr), series of compounds have been able to react with CO_2 in order to prepare metal carbonates. This is due to the strong affinity of the M-O bonds for reacting with CO_2 towards carbonate formation. This type of research has either focused on just the metal oxides, or on having the metal oxide on different types of supports. It is possible, however, that more complex compounds with MO bonds can be used for reacting with CO_2 to prepare MCO_3 groups, whilst maintaining the original crystal structure. This will result in a novel route for the preparation of mixed oxide carbonate based materials and is the basis of this work.

1.2.3   Alkaline metal based ceramics for CO_2 reactions

A variety of alkaline metal based ceramic compounds have been investigated for reacting with CO_2 resulting in the formation of a metal carbonate. These reactions also result in a secondary phase present alongside the carbonate. Ceramic materials that have been discussed in this context are Li_2ZrO_3, Li_4SiO_4 and Na_2ZrO_3.[31,56]

Li_2ZrO_3 is traditionally synthesised through the reaction of Li_2CO_3 and ZrO_2, however Naka-gawa and Ohashi considered the reverse reaction towards CO_2 capture.[57] Equation 1.3 shows a reversible reaction involving CO_2. Li_2ZrO_3 is able to capture and react with CO_2 at temperatures of up to 600 °C.

$$Li_2CO_3 + ZrO_2 \rightleftarrows Li_2ZrO_3 + CO_2 \tag{1.3}$$

The driving force of the carbonate reaction is a result of Li^+ ions diffusing from the particle pores to the surface. There they react with CO_2 gas as well as diffusing O^{2-} ions. This results in a total of three layers, Li_2CO_3, ZrO_2 and Li_2ZrO_3 as shown in Figure 1.5.
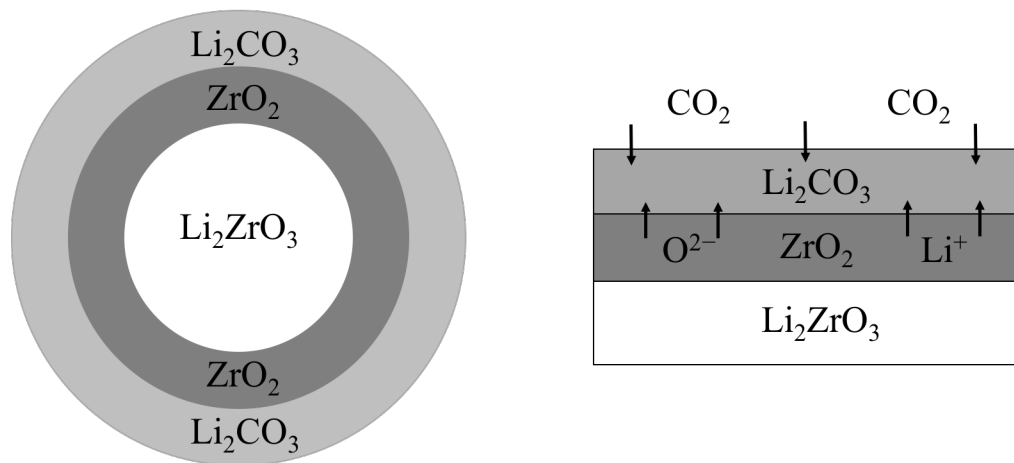
Figure 1.5: Proposed mechanism of Li_2ZrO_3 reacting with CO_2 forming a surface layer of Li_2CO_3.[57]

When using Li_2ZrO_3 the diffusion rate of Li^+ to the surface determines how much carbonate is formed, and substantially how much CO_2 is captured.

Li_4SiO_4 has also been found to react with CO_2 resulting in mixed phase of Li_2SiO_3 and Li_2CO_3.[58] This reaction can also be reversible in order to re-obtain the original silicate.

Na_2ZrO_3 reacts with CO_2 in a similar way to Li_2ZrO_3.[59, 60] However the lamellar structure of Na_2ZrO_3 has the advantage of Na^+ ions being located within the zirconate layers. This means that the Na^+ ions can diffuse quicker than in the lithium equivalent to react with CO_2. This is as an example of how mixed metal oxides can be used for reacting with CO_2, although this results in the structure dissociating into a carbonate and oxide.

1.3   Perovskites and Related Materials

1.3.1   Perovskites

The term Perovskite relates to any compound that has a crystal structure similar to that of the archetype $CaTiO_3$.[61] These compounds have the general formula ABX_3, where A is an electropositive metal (alkaline, alkaline earth metal or lanthanide), B a transition metal (smaller in size compared to A) and X represents the anions.

20

An ideal perovskite structure would show a cubic unit cell with the smaller B cations octahedrally coordinated and the larger A cations 12 coordinated by the X anions. An example of such an ideal perovskite is given in Figure 1.6, using the unit cell of $KZnF_3$ (A = K, B = Zn and X = F).
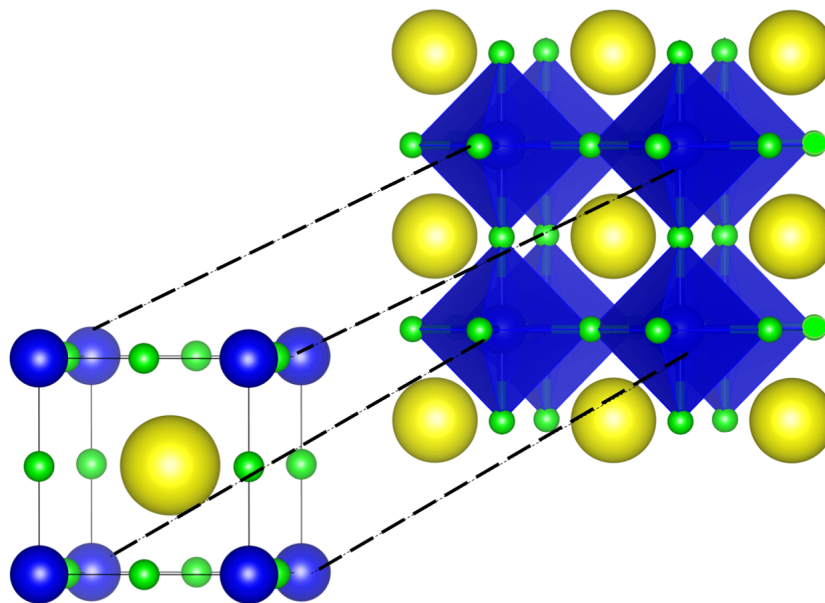
Figure 1.6: Crystal structure of an ideal cubic perovskite $KZnF_3$.[62] K, Zn and F are represented by the yellow, blue and green spheres. ZnF_6 groups via the blue octahedra.

The ideal perovskite structure however can become distorted as a result of a variety of conditions. This includes either Jahn-Teller distortion or having a large mismatch in the size of the A and B cations.[63] One of the most common types of distortion arises from the tilting of octahedra coupled with a shift in the A cation positions.[64]

In order to predict the stability range of a perovskite's structure, Goldschmidt determined a tolerance factor, t_R, for the ABX_3 phases in Equation 1.4:

$$t_R = (r_A + r_B)/\sqrt{2}(r_B + r_X) \tag{1.4}$$

r_A, r_B and r_X correspond to the ionic radii of A, B and X respectively.[65]

Investigations by Goldschmidt on existing perovskites found that an ideal cubic structure

would exist in a tolerance factor range of $0.8 \leq tR \leq 0.9$.[65]

Oxide based perovskites are known to exist in the range of $0.75 \leq t_R \leq 1.0$, of which those in the $0.815 \leq t_R \leq 0.964$ region are cubic (based on around 223 oxide compounds).[66, 67] In general, any structure which consists of an ordered array of BX_6 octahedra, or related anion deficient polyhedra (square-based pyramid, square), can be classified as distorted perovskites or perovskite-like structures. Perovskite materials have been used for a variety of different applications such as solar cells, catalysts and superconductors.[68–70] Examples of perovskite-like materials which have been explored within this work are discussed in the following sections.

1.3.2 Ruddlesden-Popper Phases

One of the key features of perovskites is that their structure is built up from the corner sharing of B-X_6 octahedra, with the A cations located in the cavities. Ruddlesden-Popper (RP) perovskites are a series of layered compounds in which rock-salt type layers are between perovskite slabs.[71, 72] The general formula for an RP phase is $AX(ABX_3)_n$ with n being the number of perovskite slabs, stacked along the c direction. The interlayers between the perovskite slabs is based on the NaCl structure, an interpenetrated face centred cubic (FCC) array of the cations and anions. Well known examples of compounds showing the RP crystal structure are those investigated by Ruddlesden and Popper themselves which are Sr-Ti-O based, Sr_2TiO_4, $Sr_3Ti_2O_7$ and $Sr_4Ti_3O_{10}$.[71, 72] These phases can be described with the general formula $A_{n+1}B_nO_{3n+1}$. The archetype of the RP phase, K_2NiF_4 (n = 1). Figure 1.7 shows examples of RP compounds with n = 1, 2 and 3.
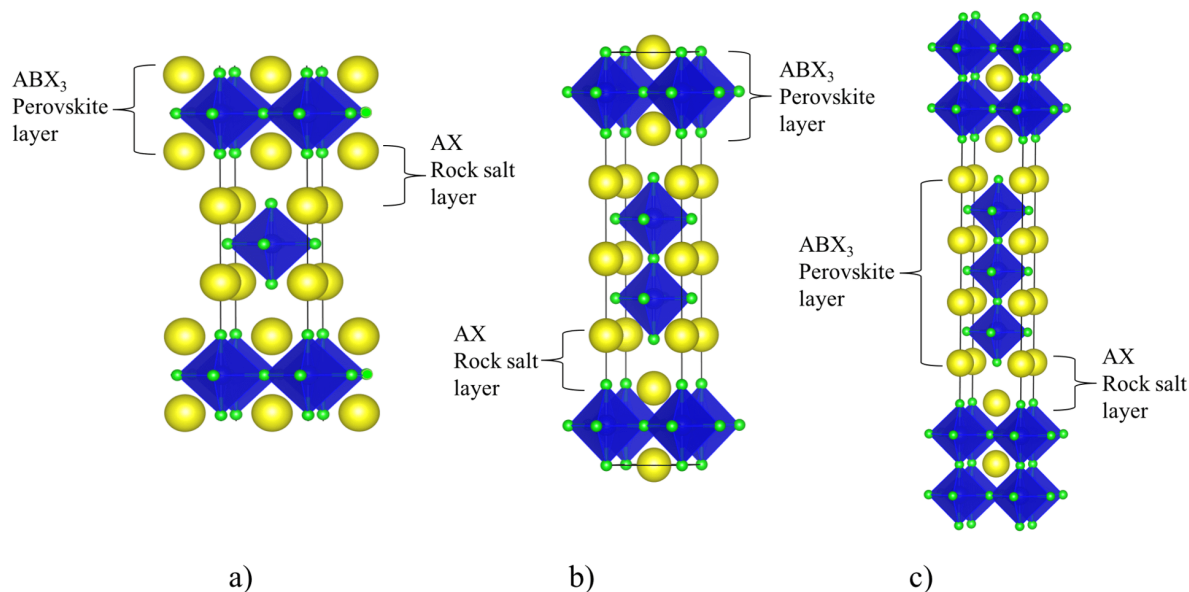
Figure 1.7: Structures of a) K_2NiF_4 (n = 1), b) $K_3Ni_2F_7$ (n = 2), and c) $K_4Ni_3F_{10}$ (n = 3).[73, 74]

These types of perovskite compounds have been found to have anion deficient counterparts that form similar structures. The main difference lies in the lower coordination number of the B cation. Anion-deficient equivalents of the RP type structures T, T' and T^* have also been shown to have compounds based on the formula A_2BX_3.

1.3.2.1 T structure

A RP phase which has n = 1 is shown in Figures 1.7 (a) and 1.8 (a), and is referred to as the K_2NiF_4-type or T structure.[75] The T structure consists of two-dimensional layers of alternating corner shared BX_6 octahedra stacked long the c-axis, which are separated by AX rock salt layers. The coordination of the A cation decreases from being a 12 coordinate in the ABX_3 perovskite, to a 9 coordinate. When all four of the equatorial B-X bonds are equal in length the symmetry becomes tetragonal ($a = b$). If these bonds are of different lengths than the symmetry adopts a orthorhombic system.

1.3.2.2 T$'$ structure

Another form of a RP phase perovskite, the T$'$ structure is shown in Figure 1.8 (b). This is also referred to as a Nd_2CuO_4-type structure, and is a result of two-dimensional sheets of corner shared BX_4 square planar units separated by fluorite layers.[75] Fluorite layers consist of a cubic close packed arrangement of the A and X ions in tetrahedral holes. In this arrangement the A cations are in a 8 coordination state with the X anions.

This type of structure may also be described as T-type with the apical anion sites of the octahedra being vacant. The anions reside within the A layers, generating the fluorite like arrangement.

1.3.2.3 T* structure

The T* structure shown in Figure 1.8 (c), has been regarded as a half way point between T and T$'$.[75] In this structure the B metal cations shows a coordination number of 5, and the polyhedra are connected via their corners. This results in the formation of two-dimensional layers that are separated by alternating fluorite and rock salt groups. The T* structure can also be described as T-type with half of the octahedral apical anions vacant. These anions reside in half of the interstitial tetrahedral sites of the A layers to generate the fluorite "spacer" units. The A cations have both 8 and 9 coordination states with the X anions.

Figure 1.8: The (a) T, (b) T$'$ and (c) T* perovskite structures. The yellow, blue and green spheres correspond with A, B and X respectively. The blue polyhedra highlight the coordination of B with X.

Due to the similarities between RP phases and the perovskite structure an extension of the tolerance factor, Equation (1.5) has been brought upon to include the different "T-type" phases. A tolerance factor which has been tailored directly for the 'T-type' phases was suggested by Chen:

$$t_f = \left[3\sqrt{2}r_X + 2\sqrt{6}(r_A + r_X)\right]/9(r_B + r_X) \qquad (1.5)$$

where r_A, r_B and r_X are the ionic radii of A, B and X respectively.[76–78] Using the tolerance factor and the ionic radii from the Shannon table, it was found that the T$'$ phase occurs for $0.96 < t_f < 1.00$ and T for $1.00 < t_f < 1.14$.[78, 79] T* has been found to occur between these two boundaries.[78]

1.3.3 Mixed anion Ruddlesden-Popper perovskites

The first type of layered perovskite like materials synthesised by Ruddlesden and Popper were based on transition metal oxides.[71, 72] In the compound $Sr_3Ti_2O_7$ distinctive layers are present of those of the octahedrally coordinated TiO_6 and those with rock-salt Sr-O structure.[72] This arrangement however, is not simply limited to just metal oxides as a variety of oxycarbonate, oxyhydroxide and oxynitrides RP type have been synthesised.[80–82]

The non-oxide anions are able to coordinate metals in a similar manner to the oxides in order to form similar structures. A variety of different mixed anion Ruddlesden-Popper compounds are presented in Figure 1.9. The image of the $Sr_4Fe_2O_6(CO_3)$, shows that the carbons are surrounded by randomly occupied oxygens from the crystal structural information.
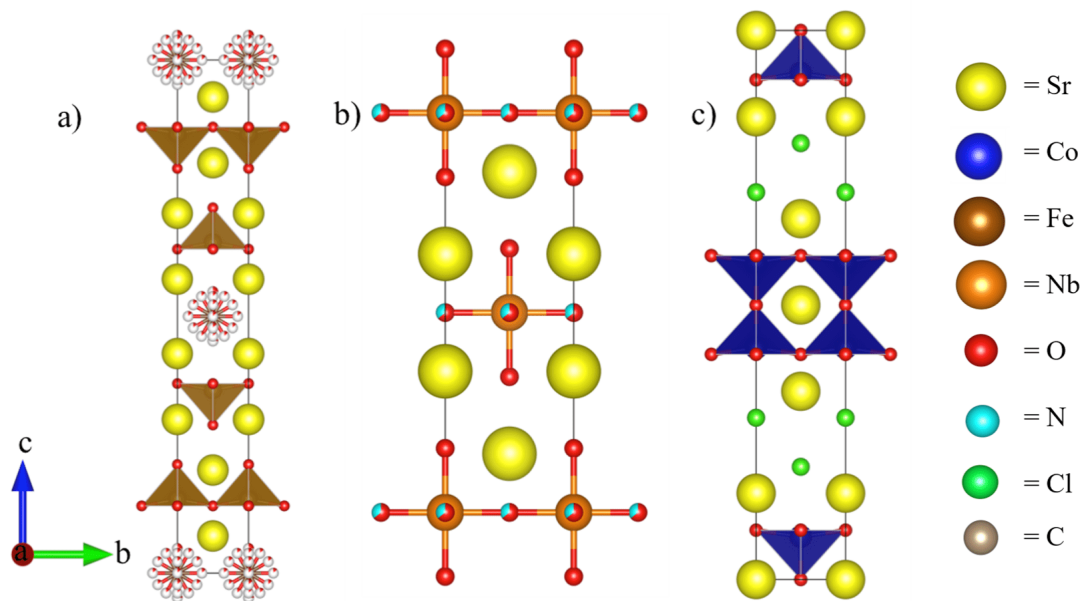
Figure 1.9: Mixed anion Ruddlesden-Popper perovskites, a) $Sr_4Fe_2O_6(CO_3)$,[83] b) $Sr_2NbO_{3.28}N_{0.72}$[82] and c) $Sr_2CoO_2Cl_2$.[84] The carbonate groups in structure a) show partial occupancy of the oxides around the carbon.

These mixed-anion perovskite like compounds have been investigated for their magnetic and superconductive properties, taking into account that different anion groups change the coordination and electronic properties of the metal. This is an example of how mixed anion compounds show a variety of properties. In the case of this study, oxycarbonate RP perovskites

will be the main focus point as new techniques have been developed for their synthesis.

1.3.4 Layered perovskite compounds

Perovskite type materials are some of the most studied in solid state and materials chemistry. These have also been explored for reacting with CO_2 and are an attractive option due to their structural stability. This use of perovskite materials for CO_2 capture has varied from surface adsorption onto compounds like $LaCoO_3$, to the reacting with layered perovskites towards forming metal carbonates.[85–87]

Tascon and Tijuca found that CO_2 binds to the surface of $LaCoO_3$ via an attraction towards the M-O$^-$ groups, similar to Mg/CaO materials between 100 to 400 $^\circ$C.[85] Below this temperature CO_2 is still adsorbed onto the surface, but via physisorption as seen with zeolites. The adsorption process itself was monitored using vibrational spectroscopy, which shows how the CO_2 forms into a carbonate on the materials surface. $LaCoO_3$ was also found to be able to adsorb CO in a similar way to CO_2.

The layered perovskite $Li_2SrTa_2O_7$ was reported by Galven *et al.* as a Ruddlesden-Popper type perovskite which showed CO_2 reaction capabilities.[86] These materials are able to capture CO_2 under humid conditions i.e in the presence of H_2O to form $LiHSrTa_2O_7$ and Li_2CO_3. This is through a cation exchange of a Li^+ ion with a H^+ in the structure forming a metal carbonate. This is also a key advantage as flue gas emissions from industrial plants contain other gases such as H_2O which can actually aid in the CO_2 capturing process. The reaction of $Li_2SrTa_2O_7$ with CO_2 is shown in Equation 1.6.

$$Li_2SrTa_2O_7 + 1/2\ CO_2 + 1/2\ H_2O \rightleftarrows LiHSrTa_2O_7 + 1/2\ Li_2CO_3 \qquad (1.6)$$

A hexagonal 6H-$Ba_4Sb_2O_9$ perovskite has also been reported by Dunstan *et al.* for reversible CO_2 adsorption reactions.[87] This type of reaction can result in the preparation of $BaCO_3$, Equation 1.7. $Ba_4Sb_2O_9$ was also found to be able to perform within 74% of its original CO_2 capturing capabilities, even after 100 reaction cycles.

$$6H\text{-}Ba_4Sb_2O_9 + 3\,CO_2 \rightleftarrows BaSb_2O_6 + 3\,BaCO_3 \qquad\qquad (1.7)$$
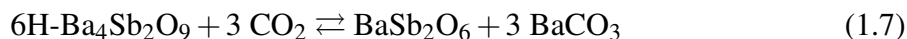
Despite the advantages of multiple reverse cycles, the energy costs of these types of reactions was found to limit the use of these materials when compared to others like CaO. These reactions show that mixed metal perovskite type materials, ($Li_2SrTa_2O_7$ and $Ba_4Sb_2O_9$) are able to react with CO_2 resulting in a mixed metal oxide alongside metal carbonates. These reactions are similar to those with Li_2ZrO_3 and Li_4SiO_4 in that they are reversible towards forming the original compound. The differences however, are in that it is a mixed metal oxide which is prepared alongside the metal carbonate. These examples show that mixed metal perovskite like materials, can be used for reacting with CO_2 in a similar way to that of CaO and MgO, towards preparing metal carbonates. These materials also have alkaline earth metal oxides within their structure which favour the formation of carbonates.

In this work a variety of solid materials which have been used to react with CO_2 for either utilisation or storage has been reviewed. Zeolite have a porous structure with voids for CO_2 molecules to be inserted within the material, physisorbed by metal cations. Alkaline earth metal oxides, MgO and CaO, react with CO_2 via an attraction to their basic $M\text{-}O^-$ groups towards forming metal carbonates. This in turn utilises CO_2 gas towards the preparation of a carbonate rather than just for storage. More complicated solids materials such as the layered perovskites $Li_2SrTa_2O_7$ and $6H\text{-}Ba_4Sb_2O_9$ can also react with CO_2 to form a metal carbonate alongside mixed metal oxides. This process as with the reaction of Ca/MgO with CO_2 can be reversed to re-obtain the original material. It has been proposed that all of these approaches can be combined towards having materials with vacant sites within their structure, $M\text{-}O^-$ groups to react with CO_2 towards forming carbonate and be part of a complex mixed metal compound. The reaction of these types of materials with CO_2 have been the focus of this project.

1.3.5 Anion Deficient Structures

All of the T, T$'$, and T* phases show the same stoichiometry, however they differ in the coordiantion state for the transition metal (B), which goes from 6 to 5 (T*) and 4 (T$'$). Structures

which are related to the perovskite or RP phases by removal of anions from the coordination of the transition metal (B) are described as having anion-deficient structures. One prime example is the removal of the equatorial anions which results in the corner-sharing octahedra being reduced to corner-sharing square planes. This can give an anion-deficient K_2NiF_4 type structure with a 213 stoichiometry e.g. Sr_2CuO_3.[88] These anion-deficient compounds have vacancies within their structures that could be exploited for "filling up" with additional different anions. An illustration of how the anion vacancies within a A_2BX_3 type structure can be filled towards a $A_2BX_2X'_2$ structure is presented in Figure 1.10. This also shows how the additional anions fill up the vacancies and expand the coordination of the B cation.
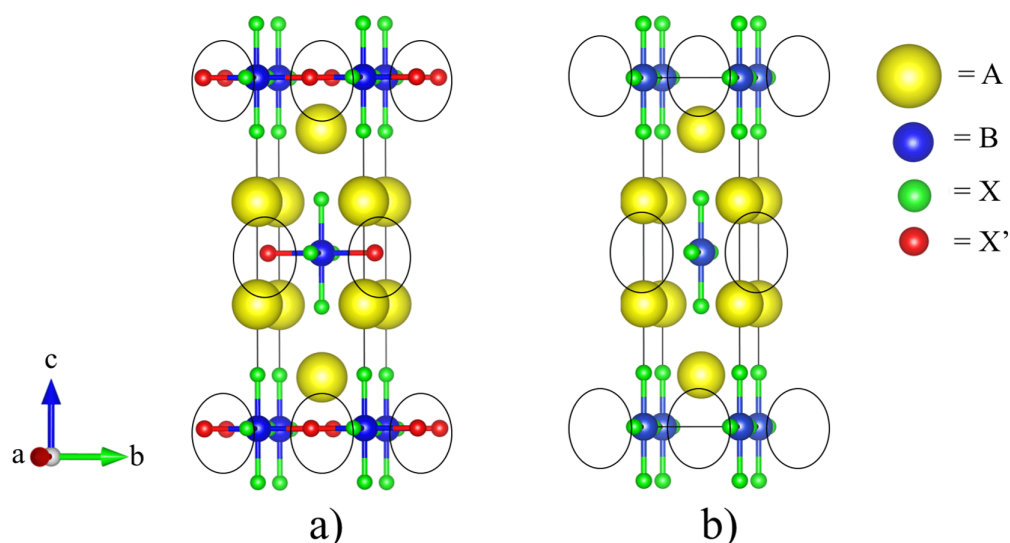
Figure 1.10: The a) A_2BX_4 which shows the K_2NiF_4 type structure, the anion-deficient version is shown with b) A_2BX_3. The vacancies within A_2BX_3 are highlighted using black ovals.

1.3.6 Anion-insertion into A_2BO_3-type compounds

In the field of material synthesis one of the techniques used for preparing novel compounds, is through either the substitution or insertion of additional anions into the crystal structure. A_2BO_3 compounds have been described as having anion-deficient K_2NiF_4 structures, which can be exploited for additional anions. The (A = Sr, Ca, Ba and B = Cu, Pd) series for example, has been investigated for substitution/insertion of fluorides, leading to a novel oxide

fluoride series of compounds.[89, 90]

Anion substitution can be used to change both the oxidation and coordination state of metal cations. The incorporation process is possible as the anion vacancies within the ionic solid can be "filled up" by the additional anions.[91] This makes anion substitution a useful technique towards novel materials.

The incorporation of additional anions in the A_2CuO_3 (A = Sr, Ca and Ba), A_2PdO_3 (A = Sr and Ba) series of compounds, as well as Ce_2MnN_3 has been investigated.

1.3.6.1 Anion-insertion into A_2CuO_3 type Compounds

Sr_2CuO_3 and Ca_2CuO_3 have both been exploited through fluorination techniques to prepare a series of oxide fluorides, $Sr_2CuO_2F_{2+\delta}$ and $Ca_2CuO_2F_{2+\delta}$.[92, 93] Both the non-stoichiometric $Sr_2CuO_2F_{2+\delta}$ ($0 \leq \delta \leq 0.57$) and stoichiometric ($Sr_2CuO_2F_2$) oxide fluorides have been reported.[92, 94, 90] Different types of synthetic routes have also been explored for preparing these mixed anion compounds. These have varied from using F_2 gas, to alternative "soft chemistry" methods with NH_4F, PVF and MF_2 (Cu and Zn) reagents used as fluorinating agents being dispersed with the precursor oxide and reacted with the oxide heated at temperatures of 200-300 °C.[89, 93] In the case of $Sr_2CuO_2F_{2+\delta}$ this has been shown to behave as a p-type superconductor, with Tc $\approx$ 64 K, through "holes" created as a result of the excess F^- ions causing the partial oxidation of Cu^{2+} to Cu^{3+}.[93] An illustration of the fluoride insertion into Sr_2CuO_3 towards $Sr_2CuO_2F_{2+\delta}$ is presented in Figure 1.11.
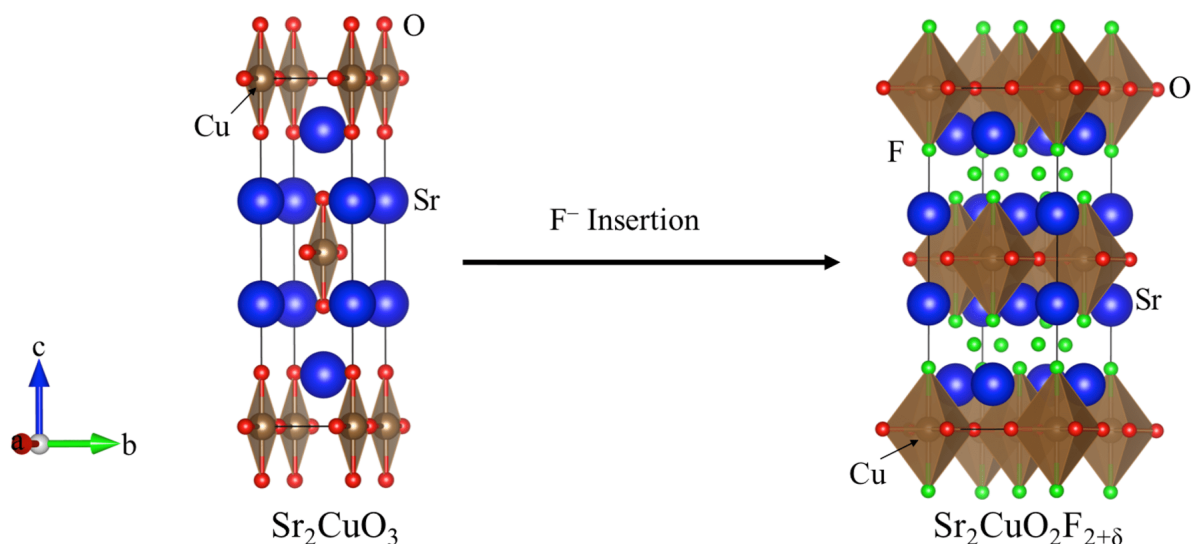
Figure 1.11: Reaction process of Sr_2CuO_3 with a fluorinating reagent to prepare $Sr_2CuO_2F_{2+\delta}$. The Sr and Cu cations are represented by the blue and brown spheres. Whilst the O and F anions are represented by the red and green spheres.

Additional fluoride anions (δ) are located within interstitial sites inside the strontium layers. $Sr_2CuO_2F_2$, a stoichiometric compound has also been reported which lacks the presence of fluorides within the interstitial sites. The small ionic radius of the fluoride anion allows this to occur. The stoichiometric oxide chloride, $Sr_2CuO_2Cl_2$ was reported, showing no extra anions due to the larger ionic radii of the Cl^- anion.[84] An illustration of the stoichiometric $Sr_2CuO_2F_2$[94] and $Sr_2CuO_2Cl_2$ compounds have been presented in Figure 1.12.
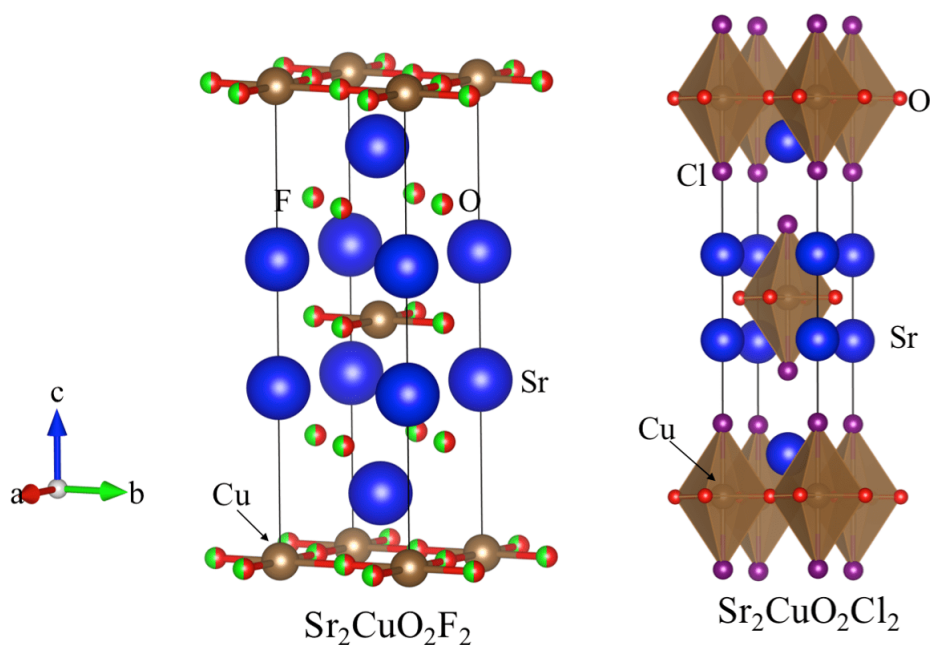
Figure 1.12: The stoichiometric $Sr_2CuO_2F_2$ and $Sr_2CuO_2Cl_2$ mixed anion compounds. The Sr and Cu cations are represented by the blue and brown spheres. Whilst the O, F and Cl anions are represented by the red, green and purple spheres. The half coloured green and red spheres shows that either fluorides or oxides can be present at these sites.

The reaction pathway for fluoride incorporation into the CuO_4 layers from Sr_2CuO_3 forming into $Sr_2CuO_2F_{2+\delta}$ has also been discussed.[93, 95] Figure 1.13 shows the CuO_4 square planar polyhedra becoming octahedra as fluoride anions are being inserted. In the octahedral coordination of copper, the oxide anions are equatorial, whilst the fluoride anions are axial. Not only does anion insertion act to fill the vacant sites, it also changes the structure as a whole. This is what sees Sr_2CuO_3 with a orthorhombic crystal system changing towards tetragonal $Sr_2CuO_2F_{2+\delta}$ also shown in Figure 1.13.
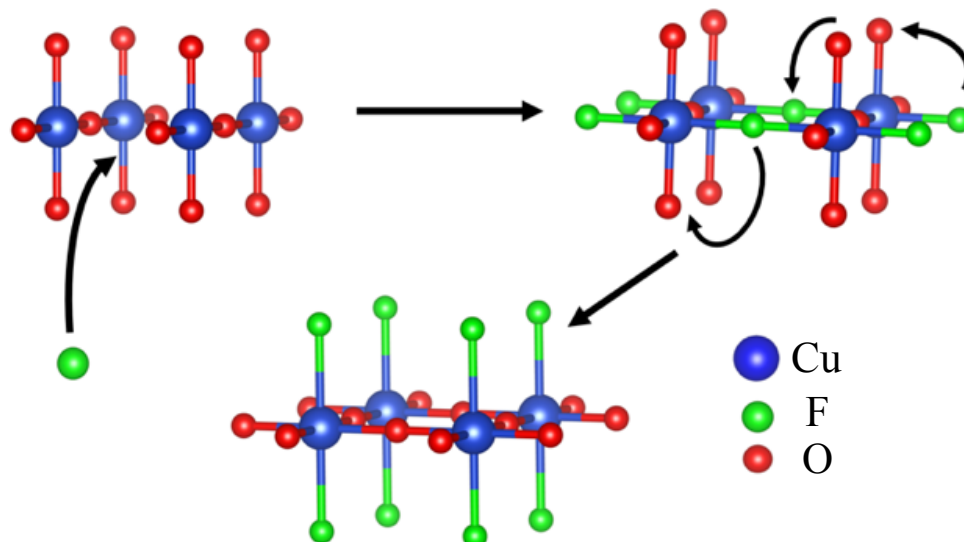
Figure 1.13: Structural rearrangement pathway of CuO$_4$ groups when fluorides are inserted into Sr$_2$CuO$_3$ to form Sr$_2$CuO$_2$F$_{2+\delta}$.

Oxygen insertion into Sr$_2$CuO$_3$ has been possible through high pressure techniques resulting in Sr$_2$CuO$_{3+\delta}$ (Figure 1.14) preparation.[96] These types of compounds show superconductive properties arising from the copper cations partially oxidising due to the presence of additional oxides.
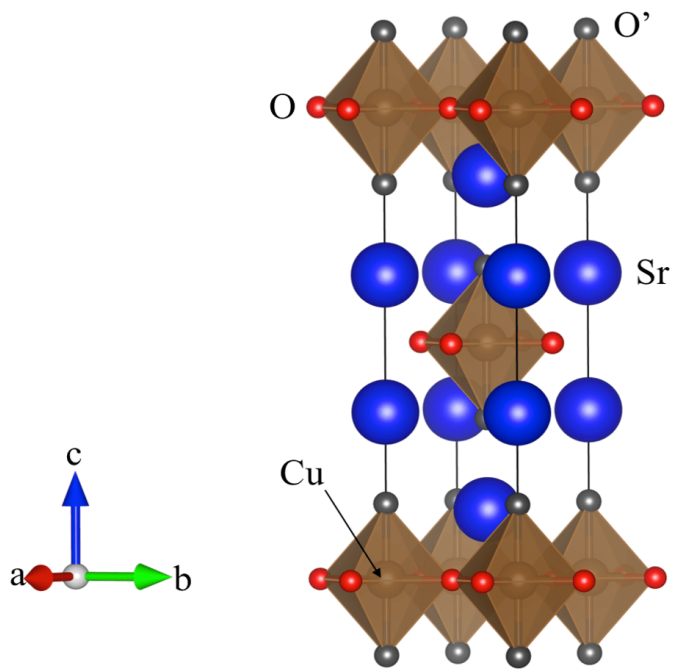
Figure 1.14: Crystal structure of $Sr_2CuO_{3+\delta}$. Sr and Cu cation represented by blue and brown spheres. O anions by red and the interstitial oxides, O' by the grey spheres.

Ca_2CuO_3 has also been explored for anion insertion due to its structural similarity with Sr_2CuO_3. Through fluorination techniques $Ca_2CuO_2F_{2+\delta}$ (Figure 1.15) has been prepared and also shows a non-stoichiometric formula, similar to that of $Sr_2CuO_2F_{2+\delta}$.[97] However unlike its strontium counterpart, this one does not have superconductive properties.
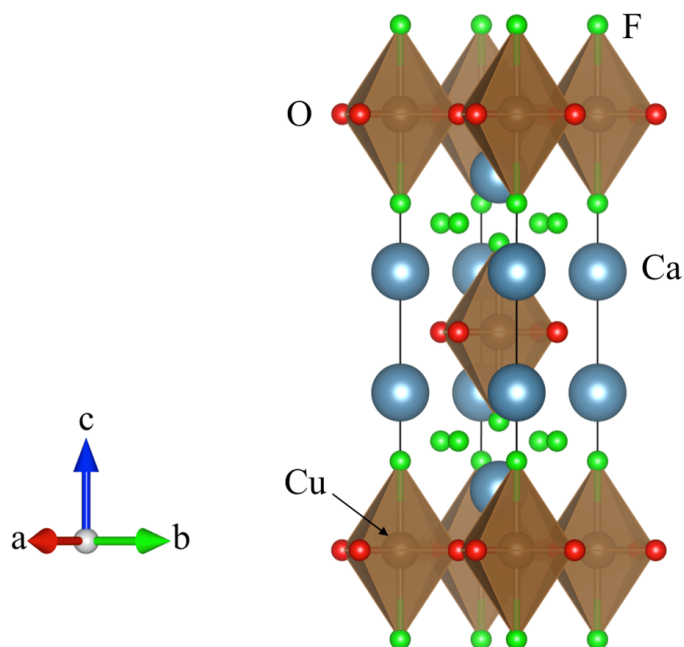
Figure 1.15: Crystal structure of $Ca_2CuO_2F_{2+\delta}$. Ca and Cu cation represented by light blue and brown spheres. The O and F anions are represented by the red and green spheres.

The cuprate series has the advantage that the B cation (copper) can expand its coordination from 4 to 6. This means that additional anions can be inserted into the structure through expanding the coordination of copper.

1.3.6.2 Anion-insertion into A_2PdO_3 type Compounds

Families of compounds where the B cation's coordination cannot be expanded have also been investigated. In particular, the palladate series of compounds which also show 213 stoichiometry and is isostructural to A_2CuO_3, has also been investigated for anion substitution.

As with cuprates the A_2PdO_3 (A = Pd, Ba) series of compounds have anion vacancies within their structure that can be exploited for anion insertion.[98] The incorporation of fluorides towards oxide fluorides has been investigated. The A_2PdO_3 compounds with A = Sr, Ba are isostructural to Sr_2CuO_3, Baikie *et al.*.[99]

In the case of the cuprates, fluorination acts to expand the coordination of copper cations from

4 (square planar) to 6 (octahedral). Not only does the coordination change but the oxidation state as well. Baikie *et al.* was able to prepare a series of compounds based on the formula $Sr_{2-x}Ba_xPdO_2F_2$.[98] These oxide fluorides have the palladium cations remain as square planar coordinated to 4 oxides, with the fluorides located between the strontium layers as shown in Figure 1.16.
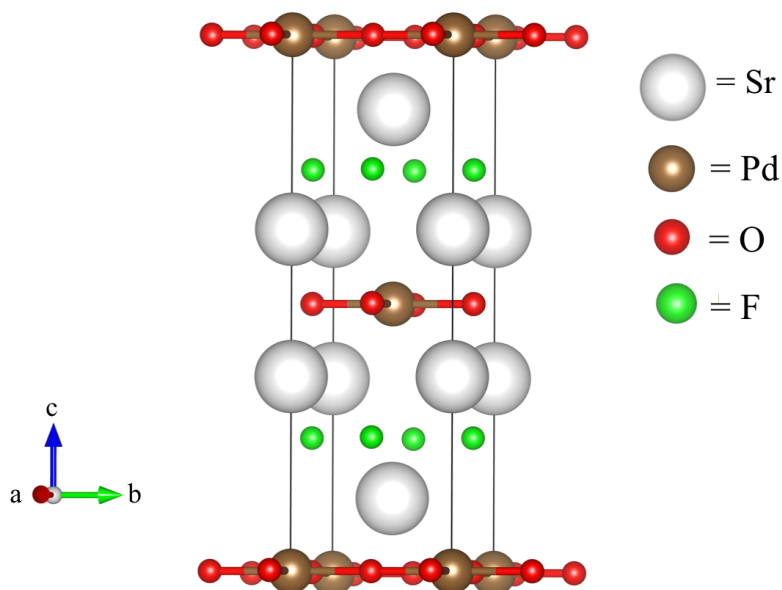
Figure 1.16: Crystal structures of $Sr_2PdO_2F_2$ showing that additional fluorides are not coordinated to the Pd cations.

The stoichiometric $Sr_2CuO_2F_2$, unlike the non-stoichiometric counter-part $Sr_2CuO_2F_{2+\delta}$, has the fluorides inserted occupying the same sites as the oxides, or located in the interstitial sites as shown previously in Figure 1.12.[94]

As seen within the formation of the $Sr_{2-x}Ba_xPdO_2F_2$ series, and $Sr_2CuO_2F_2$, anion insertion does not always result in the expansion of the coordination of the B cation. The $Ba_{2-x}Sr_xPdO_2F_2$ series has the additional anions occupy the interstitial sites whilst the palladium maintains its square planar arrangement with the fluoride anions located within the barium/strontium cation layers. This is potentially a result of the fluorides being small enough to fit within the sites, as well as the attraction present between the fluorides to the alkaline earth metal cations.

The square planar coordination has been found to be the most preferred within the Ba/Sr_2PdO_3

series. This is expected as the square planar arrangement is the most stable with this having the lowest energy form for a d^8 system. The orbital structure of Pd^{2+} in Figure 1.17, shows the 8 d-electrons arranged in a square planar and tetrahedral arrangement. This might explain why Pd^{2+}, a transition metal cation with a $4d^8$ configuration is more stable in square planar arrangement, and why coordination expansion is unfavourable. [100]

The stability for a d^8 transition metal in the square planar arrangement can be assessed through a comparison of the crystal field splitting energy. The energy for the tetrahedral and square planar coordination have both been converted to that of an octahedral value. In the tetrahedral arrangement Pd^{2+} would have a value of -0.36 Δ_o whilst in the square planar arrangement it would be -2.44 Δ_o. [101] This is due to the increased stability from filling the d_{xy} orbital, rather than having a lone electron in the $d_{x^2-y^2}$ orbital.
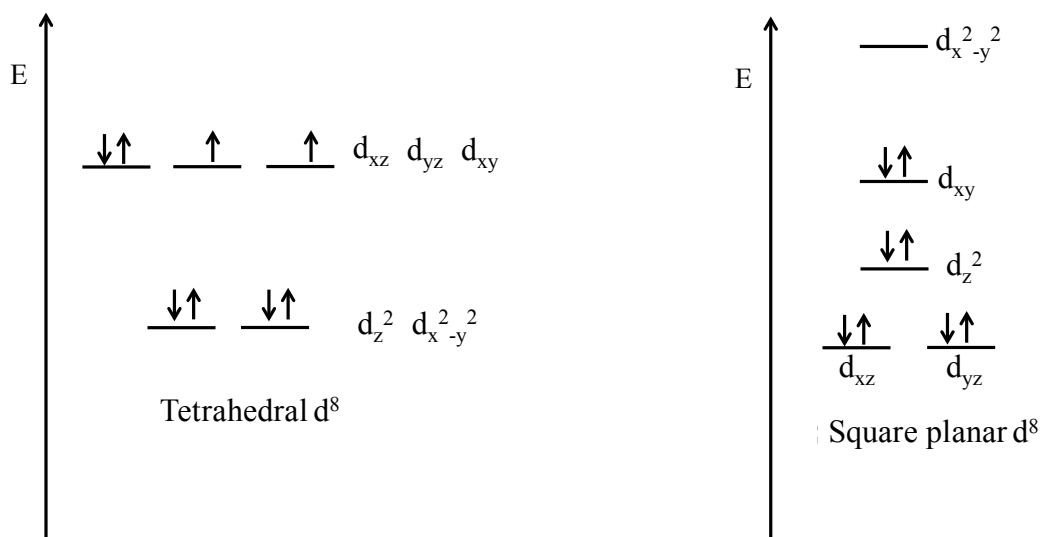
Figure 1.17: The arrangement of the 8 d-electrons in the tetrahedral and square planar coordination

1.3.7 Anion Insertion into non-oxide A_2BX_3 compounds

The Ce_2MN_3 (M = Cr and Mn) series have similar crystal structures to that of the A_2CuO_3 and A_2PdO_3 (A = Sr and Ba) series with anion vacancies. [102, 103] The formation of the mixed metal fluoro-nitride has also been found possible through the direct insertion of fluorides into Ce_2MnN_3 (Figure 1.18). This was reported by Headspith *et al.* using an alternating gases

approach of F_2 and a mixture of 10 % F_2 in N_2.[104] This allowed for the formation of the mixed anion compound $Ce_2MnN_3F_{2-\delta}$. A study of the structural refinement and magnetic moments showed that the coordination of Mn had expanded whilst remaining in the solid state. The oxidation state had also changed, resulting in a suggested mixture of $Mn^{2/3+}$.
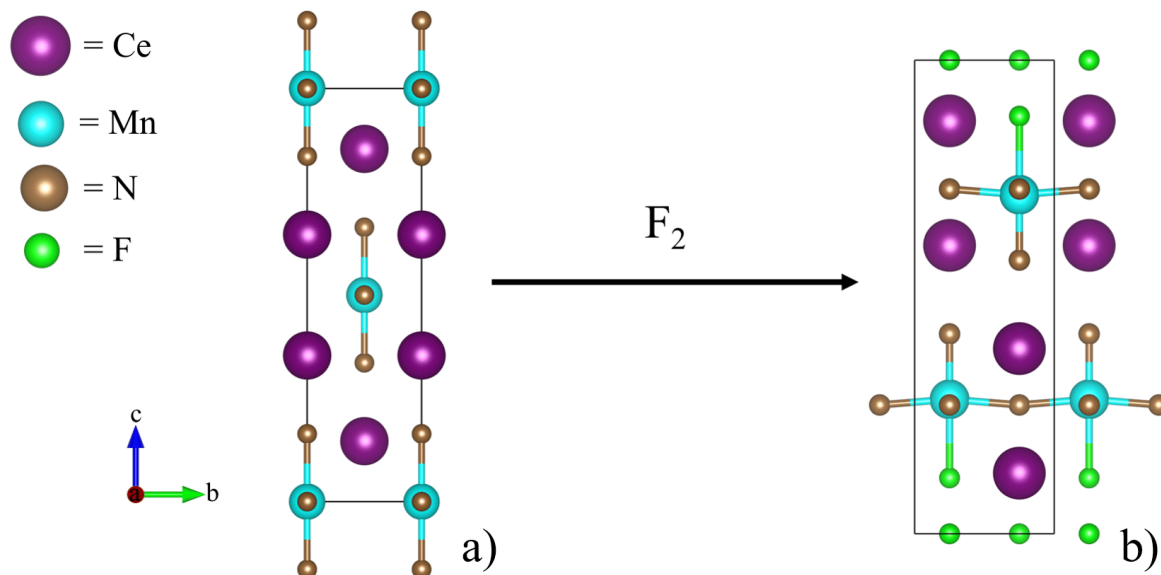
Figure 1.18: The direct reaction of Ce_2MnN_3 a) with F_2 gas to prepare $Ce_2MnN_3F_{2-\delta}$ b).

The process of fluorinating Ce_2MnN_3 was carried out in a similar manner used for that of Sr/Ca_2CuO_3 and Ba/Sr_2PdO_3 via a solid-gas reaction. The difference however, is that only anion insertion and not substitution was observed when preparing $Ce_2MnN_3F_{2-\delta}$. As with Sr_2CuO_3 to $Sr_2CuO_2(CO_3)$, anion insertion results in the symmetry increasing from an orthorhombic (Ce_2MnN_3) to tetrahedral ($Ce_2MnN_3F_{2-\delta}$) system.[104] The fluorides are bonded to the Mn along with additional nitrides and expand the coordination to a distorted octahedral arrangement with 5 nitrides and 1 fluoride. This results in changing the coordination state of cations within the solid along with the oxidation state.

1.3.8 Mixed anion compound applications

The purpose of preparing mixed anion compounds is that it can create a novel series of materials with diverse properties. In the case of oxide fluorides such as the $A_2CuO_2F_{2+\delta}$ (A

= Sr, Ca and Ba) series, these have found applications within the field of superconductivity.[105, 106] In these types of materials an excess of fluorides can result in Cu^{2+} being partially oxidised to Cu^{3+} leading to a change in the electronic properties of the material. Jansen and Letschert have synthesised solid solutions of the perovskites $CaTaO_2N$ and $LaTaON_2$ which have been used as non-toxic yellow-red dye pigments.[107] These oxide nitride types of compounds have been considered as a potential alternative to cadmium based pigments, which are toxic. Maeda and Domen explored the use of oxide nitrides and oxide sulphides for photocatalytic water splitting to produce hydrogen and oxygen.[108] These studies are just a few examples of different applications of mixed anion compounds. The aims of this project is to design and study routes to prepare mixed anion compounds through the utilisation of environmentally damaging gases such CO_2. These mixed anion compounds could then be used further for different chemical applications.

1.4   Mixed Metal Anion-Carbonate compounds

1.4.1   Mixed Metal Anion-Carbonate compounds

This work aims at utilising CO_2 as a dopant and structure "modifier" through reactions with solid materials towards preparing mixed anion compounds, in particular mixed metal oxides towards mixed metal oxide carbonates. Previous work into anion insertion found that compounds with a 213 structure, $Sr_{2-x}A_xCuO_3$ (A = Ca and Ba) can directly react with different anions (F^- and Cl^-) towards mixed anion materials. These compounds were investigated here in direct reactions with CO_2 towards preparing mixed metal oxide carbonates of the formula $Sr_{2-x}A_xCuO_3(CO_3)$. This reaction will involve CO_2 reacting with metal oxide groups (Sr-O) to form carbonates ($SrCO_3$). This approach has been seen when using other alkaline earth metal oxides that utilise CO_2 for preparing carbonates, CaO to $CaCO_3$.[43, 109]

Oxide carbonate materials are compounds which contain distinctive groups of both oxides (O^{2-}) and carbonates ($CO_3{}^{2-}$). A variety of mixed metal oxide carbonates have been reported which show Ruddlesden-Popper type perovskite structures. An example is the layered iron oxide carbonate $Sr_4Fe_2O_6(CO_3)$ which was prepared in polycrystalline form via $SrCO_3$

and $FeCO_3$ reacting under a 10% CO_2 in N_2 atmosphere at 1100 °C.[83] The crystal structure in Figure 1.19 shows the carbonates located in the strontium layers and the possible positions for the oxides in the $(CO_3)^{2-}$ groups with their partial occupancy. These carbonate groups are themselves located between the FeO_5 polyhedra.
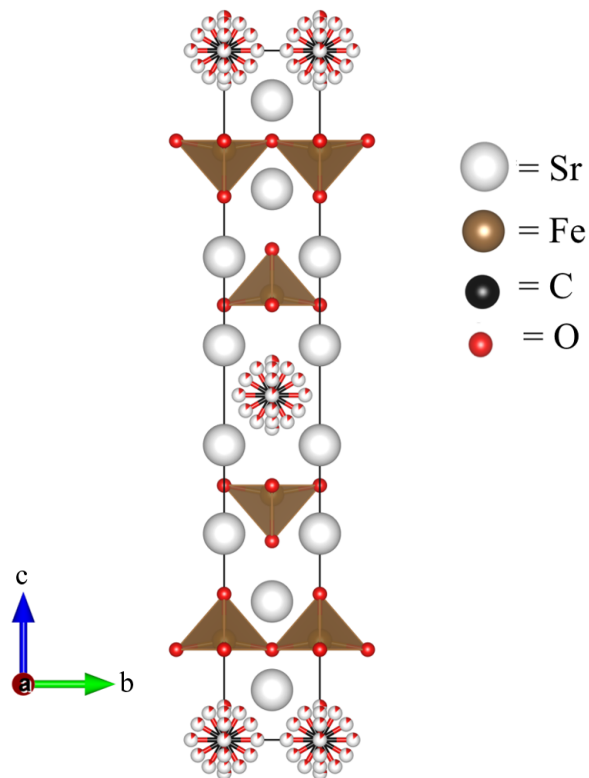
Figure 1.19: Crystal structure of $Sr_4Fe_2O_6(CO_3)$ showing the randomly occupied oxygen positions around the carbon, white spheres partially coloured in red.

Further work on this material, has shown that Fe^{3+} can be successfully substituted by other trivalent transition metals, giving the $Sr_4Fe_{2-x}M_xO_6(CO_3)$ (M = Cr, Sc, Ni and Co) series of compounds.[110, 111] These solid state solutions were prepared using stoichiometric amounts of metal oxides and carbonates and were reacted under the same conditions as for $Sr_4Fe_2O_6(CO_3)$. In each case the Ruddesden-Popper n = 3 type crystal structure had been maintained. The levels of substitution were found to be $0 \leq x \leq 1$ for Cr, $0 \leq x \leq 2$ for Sc, $0 \leq x \leq 1.5$ for Co and $0 \leq x \leq 1.1$ for Ni. The difference in the type of B cation showed to have an effect on the configuration of the carbonate groups connected to the MO_6 octahedra. This could result in the carbonates adopting either a "coat-hanger" or "flag" type arrangement as shown in Figure 1.20.
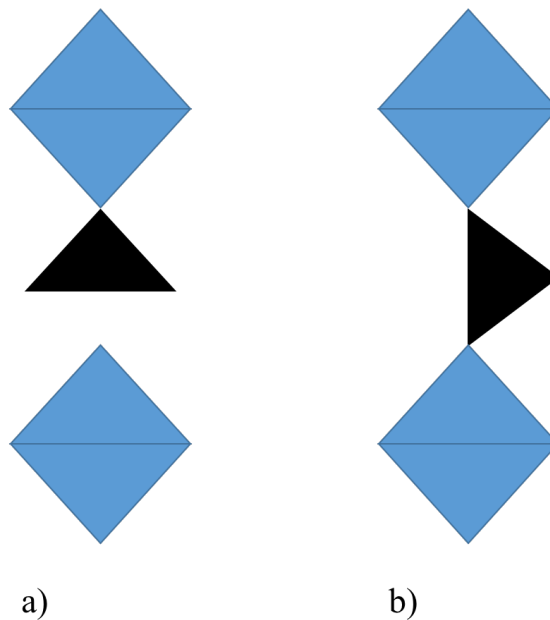
Figure 1.20: A illustration of the "coat hanger" a) and "flag" b) configuration of the carbonate ion shown by the black triangles. Either arrangement can exist in an oxide carbonate compound.

Changes in the B cation, allowed control over the magnetic properties of the oxide carbonate, as well as the configuration of the carbonates themselves.

Non-stoichiometric layered oxide carbonates have also been reported, which include $Sr_4Co_2(CO_3)O_{5.86}$ and the barium copper series $Ba_2M_xCu_{2-x-y}(CO_3)_yO_{2+\delta}$ (M = Cu, Cd, Ca; 0.05 < x < 0.25).[112, 113] These show a distortion in the oxides within the carbonates based on the bond length and angles that are located between the transition metal oxides layers. In the case of the barium-copper oxide carbonates these are described as carbocuprates in which Cu and C are both partially occupying the same sites.

1.4.2 $A_2CuO_2(CO_3)$ compounds

Another class of mixed metal oxide carbonates is based on the $A_2CuO_2(CO_3)$ (A = Sr, Ca and Ba) series.[80, 114, 115] These types of compounds have been found to have layers of ACO_3 and CuO_2 groups throughout their structure. It has also been suggested that the carbonates coordinate to the copper cations expanding their coordination from 4 to 6 resulting in a distorted

octahedral.

Multiple types of structures have also been reported for the different oxide carbonate compounds. In the case of $Sr_2CuO_2(CO_3)$ three different types of structures have been reported. In all cases a tetrahedral system is maintained with the space groups for each structure determined as *P4/mmm*, *I$\bar{4}$* and *P42$_1$2*.[80, 116, 117]The crystal structures are shown in Figure 1.21 with the reported unit cell parameters in Table 1.1.
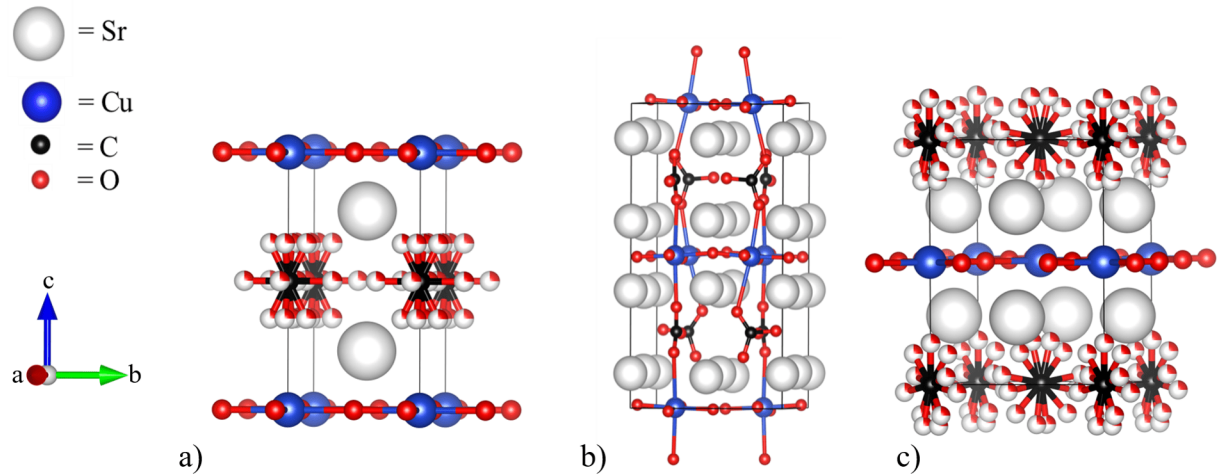
Figure 1.21: The three known structures of $Sr_2CuO_2(CO_3)$, a) *P4/mmm*, b) *I$\bar{4}$* and c) *P42$_1$2*. For a) and c) the partially occupied oxides, white spheres partially coloured in red.

Table 1.1: Unit cell parameters for the three $Sr_2CuO_2(CO_3)$ structures.

Space group	a Å	c Å	V Å^3
P4/mmm	3.9033(2)	7.4925(4)	114.15(4)
I$\bar{4}$	7.8045(1)	14.993(1)	913.22(7)
P42$_1$2	5.54364(8)	7.53823(11)	231.66(5)

One of the main difference is the position of the oxides surrounding the carbon atoms in the $(CO_3)^{2-}$ groups. For the *P4/mmm* and *P42$_1$2* structures, X-ray and neutron diffraction alongside Fourier transform maps show that the $(CO_3)^{2-}$ groups were disordered with the oxides in different positions with occupancies of 0.25. This arrangement of the $(CO_3)^{2-}$ groups is different to that reported by Miyazaki *et al.* with the space group, *I$\bar{4}$* which shows the oxides in fixed positions and forming a $(CO_3)^{2-}$ trigonal planar type configuration.[116]

This study also shows the oxide carbonate as having separate layers of CuO_6 octahedra and $(CO_3)^{2-}$ groups.

The *P4/mmm* type $Sr_2CuO_2(CO_3)$ structure was originally prepared as an intermediate during the formation of Sr_2CuO_3.[80] This was through heating stoichiometric quantities of $SrCO_3$ with CuO under a gas flow of air, nitrogen or oxygen for 14 hours at 940 °C. Miyazaki *et al.* prepared the *I4̄* phase through heating $SrCO_3$ and CuO under a O_2/CO_2 mixture at 1000 °C.[116] The *P4$_2$1$_2$* structure reported by Nakata *et al.* was found to only be present when $Sr_2CuO_2(CO_3)$ was heated to temperatures above 300 °C.[117]

In the interests of changing the chemical structure and properties of the oxide carbonate series, isovalent substitution has also been carried out by replacing strontium with barium to prepare the $Sr_{2-x}Ba_xCuO_2(CO_3)$ (0.4 > x > 2) series of compounds. As with $Sr_2CuO_2(CO_3)$ different space groups and structures have been reported for these types of compounds. In this case *I4̄* and *P4/mmm* show the same arrangement as with the $Sr_2CuO_2(CO_3)$, but with the barium occupying the strontium sites.[114, 118] The antiferromagnetic properties were also measured alongside the level of substitution. Based on this, a more complicated carbocuprate structure has been prepared which had the formula $(Ba_xSr_{1-x})_2Cu_yO_{2y+\delta}(CO_3)_{1-y}$ (0.4 ≤ x ≤ 0.65, y = 0.1) with copper occupying 10 % of the carbon sites.[119] These compounds were found to show superconductive properties up to 40 K. $Ca_2CuO_2(CO_3)$ was prepared at high pressures and temperatures of 6 GPa and 1325 °C by Kopnin *et al.*.[115] This showed a *P4/mmm* type structure with possible alignments for the oxides within the $(CO_3)^{2-}$ groups also proposed.

In the case of aliovalent substitutions, $Sr_{2-x}B_xCuO_2(CO_3)$ (B = K and Na) compounds were prepared and aimed towards replacing the Sr^{2+} with B^{1+} cations to change the oxidation state of the copper cation.[120] This synthesis involved high pressures as well as high temperatures under oxygen. This was to encourage the oxidation of Cu^{2+} to a Cu^{3+} state. The results showed for the $Sr_{2-x}B_xCuO_2(CO_3)$ series that successful doping was possible for Na at 0 ≤ x ≤ 1 and K at 0 ≤ x ≤ 0.7, with only K substitution showing superconductive properties at 13-23 K.[120]

All of the a fore-mentioned oxide carbonates have been prepared through the reaction of metal oxides and carbonates, under gaseous environments containing CO_2. These reactions

were also directed towards the stoichiometry of deserved products. Through isovalent and aliovalent substitution, it has been possible to not only prepare novel materials, but also to have them tailored towards properties such as superconductivity. Many of these oxide carbonate materials also share similarities to the 213 series $Sr_{2-x}A_xCuO_3$ (A = Ca and Ba). These 213 compounds were previously investigated for "filling up" their anion vacancies to prepare mixed anion compounds such as the $Sr_{2-x}A_xCuO_2F_{2+\delta}$ series. It is possible that CO_2 can react and "settle" within these anion vacancies with alkaline earth metal oxides to prepare carbonates resulting in $A_2CuO_2(CO_3)$ compounds.

This concept of vacancies within structures that can be filled is similar to that of porous materials such as zeolites which physisorbe CO_2 molecules into their pores.[121] These types of materials also have alkaline earth metal oxides MO (Ca, Sr, Ba) within their crystal structure. MO compounds have also been studied towards capturing CO_2 through the formation of metal carbonates at their particle surface.[42] It can therefore be proposed that these 213 type compounds could be used as a suitable candidate to capture CO_2 through their anionic vacancies and M-O groups to form metal carbonates within their structures. This can lead to the formation of mixed metal oxide carbonate compounds through direction reaction of A_2BO_3 with CO_2, to simultaneously utilise the greenhouse gas.

1.4.2.1 Structure of CO_2 and $(CO_3)^{2-}$ ion

In order to react CO_2 with solid materials to form mixed anion compounds, the fundamental chemistry of this molecule needs to be understood. CO_2 is a linear molecule which has a $D_{\infty h}$ point group. The structure consists of a carbon bonded to two oxygens via double bonds which are 116 pm in length.[122] The molecular orbital, MO diagram for CO_2 is shown in Figure 1.22. This explains how electronic orbitals from the central carbon interact with the oxygens resulting in the doubled bonded linear structure.
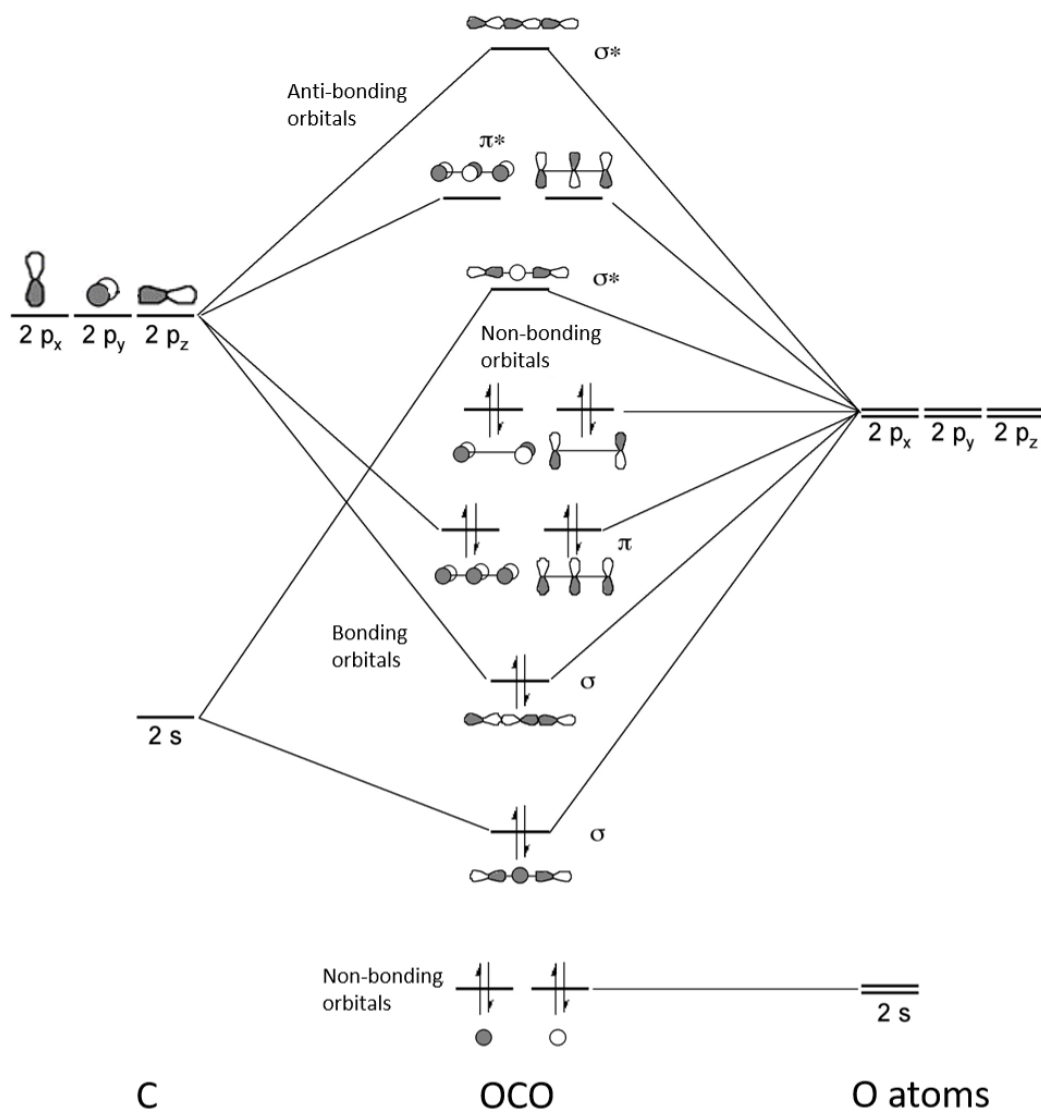
Figure 1.22: The molecular orbital diagram of CO_2 showing the types of bonding between the C and O atoms.

The MO diagram shows how the 2s and $2p_{x,y,z}$ orbitals of the C atom interact with the $2p_{x,y,z}$ orbitals of the O atoms resulting in 4, bonding, non-bonding and anti-bonding orbitals respectively. The 2s orbitals from the carbon interact with that of the $2p_z$ of the O atoms due to sharing the same group orbital symmetry. In the case of bonding orbitals two σ and two π are present which forms the two double bonds in CO_2. The lone pairs on the oxygens also contribute to the oxides having a δ- charge when considering CO_2 reactivity.

When considering the reactivity of CO_2 within the anion vacancies of crystal structures. The molecule's size needs to be taken into account. The kinetic diameter of CO_2, considering its

electron density is that of 3.3 Å.[32] Due to its linear structure with an oxygen at either side, the molecule shows no natural dipole moment. In the presence of a Lewis base, such as a metal oxide group, CO_2 has been shown to have Lewis acidic properties which causes a shift in the electronic density resulting in a δ- charge on the oxygens and a δ+ on the carbon (Figure 1.23).[123]
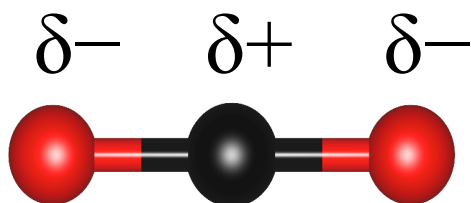
Figure 1.23: The induced dipole moment form of a CO_2 molecule showing the δ charges on the carbon and oxygens.

This type of interaction is what allows CO_2 to accept a lone pair electron on the carbon and bind to the metal oxide, MO for forming a metal carbonate, MCO_3.[109,124,125]

$(CO_3)^{2-}$ has a trigonal planar structure with a D_{3h} point group. Each of the oxides are separate to one another by an angle of $120°$. In this structure it is expected that there will be one double bond to one oxygen with two single bonds for the others. As a result of the additional oxide a carbonate will have a 2- charge. The electrons themselves are resonating which acts to affect the chemical bonds.[126] Figure 1.24 shows the Lewis structure of $(CO_3)^{2-}$ and the possible positions for the different bonds from electrons resonating.
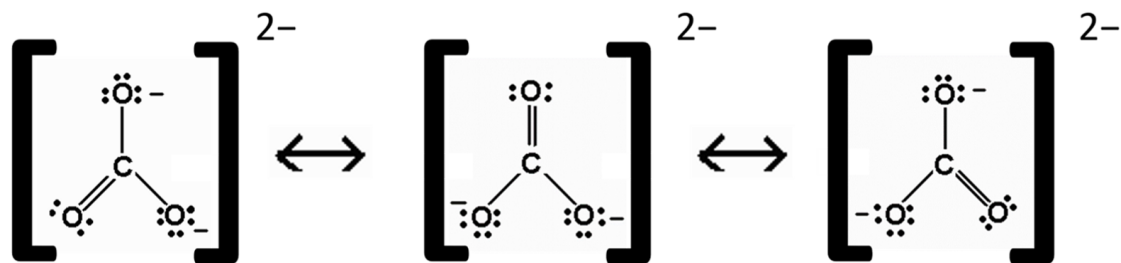
Figure 1.24: Lewis structure of $(CO_3)^{2-}$ showing the resonance of bonds.[126]

This resonance of electrons is important when considering the crystal structure of carbonate compounds. C-O has an average single bond length of 142 pm with an average C=O double

bond at 116 pm.[67] The crystal structure of carbonate groups in solids however has bond lengths which can exist between these values. This is a result of a pair of electrons being delocalised across all of the carbon-oxygen bonds. This carbonate structure is also possible through the reaction of CO_2 with metal oxide M-O$^-$ groups towards MCO_3.

When considering the formation of MCO_3 from CO_2 and a metal oxide MO, one of the ways to study this reaction is through the change in energy using thermodynamics, as well as vibrational behaviour. Thermodynamics acts to measure the change in energy resulting as MO reacts with CO_2 towards forming MCO_3. The vibrational behaviour can be used to provide information on the overall structure of the chemical bonds during the reaction.

1.4.3 Thermodynamics principles

The core principles of thermodynamics are in studying the interaction between energy and matter.[127, 128] This in particular is the flow of energy from one state to another. In the case of chemical reactions this can be used to predict the behaviour of a chemical system, and be used to determine its favourability. Energy itself can be defined as the ability to work, and when considering the energy of particles the two main types are kinetic energy (K.E.) and potential energy (P.E.). K.E. is the energy from the motion of particles such as rotation, vibration and translation. P.E. is the energy particles store within the electrostatic attraction and repulsion. The First Law of Thermodynamics states that energy can not be destroyed or created. Therefore the energy will be shifted between P.E. and K.E. via work and heat.

During a chemical reaction existing bonds are broken which requires energy (endothermic) whilst new ones are formed which releases energy (exothermic). By being able to determine the energy change under constant temperature and pressure this can be denoted by the Gibbs free energy, ΔG.

$$\Delta G = \Delta H - T\Delta S \tag{1.8}$$

Here H and S denote the enthalpy and entropy of a system respectively with T the temperature K. In the terms of studying the energy change of chemical reactions for forming carbonates,

the enthalpy H has been considered and can be defined as:

$$H = U + PV \tag{1.9}$$

where U, is the internal energy which is the total energy contained within a system, P the pressure and V the volume. Using ΔH values for the chemical bonds breaking and forming, an enthalpy of reaction ΔH_{rxn} can be determined. This is from the difference in enthalpy from the bonds being formed (product) from those being broken (reactant).

$$\Delta H_{rxn} = \sum \Delta H_{products} - \sum \Delta H_{reactants} \tag{1.10}$$

Through computational methods a thermodynamic model can be used to study novel reactions between metal oxide based compounds with CO_2 to form metal carbonates via the reaction enthalpy. In particular this can be used to determine the ΔH_{rxn} of a mixed metal oxide forming a mixed metal oxide carbonate when directly reacting with CO_2. This study has focused on the enthalpy of the reaction and not the entropy during the computational calculations. This is due to 3rd law of thermodynamics which states that for a crystalline state that approaches $T = 0$ K, the temperature the theoretical calculations were carried at, that the entropy would be typically close to zero.[129]

1.5 Vibrational spectroscopy

Spectroscopy is a technique used to study the interaction of electromagnetic radiation with matter. This technique has many applications ranging from nondestructive examination of materials to medical diagnostic imaging (MRI). In a chemical context, spectroscopy is used to study energy transitions in atoms and molecules. The transitions are interpreted and can serve to identify the molecule or potentially give information about the possible molecular structure. Spectroscopy is a powerful tool for chemists to help identify compounds that have been prepared. In order to investigate the capturing process and behaviour of CO_2 inside a material, vibrationial spectroscopy is a highly useful technique as it can be used to study the

chemical bonding in a variety of different materials. This can be used not only to identity the types of compounds present, but also provide insight into the chemical reaction taking place. An example being if it is a surface reaction or in the bulk structure of a compound.

Whilst a molecule is vibrating the chemical bonds rapidly change in length as they are extended and compressed. The oscillating changes in the bond length represents the attractive and repulsive forces in a molecule as it vibrates. The different types of vibrational modes a molecule can undergo vary, from bending and stretching to twisting. These types of oscillations have been studied and are described as behaving harmonic and anharmonically.

Different molecules will have various vibrational modes based on their type of structure. A normal mode is a result of the excitation from one state to the next highest level. The number of normal modes a molecule can have is a result of the degrees of freedom minus those of rotational and translational modes. The equation used to determine the number of modes for a molecule is given by 3N-6 for non-linear and 3N-5 for linear molecules. N is equal to the number of atoms in a molecule, with the degrees of freedom for a non-linear molecule being 3N, with 6 of the non-vibrational modes coming from translation and rotational modes (three each) for linear, and only 5 for non-linear. In the case of linear molecules such as CO_2 this will have four vibrational modes from there being only five non-vibrational modes. This is a result of one of the rotational modes resulting in no overall change in the position of the atoms.

1.5.1 Harmonic oscillations

Harmonic oscillations are a simple way of describing the vibrational behaviour of molecules based on classical mechanics. This concept comes from studying how a massless spring can oscillate when attached to two objects (diatomic molecules). A representation of a harmonic oscillation for a chemical bond within a diatomic molecule is shown in Figure 1.26. This represents how the chemical bonds oscillate during a vibration and can be described using Hooke's Equation (1.11)
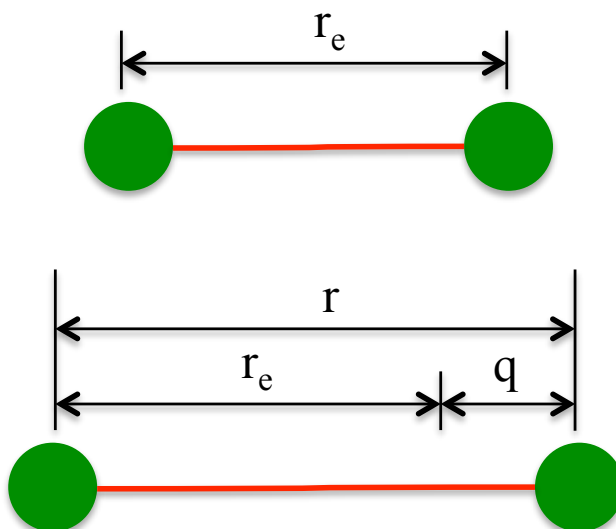
Figure 1.25: An example of a diatomic molecule being stretched as a result of being excited from absorbing energy and vibrating. q denotes the displacement (r - r_e) with r the length of the bond whilst vibrating and r_e when at equilibrium.

The restoring forces of the chemical bond as it vibrates can also be determined using the following equation:

$$F = -kq \tag{1.11}$$

where F is the restoring force of the spring, q is the displacement (r - r_e) with r the length of the bond whilst vibrating and r_e when at equilibrium and k the force constant.

The potential energy of the vibrations V, is determined using the displacement q and the force constant k.

$$V = \left(\frac{1}{2}\right)kq^2 \tag{1.12}$$

For a harmonic oscillation the vibrational energy levels are discrete and each is characterised by the quantum number v which can have values of 0, 1, 2, 3 and so forth.

$$E_v = \left(v + \frac{1}{2}\right)\frac{h}{2\pi}\sqrt{\frac{k}{\mu}} \equiv h\omega\left(v + \frac{1}{2}\right) \tag{1.13}$$

The energy E_v value is calculated at a particular frequency ω cm^{-1} using the reduced mass of the atoms μ, Planck's constant $h = 6.626 \times 10^{-34}$ m^2 kg s^{-1}, speed of light $c = 2.998 \times 10^{10}$ cm s^{-1} and the k of the bond as it vibrates.

$$\omega = \frac{1}{2\pi c}\sqrt{\frac{k}{\mu}} \tag{1.14}$$

Under a harmonic oscillation model a diatomic molecule will have equally spaced energy levels starting with $\frac{1}{2}h\omega$ at the bottom of the harmonic potential well with spacing between the layers equal to $h\omega$. The result of an excitation can have $v = 0$ going to a $v = 1$ energy level that gives the value $\Delta E_v = h\omega$, this can be used the determine the force constant and with Equation 1.14 the vibrational frequency.

For harmonic oscillations the relationship between the length of the chemical bond and energy values are represented in a potential energy well, Figure 1.26. This graph demonstrates how energy changes from the bonds expanding and compressing. For harmonic oscillations this curve is always symmetric, this makes the theoretical calculations of harmonic frequencies relatively simple.
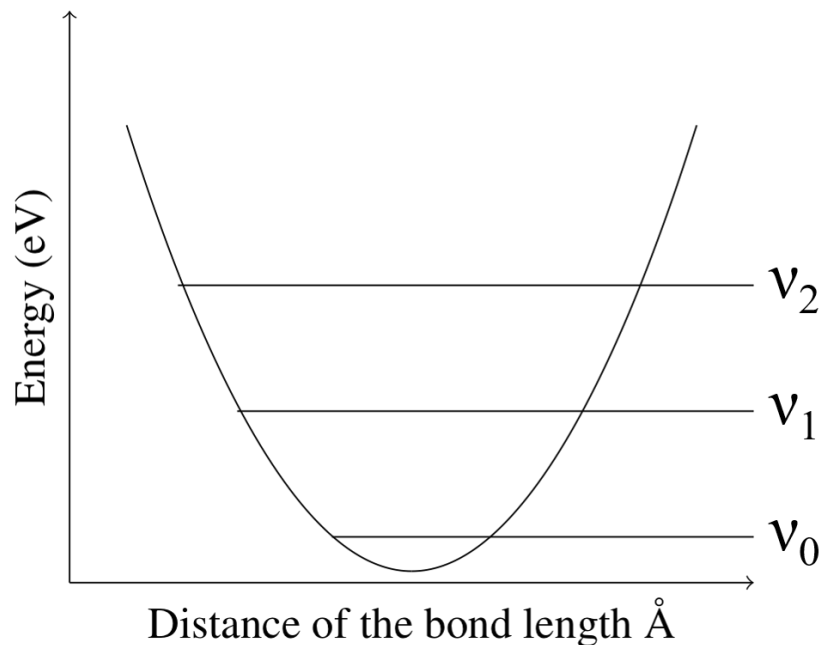
Figure 1.26: The potential energy well for a harmonic oscillation

However, the problem is that this simplified representation is of low accuracy when comparing vibrational frequencies to experimental results. Molecules vibrate via anharmonic oscillations, which is more complex than a harmonic system due to the bond energies changing significantly. An example being how chemical bonds can become weaker when stretched, as well as the repulsive forces that exist when two atoms are pushed closer together from the bonds being compressed. Thus, for calculating vibrational results that would be a better comparison to experimental data, more advanced anharmonic oscillation would need to be considered.

1.5.2 Anharmonic oscillations

The harmonic oscillation model is a simple but poor representation for how molecules behave when vibrating. When a molecule vibrates the energy levels are asymmetrically separated as they are based on anharmonic oscillations. These are much more complex than harmonic oscillations, but can provide an accurate description of molecular vibrations. Anharmonic oscillations are caused from the change in energy values as the chemical bonds are being compressed and extended. As the q decreases the nuclei of atoms will be pushed closer

together, this causes large repulsion energy values. Also as q increases the chemical bond will dissociate. The potential function with respect to the inter-atomic distance r, $V(r)$ has the following form:

$$V(r) = De\left(1 - e^{-a(r-r_e)}\right)^2$$

(1.15)

This has D_e as the dissociation energy, r_e is the equilibrium inter-atomic distance with a as a constant for the curvature. Equation 1.16 calculates the energy values in the anharmonic Morse potential .

$$E(v) = \omega\left(v + \frac{1}{2}\right) - \frac{\omega^2}{4D_e}\left(v + \frac{1}{2}\right)^2,$$

(1.16)

Here the energy of vibrations $E(v)$ is determined from the harmonic frequency ω and the vibrational quantum number v. The transition energy between two adjacent vibration levels (v and $v+1$) can also be calculated using Equation 1.17.

$$E(v+1) - E(v) = \omega - \frac{\omega^2}{2D_e}(v+1)$$

(1.17)

An example of the Morse potential is given in Figure 1.27 compared to that of the harmonic potential.[130] Significant difference in the energy curve for anharmonic systems is due to the incorporation of the dissociation energy when looking into vibrating bonds. This results in the vibrational levels no longer being equally separated due to the anharmonic constant affecting the allowed energies.

53
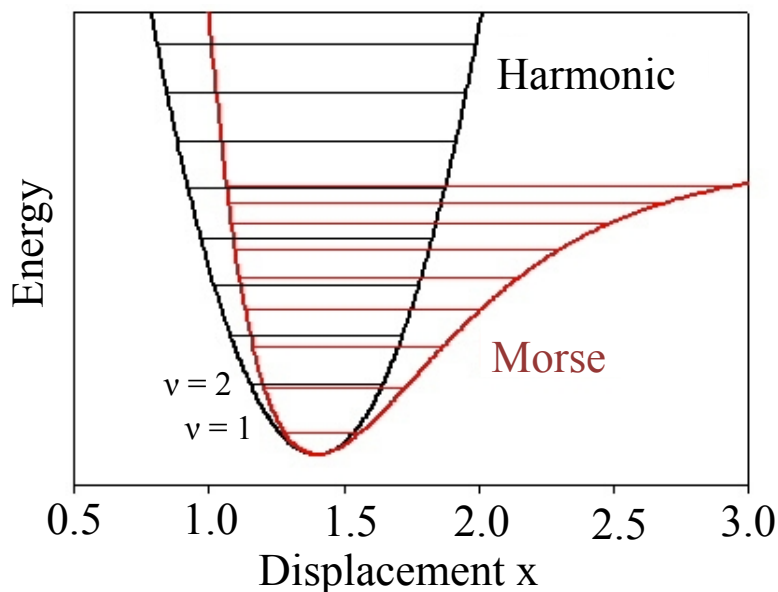
Figure 1.27: The Morse potential (red curve) is compared to that of a harmonic oscillation potential (black curve) for a diatomic molecule.[130]

In studying the vibrational behaviour of molecules to map out a reaction pathway, the types of calculations being performed will use the harmonic oscillation model. As a result these calculations would be expected to determine vibrational frequencies generally higher than experimental frequencies that behave anharmonically. In order to take this into consideration vibrational scaling factors have been used, and have been discussed in Chapter 6. This has been an attempt to improve the comparison of calculated harmonic values to experimental anharmonic frequencies, without having to resort to computationally expensive anharmonic calculation methods.

1.5.3 Vibrational behaviour of CO_2

In the field of surface sciences, studies using vibrational spectroscopy can explain how adsorbing molecules interact with a material. For example, the catalytic reaction of CO to a metal surface can be monitored by overseeing how the vibrations of C-O bonds are behaving.[131] In the specific case of studying the chemical behaviour of CO_2 as it is being adsorbed into a porous material, vibrational methods can be used to monitor how the molecule interacts within the pores of the structure.[132] This is through monitoring how the frequencies change

depending on how CO_2 is being adsorbed. This can result in either blue or red shifts being observed. Here, red shifts show a decrease in the frequency values from the chemical bonds being increased, where as blue shifts show an increase from the bonds shortening. This can be used to study what type of adsorption process is taking place from the vibrational frequencies of CO_2 on the material's surface.

One of the main areas to understand about the vibrational behaviour of CO_2 is the phenomenon of Fermi resonance. This is due to CO_2 having anharmonic vibrational behaviour which acts to change its frequency values. A brief insight into the vibrational behaviour of CO_2, as well as its non-fundamental vibrations with Fermi resonance is presented here.

The experimental vibrational frequencies for CO_2 are 667 cm^{-1} for the two bending degenerate modes (v_2 and v_2'), 1388 cm^{-1} for symmetric stretching (v_1) and 2349 cm^{-1} for asymmetric stretching (v_3) modes.[133] A representation of the different types of modes is shown in Figure 1.28 with the Infrared (IR) and Raman spectra of CO_2 in Figure 1.29.[134] For Raman spectroscopy a change in the polarisability of the molecule needs to occur for the vibration to be observed.

Symmetric stretching mode v_1 Bending mode perpendicular v_2'

Asymmetric stretching mode v_3 Bending mode parallel to plane v_2
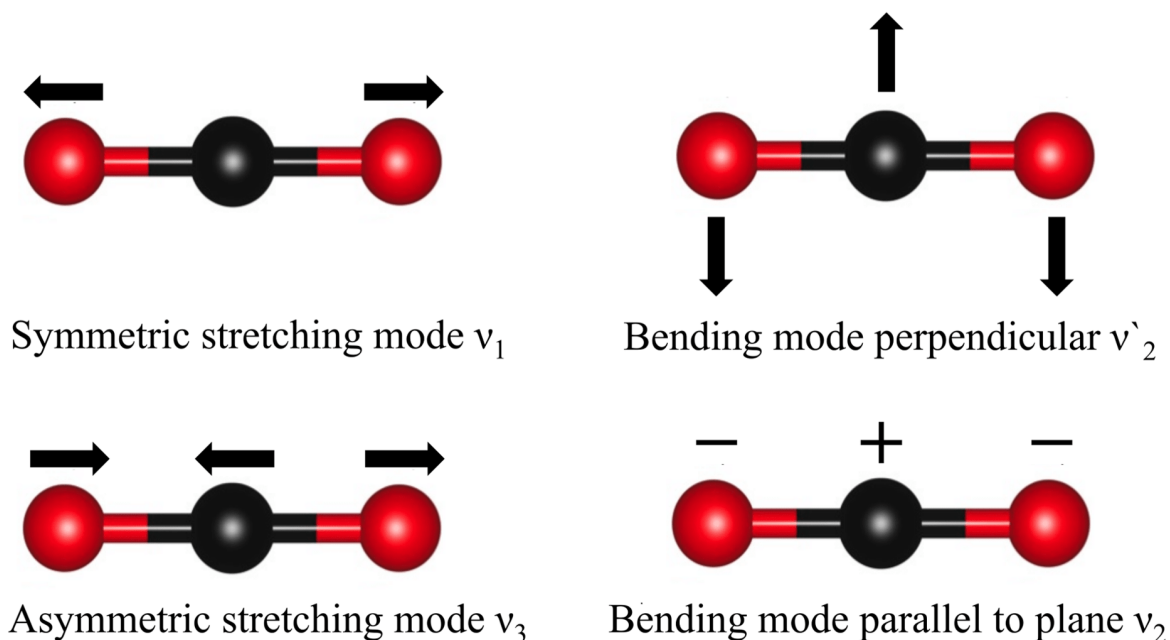
Figure 1.28: The bending and stretching vibrational modes of a CO_2 molecule.
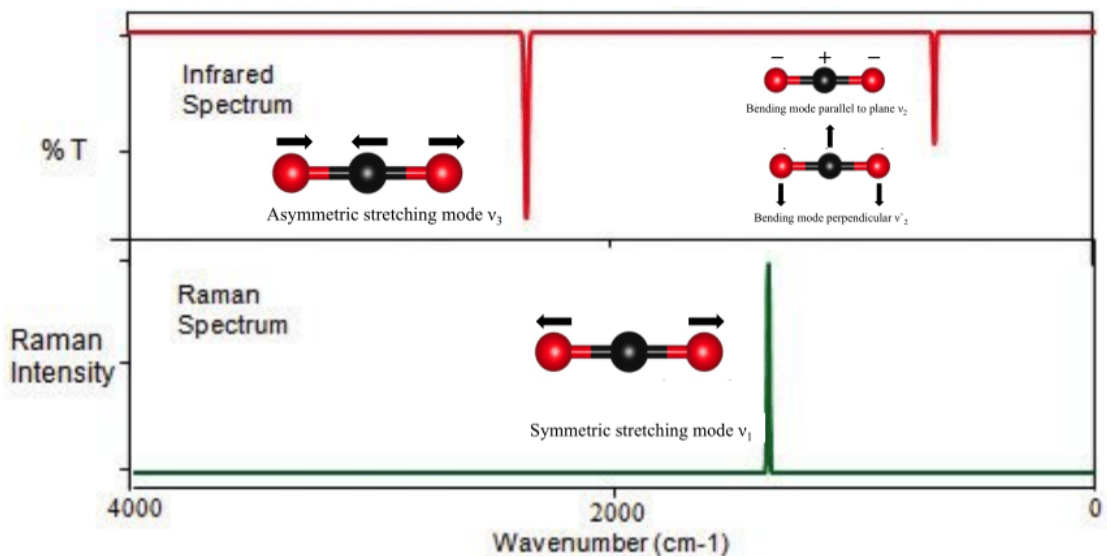
Figure 1.29: The IR and Raman spectra of CO_2 showing which modes are active in which analytical technique.[134]

Fermi resonance in CO_2 occurs when two vibrational modes which are nearly the same in energy and symmetry move closer towards each other. This results in one of the modes taking intensity from the other.[135] This phenomenon is also known as "intensity borrowing" with one band increasing at the expense of the other. These normally happen between a fundamental frequency (bending or stretching) and a overtone or combination band. Combination bands occur when more than one fundamental vibration is being excited at the same time to produce a peak which is the sum of two separate frequencies. A combination band would be for example, two separate modes such as v_2 and v_3 producing a frequency of combined values $(v_2 + v_3)$. Overtones occur when a vibrational modes is being overall excited and exceeds a transition values of one, for example $v = 0$ to $v = 2$.

CO_2 has been studied as a prime example of how Fermi resonance affects the vibrational frequencies of molecules.[136] The first overtone of CO_2 occurs with v_2 which is expected at a 2 x v_2 value of around 1334 cm^{-1}. However due to the similarity in energy and symmetry, Fermi resonance occurs between v_1 and $2v_2$. It would be expected that a strong peak would be present at 1388 cm^{-1} and a weaker peak at 1334 cm^{-1} however, Raman spectroscopy shows these peaks both have strong intensities and are moved further apart.

56

1.5.4 Vibrational behaviour of carbonate $(CO_3)^{2-}$ groups

Carbonates much like CO_2, have distinctive vibrational frequencies which can be used to determine their presence within a compound. $(CO_3)^{2-}$ being a non-linear structure with four atoms shows a total of 6 vibrational modes.[137] These have been described within Table 1.2 with their frequency values also given.

Table 1.2: The vibrational modes and frequencies of a single $(CO_3)^{2-}$ free ion.[137]

Vibrational mode	Frequency (cm^{-1})
Symmetric stretching ν_1	1064
Symmetric bending ν_2	879
Asymmetric stretching ν_3 & ν_3'	1415
Asymmetric bending ν_4 & ν_4'	680

The different vibrational modes of $(CO_3)^{2-}$ shown in Figure 1.30, are a result of the carbon oxygen bonds either bending or stretching with various ones active in either IR or Raman spectroscopy.
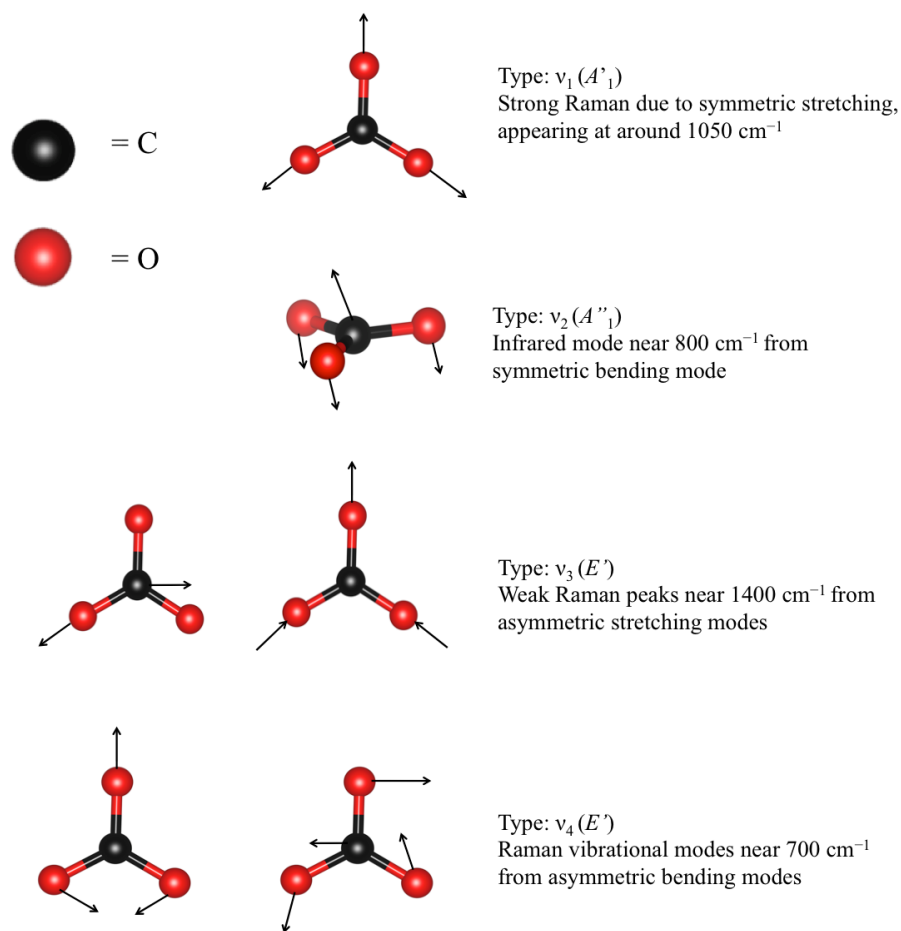
Figure 1.30: Vibrational frequencies of free $(CO_3)^{2-}$, arrows represent displacement vectors.

Vibrational frequencies can be used to monitor how the structure of CO_2 changes as it forms into a carbonate. The frequencies can also indicate how stable the structure is after being optimised into its lowest energy state using computational methods, as only positive frequencies will be present. Chapter 5 and 6 explains how computational methods were used to calculate the vibrational frequencies within the ACO_3 (A = Sr, Ba and Ca) series along with $Sr_2CuO_2(CO_3)$. The changes in the A cations will effect the reduced mass ν value and as a result the vibrational frequencies as described in Equation 1.14. This is important to consider as this could also provide insight into the reaction of AO groups with CO_2 for preparing ACO_3. The aim of this study is to provide a more in depth understanding of the carbonate groups calculated within the oxide carbonate via vibrational methods.

Chapter 2

Experimental Procedure and Computational Methodology

Solid state synthesis of compounds requires a variety of experimental and characterisation techniques. This is aimed at not only preparing materials, but also to study the in-situ reaction processes. This chapter provides a brief introduction into the techniques and equipment used throughout this project.

2.1 Synthetic Methods

The preparation of mixed anion carbonates involved firstly, the preparation of "parent" compounds using high temperature ceramic methods. This was then followed by the reaction of the starting compounds with CO_2 gas. In most cases an alternating gaseous approach was used to minimize the formation of binary carbonates as secondary phases.

2.1.1 High Temperature Ceramic Synthesis

One of the most well known solid state synthetic route for preparing polycrystalline (powder) materials is the "ceramic method". Solid precursors in polycrystalline form are initially ground together, with a volatile solvent for increased dispersion. This mixture is then heated

within a furnace for an extended period (hours to days). Many solid state reactions require temperatures (> 500 °C) as they require a high energy input. This is to over come the lattice energy within the starting reagents so the ions can move from their fixed coordination and diffuse to new positions forming a new structure.[138] This approach is important for preparing a variety of solid state materials. One of the main advantages of the ceramic method is in its simplicity compared to alternative solvent-based methods. The disadvantages are however, in the high temperature demands, and poor surface contact between grains that can result in low rates of diffusion. As repeated re-grindings and heating cycles maybe required. One of the ways to increase the contact between grains is through compression of the polycrystalline powder into pellets. This forces increased contact between the grains and can reduce the amount of regrinding and reheating cycles needed.

High temperature reactions have been the main method used in the synthesis of the various starting compounds within this project. This included the mixed metal cuprates $Sr_{2-x}A_xCuO_3$ (A = Ba and Ca), as well as oxide carbonates $Sr_{2-x}A_xCuO_2(CO_3)$ (Chapter 3), mixed metal palladate $Sr_{2-x}Ba_xPdO_3$ (x = 0 − 2) series and Ce_2MnN_3 (Chapter 4).

In this project some starting materials could only be prepared via ceramic methods in a "non-air" atmosphere. In the case of the $Sr_{2-x}Ba_xCuO_3$ (x = 0 − 0.5) series the reaction process had to be carried out under O_2 gas, whilst the preparation of Ce_2MnN_3 required and inert atmosphere such as N_2.

Many of the starting compounds were prepared from mixing reagents in stoichiometric quantities towards a desired product. The starting material would then be placed into a ceramic boat to be inserted and heated in a tubular furnace as shown in Figure 2.1. The sample would be placed as close to the thermocouple as possible so it is heated to the desired temperature.
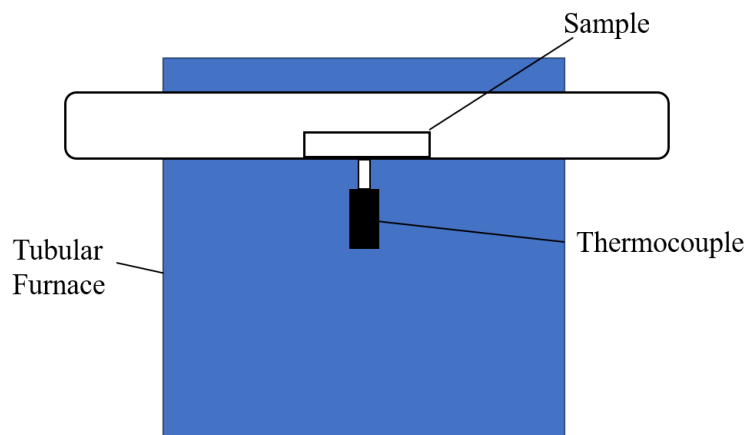
Figure 2.1: Schematic of a sample placed into a tubular furnace for heating.

These reactions would normally be carried out at 1000 °C using a 5 °C/min heating rate. The heat cycle itself could potentially last for up to 14 hours. Repeated heating cycles would be used to react any remaining reagents towards preparing a pure product phase.

2.1.2 Solid-Gas Reactions

Solid-gas reactions have been carried out for the purpose of incorporating CO_2 within the parent compounds for preparing mixed anion phases. In the case of controlling the direction of the reaction towards a desired product, an alternating gases approach had to be used. This involved first heating a sample to specific temperatures such at 1000 °C under a type of gas that the sample would be inert too. The atmosphere would normally be the same as that the starting materials was prepared at, such as air for Sr_2CuO_3 and N_2 for Ce_2MnN_3.

Once the temperature had reached equilibrium the gas could then be changed to CO_2 to react with the sample at this specific temperature. This type of synthesis has been essential for the reactions with CO_2 towards preparing the $Sr_{2-x}A_xCuO_2(CO_3)$ (A = Ba and Ca, and x = 0 – 0.5) series. This method was also applied with all other compounds so they would react with CO_2 at specific temperatures towards preparing mixed anion compounds.

2.2 Equipment

2.2.1 Furnaces

The synthesis of a variety of the compounds were carried out in two main types of furnaces. These include the box and tubular furnaces.

The box furnace (muffle or chamber furnace) used consist of a cuboidal chamber with a heating element located in the walls. The type of box furnace used was that of a a Carbolite CWF 1200, shown in Figure 2.2 and has an operational range of 25-1200 °C.

Figure 2.2: Carbolite CWF 1200 type box furnace.

The advantage of this type of furnace is in its volume as it allows a variety of samples to be inserted and to react from the same heating cycle. However, the main disadvantage of this piece of equipment is that it does not support non-air environments. As a result the tubular type furnaces were used, as these have the ability for different gaseous environments to be used during the heating cycles.

A tubular furnace consists of a cylindrical (tubular) heating region surrounded by the heating

elements and thermal insulation. The type used in this project was a Elite thermal services split horizontal tube furnace as shown in Figure 2.3. An inner reaction tube (quartz) is commonly inserted into these furnaces, in order to contain reagents, protect the delicate inner workings of the furnace from chemical emissions and to allow control over the reaction atmosphere used. The advantage of this type of furnace equipment is that different gases such as O_2 and N_2 can be used for the reactions.

Figure 2.3: Elite thermal systems horizontal tubular furnace with quartz tube inserted.

When using this equipment for solid-gas reactions, the sample would be placed into a alumina crucible and located within the tube and positioned over the thermal coupling. This is so the sample will be as close to the designated temperature as possible. Once this is complete the two ends of the tube would have quartz taps attached using small amounts of grease so the system would be air tight. Initially gas would be flushed through the system for 10 to 15 minutes to remove any air present. Afterwards the reaction program would then proceed to a desired temperature and dwell time. The gas flow was monitored using a oil bubblier located on the exhaust outlet. All reactions generally had the gas flow rate at 2-3 bubbles per second.

2.2.2 Glovebox

In order to deal with air/mostiure sensitive solids and prevent undesired reactions with either moisture, O_2 or atmospheric CO_2, samples would generally be stored inside a Ar filled glovebox.

Ce_2MnN_3 as well as its precursor compounds Ce and Mn metal, all show air and moisture sensitivity. As a result these reagents, as well as the preparation process itself would be carried out in a glove box (Figure 2.4).

Figure 2.4: A M-Braun Lab-Star glove box used in this project.

The glove box operates with a permanent circulating argon atmosphere, passing over molecular sieves and copper based catalysts, to remove moisture and oxygen. The glove box contains oxygen and moisture sensors with their levels maintained at $O_2 \leq 0.1$ ppm and $H_2O \leq 0.1$ ppm. Access in and out of the glove box is achieved via a transfer port on the side of the instrument. The port is evacuated using a rotary pump and refilled with argon gas before being opened to the main chamber. This evacuation procedure is repeated several times to minimise the amount of air entering the system.

2.3 Structural Determination

2.3.1 Crystallography

Crystalline solid compounds consist of highly ordered arrays of atoms arranged in a three-dimensional (3D) arrangement. As a result, crystals, show a high degree of symmetry that can be used to describe their structure.

2.3.1.1 Symmetry

The symmetry of crystals can be understood and studied via symmetry operations. In solid state chemistry these can be split into two groups. This includes point symmetry, where at least one point will remain unaltered after a symmetry operation, and translation symmetry which involves a movement in a direction along an axis. The most commonly used notation for the five point symmetry elements are listed below;

Inversion ($\bar{1}$) - Each point is projected through an inversion centre, creating an equivalent point through the other side,

Rotation (n) - Each point is rotated anticlockwise around an axis by an angle of $360°/n$, where, for a lattice, n can be 1, 2, 3, 4 or 6 and the element is simply noted by the integer number.

Reflection (m) - All points are reflected through a mirror plane, creating new points equidistant from the mirror.

Rotoinversion ($\bar{n}$) - Each point is first subjected to a rotation (as described above) and then an inversion through a point located on the rotation axis. This element is given the symbol $\bar{n}$ which is the integer relating to the rotation. This symmetry element is sometimes referred to as an improper rotation axis.

Rotoreflection ($\tilde{n}$) - A rotation followed by reflection in a mirror plane which is perpendicular to the rotation axis, this is given the symbol $\tilde{n}$, again with n as the integer relating to the

rotation. This element is rarely used as each one is equivalent to an alternative rotoinversion axis. A comparison of the rotoreflection and rotor inversion operations are also described in Table 2.1.

Table 2.1: Comparison between the rotoreflection and rotor inversion symmetry operations.

Axis of rotoreflection	Axis of rotoinversion
$\tilde{1}$	$\bar{2}(m)$
$\tilde{2}$	$\bar{1}$
$\tilde{3}$	$\bar{6}$
$\tilde{4}$	$\bar{4}$
$\tilde{6}$	$\bar{3}$

When considering 3D crystal structures the symmetry can be extended with further operations possible such as translational components.

Rototranslation (n_m) - This is referred to as a screw axis, which is a combination of a rotation of $360°/n$ followed by a translation parallel to the rotation axis. The n_m symbol represents these symmetry operations where the rotation, m is the integer and the translation is over a distance of m/n. An example of a screw axis is 3_1 where there is a rotation of $360°/3 = 120°$ and a translation of 1/3 of the length of the unit cell along the rotation axis. [139]

Reflectotranslation - Referred to as a glide plane and is a combination of two symmetry operations. In this case a reflection followed by a translation parallel to the mirror plane. There are three different combinations which are labelled either a, b and c, referring to a translation along these respective axes of 1/2 the unit cell. An n labelled glide plane, which involves a diagonal translation of 1/2 across one face or through the body of the unit cell and a d (diamond glide) which involves the same motion across 1/4 of the unit cell.

2.3.1.2   Crystal Systems

Crystal systems can be described through the unit cells which are repeatable units of one or more atoms. These can be used to represent the symmetry of the crystal system. A unit cell

is a three dimensional section of a structure, which when translated by a distance equal to its dimensions act as the building blocks to yield the overall crystal structure and its type of symmetry. The dimensions of the unit cell can be defined by the length of the edges, a, b and c as well as the angles that lie in between α, β and γ. The angle α is always present between b and c, β between a and c and γ between a and b. These are shown within a unit cell in Figure 2.5.
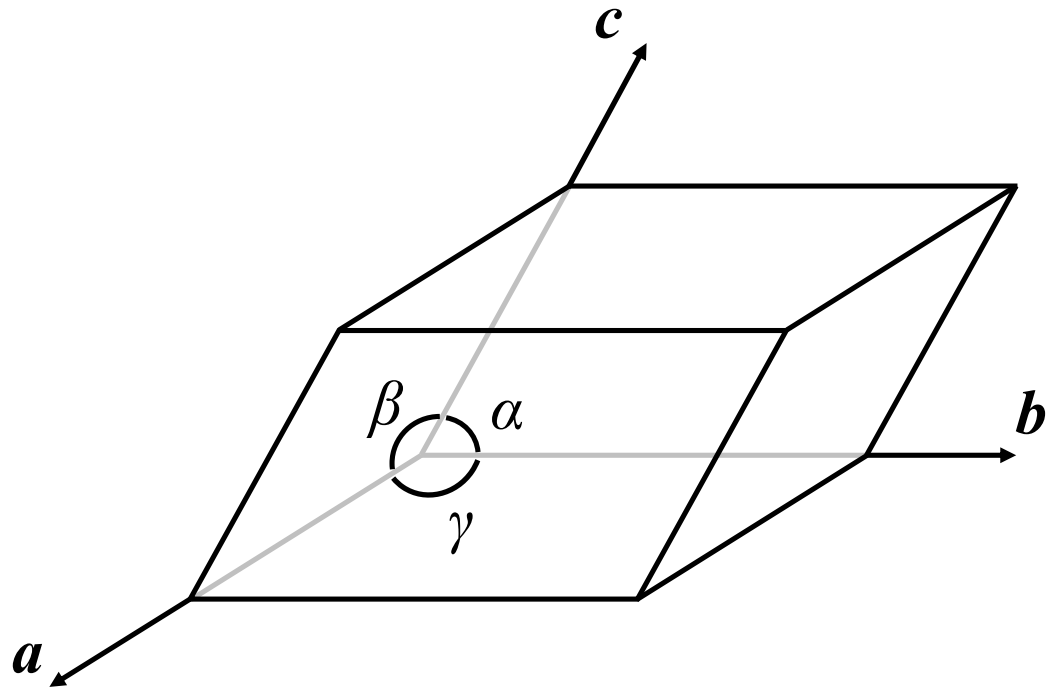
Figure 2.5: The vectors and angles representing the unit cell.

In crystallographic terms the unit cell of any possible ordered crystalline material can be classified within one of the seven crystal systems. This is dependent on its symmetry which is related to the cell dimensions and angles between the unit cell vectors. The general relationships between the crystal systems to the lattice parameters is outlined in Table 2.2.

Table 2.2: The seven crystal systems

System	Unit cell
Triclinic	$\alpha \neq \beta \neq \gamma \neq 90°, a \neq b \neq c$
Monoclinic	$\alpha = \gamma = 90°, \beta \neq 90°, a \neq b \neq c$
Orthorhombic	$\alpha = \beta = \gamma = 90°, a \neq b \neq c$
Trigonal/rhombohedral	$\alpha = \beta = \gamma \neq 90°, a \neq b \neq c$
Hexagonal	$\alpha = \beta = 90°, \gamma = 120°, a = b \neq c$
Tetragonal	$\alpha = \beta = \gamma = 90°, a = b \neq c$
Cubic	$\alpha = \beta = \gamma = 90°, a = b = c$

The type of crystal systems acts to reflect the type of symmetry of the unit cell. A cubic unit cell has the highest level of symmetry with the lowest being triclinic.

2.3.1.3 Lattices

The description of crystalline materials can be carried out via the mathematical concept of lattices. A lattice is made from the infinite ordered array of points that each show identical surroundings.[139]

Lattice types can be placed into four different groups: primitive (P), body centred (I), all face-centred (F), and face-centred in a given direction (A-centred, B-centred, C-centred), A, B or C. A representation of all the different lattice types is presented within Figure 2.6 with all lattice types represented with a cubic system for simplicity. In all cases the lattices are defined with their origins (0,0,0) set on a lattice point. Depending where a point is in the lattice defines how much of that particular point contributes to one of the unit cells, and how much is shared with others. Lattice points at the corners of a unit cell are shared between 8 adjacent cells, points on faces between 2, edges by 4 and a lattice point in the centre contributes 1 single point to the unit cell.
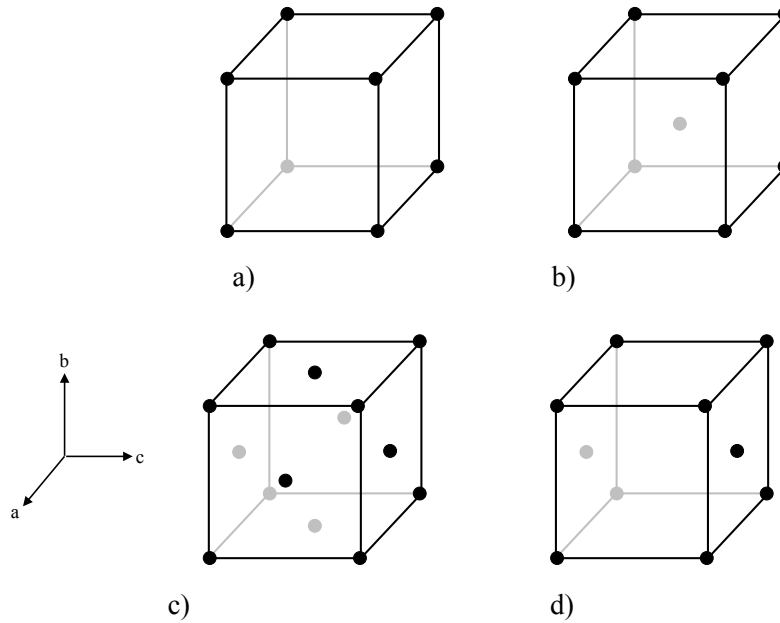
Figure 2.6: Representations of the different types of lattices showing (a) primitive (P), (b) body-centred (I), (c) face-centred (F) and (d) C-centred lattices.

The four different lattice types are then combined with the seven crystal systems to further categories the crystalline systems in the form of the 14 Bravais lattices. This has the crystal system types defined by their minimum symmetry requirement. All 14 Bravais lattices are shown in Figure 2.7

Crystal system	Lattice symbol	Minimum symmetry requirements
Triclinic	aP	None
Monoclinic primitive	mP	One two-fold axis or one symmetry plane
Monoclinic centred	mC	
Orthorhombic primitive	oP	Any combination of three mutually perpendicular two-fold axes or planes of symmetry
Orthorhombic C-face-centred	oC	
Orthorhombic body-centred	oI	
Orthorhombic face-centred	oF	
Tetragonal primitive	tP	One four-fold axis or one four-fold improper axis
Tetragonal body-centred	tI	
Trigonal (Rhombohedral)	hR	One three-fold axis
Hexagonal primitive	hP	One six-fold axis or one six-fold improper axis
Cubic primitive	cP	Four three-fold axes along the body diagonals
Cubic body-centred	cI	
Cubic face-centred	cF	

Figure 2.7: Description of the 14 Bravais lattices.

The next step towards describing the structure of 3D shapes lies in the symmetry elements which can give rise to multiple types of point groups. A point group is a label used to describe an isolated shape based on the point symmetry it possesses. These types of groups, as with point symmetry elements show that at least one point will remain unaltered. In the case of 3D shapes with a crystal system there are in total 32 point groups which are possible. When the 32 point groups are combined with the 14 Bravais lattices and the translational symmetry elements, this can result in describing the 230 space groups. These space groups are used to classify all the possible 3D repeating patterns within a crystalline material.

2.3.1.4 Space groups and Notations

Each of the 230 groups are usually defined in the terms of symmetry elements that they posses. These groups are numbered and contain unique symbols used to describe their most significant symmetry elements. The symbol can be split into two sections, the first being a label for the type of lattice present i.e P, F, I, A, B, C, R (Primitive to Rhombohedral) with the second set of symmetry elements defined by the Hermann-Mauguin symbols. These symbols refer to the type of symmetry operations present along the a, b and c directions. For example, the space group 71, *Immm*, describes a body-centred lattice with the Hermann-Mauguin symbols showing that a mirror plane is present in the a, b and c directions. The number of space groups possible for each crystal system which amounts to 230, is presented in Table 2.3.

Table 2.3: Number of space groups in each crystal system

System	Number of space groups
Triclinic	2
Monoclinic	13
Orthorhombic	59
Trigonal/rhombohedral	25
Hexagonal	27
Tetragonal	68
Cubic	36
Total	230

These space groups are able to describe all the possible 3D repeating patterns available for crystalline materials.[139]

2.3.1.5 Position of Lattice Points

In order to describe completely the crystal structure of a material it is necessary to include the atomic positions of each atom present within the unit cell. One of the simplest ways to do this is to have one lattice point set as the origin with the coordinates fixed at (0,0,0) in the a, b and c direction of the unit cell. Other lattice points can then be described through the given vector of $\mathbf{P}(uvw)$ and fully through Equation 2.1:

$$\mathbf{P}(uvw) = u\mathbf{a} + v\mathbf{b} + w\mathbf{c} \qquad (2.1)$$

where u, v and w are taken as the integers. Using this type of labelling a point can be described in relation to the origin. For example if $\mathbf{P}(101) = 1\mathbf{a} + 0\mathbf{b} + 1\mathbf{c}$. This has one point in the unit along the a and c axis direction, with no movement in the b. This point can then be labelled as (101). It is also possible for the u, v and w values to be negative represented by $\bar{u}$, $\bar{v}$ and $\bar{w}$. An example of a label for a point can be $0\bar{1}0$ which is located one unit cell along -b.

This type of atomic position notation can also be used to describe the lattice planes within a unit cell. Lattice planes are those that contain at least three lattice points. These also act to periodically intersect the overall lattice structure. Miller indices are used to describe the lattice planes and correspond to the reciprocal of a point at which a plane intersects the unit cell at each edge. The Miller planes are represented by the letters *h*, *k* and *l* in the form of (*h*, *k* and *l*). One example is a (020) plane which intercepts 1/2 along the *b* axis, but does not intercept the others. In this notation the Miller indices have their numerical values reduced to the lowest set of integers if necessary. Miller indices are highly important in powder X-ray diffraction and are used to label the peaks within a pattern.[140]

2.4   Diffraction

2.4.1   Theory of Diffraction

One of the major techniques for determining the structure of crystalline solids is centred on the work of English physicists Sir W. H. Bragg.[141] This work involved diffraction of X-rays by a solid to identify its crystal structure and showed how the face shape of crystals are related to the reflection of X-ray beams at certain angles present in the structure.

Diffraction is a result of the interaction of waves to result in a diffractogram/interference pattern. Waves, which are described as having large wavelengths (e.g. 4000-7000 Å) are scattered elastically (i.e. without change in energy) and are refracted by atoms. Those which show a wavelength that is either of a similar or smaller size than that of the atomic spacing within a crystalline material, can interact within the crystal to be diffracted. The scattered waves from an ordered array of atoms can either constructively (in phase) or destructively (out of phase) interact with one another with an illustration shown in Figure 2.8.
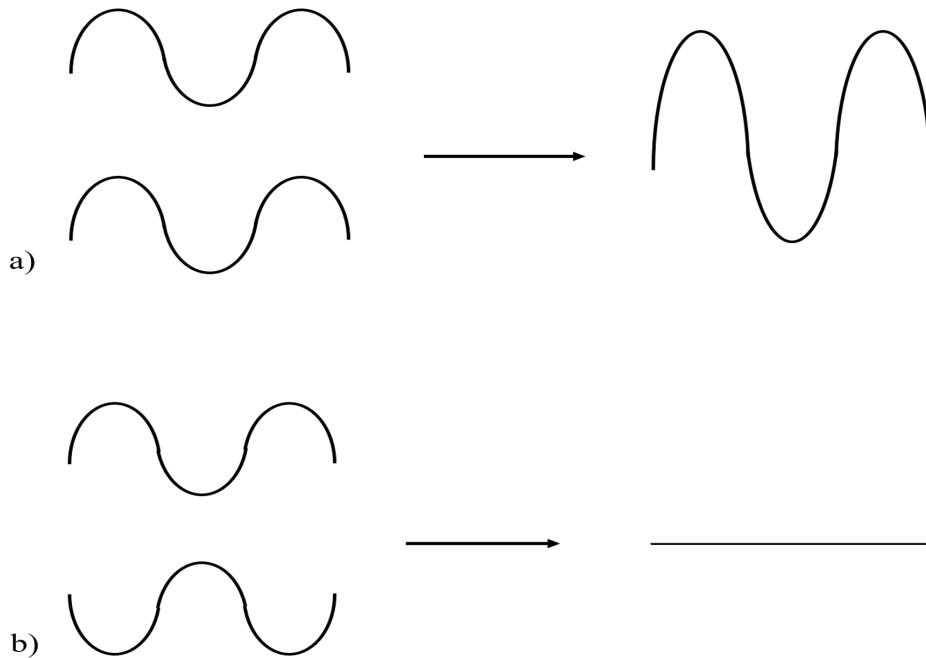
Figure 2.8: The constructive a), and destructive b), wave interference for X-rays.

The phase of each wave with respect to one another is dependent on the atoms and crystal structure and as a result will diffract in a unique manner.

W. H. Bragg's work showed a simple and frequently used description of how diffraction from a crystal structure occurs. This assumes that the partial specular reflection of incident radiation occurs along a series of parallel layers of atoms (Figure 2.9). As crystalline structures tend to have an ordered array, thousands of planes of the atoms are able to reflect a small fraction of the incident radiation.

X-rays have been found to have a wavelength between 1×10^{-8} to 1×10^{-10} meters with a frequency between 1×10^{16} to 1×10^{20} Hz. C. G. Barkla showed that X-rays can be polarised by scattering from solids, due to the wavelengths of X-rays being comparable with that of atom spacing in crystals (1×10^{-10} m).[142] This type of electromagnetic radiation could therefore be used to map out the atomic arrangements in crystals via diffraction patterns.[143]

The resulting reflected beams can interact in either a constructive or destructive manner. Constructive interference will only occur when the phase difference between the reflected waves is an integer number of wavelengths. The conditions in which a constructive interference can occur can be described by the Braggs equation (Equation 2.2);

$$n\lambda = 2d\sin\theta \qquad (2.2)$$

where n is an integer, λ the wavelength, d the spacing between the lattice planes and θ is the angle between the incident radiation and plane of atoms. The equation can only be applied in cases where $\lambda \leq 2d$.
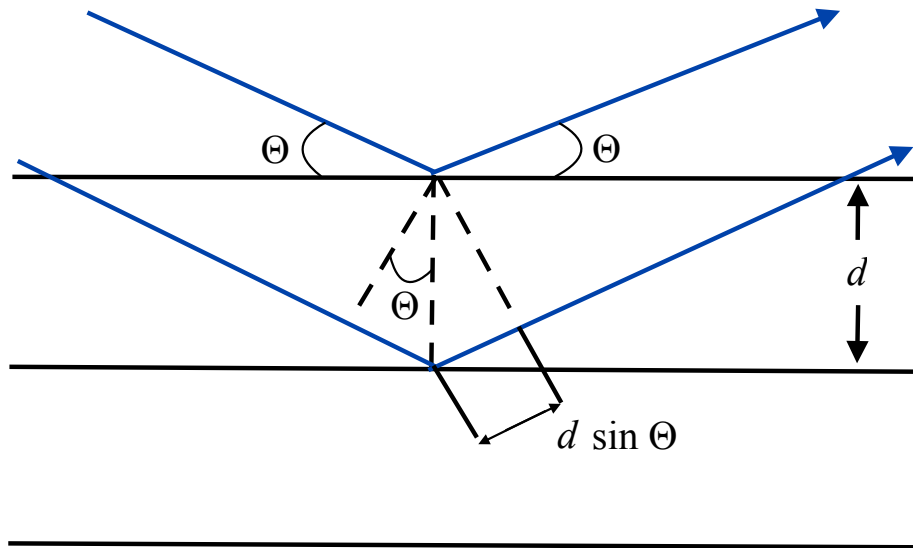
Figure 2.9: Representation of the diffraction of radiation within the crystalline atomic layers used to derive Bragg's equation. d is the spacing between the parallel atomic planes and θ is the angle between the planes and incident radiation.

Each type of crystal is a result of multiple groups of planes separated by different d spacings. These are referred to, as previously mentioned, as Miller indices labelled hkl. The crystal planes themselves are susceptible towards the atomic size and crystal structure, hence collection of the diffraction radiation from each family of planes provides a unique pattern.

Structural information on the relative atomic positions can be derived from the intensity of the constructive waves. The main method for studying the crystal structure of polycrystalline materials is powder X-ray diffraction which is discussed in section 2.4.3.

2.4.2 Generation of X-rays

In general X-rays are produced as a form of electromagnetic radiation with a value of wavelength (λ) = 0.1 nm. The X-rays themselves are a result of electrons from a high voltage cathode i.e. a tungsten filament, being bombarded onto a metal target.[144] In the case of the XRD equipment used, an anode of copper acts as the metal target in a vacuum tube. A schematic of a laboratory X-ray tube is presented in Figure 2.10.
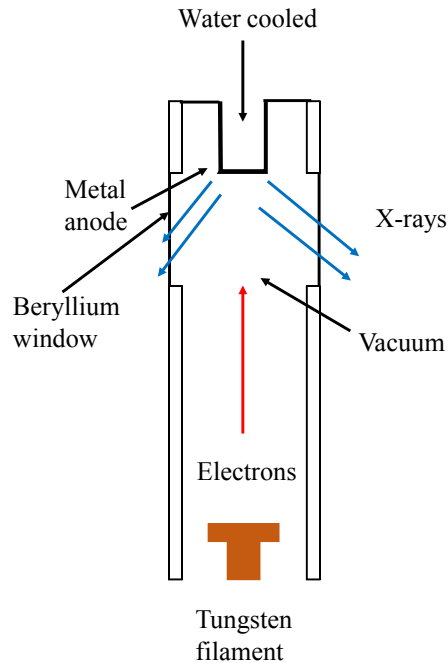
Figure 2.10: Schematic diagram of a X-ray generating tube.

X-ray radiation is generated via the rapid deceleration of electrons as they hit the metal target. This form of radiation is referred to as Bremsstrahlung radiation. Additionally, electrons from the filament can knock electrons, in the target, from the inner shells of the atoms e.g. 1s K shell. This vacancy is then filled by one of the electrons from the outer orbitals (2p and 3p) immediately occupying the vacant 1s level. The release in energy from this movement of electrons to different orbital is what causes the transmission of X-ray and is describe in Figure 2.11.
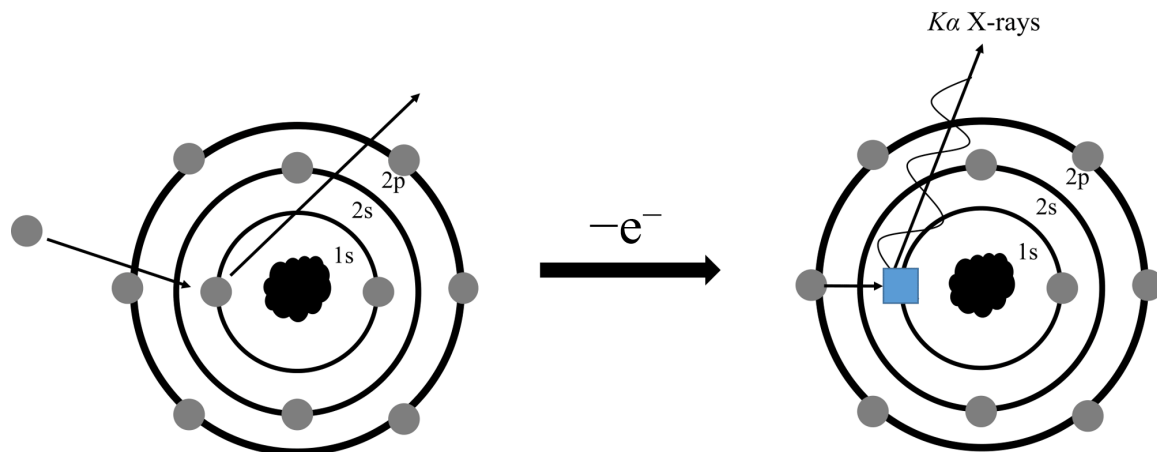
Figure 2.11: Illustration of X-ray generation. The electrons are represented with grey spheres, the nucleus of the atom by the black central cluster. The electron vacancy is represented by the blue box.

This process of X-ray generation results in the release of two types of radiation beams, the stronger K-α radiation and the weaker K-β. These labels are derived from the type of electron removed, i.e. K for a 1s electron, and the subscript α indicates that the electron goes down one energy level ($2p \rightarrow 1s$), β for two ($3p \rightarrow 1s$) energy levels. An illustration of the movement of the electrons from different energy levels is shown in Figure 2.12 for copper metal. Of the radiation types, K-α is often the most used for analysing samples, with K-β filtered out using either a silicon or germanium monochromator. A copper source will have wavelength values for each type of radiation with K-α = 1.54184 Å and K-β = 1.39222 Å. Figure 2.13 shows the X-ray emission spectra which has two sets of doublets corresponds to K-α_1, K-α_2 as well as K-β_1 and K-β_2.[145]
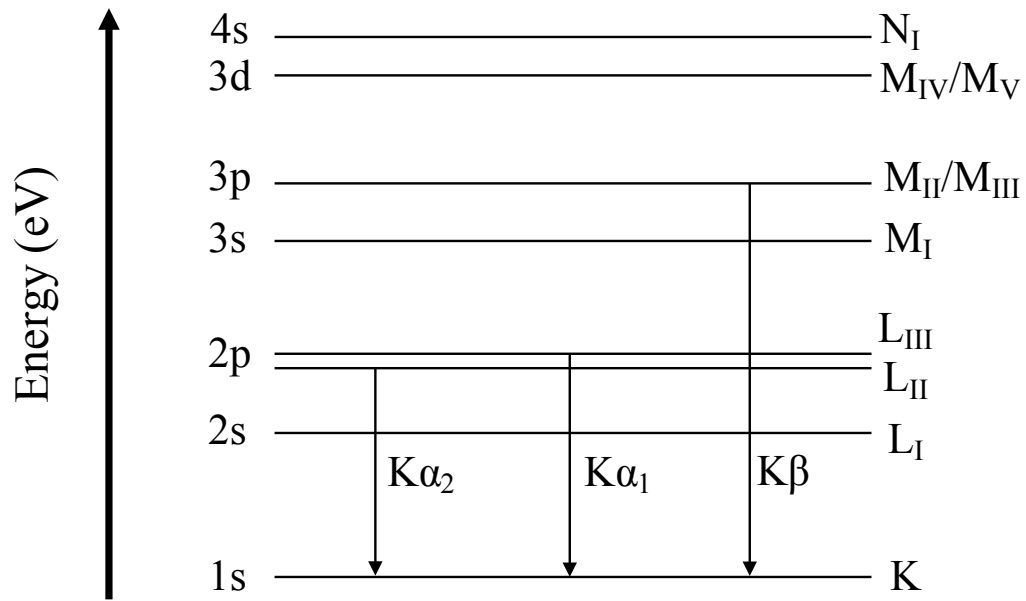
Figure 2.12: Representation of energy levels and changes involved in a X-ray emission.[145]
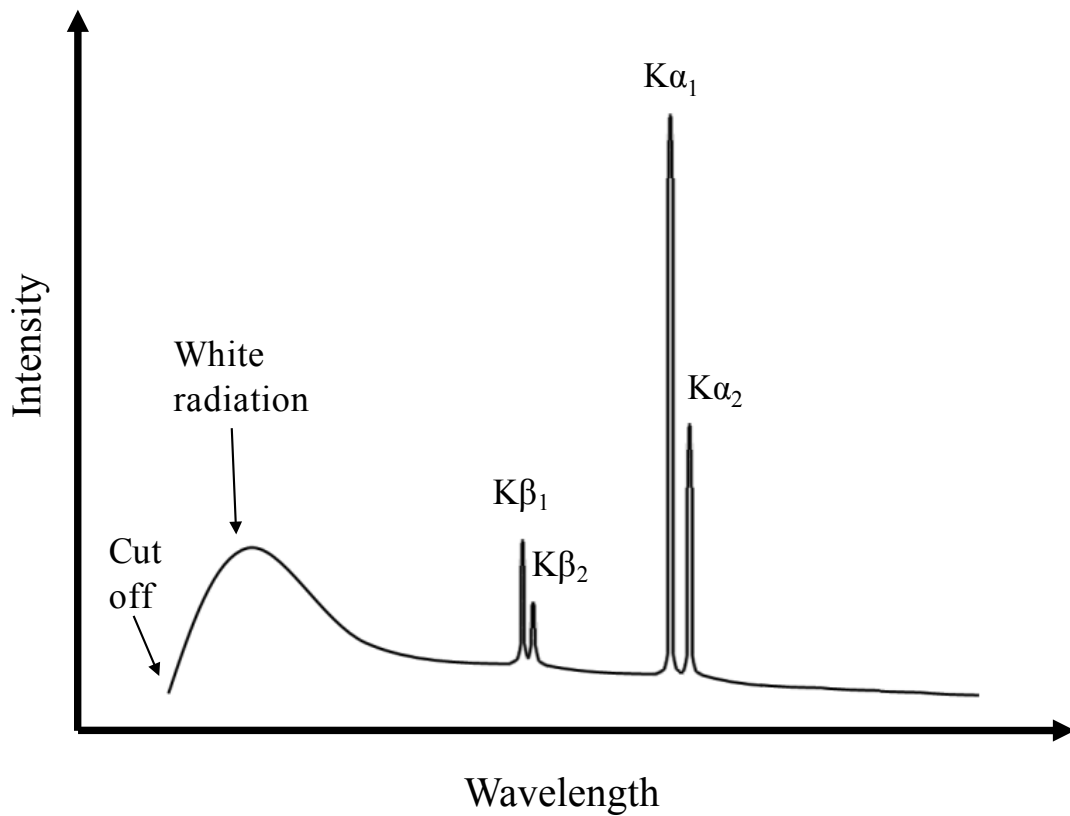
Figure 2.13: Representation of X-ray emission spectrum.[144, 145]

Both types of radiation show doublets resulting in a 1 and 2 value. This stems from the

different spin states possible for the *p* electrons making the transition, to the spin of the vacant 1*s* orbital. In the case of K-α, the 2*p* electrons have a total angular momentum given by the quantum number $j = l \pm s$, where *l* is the orbital quantum number and *s* is the spin quantum number. In the case of a 2*p* electron $l = 1$ and as a result, *j* can be either 3/2 or 1/2. This can result in the following transitions for each type of K-α as shown in Equation 2.3.

$$2p_{3/2} \xrightarrow{K-\alpha_1} 1s_{1/2} \quad \text{and} \quad 2p_{1/2} \xrightarrow{K-\alpha_2} 1s_{1/2} \tag{2.3}$$
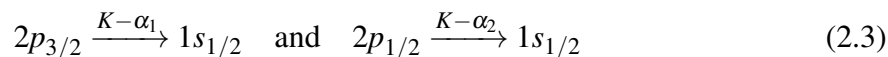
In some X-ray experiments when the two separate types of K-α radiation is observed, the weaker K-α_2 can be removed.[146]

2.4.3 Powder X-ray Diffraction (PXRD)

The characterisation of the crystal structure of a material requires the detection of all diffracted X-rays from as many, if not all of the crystal planes. In order to meet the Bragg conditions either the angle or the wavelength of the incident radiation must be varied. In single-crystal X-ray diffraction a fixed wavelength of X-rays is diffracted from a rotating crystal. In this way all of the lattice planes can be passed through the required Bragg angle. As a result it is also necessary for an X-ray detector to be present at all possible diffraction angles. Knowing the wavelength of the radiation used, along with the 2θ angle that results in each diffraction, the *d* spacing of the lattice planes can be determined. The most commonly used collection methods to obtain diffraction data from polycrystalline materials, is PXRD. This technique is widely used within solid state laboratories and has played a key part in the characterisation of materials within this project. Powdered materials are made up of very large numbers of small crystals randomly orientated to one another. As a result when the X-ray beam interacts with the crystals that are orientated to meet the Bragg conditions of each plane, a series of diffracted X-rays cones will result as shown in Figure 2.14. By passing a detector at known 2θ angles through these cones a diffraction pattern for a sample is produced.[147]
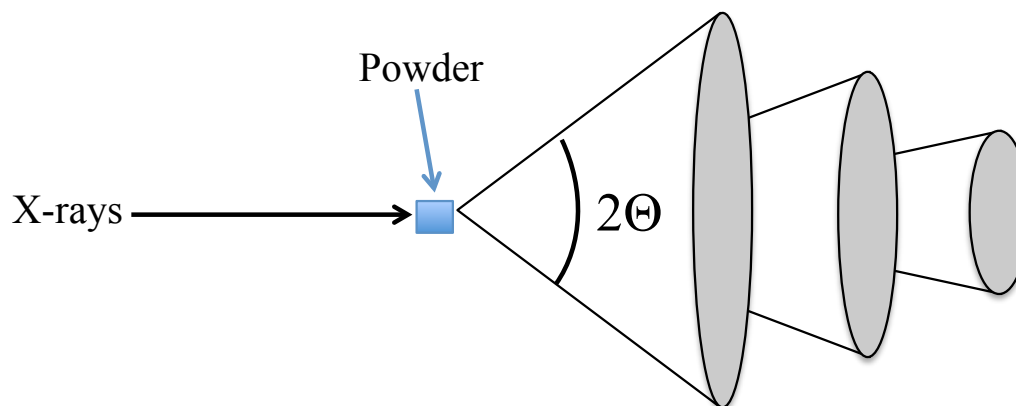
Figure 2.14: Representation of the X-ray diffraction cones produced from analysing a sample.

2.4.4 Equipment for Powder X-ray Diffraction

PXRD data is normally collected using a specialised piece of equipment called a diffractometer. There are a variety of different approaches that can be used for the collection of PXRD data and several possible geometries for the diffractometer configuration. In this project all PXRD was carried out in reflection mode using a PANalytical Empyrean Series 2 Diffractometer with the Bragg-Brentano geometry. This type of geometry acts to rotate both the detector as well as the sample as shown in Figure 2.14. This set-up has the X-ray source, sample centre and detector all at positions on the circumference of an imaginary circle known as the measuring circle.

The sample is rotated θ degrees whilst the detector is rotated by a value of 2θ degree. This is to ensure that the sample remains at a tangent to the measuring circle. The angle between the X-ray incident and diffracted beam is determined by $180°$ - 2θ. The Bragg-Brentano geometry is shown in Figure 2.15.
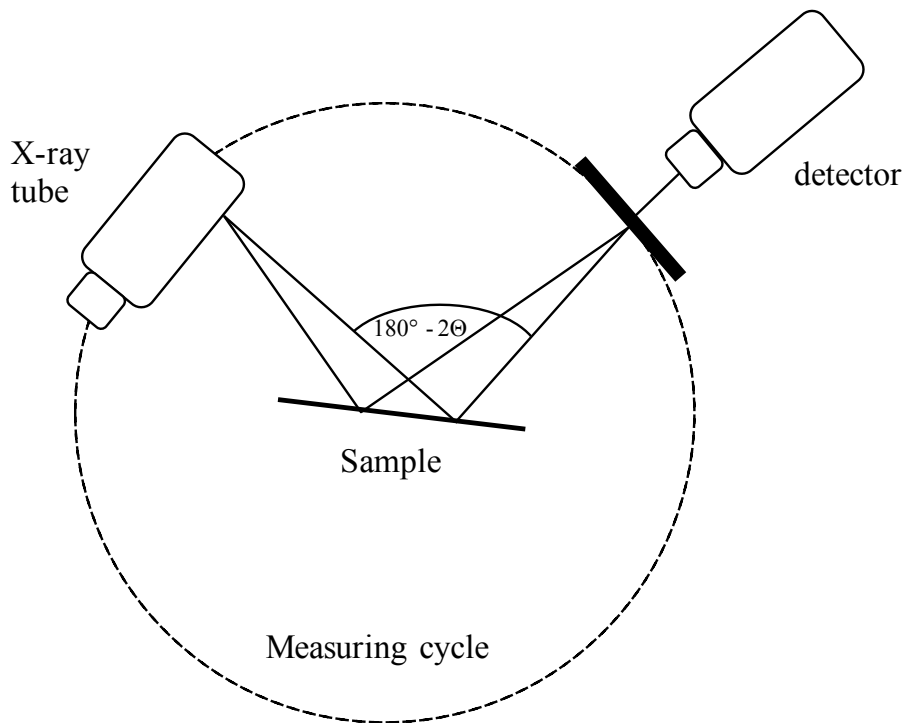
Figure 2.15: Schematic diagram of the Bragg-Brentano geometry, with X-rays diffracting over a sample with a rotating detector.

The sample to be analysed is placed upon a flat plate, of a suitable circular size at the centre of the goniometer. The sample is then rotated during analysis around its perpendicular axis to provide a good average crystallite orientation. For much of this work a zero-background Si sample holder was used. This allowed samples of low quantity to be analysed without contribution from the holder to the diffraction pattern.[148]

2.4.5 X-ray Detectors

X-ray detectors act to convert X-ray photons scattered from compounds under study to be converted into an electrical signal. The arrangement of the atoms and their nature leads towards producing a diffractogram of the crystalline structure.[149] Two of the most common types of detectors used for PXRD equipments is that of scintillation and gas-filled detector. This work included the use of only a scintillation detector for analysis. The approach works by converting the X-ray photons in an electrical signal. The X-rays collide onto a phosphor screen, coated on a thallium-doped sodium iodide crystal. This then converts the X-rays to

photons which are then subsequently converted to voltage pulses via a photomultiplier tube. The signal from the voltage pulse is then recorded for data analysis.[150]

2.5   Rietveld Refinement

One of the most common methods used for determination of crystalline structures from PXRD data is through Rietveld refinements.[151] Specialised software calculates a theoretical diffraction pattern based on a proposed model and is then compared to experimental data. The aim is to decrease the difference between the two phases, so modifications are applied to the theoretical pattern. Rietveld refinements are usually carried out using the computer software program GSAS.[152] Using a least-square refinement the quantity that is minimised is the residual, S_y described in Equation 2.4 as:

$$S_y = \sum_i w_i(y_i - y_{ci})^2 \tag{2.4}$$

where w_i is $1/y_i$, y_i is the observed intensity at the i th step and y_{ci} is the calculated intensity at the i th step.[151] This type of minimisation is known as a least-squares refinement.

A diffraction pattern will contain various Bragg reflections which contribute to the intensity, y_i, observed at any arbitrary point i, present in the pattern. Calculated intensities, y_{ci}, are determined from the $|F_K|^2$ values. This is the structural factor and is calculated using the structural model by summing up the calculated contributions from the neighbouring Bragg reflections, as well as the background.

$$y_{ci} = s\sum_K L_k \mid F_K \mid^2 \phi(2\theta_i - 2\theta_k)P_kA + y_{bi} \tag{2.5}$$

s = scale factor

K = Miller indices $h\,k\,l$, for a Bragg reflection

L_K = Lorentz, polarisation and multiplicity factor,

ϕ = reflection profile function

P_K = preferred orientation function

A = adsorption factor

F_K = structure factor for the Kth Bragg reflection

y_{bi} = background intensity at the ith step

The significance of these variables, has been discussed in the following sections.

2.5.1   Lorentz, Polarisation and Multiplicity Factors, L_K

A laboratory diffractometer will generally produce unpolarised X-rays for sample analysis. However, on contact with the crystallites within a sample, polarisation can take place which reduces the intensity of the detected X-rays.[150] The variation of a polarised beam can be given by the polarisation factor P;

$$P = 1/2(1+\cos^2 2\theta) \tag{2.6}$$

The Bragg angle for a reflection, θ, will occur over a very small range, rather than an idealised exact θ value. The extent of this range shows a 2θ dependence that is known as the Lorentz factor.[153] The Lorentz factor can be added to the polarisation factor to account for the non-ideal Bragg reflections. This results in the modified version of the polarisation factor as;

$$P = (1+\cos^2 2\theta)/(\sin^2 2\theta \cos\theta) \tag{2.7}$$

One of the consequences of a diffraction pattern from a powdered sample, is that it is made up of rings (diffraction cones) as shown in Figure 2.14. These rings can overlap with those of equivalent diffraction planes for example in a cubic system the 100, 010 and 001 all contribute to the diffraction pattern at the same point. Therefore, the multiplicity factor is needed to take this into account for refinements.

2.5.2 Reflection Profile Function, ϕ

Bragg's law implies that polycrystalline materials will result in a diffraction pattern which consists of a flat background and perfectly defined lines corresponding to each Bragg reflection. In reality this is not the case as a number of factors such as instrumental and sample contributions (crystal defects and particle size) can result in diffraction of various shapes. The reflection profile function, ϕ describes the profile of each reflection and approximates the effects of both the instrumental and sample factors. This type of function is required when fitting diffraction data. In the case of PXRD, the Gaussian (2.8), Lorentzian (2.9) and pseudo-Voigt (2.10) profile functions are used for modelling the peaks.

$$\frac{C_0^{1/2}}{H_K \pi^{1/2}} \exp(-C_0(2\theta_i - 2\theta_k)^2 / H_k^2) \tag{2.8}$$

$$\frac{C_1^{1/2}}{\pi H_K} 1 \left/ \left[1 + C_1 \frac{(2\theta_i - 2\theta_k)^2}{H_k^2} \right] \right. \tag{2.9}$$

$$\eta L + (1 - \eta) G \tag{2.10}$$

In these Equations 2.8 and 2.9, $C_0 = 4\ln 2$, $C_1 = 4$, the mixing parameter $\eta = NA + NB*(2\theta)$ where NA and NB are the refinable values. The peak width, H is taken as the full-width-at-half-maximum (FWHM) and is defined as:

$$H^2 = U\tan^2\theta + V\tan\theta + W \tag{2.11}$$

In Equation 2.11 the definable parameters are that of U, V and W.

2.5.3 Preferred Orientation Function, P_K

Preferred orientation is a result of the crystallites in a sample have a tendency to orientate in one type of direction over the others. This can be caused when a sample's surface is

compressed whilst being prepared in a sample holder. This can result in a greater number of certain families of planes being exposed to the X-ray beam, which will increase the peak intensities for these reflections. Software such as GSAS can provide corrections if this occurs, but were not applied within this work.[152, 154]

2.5.4   Absorption Factor, A

Absorption can result in the beam intensity being removed and a decrease in the intensity of diffraction peaks. When a diffractometer is operating with an ideal Bragg-Brentano geometry the effect of absorption should be uniform across the entire 2θ range, with the need for corrections. However, in the case where highly absorbing materials are analysed, a 2θ dependence, particularly at low angles may occur resulting in reduced thermal parameters in the refinement. Various numbers of corrections are available if this problem should occur.

2.5.5   Structure Factor, $\mathbf{F}_K$

By combining the waves scattered from each plane of atoms, the total diffraction intensity of a unit cell can be calculated. This is referred to as the structure factor, F_K with K indicating each set of (*hkl*) planes and is given by:

$$F_K = \sum_j N_j f_j \exp[2\pi i(hx_j + ky_j + lz_j)]\exp[-M_j] \tag{2.12}$$

where

hkl = Miller indices

x_j, y_j, z_j = atomic positions of the nth atoms,

N_j = site occupancy multiple for the j atom site,

$M_j = 8\pi^2 u^2{}_s \sin^2\theta/\lambda^2$,

$u^2{}_s$ = root-mean-square thermal displacement of the nth term parallel to the diffraction vector,

f_j = atomic scattering factor.

The scattering factor, f_j is related to the distribution of the scattering density. In the case of X-rays, these are scattered via electron clouds. The scattering factor for X-ray diffraction is shown to be 2θ dependent and is described in Equation 2.13.

$$f_j = \sum_{j=1}^{4} a_j \exp[-b_j(sin^2\theta/\lambda^2)] + c \qquad (2.13)$$

Here a_j, b_j and c are the Cromer-Mann coefficients, specific to each atom and can either be experimentally derived or obtained via quantum mechanical calculations. The intensity of diffraction peaks decreases with increasing values of θ.

2.5.6 Background, y_{bi}

In a diffraction pattern the background can contribute to unwanted contributions from a variety of causes such as, amorphous materials, scattering from the sample holder to inelastic scattering. In order to account for these types of contributions the background must be taken into account. A variety of methods exist to achieve this such as, using tables of known instrumental background, linear interpolation between user defined points to modelling background functions. Refinement software packages, such as GSAS provide a variety of possible background functions, which can be used to describe the specific background characteristics of each pattern. In the case of this work the two main functions used were the Chebyschev series and the fifth function type power series.

2.5.7 Quality of Fit Criteria

In a Rietveld refinement pattern, a difference profile plot between the experimental and calculated values are provided. Using this comparison a numeral representation of the fit quality can also be determined.

When assessing the quality of fit for a refinement the weighted profile R-factor (R_{wp}), reflection intensity R-factor (R_p), expected R-factor (R_{exp}), and χ^2 values are used and defined

as:

$$R_{wp} = \left(\sum_i w_i [y_i(obs) - y_i(calc)]^2 / \sum_i w_i [y_i(obs)]^2 \right)^{1/2} \tag{2.14}$$

$$R_p = \sum_i |y_i(obs) - y_i(calc)| / \sum_i y_i(obs) \tag{2.15}$$

$$\chi^2 = R_{wp} / R_{exp} \tag{2.16}$$

$$R_{exp} = \left[(N - P) / \sum_i^N w_i y_i(obs)^2 \right]^{1/2} \tag{2.17}$$

Here w_i is a weighting factor, y_i(obs) and y_i(calc) are the observed and calculated intensities, with N as the number of observations and P the number of parameters.

For an ideal refinement the values of R_{wp} and R_p should be reduced as much as possible, with χ^2 being a value of 1.

2.6 Thermogravimetric Analysis (TGA)

2.6.1 TGA Equipment

Thermal gravimetric analysis (TGA) operates by the mass of a sample being monitored under a controlled atmosphere and temperature.[155, 156] During the procedure, the sample mass can either increase or decrease depending on the type of chemical reaction taking place. The sample itself is placed in a furnace chamber on an accurate balance for its mass to be measured, whilst being subjected to increasing temperatures.

The TGA equipment used in this project was that of a Mettler TGA/DSC 1 STAR system, with the results analysed using STAR evaluation software. A TGA run is carried out by first measuring the sample to an approximate value whilst in an alumina crucible. This is then

inserted into the furnace chamber onto a hotplate/balance that allows the temperature and mass of the sample to be measured simultaneously. Over the heating cycle the sample's mass can be measured to a 0.0001 mg level of accuracy. A schematic of the TGA equipment used is shown in Figure 2.16. This representation has the sample mass being measured whilst in a furnace when heated to different temperatures. This results in an in-situ TGA curve, which can measure the change in mass over time and temperature. This representation also shows that within this set-up multiple gas cylinders can be attached to alternate between different types of atmospheres during experiments.
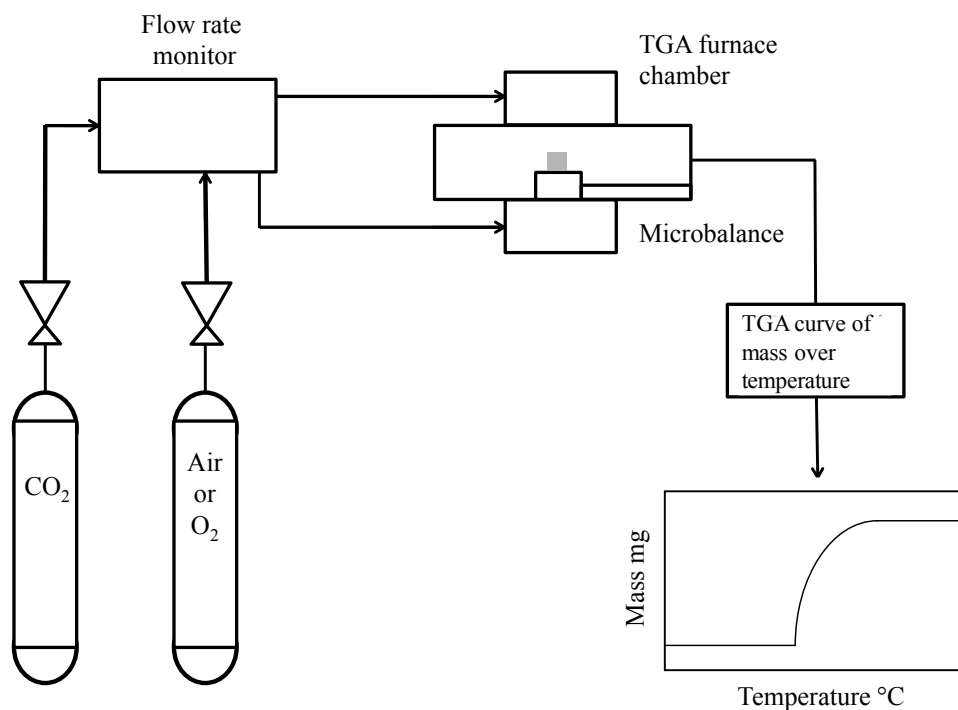
Figure 2.16: Schematic of TGA equipment showing how a sample's mass can be measure in-situ, to prepare a TGA curve.

Once a TGA curve has been determined the change in mass of a sample at different temperatures and conditions can be calculated. Figure 2.17 shows the mass of a sample increasing during a TGA experiment.

Measurements using TGA have been primarily aimed to determine the thermal stability of materials as well as their chemical composition. This can be used to identify organic compounds via decomposition temperatures, ad/desorption and oxidation/reduction properties. These are kinetic processes and using data obtained through TGA, the reaction rates can

be determined. This is from measuring how much the mass changes over time, at different temperatures and different heating rates.

TGA is also able to provide insight into the mechanisms of solid-gas reactions. Janke *et al.* was able to monitor the hydrogenation of CO_2 towards methane through TGA, by observing the increase in mass of the catalyst as it adsorbes CO_2, then losses it under a H_2 atmosphere.[157]
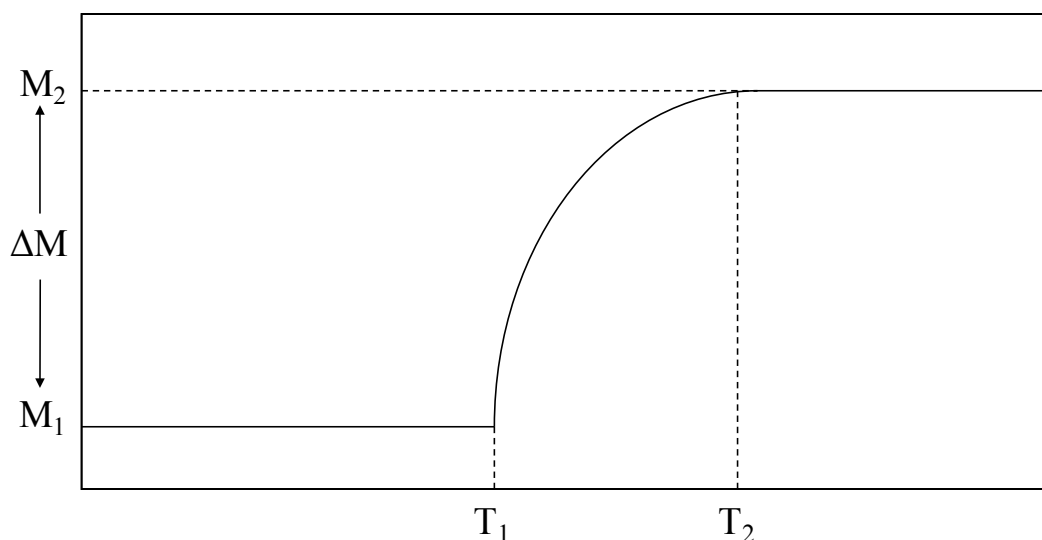
Figure 2.17: A TGA curve showing the mass of a sample increasing at different temperatures.

Other analytical methods such as IR spectroscopy and mass spectrometry (MS) can also be coupled with TGA. This allows added analysis for different groups such as H_2O and organic materials to be characterised as well as quantified.[158]

2.6.2 TGA in this work

In this work TGA was carried of extensively with the dual aim of performing solid-gas reactions and to monitor the gas uptake at the same time. Much of this work has involved reacting mixed metal oxides with CO_2 in order to prepare mixed metal oxide carbonates. This reaction results is an expected increase in the sample mass. This is due to CO_2 being taken up from the gas flow to react with the oxide forming carbonates. Alkaline earth metal oxides AO (A = Mg, Ca, Sr, Ba) have a strong affinity for reacting with CO_2 towards binary carbonates,

ACO_3.[159] In order to avoid decomposition towards binary carbonates and to prepared desired products. An alternating gases approach was used. This involved heating a sample to specific temperatures under an inert atmosphere. Then once the temperature of the TGA chamber was stable, CO_2 would be introduced to react with the sample. After a specific reaction time the sample would then be cooled to room temperature under the inert gas. This would allow the sample to react with CO_2 under conditions that would favour the formation of the mixed metal oxide carbonate, and minimise formation of the binary carbonate by-product during cooling.

By utilising the programming abilities of the TGA equipment. This not only allowed an easy way of alternating gases towards desired products, but it also provided an in-situ measurement of the sample mass changing. This was used to determine the quantity of CO_2 that was utilised towards forming the oxide carbonate, as well as the reaction rate order and rate of reaction.

2.7   Fourier Transform Infrared FTIR spectroscopy

Infrared (IR) spectroscopy is used to study the vibrational motions of molecules. Different types of motions among the different groups of atoms can cause the molecules to absorb various amounts of energy. This can be used for the identification of atoms and how they are bonded or grouped in an unknown compound. Absorption of energy in the infrared region lies between $\lambda = 4000 - 200$ cm^{-1}, and arises from changes in the vibrational energy of the molecules. Analysis of the vibrational behaviour of samples was carried out using a a Perkin Elmer diamond tipped FT-IR, Figure 2.18.
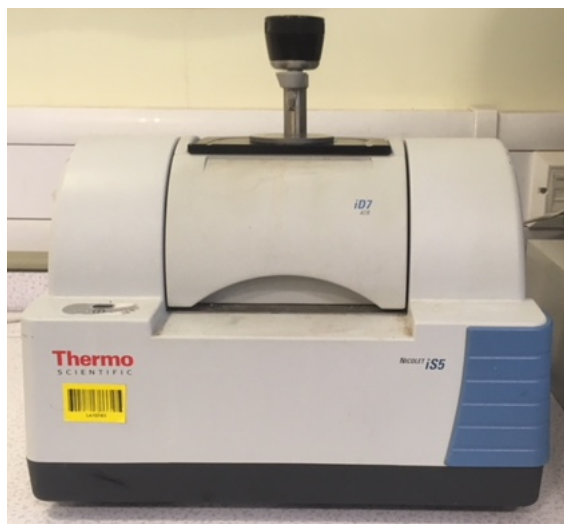
Figure 2.18: A Perkin Elmer diamond tipped FT-IR.

One important condition for analysing samples with IR spectroscopy is that only vibrations that result in a change in the electric dipole moment will be observed.[160] For example, stretching vibrations in a homonuclear diatomic molecule (O_2, N_2, and Br_2) will not produce a change in the dipole moment.[161] This means that these molecules will not be detected using IR spectroscopy. On the other hand molecules such as CO and IBr can be detected as these do contain a permanent dipole moment.

2.8 Computational Methodology

In this work computational chemistry methods have been employed for studying the reaction of metal and mixed metal oxides with CO_2 towards carbonate compounds. Chapter 5 has provided a thermodynamic study of CO_2 reacting within a cluster of AO (A = Sr, Ca and Ba) towards forming surface ACO_3, in the bulk of SrO towards $SrCO_3$ and in the bulk Sr_2CuO_3 towards $Sr_2CuO_2(CO_3)$. The vibrational behaviour of the carbonate groups have also been studied using computational methods, and has been discussed in Chapter 6.

2.8.1 Schrödigner equation

The application of quantum methods for studying atoms, molecules and materials has been a long standard technique to aid and even exceed laboratory research. In the terms of quantum chemistry, molecules can be represented as collections of positively charged nuclei and negatively charged electrons with electrostatic interactions present between them. When studying these types of systems the properties can be described via a wavefunction $\psi(r,R)$ which is dependent on the position of all the nuclei (R) and electrons (r). A key concept within quantum mechanics is in solving the Schrödinger equation. In the case of the time-independent non-relativistc Schrödinger equation, this can be solved to provide the necessary information for the wave function ψ (r,R), as well as the corresponding energy of the system E.[162] The time-independent Schrödinger:

$$\hat{H}\psi(\text{r,R}) = E\psi(\text{r,R}) \tag{2.18}$$

is dependent on the Hamiltonian operator $\hat{H}$, which describes the interaction between particles within a molecular or solid system. The Hamiltonian in non-realistic form can be broken down into the total kinetic energy operators for the nuclei ($\hat{T}_n$) and electrons ($\hat{T}_e$). The nuclei-electron attraction ($\hat{V}_{en}$) operator along with the nuclei-nuclei ($\hat{V}_{nn}$) and electron-electron ($\hat{V}_{ee}$) repulsive operators. When studying a system composed from N_α nuclei and N_e electrons the Hamiltonian operator can be represented in the following form:

$$\hat{H} = \underbrace{-\frac{1}{2}\sum_{\alpha}^{N_\alpha}\frac{1}{M_\alpha}\nabla_\alpha^2}_{\hat{T}_n} + \underbrace{\sum_{\alpha<\beta}^{N_\alpha,N_\alpha}\frac{Z_\alpha Z_\beta}{|R_\alpha - R_\beta|}}_{\hat{V}_{nn}} - \underbrace{\frac{1}{2}\sum_{i}^{N_e}\nabla_i^2}_{\hat{T}_e} + \underbrace{\sum_{i<j}^{N_e,N_e}\frac{1}{|r_i - r_j|}}_{\hat{V}_{ee}} + \underbrace{\sum_{\alpha,i}^{N_\alpha,N_e}\frac{Z_\alpha}{|R_\alpha - r_i|}}_{\hat{V}_{en}} \tag{2.19}$$

where Z_α is the charge of the α-th nucleus and M_α is the mass in atomic units. The position of the α-th nucleus is represented by R_α and the i-th electron is r_i. The Laplacian operator, ∇^2 is the kinetic energy and is the sum of second partial derivatives of the function with respect to each independent variable, Equation 2.20.

$$\nabla^2 = \frac{\delta^2}{\delta x^2} + \frac{\delta^2}{\delta y^2} + \frac{\delta^2}{\delta z^2} \tag{2.20}$$

This is a compact form to represent the Cartesian coordinates (x, y and z) as the particle is moving. [163, 164]

The Hamiltonian operator is essential for being applied within quantum mechanical methods and for studying molecular and solid systems. By using an accurate description of the Hamiltonian, the total energy of the system E can be determined. The energy values can then be used to determine the electronic, vibrational and rotational transitions that exist within a system. This is very important when studying the vibrational behaviour of molecules and solids which can be used for a variety of applications, from monitoring chemical reactions to determining transition states.

2.8.2 Born-Oppenheimer approximation

Solving the Schrödinger equation can be a computationally expensive task due to the number of calculations required for both the nuclei and electrons. As a result, approximations have been developed in order to reduce the calculation costs. The Born-Oppenheimer approximation is an approximation method that compares the mass of the nuclei to that of the electrons. [165] It treats the nuclei as being stationary when compared to the electrons. This makes the task of calculating the systems less computationally expensive and quicker as a result and leads to the concept of potential energy surfaces, PES. The PES describes the energy of a system as a function of certain parameters for example the atomic positions.

The Born-Oppenheimer approximation is highly important within quantum chemistry and is applied due to its simplicity and high levels of accuracy. This approximation states that as electrons are moving at considerably higher speeds than that of the nuclei, that they can be considered as moving in a system of fixed nuclear positions. By applying this approximation to the Hamilton operator (Equation 2.19) for N_e electrons, can be simplified as shown in Equation 2.21.

$$\hat{H} = -\frac{1}{2}\sum_{i}^{N_e}\nabla_i^2 + \underbrace{\sum_{i<j}^{N_e,N_e}\frac{1}{|r_i - r_j|}}_{\hat{V}_{ee}} + \underbrace{\sum_{\alpha,i}^{N_\alpha,N_e}\frac{Z_\alpha}{|R_\alpha - r_i|}}_{\hat{V}_{en}} \qquad (2.21)$$

By taking into consideration the Born-Oppenheimer approximation, this has reduced the Schrödinger equation whilst retaining the $\hat{V}_{en}$ energy . Therefore the total wave function of a system can be described for the total nuclei $[\psi_n(R)]$ and electron $[\psi_e(r;R)]$ wave functions:

$$\psi(r,R) = \psi_e(r;R)\psi_n(R) \qquad (2.22)$$

2.8.3 Density Functional Theory (DFT)

One of the most common approaches for studying the quantum chemistry of materials, and molecules is through Density Functional Theory (DFT).[166, 167] This approach carries out calculations based on the electronic density ρ of the ground state of a system using mathematical functionals (function of a function). The concept of DFT is that if E is the lowest potential energy of a system, i.e. the ground state, then E can be represented as a functional F of the electron density.

$$E = F[\rho] \qquad (2.23)$$

Using the ρ significantly speeds up calculations. This is preferred over the many-body electronic wavefunction which is a function of 3N variables (the coordinates of all N atoms in the system). Hence for a many-body system this would be very complicated and computationally expensive. The ρ is only a function of x, y, z therefore has only three variables. This makes solving the energy of the system much simpler.

This is far more efficient than other methods previously used in quantum chemistry such as Hartree-Fock theory.[168–170] HF approach requires using all the electronic and atomic coordinates to solve the Schrödinger equation. Hence by knowing the electron density and using a functional, the total energy of a many-body system can be determined, and is described with

the different components:[171]

$$E[\rho] = T[\rho] + V_{en}[\rho] + V_{ee}[\rho] \qquad (2.24)$$

The energy functional $E[\rho]$ is the sum of the kinetic energy of the electrons $T[\rho]$, the Coulomb interactions between electrons and the nuclei $V_{en}[\rho]$, and the interaction energy between electrons $V_{ee}[\rho]$.

$V_{en}[\rho]$ can be further expanded upon and expressed as an explicit functional of the density:

$$V_{en}[\rho] = -\int \sum_{a=1}^{N_a} \frac{Z_a}{|R_a - r|} \rho(r) dr, \qquad (2.25)$$

This has Z_a and R_a representing the charge and position of the a-th nucleus, respectively. It is assumed that for a specific molecular system, $V_{en}[\rho]$ can solely determine all the characteristic properties. The remaining terms are used to describe a universal functional $F[\rho]$, which is independent from a particular system.

$$F[\rho] = T[\rho] + V_{ee}[\rho] \qquad (2.26)$$

The kinetic energy of electrons $T[\rho]$, can be solely used to describe the energy functional in a system, where the electrons are non-interacting.

$$T[\rho] = -\frac{1}{2} \sum_{i=1}^{N_e} \langle \phi_i(r) | \nabla_i^2 | \phi_i(r) \rangle \qquad (2.27)$$

Here, ϕ_i(r) describes a set of one-electron orbitals that are related to the electron density, ρ:

$$\rho = \sum_{i=1}^{N_e} |\phi_i(r)|^2 \qquad (2.28)$$

As $F[\rho]$ is a universal functional of the density regardless of the distance between electrons. $T[\rho]$ can also be regarded as a universal functional.

The interaction energy between electrons $V_{ee}[\rho]$ is comprised of two parts. Firstly the electron-electron repulsion energy $J[\rho]$:

$$J[\rho] = \frac{1}{2} \int \int \frac{\rho(r)\rho(r')}{|r-r'|} dr'dr, \qquad (2.29)$$

which is also describes as being a universal functional of ρ. The second part used to define $V_{ee}[\rho]$ is referred to as the exchange-correction functional $E_{xc}[\rho]$:

$$V_{ee}[\rho] = J[\rho] + E_{xc}[\rho] \qquad (2.30)$$

which has been discussed more in-depth in the following section.

2.8.4 Exchange-correlation E_{xc} functionals

The exchange-correlation E_{xc} energy is important to describe how electrons interact with one another, and has even been referred to as "nature's glue".[172] For studying chemical reactions in which bonds are being broken and made, to vibrational simulations that study how bonds are being bent and stretched, an understanding of the E_{xc} energy is essential. The true expression for the E_{xc} energy is unknown so approximations are made when be applied within DFT calculations. The E_{xc} functional can be split into the exchange functional $E_x[\rho]$, which is a result of the indistinguishability of electrons, and a correlation functional $E_c[\rho]$, which describes the simultaneous movement of electrons:

$$E_{xc}[\rho] = E_x[\rho] + E_c[\rho] \qquad (2.31)$$

A great deal of work has been carried out towards investigating different types of E_{xc} functionals that are used for studying the properties of atoms and molecules. These different types can be placed into various classes that are arranged via a system of increasing complexity called Jacobs Ladder.[173] The concept of Jacobs ladder is to have increasing accuracy and performance of the functional, but also to show the increase in complexity.

The two main types of E_{xc} functionals that can be used are Local (spin) Density Approximation LDA and Generalised Gradient Approximations GGA[174],[175] LDA type functionals are at the base of Jacob's ladder and are described as the simplest form of expressing E_{xc} energy. This method is based on the free gas electron model and depends solely on the values of electrons at different points in space. Although these functionals are computationally cheap to use their accuracy is limited. This arises from the bonds lengths being underestimated by overestimating the bond strength. GGA improves upon LDA by including inhomogeneities in the electron density, in order to expand and soften the bonds preventing the issue of underestimating the bond lengths. More advanced functionals are referred to as Hybrid functionals such as B3LYP that include experimental values to improve their accuracy. This however means the method is no longer being based on just first principles but experimental data as well.[176]

In this project a variety of functionals have been used to study the interaction of CO_2 within the structure of solid compounds towards forming carbonates.[177–180]

The Perdew-Burke-Ernzerhof, PBE functional is one of the most used types of GGA functionals in solid-state calculations.[177] This type of functional depends explicitly on the electron density ρ and the density gradient:

$$E_{xc}^{PBE}[\rho] = \int \rho(r) \varepsilon_{xc}^{PBE}(\rho, \triangledown \rho) dr \tag{2.32}$$

PBE acts to approach the uniform electron gas limit for slowly moving densities and is regarded as one of the best methods for studying the bulk of solids compared to molecular systems. One of the problems with this type of functional however, is that it overestimates the lattice constants by 1-3 %. This can affect other equilibrium properties such as magnetism and surface energies.

In order to improve the accuracy of these calculations for solid systems a revised version of PBE, PBEsol has been developed.[178,181] This functional type has been designed for recovering the original gradient expansion for the exchange section over a wide range of density gradients. The correlation piece is adjusted to reproduce the uniform electron gas surface energies accurately. Due to PBEsol depending less on the gradient this functional is biased

towards solids. This can lead to lattice constants and other equilibrium properties for density packed systems being calculated with greater accuracy than standard PBE.[181] Despite these corrections however, PBEsol has generally been found to be less accurate for molecular bond energies when compared to PBE, thus making its application preferable towards solid systems.[182]

Another class of functionals that can be used are meta-GGA, which include the orbital kinetic densities. The orbital kinetic density is equal to the kinetic energy of the independent particles. In this project the types of functionals that have been used are, Tao-Perdew-Staroverov-Scuseria (TPSS) as well as a revised version revTPSS fucntionals. The incorporation of the kinetic density can result in improvements to molecular properties and surface energies.[183, 184] As with PBEsol, the revised version of TPSS could improve the accuracy for solid state systems.

2.8.5 Basis Sets

In *ab initio* programs, basis sets can be chosen as a way to represent the atomic/molecular orbitals of a system.[185–187] The Linear combination of atomic orbitals (LCAO) is a method within quantum chemistry that approximates molecular orbitals (MOs) as a linear combination of the atomic orbitals, AOs. An initial assumption is that the number of MOs is equal to the number of AOs included in the linear expansion. This can be simplified as, nAOs combine to form nMOs, which can be numbered $i = 1$ to n and which may not all be the same. The expression (linear expansion) for the i th molecular orbital would be:

$$\phi_i = \sum_r c_{ri} \chi_r \qquad (2.33)$$

where ϕ_i is a MO represented as the sum of n atomic orbitals χ_r, each multiplied by a corresponding coefficient c_{ri}, and r (numbered 1 to n) represents which AO is combined in the term. The coefficients are the weights of the contributions of the n atomic orbitals to the molecular orbital.

The number of basis functions used to construct each AO can be expanded such as with

double-zeta (DZ) to triple-zeta (TZ) basis sets that represent using two and three basis functions respectively. By having multiple functions the AO can be treated as either being diffused or compressed when constructing a MO. Basis sets can also be used to account for the valence orbitals, with the inner orbitals described using a different method. The introduction of polarisation also allows the basis sets to perform with greater accuracy as they accounts for the AO behaving as multiple orbitals of greater magnitude than in the minimal basis.

2.8.6 Pseudopotentials

For calculating large systems, approximations are needed in order to make them perform faster with less computational demands. In many of these systems the core electrons of the atoms do not engage in the actual chemical reactions. This consideration of the core electrons is especially important for studying chemical reactions within the bulk crystal structure of materials. The pseudopotentials can be used to accurately replace the core electrons when carrying out the calculations.[188–190] This means that only the valence electrons need to be considered.

2.8.7 Optimisation of structures

In order to determine the enthalpy of reaction (ΔH_{rxn}) from the energy of the reactants and products, as well as the vibrational frequencies off these systems. All systems have to first be geometrically optimised. During an optimisation the electronic structure is being reiterated until it reaches a specific level of convergence. The optimisation of each different system is achieved via a BFGS algorithm. This is an iterative method for solving unconstrained nonlinear optimisation problems towards the lowest energy optimised state. The method uses a mathematical procedure that generates a sequence by improving approximate solutions for a class of problems, in which the nth approximation is derived from the previous ones. This method is used during the optimisation to continuously optimise a system's energy until it reaches below a set convergence level of 1×10^{-7} atomic units in this study. Once this is achieved the system will be calculated into its lowest energy state. As a result the optimisation calculations are carried out before any others. One of the ways to confirm that the structure is

in its optimum energy state is through vibrational calculations. If the structure is in its lowest energy state it will only calculate positive vibrational frequencies.

In the terms of the crystal structure of materials the initial coordinates of the atoms are usually taken, from those found from reported experimental XRD data. In this work the Inorganic Crystal Structural Database (ICSD) was used as the source for this information. The crystallographic information was provided in the form of a crystal information file (.cif). The coordinates and lattice parameters can then be imported into a input file. Throughout this project both Cartesian and fractional coordinates of systems have been used for different calculations. In the case of lone molecules, such as CO_2, these can be placed within a unit cell of known dimensions to be given the freedom for optimisation.

2.8.8 Thermodynamics of reactions

The work reports a study of metal oxides, AO (A = Sr, Ca and Ba), and mixed metal oxides, Sr_2CuO_3, reacting with CO_2 towards carbonate based compounds. Using computational methods a thermodynamic study of the chemical reactions between the A-O groups with CO_2 has been carried out. The calculated energy change from the reactants to the product can be used to determine the enthalpy of reaction ΔH_{rxn}. ΔH_{rxn} values have been calculated for both cluster (part of the crystal structure) and bulk (entire crystal structure) type systems of the oxides. These calculations have only focused on a purely thermodynamic study through only determining the reaction enthalpy values.

If the energy content of the reactants is greater than that of the products, this will make the reaction exothermic with a $-\Delta H_{rxn}$ value. This will also mean that the products are in the most energy stable state. If the products have greater energy content this will make the reaction endothermic with a $+\Delta H_{rxn}$ value. This will mean that the reactants are the more stable phase. Equation 2.34 shows how the difference in energy values for the reactants and products can be used to determine the ΔH_{rxn}.

$$\Delta H_{rxn} = \sum H_f(Products) - \sum H_f(Reactants) \tag{2.34}$$

Using DFT methods the energy content of an optimised (lowest energy) system has been determined for the separated reactants, CO_2 and metal oxide. The energy value was also determined for a system where CO_2 was optimising with a metal oxide groups towards forming a metal carbonate. Equation 2.35 represents how the ΔH_{rxn} for these carbonate reaction have been determined.

$$\Delta H_{rxn} = \Delta H_f(ACO_3) - \Delta H_f AO - \Delta CO_2) \tag{2.35}$$

The calculated results were compared to those experimentally determined via the same equation using values reported within the CRC Handbook of Chemistry and Physics.[122] However, one of the main factors to consider is that the computational calculations were all carried out at temperature of 0 K. In order to compensate the calculation being carried under these conditions, thermal corrections have been applied to the energy values. This includes the translational, rotational and vibrational contributions.

By being able to construct an accurate method for calculating the ΔH_{rxn} for known reactions, such as SrO reacting with CO_2 towards $SrCO_3$. This same methodology can then be applied for calculating the ΔH_{rxn} for the novel reaction of Sr_2CuO_3 with CO_2 towards $Sr_2CuO_2(CO_3)$, which has also been developed experimentally within this project.

2.8.9 Thermal correction

The ΔH_{rxn} value for the bulk calculations were determined using the overall electronic total energy, U_{DFT} along with various corrections. The ΔH_{rxn} for the solid species such as $SrCO_3$ and Sr_2CuO_3 were determined using Equation 2.36.

$$\Delta H_{rxn} = U_{DFT} + U_{ZPE} + U_{vib} \tag{2.36}$$

This has the U_{DFT} alongside the zero-point energy correction, U_{ZPE}, and vibrational contribution, U_{vib}. In order to achieve these corrections the harmonic vibrational frequencies of all phases had to be determined. U_{ZPE} refers to the energy at absolute zero which is the low-

est amount of energy a system can have at its ground state.[191] Using Equation 2.37 and the vibration frequencies, U_{ZPE} can then be determined.[129]

$$U_{ZPE} = \frac{1}{2}h\nu \tag{2.37}$$

U_{vib} is determined using the vibrational frequencies as shown in Equation 2.38.[129] These terms are defined as $R = 8.315$ J mol^{-1} K^{-1}, $h = 6.626 \times 10^{-34}$ J s, $c = 2.998 \times 10^{10}$ cm s^{-1}, ω = vibrational frequency cm^{-1}, $k\beta = 1.381 \times 10^{-23}$ J K^{-1} and T = temperature K. U_{vib} is determined in J mol^{-1} via this equation which is then converted to hartrees.

$$U_{vib} = \frac{R \times \left(\frac{hc\omega}{k\beta}\right)}{exp\left(\frac{hc\omega}{Tk\beta}\right) - 1} \tag{2.38}$$

In the case of CO_2, a linear gaseous molecule, the translational and rotational contributions $U_{trans+rot}$ and the ideal gas equation $PV = RT$, was also included, Equation 2.39.

$$\Delta H_{rxn} = U_{DFT} + U_{ZPE} + U_{vib} + U_{trans+rot} + PV \tag{2.39}$$

The $U_{trans+rot}$ is the sum of translational (3/2 RT) and rotational (RT) contributions. Along with $PV = RT$ this gives the total contribution for linear gas species like CO_2 as 7/2 RT.

These types of corrections are also important as they can be used to provide an accurate assessment of the energetics involved in the reaction. This also makes the theoretical model closer towards the experimental reaction that occur at 1273 K.

2.8.10 Vibrational calculations

The vibrational frequencies are determined using from the optimised coordinates of either a crystal structure or a singular molecule. When this system is allowed to vibrate the frequencies are determined via Equation 2.40:

$$\omega = \frac{1}{2\pi c}\sqrt{\frac{k}{\mu}} \qquad (2.40)$$

here ω is the vibrational frequencies in cm^{-1}, k is the force constant ($\mathrm{kg\ m\ s}^{-2}$), μ the reduced mass and c the speed of light (2.998×10^8 m s^{-1}). μ is determined from the mass values of each atom that is involved in each vibration. When the bonds in a molecule are vibrating the force constant k, can be determined via a diagonalisation of the mass-weighted Hessain matrix. The Hessian matrix is the matrix of the 2nd derivatives of the energy with respect to the geometry.[192] This is done for vibrational modes with the Hessian based on the Cartesian rather than fractional coordinates. In order to calculate a 2nd derivative, the 1st derivative is determined for a given geometry, then the geometry is altered and a self-consistent field, SCF calculation is carried out on the new coordinates to re-calculate the derivatives. The SCF method is an iterative method that involves obtaining a more accurate set of coordinates to re-calculate the derivative to greater accuracy. The 2nd derivative is determined from the difference of the two first derivatives divided by the step size. For the treatment of two Cartesian coordinates i and j the Hessian can be defined as shown in Equation 2.41.

$$H_{i,j} = \frac{\delta^2 E}{\delta x_i \delta x_j} \qquad (2.41)$$

For a simple two atom system the force vector for the first X_1 and second X_2 atoms would be equal to:

$$F_1 = \frac{\delta E}{\delta X_1} = \frac{\delta^2 E}{\delta X_1 \delta X_1}\Delta X_1 + \frac{\delta^2 E}{\delta X_1 \delta X_2}\Delta X_2 \qquad (2.42)$$

$$F_2 = \frac{\delta E}{\delta X_2} = \frac{\delta^2 E}{\delta X_2 \delta X_2}\Delta X_2 + \frac{\delta^2 E}{\delta X_2 \delta X_1}\Delta X_1 \qquad (2.43)$$

The Hessian can then be written in matrix form along side the displacement vectors X (change in coordinates) to determine the force constant k from the force vectors of the two atoms, F_1 and F_2.

$$\begin{bmatrix} \frac{\delta^2 E}{\delta X_1 \delta X_1} & \frac{\delta^2 E}{\delta X_1 \delta X_2} \\ \frac{\delta^2 E}{\delta X_2 \delta X_1} & \frac{\delta^2 E}{\delta X_2 \delta X_2} \end{bmatrix} \begin{bmatrix} \Delta X_1 \\ \Delta X_2 \end{bmatrix} = \begin{bmatrix} F_1 \\ F_2 \end{bmatrix}$$

This same methodology can then be expanded and applied for determining the force constant k of a many atom system with the Hessian matrix.

$$\begin{bmatrix} \frac{\delta^2 E}{\delta X_1 \delta X_1} & \frac{\delta^2 E}{\delta X_1 \delta X_2} & \cdots & \frac{\delta^2 E}{\delta X_1 \delta X_n} \\ \frac{\delta^2 E}{\delta X_2 \delta X_1} & \frac{\delta^2 E}{\delta X_2 \delta X_2} & & \\ \vdots & & \ddots & \\ \frac{\delta^2 E}{\delta X_n \delta X_1} & & & \frac{\delta^2 E}{\delta X_n \delta X_n} \end{bmatrix} \begin{bmatrix} \Delta X_1 \\ \Delta X_2 \\ \vdots \\ \Delta X_n \end{bmatrix} = \begin{bmatrix} F_1 \\ F_2 \\ \vdots \\ F_n \end{bmatrix}$$

Through computational methods the Hessian matrix for an entire system vibrating can be calculated using the change in coordinates and energy values. Using this the force constant k, can be determined which can be used along with the reduced mass, μ towards the vibrational frequencies, Equation 2.39. Intensities of the vibrational frequencies can also be determined using the transition dipole moments. This shows how likely the different vibrations are to appear.

2.8.11 Software

2.8.11.1 Orca

Orca was employed for a variety of calculations involving a fragment of an overall structure.[193] This type of program can be used for both *ab initio* DFT, as well as semi-emperial calculations, that also depend on experimental data. This software was employed for the cluster based calculations.

2.8.11.2 CP2K

For many of the calculations, DFT was applied using the software package CP2K/QUICKSTEP.[194] This program can be used for a variety of different applications such as geometric optimi-

sations, determining binding energies as well as vibrational frequencies. CP2K works by using DFT via the hybrid Gaussian-Plane Waves (GPW) method.[195] This uses atom-centred Gaussian-type basis to describe the wave function of the system and auxiliary plane wave basis to describe the electron density. This is used to accurately and quickly solve the Kohn-Sham equation in DFT by using approximations for the wave function and electron density.

Chapter 3

Direct reaction of $Sr_{2-x}A_xCuO_3$ compounds with CO_2

3.1 Crystal structure of Sr_2CuO_3 and $Sr_2CuO_2(CO_3)$

The A_2CuO_3 (A = Sr, Ca and Ba) series of compounds are classed as having one-dimensional structures, with connecting chains of square planar CuO_4 groups. The structure of Sr_2CuO_3 and Ca_2CuO_3 has also been described as anion-deficient equivalents of the structures of K_2NiF_4-type compounds such as La_2CuO_4 and Nd_2CuO_4 respectively.[88, 196] These have anion vacancies present throughout the crystal structure alongside the Cu-O chains, and can potentially be used as host sites for additional anions. A comparison of the anion deficient A_2CuO_3 structure to that of the K_2NiF_4 is shown in Figure 3.1. The anion vacancies are measure as the distance between the centre of the A cations in the c direction of the unit cell.
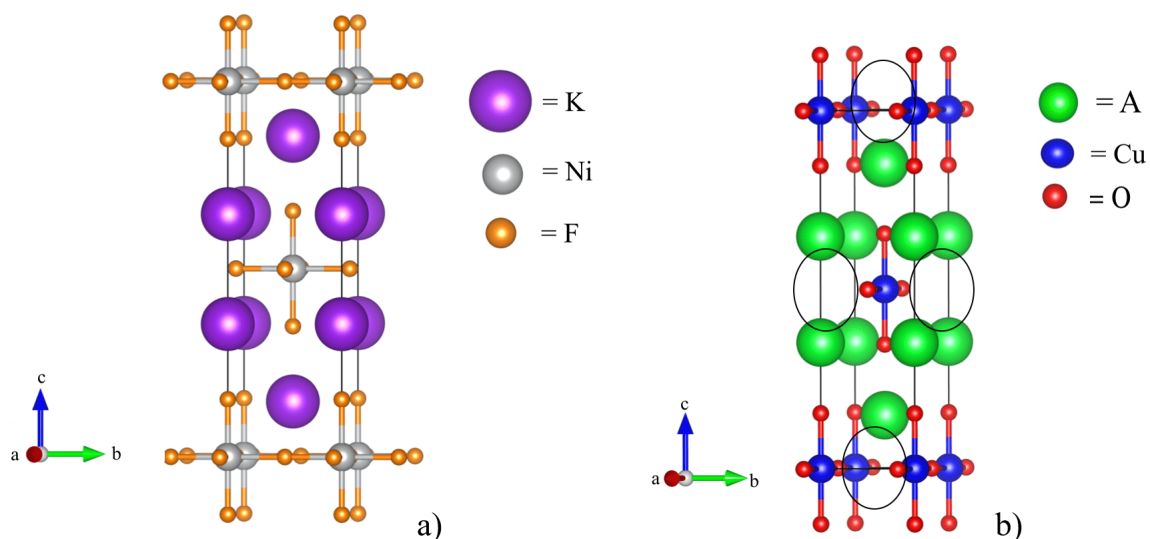
Figure 3.1: Crystal structures of K_2NiF_4 (a) and of A_2CuO_3 (b). The anion vacancies in A_2CuO_3 are highlighted using the black ovals.

Sr_2CuO_3 has been reported with two different types of unit cells, one with the oxide as the origin and a 2nd unit cell with a copper cation as the origin.[88, 197] A comparison of the different structures of Sr_2CuO_3 has been shown within Figure 3.2. Both structures have *Immm* space groups with (a) have the lattice parameters of (a = 12.7163(2), b = 3.9159(1), c = 3.5032(1)) and (b), (a = 3.9089(2), b = 3.4940(2), c = 12.6910(7)).
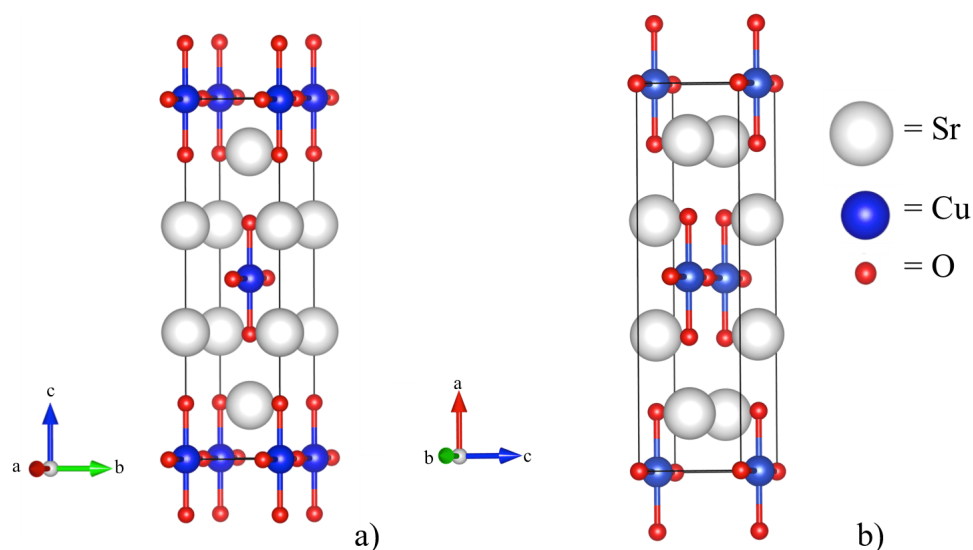
Figure 3.2: A comparison of the two unit cells of Sr_2CuO_3 with a copper cation a), and an oxide b) set as the origin.

Through anion insertion the coordination state of the copper cations, as well as their oxidation state can be changed. In these compounds the Cu^{2+} cation has the ability within the crystal structures to expand its coordination state from 4 (square planar) to 6 (octahedral). There is also the possibility of the copper cation to be oxidised to a higher oxidation state such as Cu^{3+}. The incorporation of F^- into Sr_2CuO_3 for example results in the high temperature (46 K) superconductor $Sr_2CuO_2F_{2+\delta}$ and has the copper expanding its coordination number from 4 to 6 as well as showing a $Cu^{2+/3+}$ mixed valence.[92] This compound is an example of how anion vacancies can act as "reaction sites" for preparing novel mixed anion compounds with new properties.

One of the aims of this project is to investigate how direct insertion and reaction within these anion vacancies can lead to novel materials. In order to do this, a clear understanding of the anion vacancies and how they are arranged within the crystal structure is important.

This work investigates utilising the anion vacancies within alkaline earth metal cuprates (A_2CuO_3) as hosting/reaction sites for CO_2. These vacancies have potential to store CO_2, similar to porous materials like zeolites, but have A-O (A = Sr, Ca and Ba) groups which react and form a carbonate.[198, 199] It is proposed that within these vacancies CO_2 directly

reacts with A-O groups to prepare a mixed metal oxide carbonate based on the formula $Sr_{2-x}A_xCuO_2(CO_3)$ (x = 0 − 2). In this way CO_2 can be utilised as a chemical reagent for the preparation of mixed metal oxide carbonates. Studies by Juhasz *et al.* and Homonnay *et al.* found that $Sr_{0.95}Ca_{0.05}Co_{0.5}Fe_{0.5}O_{3-\delta}$, which is anion-deficient and has alkaline earth metal oxides, is able to absorbe CO_2 at 950 °C in the oxygen vacancies resulting in a mixed phase of $(Ca,Sr)CO_3$, $Co_xFe_{3-x}O_4$ and $(Ca,Sr)(Fe,Co)_2O_4$.[200, 201]

$Sr_2CuO_2(CO_3)$ was reported by Babu *et al.* as an intermediate during the formation of Sr_2CuO_3 from $SrCO_3$ and CuO with a primitive unit cell structure (*P4/mmm*).[80] The synthetic process was then developed by Miyazaki *et al.*, with $SrCO_3$ and CuO reacting under a O_2/CO_2 gaseous mixture.[116] Miyazaki *et al.* also reported a different crystal structure as a body-centred ($I\bar{4}$) tetragonal different to the primitive structure reported by Babu *et al.*. In both cases the crystal systems are tetragonal with carbonate groups located within the strontium layers. Structures of both unit cells are presented in Figure 3.3 with lattice parameters in Table 3.1. The structural information on each in shown in Chapter 10, appendix, Tables 8.1 and 8.2.
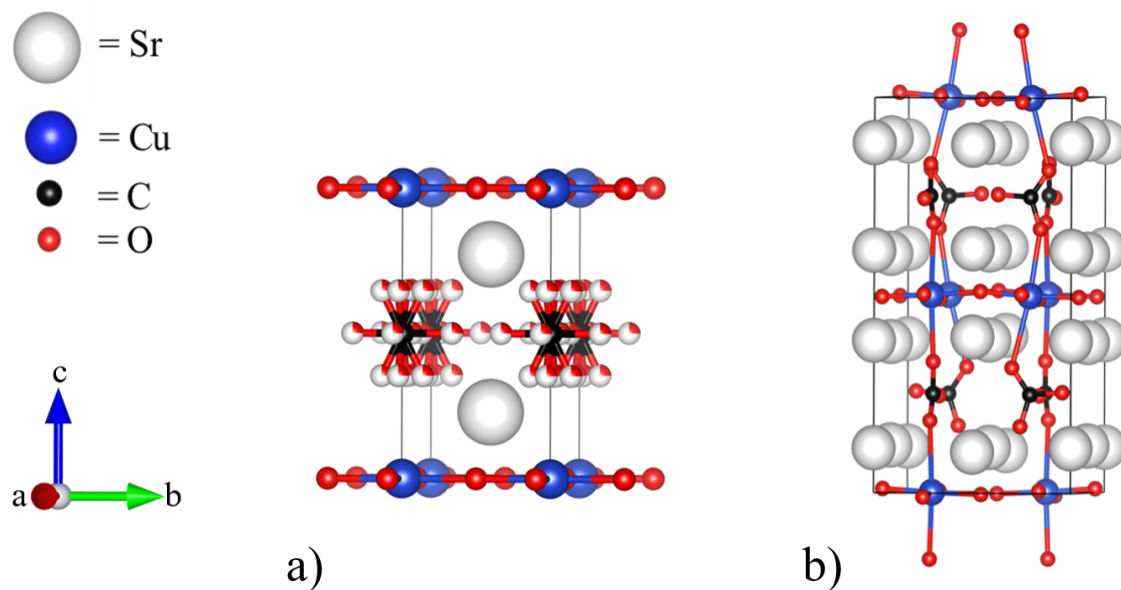
Figure 3.3: The two different types of crystal structures of $Sr_2CuO_2(CO_3)$ reported by a), Babu *et al.*[80] and b) Miyazaki *et al.*[116]

Table 3.1: Comparison of the unit cells parameters and space groups for $Sr_2CuO_2(CO_3)$ reported by Babu *et al.* and Miyazaki *et al.*.[80, 116]

Model	Space group	$a(Å)$	$c(Å)$	$V(Å^3)$
Babu *et al.*	*P4/mmm*	3.9033(2)	7.4925(4)	114.153
Miyazaki *et al.*	*I$\bar{4}$*	7.8045(1)	14.993(1)	913.227

A third structure of $Sr_2CuO_2(CO_3)$ (Figure 3.4) has also been reported by Nakata *et al.* that is only present at temperatures of over 300 °C.[117] As with the other structures, this has a tetragonal crystal system, but with the space group, ($P42_12$). This structure also has the carbons located at the unit cell origin, with the cell parameters of $a = 5.54364(8)$ Å and $c = 7.53823(11)$ Å with the carbonate groups located between the CuO_2 layers.
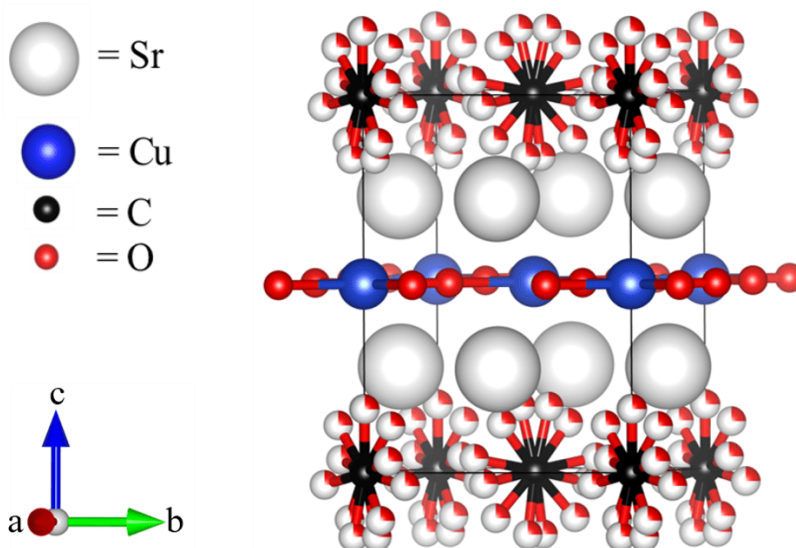
Figure 3.4: Structure of $Sr_2CuO_2(CO_3)$ reported above 300 °C. The white spheres partially coloured by red are sites where the oxygen atoms have an occupancy of 0.25.[117]

Babu *et al.* reported the carbonates as positioned around the strontium sites.[80] This resulted in separate and distinctive $SrCO_3$ and CuO_2 layers. Miyazaki however, reported the carbonate groups being coordinated to that copper sites.[116] Resulting in an expansion of copper's coordination from 4 (square planar) to 6 (octahedral). This is similar to the structural changes

shown when fluoride is inserted into Sr_2CuO_3 to prepare $Sr_2CuO_2F_{2+\delta}$.[92] Both oxide carbonate models have been adopted to describe the structure of prepared compounds.

3.2 Experimental

3.2.1 Material preparation

Sr_2CuO_3 was prepared via a high temperature method using polycrystalline ACO_3 (A = Sr, Ba and Ca) (98.5% BDH GPR), and CuO (96.0% BDH GPR). All reagents were stored in an oven at approximately 100 °C to prevent moisture contamination. The reagents were mixed in a stoichiometric ratio to prepare 1g of product, with acetone to produce a dispersed homogenous mixture. The reaction scheme 3.1 shows how the $Sr_{2-x}A_xCuO_3$ (A = Ca and Ba) series of compounds can be prepared from stoichiometric quantities of $SrCO_3$, ACO_3 and CuO.

This mixture was placed into an aluminia crucible and inserted into a box/tubular furnace and heated to 1000 °C for 14 hours in static air. Intermediate regrinding and reheating cycles were carried out until high purity products (> 99%) was achieved and confirmed using X-ray diffraction analysis. These samples were then used for reacting with CO_2 gas.

$$2\text{–x } SrCO_3 + x\, ACO_3 + CuO \rightarrow Sr_{2-x}A_xCuO_3 + 2\, CO_2 \qquad (3.1)$$
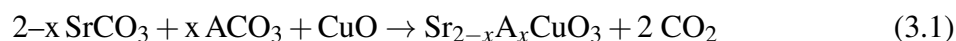
Once a pure sample of A_2CuO_3 (A = Sr and Ca) had been prepared, the next step was to react the compounds with CO_2 gas. Reaction of the oxide and CO_2 was followed in-situ using thermogravimetric analysis TGA at a flow rate of 100 ml/min, with a heating rate of 100 °C/min. These conditions were maintained in all reactions and atmospheres. Samples (50 mg) were placed into an alumina crucible and then inserted into the TGA furnace chamber. The samples were initially heated to 1000 °C under air to prevent decomposition of the oxide into undesired compounds such as $SrCO_3$. The temperature was held at 1000 °C for 2 mins to equilibrate the system, the gaseous atmosphere was then changed from air to pure CO_2. After a 15 minute heating cycle under CO_2 at 1000 °C, the gas was then switched back to air

for the samples to cool to room temperature.

3.2.2   Charaterisation

3.2.2.1   Powder X-Ray Diffraction (PXRD)

Powder X-Ray Diffraction (PXRD) was carried out on a PANalytical Empyrean Series 2 Diffractometer operating $CuK_{\alpha1}$ (λ = 1.54056 Å) radiation. Samples were scanned using an automatic slit at a step size of 0.026° and a net time per step of 304.2 s at a power setting of 45 kV and 30 mA. A $2\theta°$ range of 5-80 was used as the scanned area. Subsequent analysis was performed in HighScore Plus 1 using the PDF-2 2012 database of powder patterns.[202] The data collected for Rietveld refinements had a scan range from 5-120 with a 1/4° fixed slit at a step size of 0.026° and a net time per step of 1221.45 s using a power setting of 45 kV and 40 mA. The powder diffraction data was analysed by profile analysis as implemented in the GSAS suite of programs via the EXPGUI software.[152, 154]

3.2.2.2   Thermogravimetric analysis (TGA)

Thermogravimetric analysis (TGA) was carried out using a Metler Toledo TDA/DSC 1Star System which showed the mass of the sample changing at different temperatures and gases. CO_2, O_2 and air atmospheres were used. All gas flow rates were maintained at a value of 100 ml/min and the temperature ramp rate was at 100 °C/min. A standard reaction would involve inserting a single sample into the TGA furnace at room temperature to be exposed to the gaseous atmosphere before heating. The overall change in mass of the sample was determined through subtracting the value at the start of the reaction, to that at the end of the reaction when the mass of the sample was allowed to reach equilibrium. This was to give a quantitative value of the amount of CO_2 utilised in the oxide. By monitoring the change in mass over time this also allowed the kinetics of the reaction to be studied.

3.2.2.3 Fourier Transform Infrared (FTIR) Spectroscopy

The application of FTIR spectroscopy was used to identify any carbonate groups present within a sample. This could either be in the form of surface adsorbed carbonates or any CO_2 that may have reacted within the solid. The equipment used was that of a Perkin Elmer diamond tipped FT-IR. When analysing each sample the scans carried out used a resolution factor of 1. This was to prevent background noise interfering with the spectrum and allow the peaks to be refined for identifying the compound. A scan range between 600 - 3000 cm^{-1} wavenumber was used to show peaks associated with either CO_2 or any carbonates.

3.3 Results and Discussion

3.3.1 Reaction of CO_2 with Sr_2CuO_3 towards $Sr_2CuO_2(CO_3)$

3.3.1.1 Structural Characterisation of Sr_2CuO_3

The synthesis of Sr_2CuO_3 from $SrCO_3$ and CuO resulted in a dark brown polycrystalline product. The identity of this sample as Sr_2CuO_3 was confirmed through PXRD analysis as all the peaks matched those reported for the cuprate and with no other peaks found and confirms the sample as single phase. Rietveld refinements used the X-ray diffraction data for the model of Sr_2CuO_3 by Weller and Lines.[88] The background was initially modelled using the Cosine Fourier series with twelve terms. The multi-term Simpson's rule integration of the pseudo-Voigt was used in order to model the peaks shapes within the pattern.[203, 204] The parameters refined were: the cell parameters (*a, b, c*), scale factors, isotropic thermal parameters U$_{iso}$, the asymmetry and sample displacement (shift). The refinement was found to be in reasonable agreement with the model reported by Weller and Lines with R-values of R$_{wp}$ = 13 % and R$_p$ = 9 %. The refinement patterns and unit cell parameters are presented in Figure 3.5 and Table 3.2.[88]
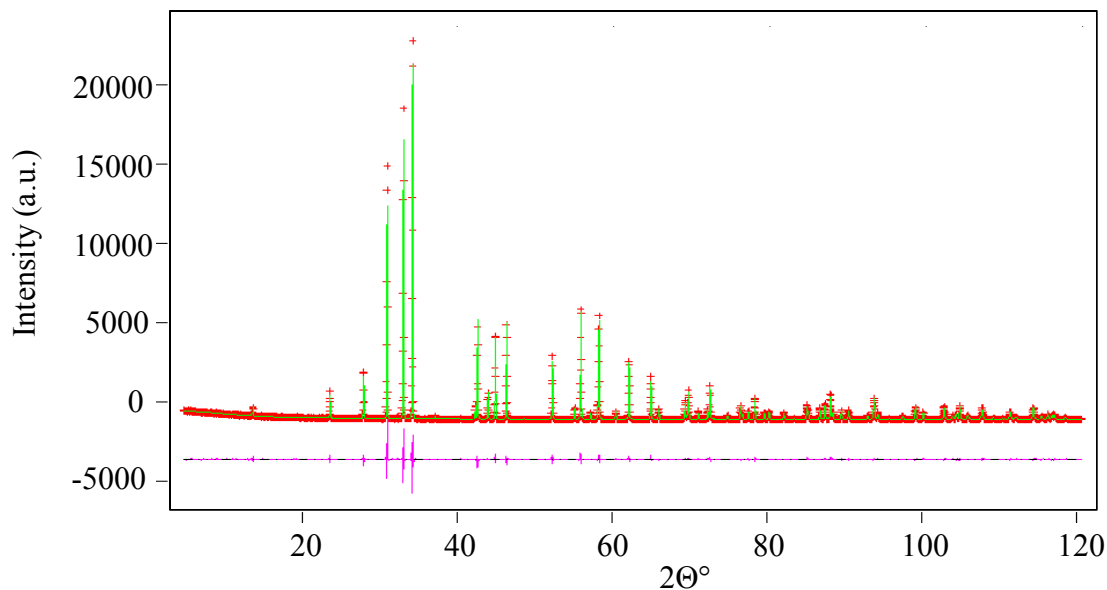
Figure 3.5: X-ray powder diffraction profiles of Sr_2CuO_3 using the model by Weller and Lines showing observed (red crosses), calculated (green) and difference (purple) patterns.[88]

Table 3.2: Comparison of the lattice parameters (Å) and unit cell volume ($Å^3$) from the refinement of Sr_2CuO_3 compared to those reported by Weller and Lines.[88]

Model	a Å	b Å	c Å	V ($Å^3$)
Weller and Lines	12.7163(2)	3.9159(1)	3.5032(1)	174.44(1)
This work	12.7229(10)	3.9185(40)	3.5046(1)	174.72(6)

Once Sr_2CuO_3 had been prepared the next step was to carry out reactions with CO_2 gas. The aim of these reactions were to directly insert CO_2 into the anion vacancies of the crystal structure to form $Sr_2CuO_2(CO_3)$.

3.3.1.2 Reaction of Sr_2CuO_3 with CO_2 to prepare $Sr_2CuO_2(CO_3)$

In literature, the oxide carbonate $Sr_2CuO_2(CO_3)$ was originally prepared through the reaction of $SrCO_3$ and CuO under a (CO_2/O_2) gas mixture.[80, 117, 116] Therefore, no direct reaction between Sr_2CuO_3 with CO_2 has been reported. As a result, various reactions with CO_2 using different temperatures and conditions were initially investigated to determine what param-

113

eters would drive the reaction towards high purity $Sr_2CuO_2(CO_3)$. Firstly Sr_2CuO_3 was heated to 1000 °C then cooled back down to room temperature completely under CO_2 gas. The sample was then analysed by PXRD and showed a mixture of $Sr_2CuO_2(CO_3)$ along side $SrCO_3$.[117, 205]

The secondary phase is potentially a result of Sr_2CuO_3 reacting with CO_2 and forming $SrCO_3$ as an intermediate process before the generation of $Sr_2CuO_2(CO_3)$. The TGA curve in Figure 3.6 shows the mass of the sample in-situ during the reaction with CO_2 gas. The curve shows that the sample mass starts to increase gradually from the oxide reacting with CO_2, at 400 °C then at a greater rate at 600 °C and 700 °C.
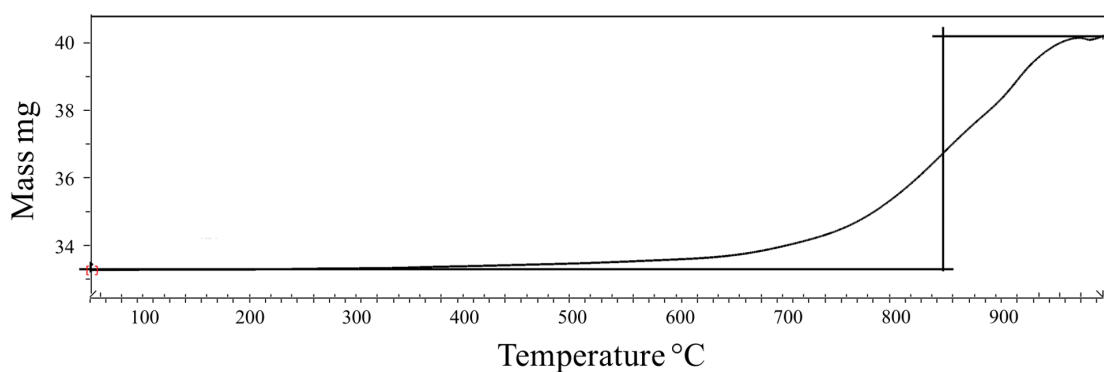
Figure 3.6: TGA curve showing the mass increase of Sr_2CuO_3 heated to 1000 °C under CO_2.

During the fluorination of Sr_2CuO_3 towards $Sr_2CuO_2F_{2+\delta}$ by Francesconi *et al.*, certain fluorinating reagents such as NH_4F, were found to result in side products such as SrF_2.[93] It is possible that a similar process in occurring as CO_2 is passing over Sr_2CuO_3, decomposition is taking place resulting $SrCO_3$. It is when the temperature reaches 1000 °C that the $Sr_2CuO_2(CO_3)$ is then starting to form. This relates to the original method for preparing the oxide carbonate at 950 °C.[80, 116]

The reaction of Sr_2CuO_3 heated to 1000 °C solely under CO_2 resulted in a mixed phase of $SrCO_3$, CuO and $Sr_2CuO_2(CO_3)$. In order to drive the reaction towards primarily the oxide carbonate, and reduce other phases different reaction conditions were investigated. One of the methods used was to heat Sr_2CuO_3 to a specific temperature under air, then to change the gas type to CO_2. The sample would then be maintained under these conditions for 15 minutes to avoid the risk of decomposition to $SrCO_3$. Afterwards the gas would then be switched

back to air and cooled down to room temperature. Sr_2CuO_3 was originally prepared under air at 1000 °C, therefore it was considered stable under these conditions. The temperatures initially investigated for reacting Sr_2CuO_3 with CO_2 were 500, 700 and 900 °C. After each reaction the sample was then analysed using PXRD (Figure 3.7) to show what products had been formed at each temperature.
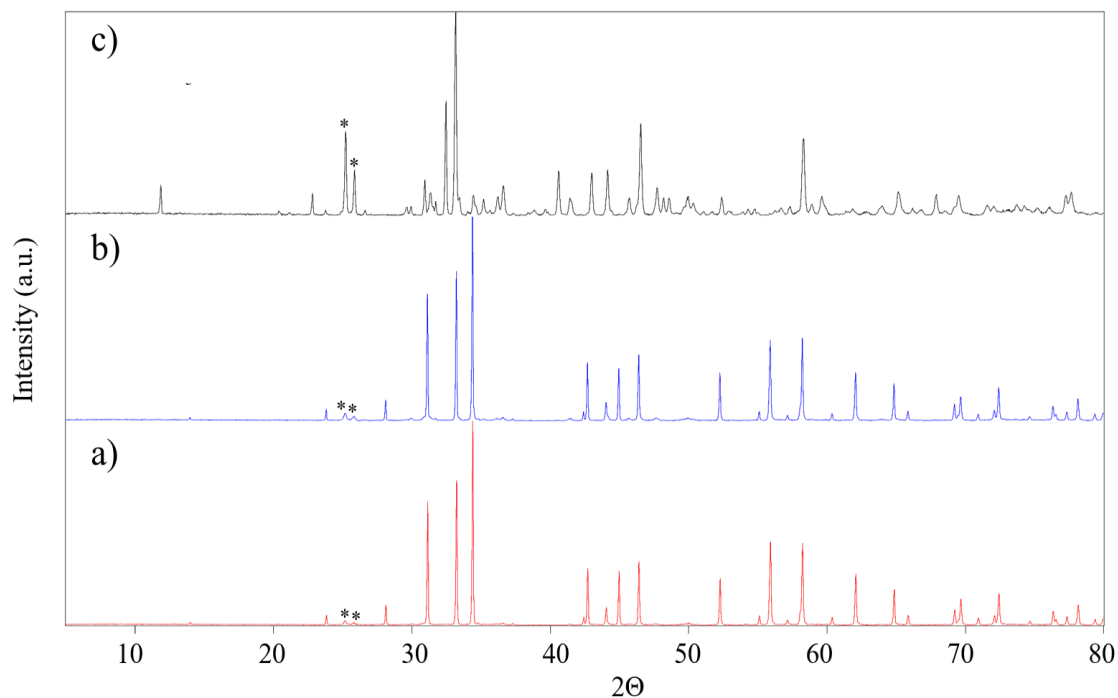
Figure 3.7: PXRD patterns of the samples prepared from heating Sr_2CuO_3 to a) 500, b) 700 and c) 900 °C in air then maintained at these temperatures under CO_2 for 15 minutes. Each PXRD pattern shows the main peaks belonging to the secondary phase $SrCO_3$ (*).

The PXRD patterns showed that at 700 °C or below, Sr_2CuO_3 would start to decompose to $SrCO_3$ under CO_2. However, at 900 °C it was found that $Sr_2CuO_2(CO_3)$ was starting to form (two main peaks at approximately $2\theta = 32.5°$) within the sample, yet $SrCO_3$ was still present. A study by Alikhanzadeh-Arani *et al.* found that preparing Sr_2CuO_3 via a sol-gel at 900 °C would result in $SrCO_3$ formation being favoured.[206] The temperature was then increased to 1000 °C and showed to favour the formation of $Sr_2CuO_2(CO_3)$ with a minimum amount of $SrCO_3$ present. A comparison of the PXRD patterns from the sample to that of Babu *et al.* in Figure 3.8, confirms the identity of $Sr_2CuO_2(CO_3)$.[80]
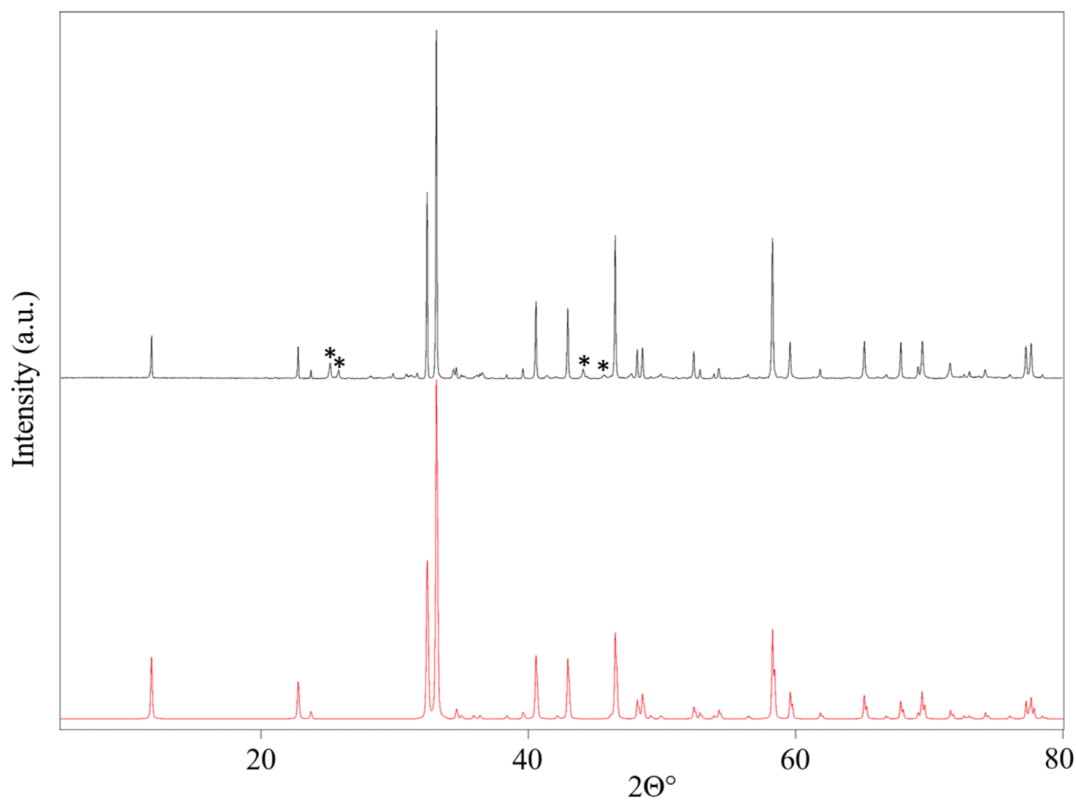
Figure 3.8: PXRD pattern of $Sr_2CuO_2(CO_3)$ (black) prepared at 1000 °C with peaks from $SrCO_3$ (*) synthesised using alternating gases compared to a PXRD pattern of $Sr_2CuO_2(CO_3)$ (red) reported by Babu *et al.*[80]

Through alternating the reaction atmospheres between air and CO_2 at 1000 °C, a novel approach to prepare $Sr_2CuO_2(CO_3)$, with minor impurities of $SrCO_3$ was provided. This approach avoids the use of more complex routes such as the reaction of gaseous mixtures as reported by Miyazaki *et al.*.[116]

This reaction was carried out in-situ under TGA monitoring, allowing a study of the "real time formation" of the oxide carbonate. A TGA curve of this reaction is given in Figure 3.9, showing at what temperatures Sr_2CuO_3 increases in mass under CO_2. During the reaction the mass would initially decrease due to the removal of moisture on the sample. It would then remain constant up to 1000 °C until the gas was switched to pure CO_2.
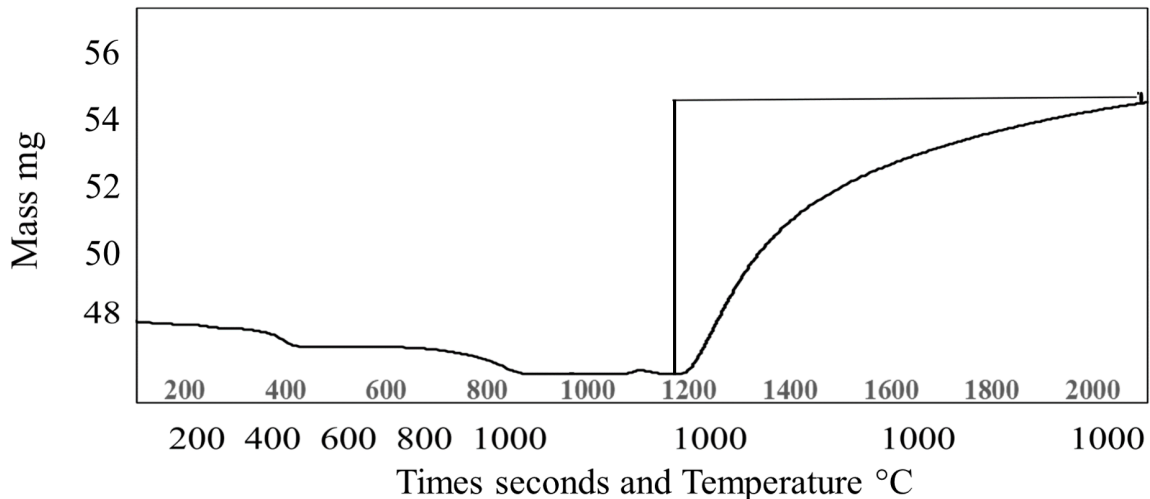
Figure 3.9: TGA curve of Sr_2CuO_3 heated to 1000 °C in air, left under CO_2 for 15 minutes then cooled to room temperature. The change in mass is measured from the point the gas is changed to CO_2.

This reaction resulted in the sample increasing its total mass by approximately 16 % which is simialr to other mass increases from similar experiments at 14.5%. This increase will be a result of the incorporation of CO_2 from the gas flow into the structure of Sr_2CuO_3 towards forming $Sr_2CuO_2(CO_3)$.

3.3.2   Characterisation of $Sr_2CuO_2(CO_3)$

The PXRD patterns showed that $Sr_2CuO_2(CO_3)$ had been prepared, with minimum $SrCO_3$ impurities. The lattice constants and atomic positions of the oxide carbonate phases could be determined, along with the quantification of the two phases using 2-phase Rietveld refinements. The two different reported structures for $Sr_2CuO_2(CO_3)$ at room temperature by Babu et al. and Miyazaki et al. were used for the refinements.[80, 197] This was also to determine which model would have the best agreement with the sample. The third model of $Sr_2CuO_2(CO_3)$ reported by Nakata et al. ($P42_12$), was found to only be present at temperatures of approximately 300 °C and as a result was not used for the refinements.[117]

The refinement pattern for each model, as well as the R-values and unit cell parameters have been reported within Figures 3.10 and 3.11, and Table 3.3. For the two-phase refinements

the pattern reported by Antao and Hassan was used for $SrCO_3$.[205] The background was modelled using the fifth functional power series type in GSAS with 6 terms. The multi-term Simpson's rule integration of the pseudo-Voigt was used to model the peaks shapes within the pattern.[203, 204] The parameters refined were: the cell parameters (*a, b, c*) and scale factors for both phases. The isothermal parameter U_{iso} were also refined for all atoms in each phase. The asymmetry and shift of the peaks were also refined along with the Lorentzian anisotropic strain broadening.
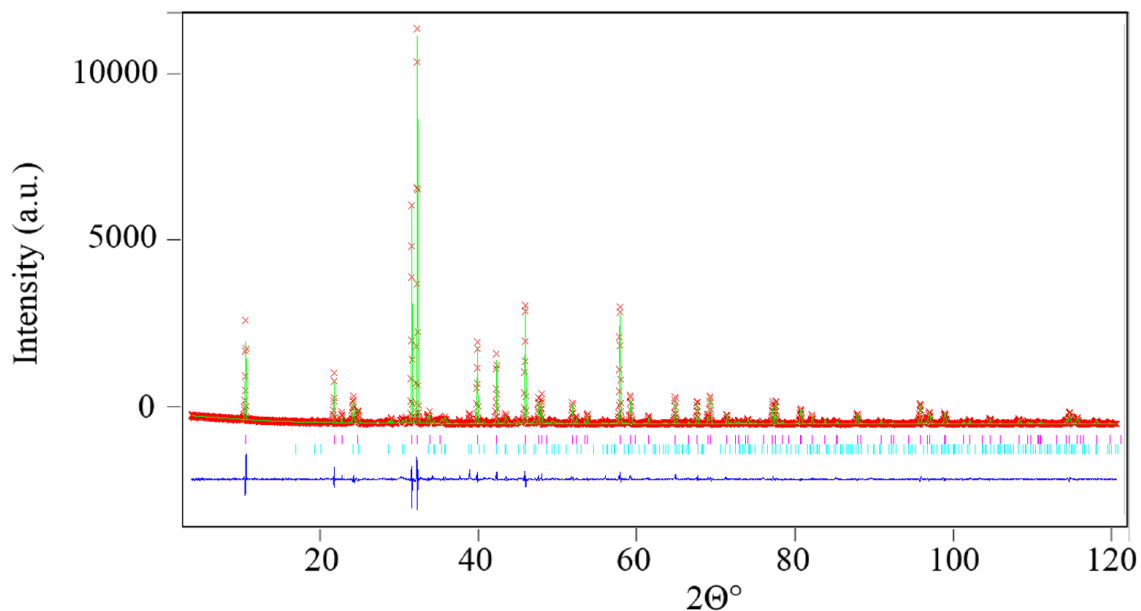
Figure 3.10: X-ray powder diffraction profiles of $Sr_2CuO_2(CO_3)$ using the model provided by Babu *et al.* showing observed (red crosses), calculated (green) and difference (light blue) patterns.[80] The ticks represent $Sr_2CuO_2(CO_3)$ (pink) and the $SrCO_3$ (blue) impurities.
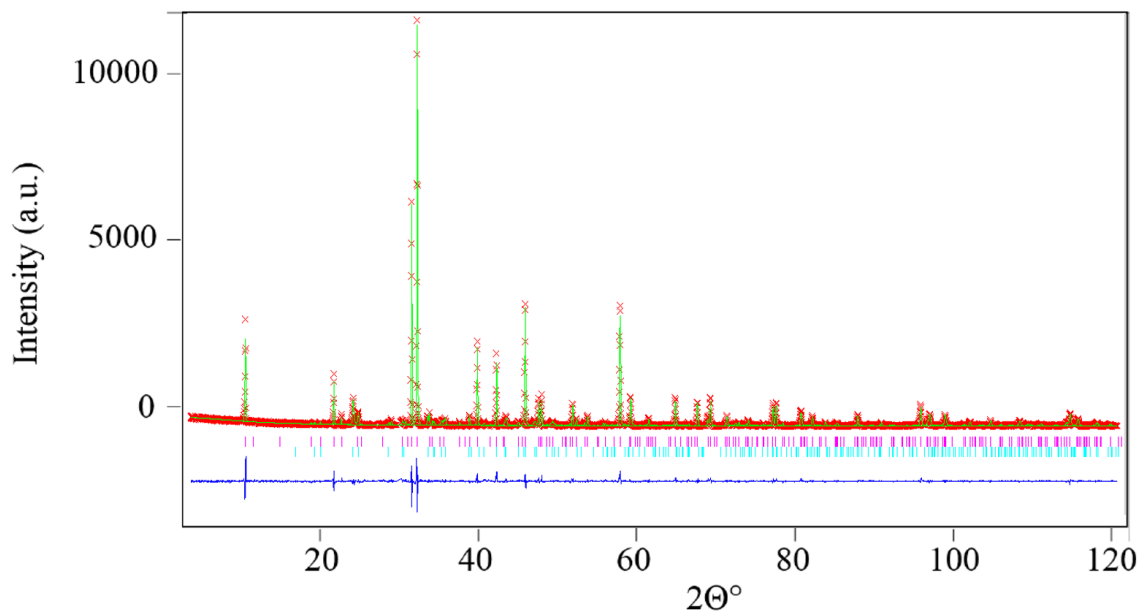
Figure 3.11: X-ray powder diffraction profiles of $Sr_2CuO_2(CO_3)$ using the model provided by Miyazaki *et al.* showing observed (red crosses), calculated (green) and difference (purple) patterns.[116] The ticks represent $Sr_2CuO_2(CO_3)$ (pink) and the $SrCO_3$ (blue) impurities.

Table 3.3: Comparison of the unit cells parameters Å and space groups of the different crystal structures reported for $Sr_2CuO_2(CO_3)$.

Model	a Å	c Å	Volume ($Å^3$)	R_{wp}	R_p	χ^2
$Sr_2CuO_2(CO_3)^{80}$	3.90342(4)	7.49722(13)	114.233(4)	17.61	12.43	3.399
$Sr_2CuO_2(CO_3)^{116}$	7.80673(7)	14.99413(22)	913.817(25)	15.71	11.37	2.721

The R_{wp} and R_p values act to determine how the experimental data matches up with the reported crystal structural data of $Sr_2CuO_2(CO_3)$. Using the different models for the oxide carbonate it was found that both were shown to be in close agreement with the prepared $Sr_2CuO_2(CO_3)$ with a difference of around 2% and 1% respectively. As a result, the model reported by Babu *et al.* has been used for further refinements of oxide carbonate compounds within the $Sr_{2-x}A_xCuO_2(CO_3)$ series. This model has also been used to describe the following compounds of $Ca_2CuO_2(CO_3)$ and $Sr_{2-x}Ba_xCuO_2(CO_3)$ $(0.5 \leq x \leq 2)$ which have also been investigated within this project.[115, 207] The refined data and structural parameters

119

for $Sr_2CuO_2(CO_3)$ using the model by Babu *et al.* are reported in appendix, Table 8.3.[80] In both cases it was found that the amount of $SrCO_3$ remaining within the phase consisted approximately below 15 %. The quantities of each phase has been presented in Table 3.5.

Table 3.4: Quantities of $Sr_2CuO_2(CO_3)$ and $SrCO_3$ in each phase using the different reported models of the oxide carbonates.

Model	$Sr_2CuO_2(CO_3)\%$	$SrCO_3\%$
Babu *et al.*[80]	85.5 ±0.1	14.5 ±0.2
Miyazaki *et al.*[116]	86.2 ±0.1	13.8 ±0.2

The structure of $Sr_2CuO_2(CO_3)$ with the refined structural parameters is presented in Figure 3.12. It shows the oxides surrounding each carbon atom within the carbonate groups having an occupancy of 0.25 and their possible sites of occupancy. This is a consequence when using the model of $Sr_2CuO_2(CO_3)$ reported Babu *et al.* with various possible positions of the oxides around the carbons within the CO_3 groups.[80] Therefore, it is difficult to determine the actual positions of these types of oxides. As a result of there various possible locations high isothermal values are determined.
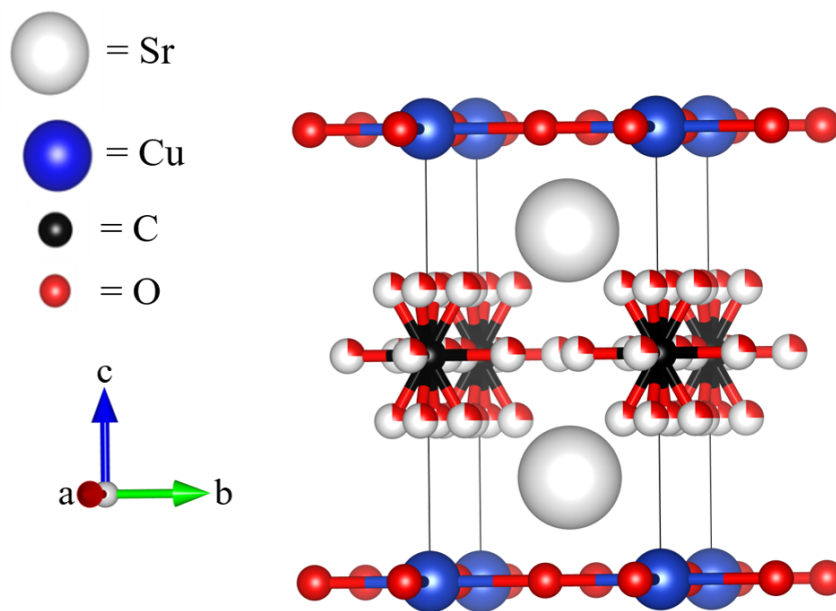
Figure 3.12: $Sr_2CuO_2(CO_3)$ structure determined through Rietveld refinements. The white spheres partially coloured in red represent the partially occupied oxides.

FTIR spectroscopy was also used to study the vibrational behaviour of the carbonate groups within $Sr_2CuO_2(CO_3)$, with the IR spectrum in Figure 3.13. This would then be compared with vibrational frequencies for the oxide carbonate reported by Armstrong *et al.* in Table 3.4.[207]
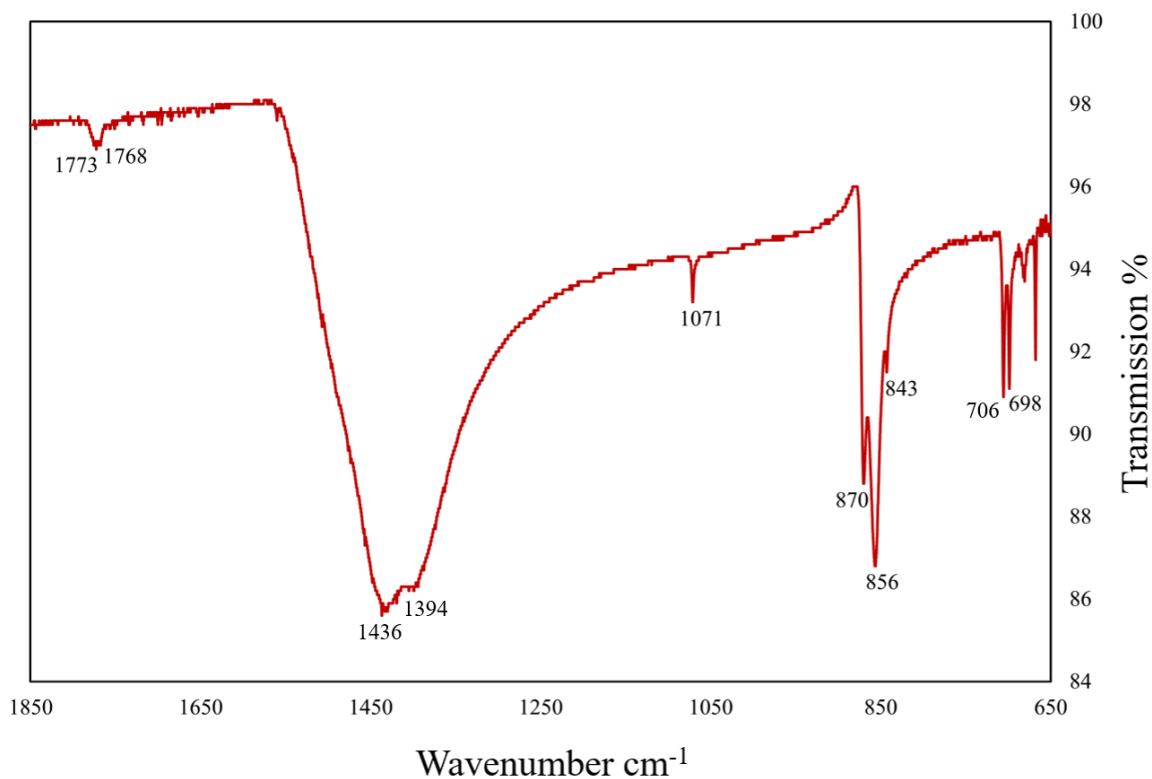
Figure 3.13: IR spectrum of $Sr_2CuO_2(CO_3)$ with the vibrational frequency belonging to the carbonate groups labelled.

Table 3.5: The values for the vibrational modes of $Sr_2CuO_2(CO_3)$ determined within this project compared to those reported by Armstrong *et al.*.[207]

Vibrational mode cm^{-1}	This project	Armstrong *et al.*[207]	Difference
	(1)	(2)	(1) - (2)
Symmetric stretching ν_1	1071	1072	-1
Symmetric bending ν_2	870	870	0
Asymmetric stretching ν_3	1436	1449	-13
Asymmetric stretching ν_3'	1394	1412	-18
Asymmetric bending ν_4	706	704	2
Asymmetric bending ν_4'	698	704	-6
RMSD	N/A	N/A	9.4

A comparison of the vibrational frequencies show the values agree within an RMSD value of

122

9.4 cm^{-1}. The greatest difference observed was that of both asymmetric stretches within $\geq$10 cm^{-1}. This difference could be attributed to the phase being a mixture of $Sr_2CuO_2(CO_3)$ and $SrCO_3$ which have similar vibration frequency values. It is proposed that as the $SrCO_3$ makes up only 15% of the phase then the vibrational frequencies detected will primarily come from the oxide carbonate. Future work will aim towards preparing samples of greater purity for a better vibrational study.

In summary, through alternating between CO_2 gas and air, Sr_2CuO_3 forms $Sr_2CuO_2(CO_3)$ via direction reaction with CO_2 at 1000 °C. These reactions were monitored under real time conditions via TGA analysis as the heating process and reagent gas could be supplied in-situ. This provides a step by step monitoring of how the sample mass changes over the reaction with CO_2, this has allowed the quantity of CO_2 captured during $Sr_2CuO_2(CO_3)$ formation to also be determined.

3.3.3   Quantification of CO_2 Utilised

Sr_2CuO_3 captures and utilises CO_2 through the formation of $Sr_2CuO_2(CO_3)$ via a solid-gas reaction. This was carried out in-situ using TGA, with the change in mass along the reaction monitored. Using the difference in mass from Sr_2CuO_3 before and after the reaction from the TGA curve, the quantity of CO_2 utilised by Sr_2CuO_3 has been measured. This measurement of the change in mass is shown within the TGA curve in Figure 3.9. The mass change from four TGA curves were used in order to determine an average value of mmol of CO_2 captured per gram of solid, (mmol/g). This being the standard unit measurement used for determining CO_2 capturing capability of materials.[13] The uncertainty for the CO_2 capturing capacity was also calculated from the TGA balance errors at $\pm$ 0.005 mg and shown in Table 3.6. The average amount of CO_2 capturing and utilisation capacity of Sr_2CuO_3 was determined to be 3.80 with an RMSD from the uncertainties at 0.01 mmol/g using the data from TGA.

Table 3.6: CO_2 capturing capacity of Sr_2CuO_3 and Uncertainty over a range of reactions

TGA curve	CO_2 capturing capacity mmol/g	Uncertainty mmol/g
1	3.778	0.004
2	3.661	0.004
3	3.838	0.004
4	3.911	0.004
Average	3.797	0.007

Alongside TGA, the quantity of CO_2 captured was also determined using the mass % values of the phases produced from the reaction. The reaction between Sr_2CuO_3 and CO_2 resulted in a mixed phase product consisting of 85.5 % of $Sr_2CuO_2(CO_3)$ and 14.5 % of $SrCO_3$, Table 3.4. The TGA curve from this reaction showed that the mass of the end product was that of 54.5841 mg. Using this value the mass %, mass of product and mass of CO_2 content from each phase can be determined and used to calculate the amount of CO_2 that was captured, Table 3.7

Table 3.7: Overall mass and mass % of $Sr_2CuO_2(CO_3)$ and $SrCO_3$ in product phase. Along with mass of CO_2 captured.

Phases	Mass %	Mass mg	CO_2 mass mg
$Sr_2CuO_2(CO_3)$	85.5 %	44.6694	6.207
$SrCO_3$	14.5 %	7.9147	2.646

Based on the Rietveld refinement results the overall amount of CO_2 captured was that of 8.853 mg by 47.1048 mg of $Sr_2CuO_2(CO_3)$. These values were then used and determined a CO_2 capturing capability of 4.28 mmol/g with an error of $\pm$ 0.01 mmol/g . This value is greater than that calculated using the TGA data at 3.80 mmol/g. The difference in values could be due to none of the possible CuO being detected within the product phase. It is proposed that CuO is not detected in the XRD data as its peaks are overshadowed by that of the other phases. As a result it is likely that the mass % of $Sr_2CuO_2(CO_3)$ and $SrCO_3$ would actually be less than what is reported. This would mean that the amount of CO_2 captured based on the mass % would be less.

Compared to amine based compounds which are used for CO_2 capture at an average 8.19 mmol/g, the strontium cuprate does not act as an improved alternative.[124] The values that are determined however, are greater than that of certain zeolite compounds (1.13 and 1.90 mmol/g) and mesopores MgO compounds at 1.82-2.27 mmol/g.[208, 209] Sr_2CuO_3 itself is not intended to act as a replacement for known CO_2 capturing/storing materials. However, it has been found to capture quantities of CO_2 higher than known solids. The captured CO_2 is then directed towards utilising the gas for preparing complex inorganic compounds.

3.3.4 Reaction kinetics of Sr_2CuO_3 with CO_2 forming $Sr_2CuO_2(CO_3)$

The direct reaction of Sr_2CuO_3 with CO_2 to prepare $Sr_2CuO_2(CO_3)$ was carried out in-situ using TGA equipment. The approach not only allowed control of various parameters such as temperature and gas type, it also allowed an in-situ monitoring of the mass of the sample over the reaction. Another benefit of this method was being able to measure the time of the reaction as it is being carried out. Using the change in mass over time, the order of the reaction as well as the reaction rate, k has been determined.

Using the TGA curve of mass vs time the points where Sr_2CuO_3 only increases in mass as it reacts with CO_2 to produce $Sr_2CuO_2(CO_3)$ was identified, Figure 3.14. The data points on the TGA curve were identified at 33.4466 mg (655 seconds) to 37.6611 mg (1355 seconds). After this point the mass would stop increasing and then plateau.
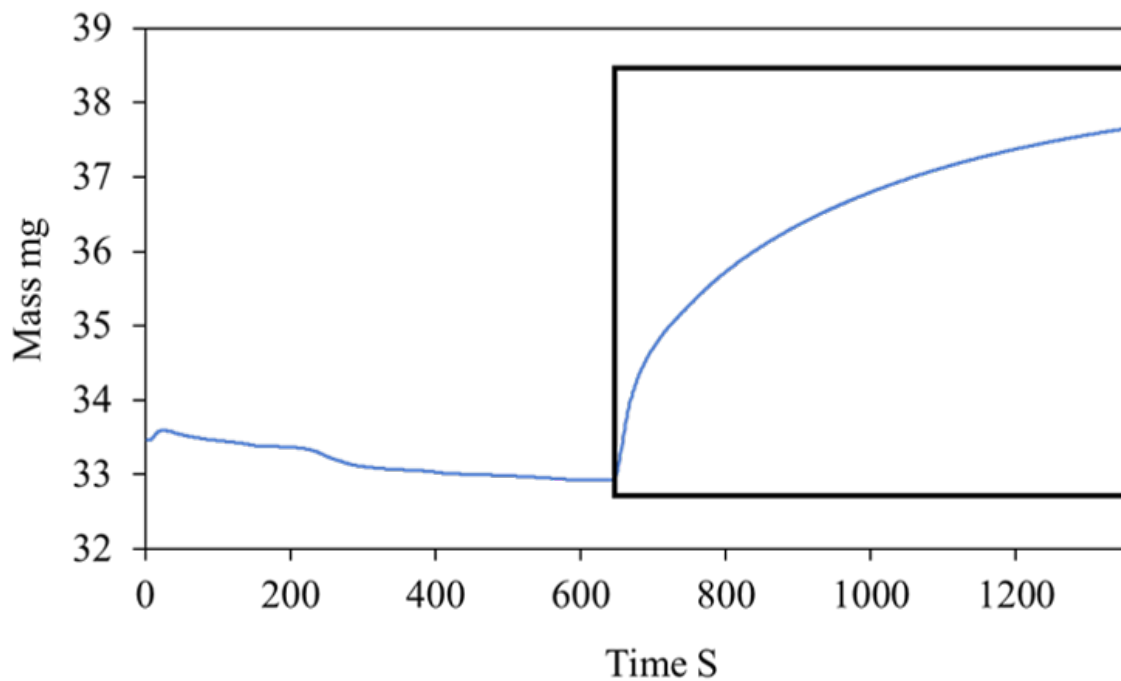
Figure 3.14: Selected area on TGA curve of mass vs time where the mass of Sr_2CuO_3 only increases as it reacts with CO_2 forming $Sr_2CuO_2(CO_3)$.

During these points the mass of the sample increased by 4.2145 mg as Sr_2CuO_3 reacted with CO_2 forming $Sr_2CuO_2(CO_3)$. It was determined that for every 1 mg of CO_2 captured, 7.9361 mg of Sr_2CuO_3 was consumed to form $Sr_2CuO_2(CO_3)$. Using this relationship the amount of Sr_2CuO_3 consumed at each second from the amount of CO_2 captured could be determined. The amount of Sr_2CuO_3 that was being consumed could then be subtracted from the original mass of Sr_2CuO_3. This would provide a trend line showing the mass of Sr_2CuO_3 decreasing over time as it is consumed to prepare $Sr_2CuO_2(CO_3)$, Figure 3.15.
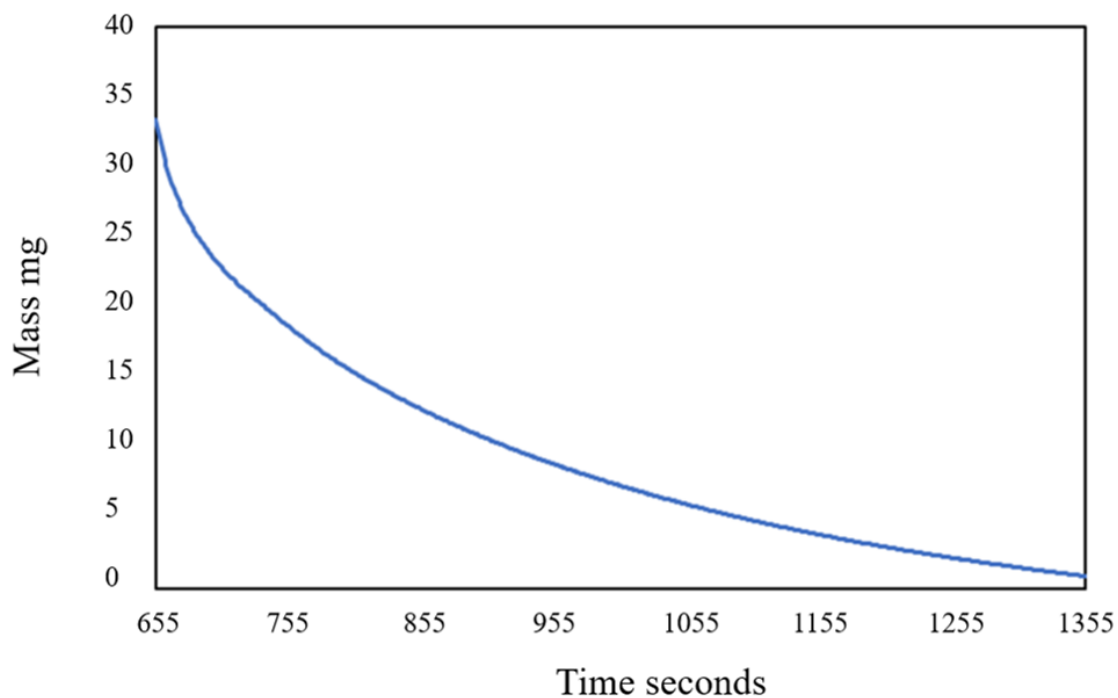
Figure 3.15: Decrease in mass of Sr_2CuO_3 as it reacts with CO_2 to produce $Sr_2CuO_2(CO_3)$.

The rate of the reaction can be determined through the relationship between the concentration of Sr_2CuO_3 vs time. The orders of reaction that would be possible are 0, 1st and 2nd orders. The trendline of the graph can also then be used to determine a quantitative value for the rate constant k. Figure 3.16 shows three different graphs for concentration vs time, (1) moles of Sr_2CuO_3 vs time seconds, (2) ln(moles) of Sr_2CuO_3 vs time seconds, and (3) 1/(moles) of Sr_2CuO_3 vs time seconds.
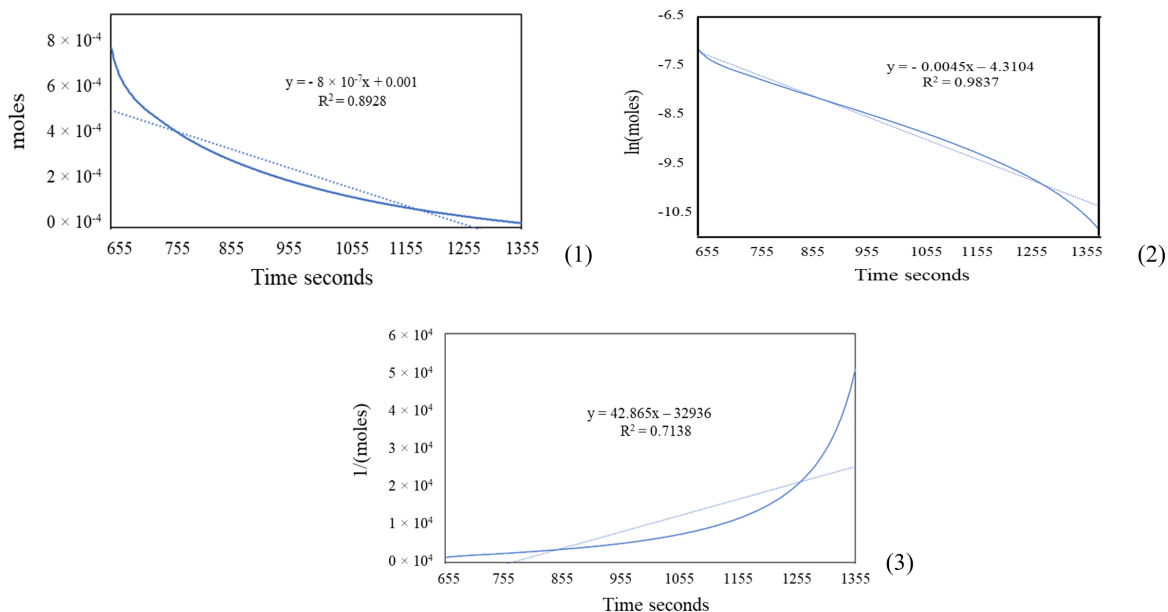
Figure 3.16: Three concentrations vs time graphs, (1) moles of Sr_2CuO_3 vs time seconds, (2) ln(moles) of Sr_2CuO_3 vs time seconds, and (3) 1/(moles) of Sr_2CuO_3 vs time second. Equations of trendlines and R^2 are given for each.

The trendline, (2) ln(moles) of Sr_2CuO_3 vs time seconds, shows an R^2 value closest towards 1 and the straightest line compared to the others. This indicates that the reaction, Sr_2CuO_3 + $CO_2 = Sr_2CuO_2(CO_3)$ is of 1st order. A value for the rate constant is also determined from the slope of the trendline at 0.0045 S^{-1}.

Through utilising TGA methods an alternating gaseous method has been developed for Sr_2CuO_3 to directly react with CO_2 to produce $Sr_2CuO_2(CO_3)$. The in-situ analysis of the mass vs time during this reaction has also allowed the kinetics of this reaction to be determined. Through using the change in mass over time it has been determined that the reaction is of 1st order with a rate constant of 0.0045 S^{-1}. This provides an understanding of the kinetics of this novel reaction for CO_2 capture.

3.3.5   Reversibility of $Sr_2CuO_2(CO_3)$ towards re-forming Sr_2CuO_3

A variety of materials such as zeolites and metal organic frameworks (MOFs) have not only been investigated for CO_2 capturing capabilities, but also for their regenerability abil-

ities.[210,211] This is so captured CO_2 can be removed in order for the material to be reused. Layered perovskite materials such as $Li_2SrTa_2O_7$ and $Ba_4Sb_2O_9$ are able to react with CO_2 giving a mixed phase of oxides and carbonates. These reactions can be reversed in order to re-form the original mixed metal oxide compounds to be used for repeated CO_2 capture.[87,212] This differs from the work in this project which aims at direct reactions with CO_2 towards the preparation of high purity inorganic compounds. It however, has been investigated if CO_2 can be removed from the prepared oxide carbonate to re-form the original mixed metal oxide.

In this work CO_2 has been found to directly react with Sr_2CuO_3 to form $Sr_2CuO_2(CO_3)$. It has also been found that CO_2 can be removed from $Sr_2CuO_2(CO_3)$ in order to re-form Sr_2CuO_3.

3.3.5.1 CO_2 extraction from $Sr_2CuO_2(CO_3)$ under Air

During the formation of $Sr_2CuO_2(CO_3)$, the oxide Sr_2CuO_3 was heated under alternating gases of air and CO_2. As a result, the first series of reversibility reactions were carried out under air. The first reverse cycle had a sample of $Sr_2CuO_2(CO_3)$ heated to 1000 °C in air for 15 minutes. This resulted in a mixed phase sample of Sr_2CuO_3 and $Sr_2CuO_2(CO_3)$. The next reaction then had the time increased to 60 minutes to remove as much CO_2 as possible and to re-form the oxide. PXRD patterns from the reactions have been compared in Figure 3.17. The comparison shows that 60 minutes drives the reaction to Sr_2CuO_3, compared to 15 minutes which showed unreacted $Sr_2CuO_2(CO_3)$ still present.
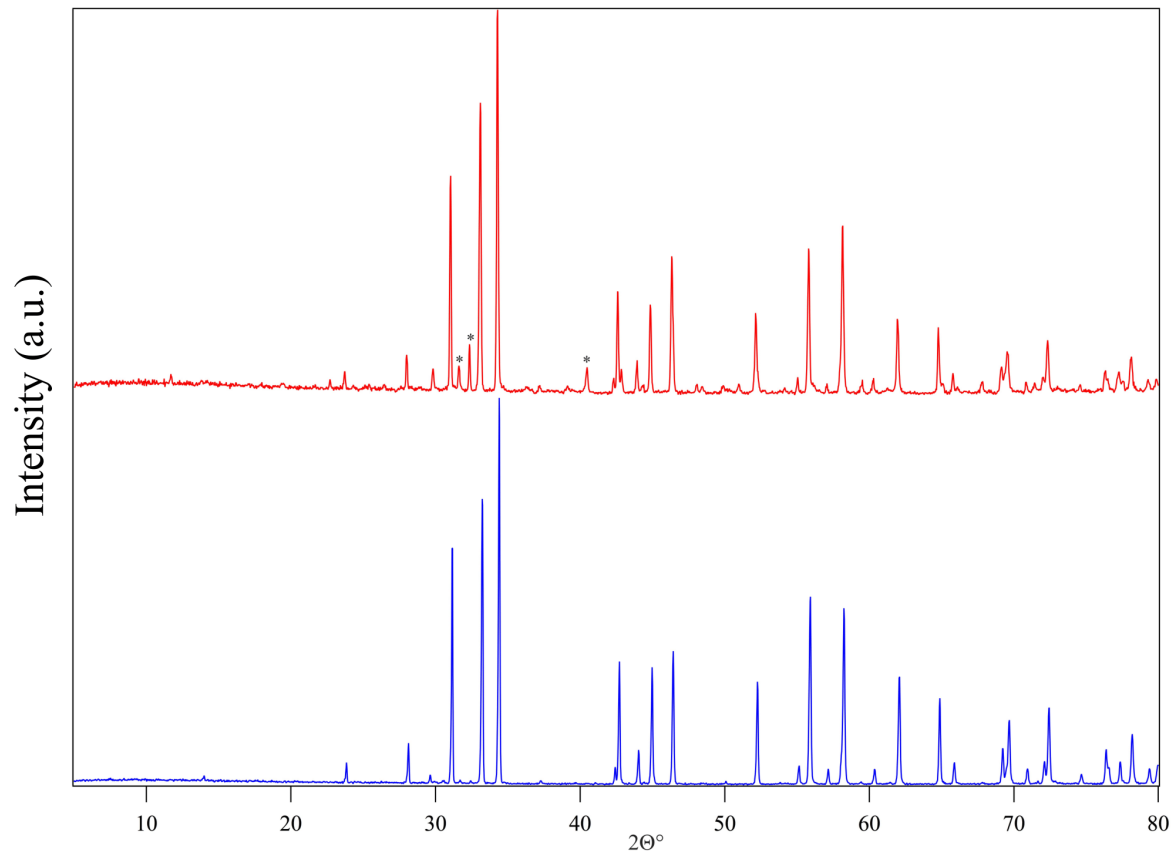
Figure 3.17: Comparison of a 15 minute (red) and 60 minute (blue). The peaks marked with (*) belong to that of $Sr_2CuO_2(CO_3)$.

As with the incorporation of CO_2, the reverse extraction reactions were also carried out in-situ within a TGA instrument. The TGA curve from the reverse reaction (Figure 3.18) shows an inverse trend compared to the incorporation reaction (Figure 3.9) as CO_2 is extracted when the temperature reaches 1000 $^\circ$C.
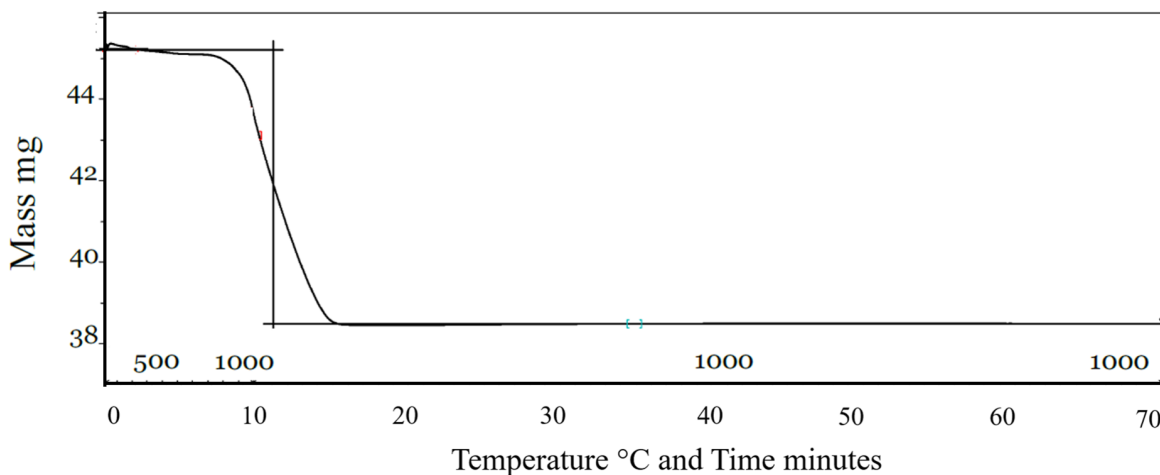
Figure 3.18: TGA curve of the extraction of CO_2 from $Sr_2CuO_2(CO_3)$ over a 60 minute heating cycle in air at 1000 °C.

Once a method had been developed to remove CO_2 and re-form Sr_2CuO_3, the next step was to investigate if multiple incorporation and extraction reactions were possible. A total of three reverse cycles were carried out for each sample. PXRD patterns of the sample after each reverse cycle is shown in Figure 3.19 with Rietveld refinements carried out on each pattern. This allowed the quantity of Sr_2CuO_3 and $Sr_2CuO_2(CO_3)$ for the 1st and 2nd reverse reactions to be determined. These two-phase refinements used a background modelled using the power series in the fifth functional power series type with 6 terms. The multi-term Simpson's rule integration of the pseudo-Voigt was used in order to model the peaks shapes within the pattern.[203, 204] The parameters refined were: the cell parameters (*a, b, c*) and scale factors for both phases. The U_{iso} parameters were also refined with the Sr and Cu atoms from each phase constrained to one another. The asymmetry and shift of the pattern was also refined along with the Lorentzian anisotropic strain broadening. The quantities of the oxide and oxide carbonate have been presented in Table 3.8.
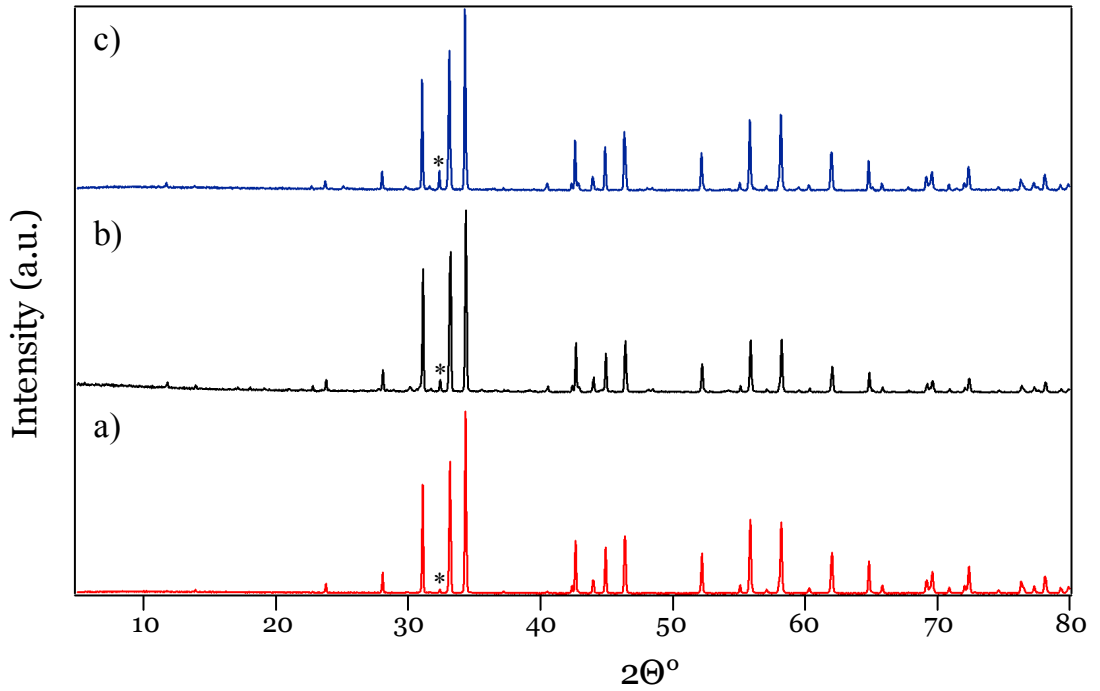
Figure 3.19: PXRD patterns of re-formed Sr_2CuO_3 after the a) first, b) second and c) third extraction cycle under air. The (*) peaks denotes those belonging to $Sr_2CuO_2(CO_3)$.

Table 3.8: The quantities of Sr_2CuO_3 and $Sr_2CuO_2(CO_3)$ obtained after the 1st and the 2nd reverse reactions under air.

Reverse reaction	R_{wp}	R_p	Sr_2CuO_3 (%)	$Sr_2CuO_2(CO_3)$ (%)
1st	16.8	11.2	97.9 ± 0.08	2.1 ± 0.18
2nd	17.5	12.5	96.9 ± 0.15	3.1 ± 0.19

The PXRD pattern from the 3rd reverse reaction showed a total of three phases being present. These were identified as $Sr_2CuO_2(CO_3)$, Sr_2CuO_3 and $SrCuO_2$.[80, 197, 213] Using Rietveld refinements (Figure 3.20) the quantities of each different phase from the 3rd reverse reaction was identified as Sr_2CuO_3 (84.5 ± 0.1 %), $Sr_2CuO_2(CO_3)$ (11.6 ± 0.2 %) and $SrCuO_2$ (3.9 ± 0.2 %). These three-phase refinements had the background modelled using the power series in the fifth functional power series type with 6 terms. The multi-term Simpson's rule integration of the pseudo-Voigt was used in order to model the peaks shapes within the pattern.[203, 204] The parameters refined were: the cell parameters (*a, b, c*) and scale factors for both phases.

The U_{iso} parameters were also refined with the Sr and Cu atoms from each phase constrained to one another. The asymmetry and shift of the pattern was also refined along with the Lorentzian anisotropic strain broadening. The R-values for this refinement were also reported as R_{wp} = 17.61 % and R_p = 11.9 %.
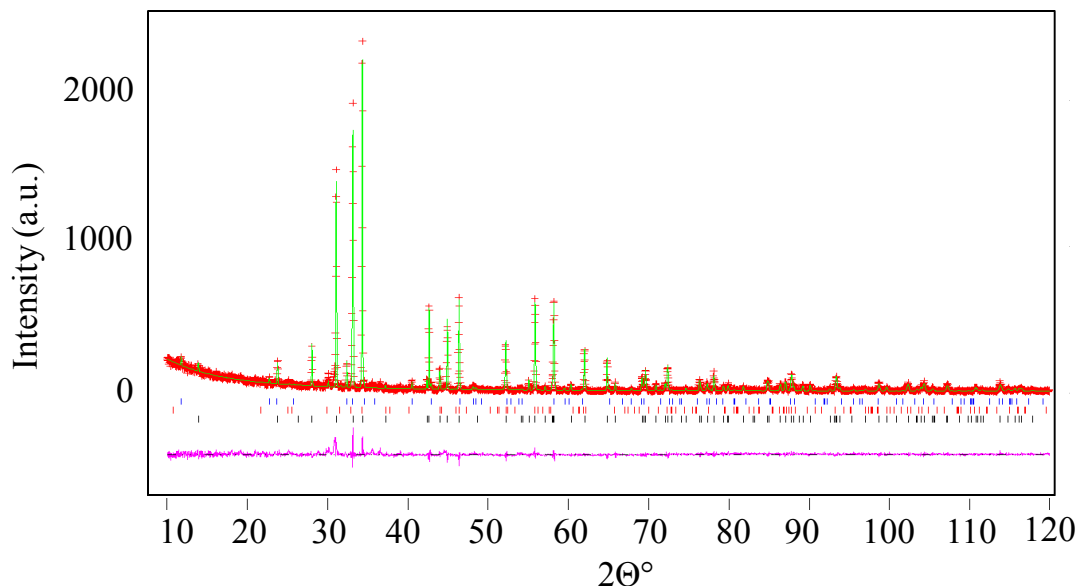
Figure 3.20: X-ray powder diffraction profiles of Sr_2CuO_3 obtained from the 3rd reverse cycle under air. Shown is the observed (red crosses), calculated (green) and difference (purple) patterns. The ticks represent Sr_2CuO_3 (black), $SrCuO_2$ (red) and $Sr_2CuO_3(CO_3)$ (blue).

It is proposed that after the 3rd reverse cycle that repeated heating of the sample is causing degradation to occur. This means that the reaction is no longer a simple conversion from $Sr_2CuO_2(CO_3)$ to Sr_2CuO_3 but other compounds are being formed, possibly to give Sr_2CuO_3 as the main phase. Another risk is that the repeated heating cycles are causing sintering of the particles which can effect their reactivity. In the case of CaO, repeated heating reactions have resulted in a diminished reactivity towards CO_2 when forming $CaCO_3$.[214]

Re-formed Sr_2CuO_3 was then reacted with CO_2 to re-form $Sr_2CuO_2(CO_3)$. PXRD patterns of the oxide carbonates after each of the reactions are shown in Figure 3.21. It was found that $Sr_2CuO_2(CO_3)$ could be re-formed over the multiple cycles with $SrCO_3$ still present. This showed that the reheating cycles had not affected the reactivity with CO_2. This is seen even for the reaction after the 3rd reverse cycle which showed $Sr_2CuO_2(CO_3)$ remaining alongside $SrCO_3$.

133
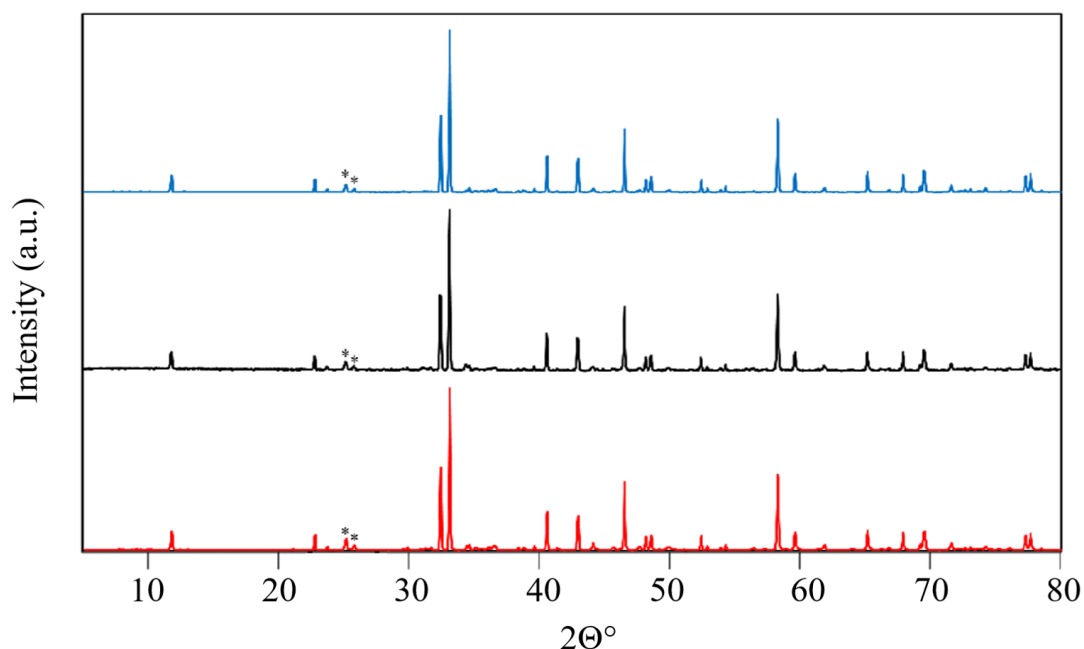
Figure 3.21: PXRD patterns of $Sr_2CuO_2(CO_3)$ from the 1st (blue), 2nd (black) and 3rd (red) reactions of Sr_2CuO_3, re-formed under air with CO_2. (*) peaks belong to $SrCO_3$.

The reversibility reactions under air showed that Sr_2CuO_3 can be re-formed through CO_2 extraction. However, the results also showed that unreacted $Sr_2CuO_2(CO_3)$ would also still be present within the sample. Sr_2CuO_3 which was obtained from the reversibility reactions was also able to react with CO_2 towards $Sr_2CuO_2(CO_3)$ in the same way as the original reaction. The next step was to investigate the reversibility under O_2 in an attempt to improve the reaction towards forming Sr_2CuO_3.

3.3.5.2 CO_2 extraction from $Sr_2CuO_2(CO_3)$ under O_2

Under air, CO_2 was extracted from $Sr_2CuO_2(CO_3)$ to re-form Sr_2CuO_3 at 1000 °C. However this was not a full extraction as some of the oxide carbonate was still present within the sample. O_2 gas was then used as it was proposed that the excess oxygen would drive the reverse reaction further towards forming the oxide. PXRD patterns of the 1st and 2nd reverse cycles confirmed that Sr_2CuO_3 and $Sr_2CuO_2(CO_3)$ were present. Refinement of the patterns from these reactions are shown in Figures 3.22 and 3.23. The main peaks belonging to the unreacted $Sr_2CuO_2(CO_3)$ have also been highlighted (*) within these refinements.
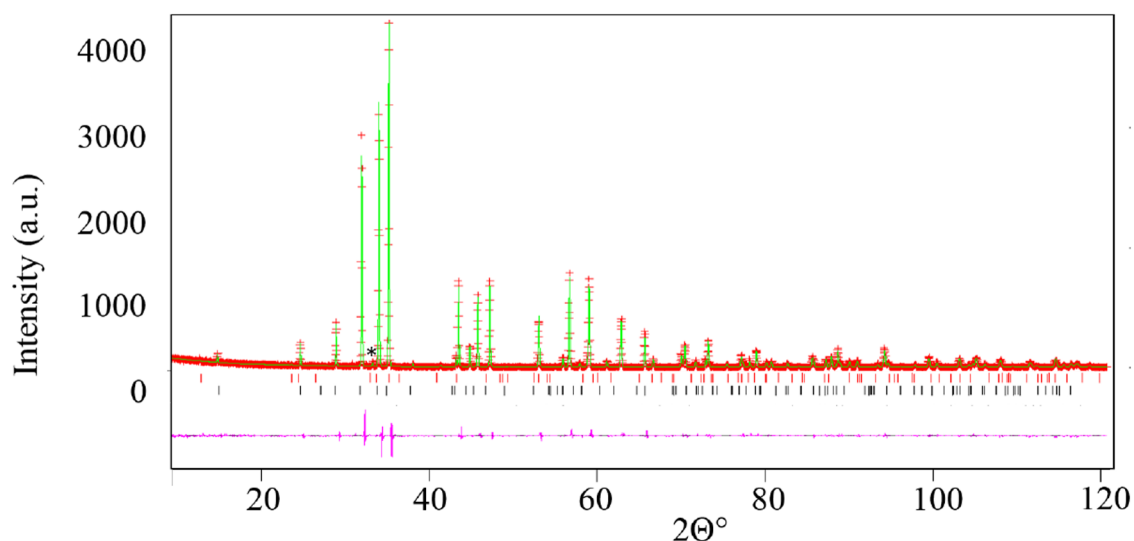
Figure 3.22: X-ray powder diffraction profiles of Sr_2CuO_3 obtained from the 1st reverse cycle under O_2 gas. Shown is the observed (red crosses), calculated (green) and difference (purple) patterns. The peaks marked with (*) are those belonging to $Sr_2CuO_2(CO_3)$ impurities. The ticks represent Sr_2CuO_3 (black) and $Sr_2CuO_3(CO_3)$ (red).
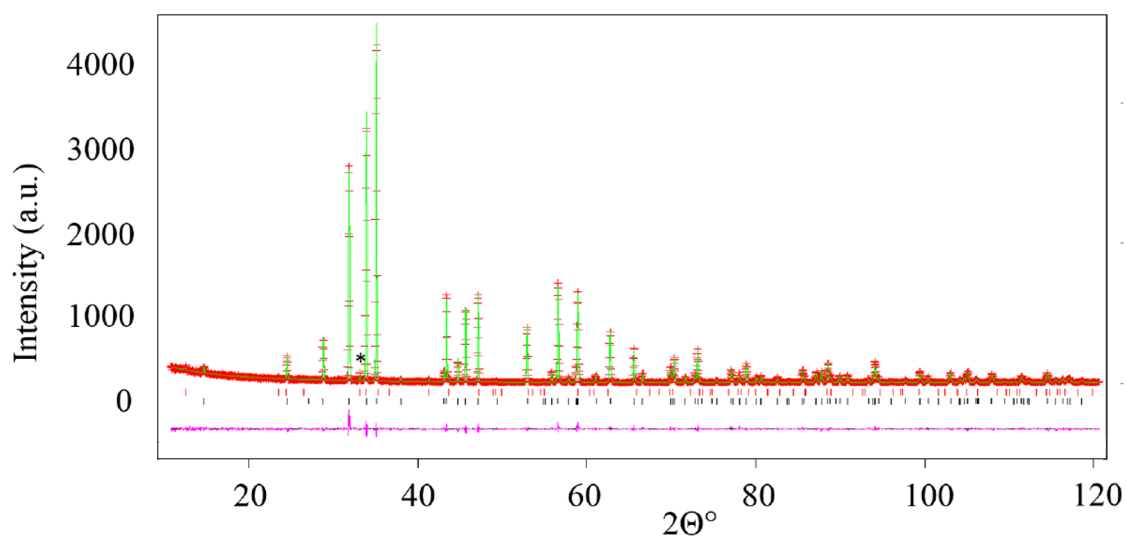
Figure 3.23: X-ray powder diffraction profiles of Sr_2CuO_3 obtained from the 2nd reverse cycle under O_2 gas. Shown is the observed (red crosses), calculated (green) and difference (purple) patterns. The peaks marked with (*) are those belonging to $Sr_2CuO_2(CO_3)$ impurities. The ticks represent Sr_2CuO_3 (black) and $Sr_2CuO_3(CO_3)$ (red).

The quantification of remaining unreacted $Sr_2CuO_2(CO_3)$ was determined via a two phase

Rietveld refinement. The parameters refined were: the cell parameters (*a, b, c*) and scale factors for both phases. The U_{iso} parameters were also refined with the Sr and Cu atoms from each phase constrained to one another. The asymmetry and shift of the pattern was also refined along with the Lorentzian anisotropic strain broadening. Table 3.9 shows for each reverse reaction the amount of unreacted oxide carbonate present as well as the R-values for the refinement. As with the trend when air was used, the amount of remaining $Sr_2CuO_2(CO_3)$ after each cycle was found to increase.

Table 3.9: The quantities of $Sr_2CuO_2(CO_3)$ that are retained after the 1st and 2nd reverse cycle under O_2.

Reverse reaction	R_{wp}	R_p	Sr_2CuO_3 (%)	$Sr_2CuO_2(CO_3)$ (%)
1st	16.4	10.9	97.9 ± 0.08	2.1 ± 0.18
2nd	13.8	9.2	96.5 ± 0.15	3.5 ± 0.19

Also as with air, the 1st and 2nd reverse cycles only showed Sr_2CuO_3 and $Sr_2CuO_2(CO_3)$ to be present. Using PXRD it was found that the 3rd reverse cycle had resulted in three-phases with $SrCuO_2$ also present.[213] Rietveld refinement (Figure 3.24) determined the quantification of these phases as, Sr_2CuO_3 (86.4 ± 0.1), $Sr_2CuO_2(CO_3)$ (11.0 ± 0.4) and $SrCuO_2$ (2.6 ± 0.3) with the R-values, $R_{wp} = 18.7$ and $R_p = 12.5$ %. The synthesis of $SrCuO_2$ has been reported by Ohashi *et al.* through the reaction of $SrCO_3$ with CuO when heated to temperatures between 800-1100 °C under O_2.[215]
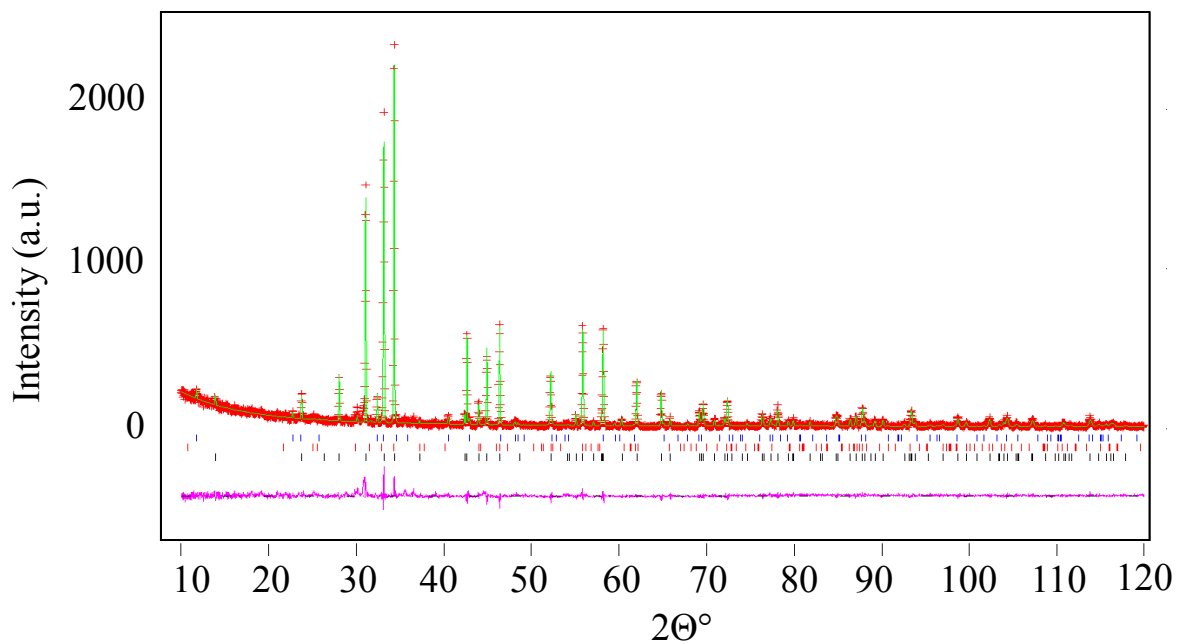
Figure 3.24: X-ray powder diffraction profiles of Sr_2CuO_3 obtained from the 3rd reverse cycle under O_2 gas. Shown is the observed (red crosses), calculated (green) and difference (purple) patterns. The ticks represent Sr_2CuO_3 (black), $SrCuO_2$ (red) and $Sr_2CuO_3(CO_3)$ (blue).

The 1st reverse reaction showed that 2.1 % of the total mass remained was that of the oxide carbonate. This would increase further to 11.0 % by the third reverse cycle. A comparison of the PXRD patterns after each reverse cycle under O_2 has also been presented in Figure 3.25.

The amount of Sr_2CuO_3 obtained after each reverse reaction has been compared when using air and O_2 gas. This was to assess which method is better for extracting the CO_2 and re-forming the original oxide. Identification of the phases present from the 1st and 2nd reverse reactions using both gases is shown in Table 3.10.
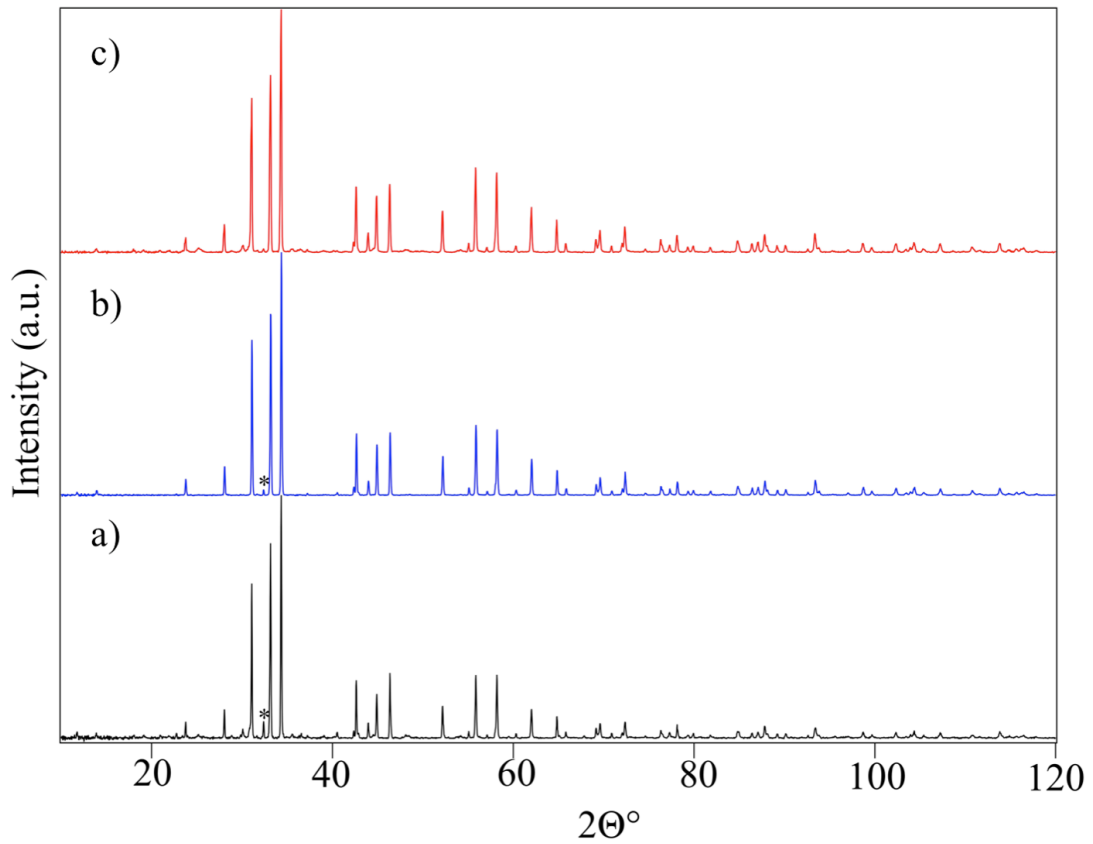
Figure 3.25: A comparison of the PXRD patterns for Sr_2CuO_3, obtained from the a) 3rd, b) 2nd and c) 1st reverse reactions. The (*) marked peaks belong to unreacted $Sr_2CuO_2(CO_3)$.

Table 3.10: A comparison of the quantities of $Sr_2CuO_2(CO_3)$ and Sr_2CuO_3 within the samples after the 1st and 2nd reverse cycle under O_2 and air.

Reverse reaction 1	Sr_2CuO_3 (%)	$Sr_2CuO_2(CO_3)$ (%)
Air (1)	97.9	2.1
O_2 gas (2)	97.9	2.1
Difference (1) - (2)	0	0
Reverse reaction 2	Sr_2CuO_3 (%)	$Sr_2CuO_2(CO_3)$ (%)
Air (1)	96.9	3.1
O_2 gas (2)	96.5	3.5
Difference (1) - (2)	0.4	-0.4

The comparison shows for the 1st reverse reactions the amount of remaining $Sr_2CuO_2(CO_3)$ and Sr_2CuO_3 is maintained within the uncertainties.. Under both gas types the 3rd reverse reaction resulted in three phases within the sample, Sr_2CuO_3, $Sr_2CuO_2(CO_3)$ and $SrCuO_2$. The quantity of these phases have been compared to one another in Table 3.11.

Table 3.11: A comparison of the quantities of $Sr_2CuO_2(CO_3)$, Sr_2CuO_3 and $SrCuO_2$ within the samples after the 3rd reverse cycle under both air and O_2.

Reverse reaction 3	Air	O_2 gas	Difference (1) - (2)
Sr_2CuO_3 (%)	84.5	86.4	-2.1
$Sr_2CuO_2(CO_3)$ (%)	11.6	11.0	0.6
$SrCuO_2$ (%)	3.9	2.6	1.3

A comparison of the quantities of each phases present from the 3rd reverse cycle shows re-formation of Sr_2CuO_3, is more favoured under O_2 than air. This is potentially due to the O_2 atmosphere allowing Sr_2CuO_3 to form before further reactions take place resulting in side products like $SrCuO_2$.

As in the case of the reversibility under air, the re-formation of $Sr_2CuO_2(CO_3)$ over multiple cycles has also been investigated using the same original conditions. Figure 3.26 shows that despite the repeating extraction reactions the oxide carbonate is able to re-form in the same way as the original reaction. Although $SrCO_3$ is still present in the sample, $Sr_2CuO_2(CO_3)$ is the main phase.
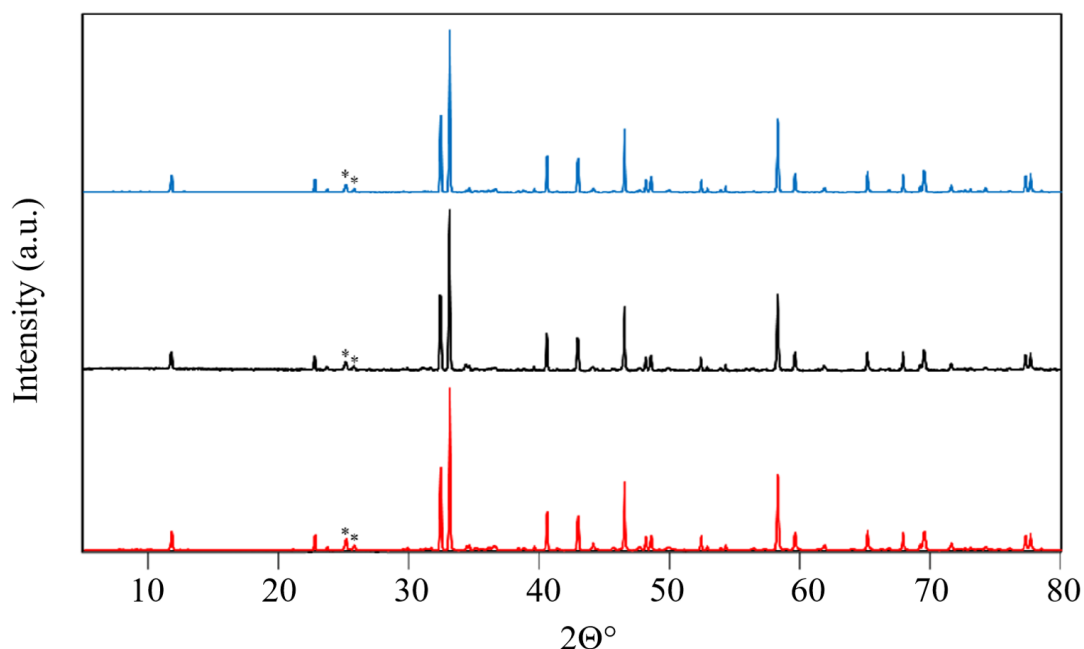
Figure 3.26: PXRD patterns of $Sr_2CuO_2(CO_3)$ from the 1st (blue), 2nd (black) and 3rd (red) reactions of Sr_2CuO_3 that is re-formed under O_2 and is then reacted with pure CO_2. (*) peaks belong to $SrCO_3$.

It has been found that by heating $Sr_2CuO_2(CO_3)$ under air or O_2 that Sr_2CuO_3 can be re-formed over multiple cycles. Through PXRD and Rietveld refinements the remaining $Sr_2CuO_2(CO_3)$ from the reverse cycles has been identified and quantified. These results also show that after each reverse reaction the quantity of the oxide carbonate within the sample increases. The cause of this is likely due to CO_2 strongly bonding within the bulk of the structure as a carbonate in $Sr_2CuO_2(CO_3)$. This will make it difficult to remove and re-form the original oxide. A possible cause for the increased amount of oxide carbonate remaining is potentially the particles themselves being altered and affecting the reaction. Solid materials used for CO_2 capture and utilisation such as CaO, have been found to have decreased reactivity as a result of sintering from repeated heating reactions.[214] Therefore this could also be occurring in this study from the repeating reactions at 1000 °C.

3.4 Conclusion

This part of the work presents a novel concept of utilising the anion vacancies within solids for the simultaneous capture and utilisation of CO_2 towards oxide carbonate compounds. Initial reactions of Sr_2CuO_3 under CO_2 gas below and at 1000 °C showed that the mixed metal oxide would decompose to $SrCO_3$ and CuO. As a result, an alternating gases approach between CO_2 and air was designed so Sr_2CuO_3 would only react with CO_2 at 1000 °C, with the heating and cooling stages in air. These results showed that CO_2 could be directly incorporated into Sr_2CuO_3 to prepare $Sr_2CuO_2(CO_3)$ with minor impurities of $SrCO_3$ under these conditions. This approach also allowed in-situ TGA to monitor the reaction as it is occurring, as well as, to obtain high purity compounds from the reaction with CO_2. The formation of $SrCO_3$ is likely a result of Sr_2CuO_3 decomposing under CO_2 gas below 1000 °C which is preceding that of $Sr_2CuO_2(CO_3)$.

The extraction of CO_2 from the oxide carbonate and the re-formation of Sr_2CuO_3, has also been investigated over multiple reverse cycles. It was found that when heated under air or O_2 that CO_2 could be extracted and provides a novel route to preparing Sr_2CuO_3. The reverse reactions also showed that the conversion from Sr_2CuO_3 to $Sr_2CuO_2(CO_3)$ would degrade over multiple cycles. This has been proposed to be a result of the oxide carbonate remaining within the phase after each reverse reactions, as well as other phases such as $SrCuO_2$ also being present. Nevertheless, the results show that the incorporation and extraction of CO_2 into and from the structures of Sr_2CuO_3 and $Sr_2CuO_2(CO_3)$ is a repeatable process.

Through an alternating gases approach, direct CO_2 incorporation into solids with anion vacancies has been possible for preparing an oxide carbonate. By controlling parameters such as temperatures and gas type this method could also be extended to other compounds containing alkaline and alkaline earth metals for utilising other environmentally harmful gases for preparing novel compounds.

3.5 $Sr_{2-x}A_xCuO_3$ (A = Ca and Ba, $0 \leq x \leq 2$) Compounds

In the solid-solution $Sr_{2-x}A_xCuO_3$ (A = Ca and Ba) series the partial substitution of strontium can result in the preparation of varies compounds that have the same type of crystal structure as each other.[196, 216–218] These compounds show orthorhombic and body centred unit cells with the A cations maintaining a coordination state of 7. Hence all $Sr_{2-x}A_xCuO_3$ (A = Ca and Ba) compounds will also have anion vacancies. The difference in the A cations however, will have an effect on the size of the vacancies, as well as the size of the unit cell. Going down the group the size of the alkaline earth metal cation increases, so does the size of the anion vacancies as shown in Table 3.15.[219]

Table 3.12: Comparison of the ionic radii of the Ca^{2+}, Sr^{2+}, and Ba^{2+} cations with the anion vacancies for the A_2CuO_3 (A = Sr, Ca and Ba) structures.[219]

Cation	Ionic radii (Å)	Anion vacancy (Å)
Ca^{2+}	1.06	3.25[196]
Sr^{2+}	1.21	3.50[88]
Ba^{2+}	1.38	3.91[218]

The enthalpy of reaction ΔH_{rxn}, values for CO_2 towards the AO (A = Ca, Sr and Ba) for forming metal carbonates is presented in Table 3.12.[122] This shows that not only does the size of the anion vacancies increase moving down the group but the affinity for reacting with CO_2 as well.

Table 3.13: Comparison of the enthalpy of reaction $\Delta H°_{rxn}$, for formation of a carbonate from AO (A = Ca, Sr and Ba) groups reacting with CO_2 understand temeprature and pressure.

Formation of carbonate	Enthalpy of formation kJ/mol
$CaO \rightarrow CaCO_3$	-179.3
$SrO \rightarrow SrCO_3$	-234.6
$BaO \rightarrow BaCO_3$	-271.5

3.5.1 $Sr_{2-x}Ba_xCuO_2(CO_3)$ $(0.5 \leq x \leq 2)$

The $Sr_{2-x}Ba_xCuO_2(CO_3)$ $(0.5 \leq x \leq 2)$ solid-solution series, in which barium occupies the same sites as the strontium shows different types of possible structures. Lappas *et al.* and Armstrong.*et al.* reported $I\bar{4}$ and *P4/mmm* type structures respectfully. Armstrong.*et al.*.[114, 207] In both cases the structures have separate layers of metal carbonates and CuO_2 planes. One of the main features in these types of compounds is the disordered nature of the carbonate groups. Ordering of the carbonate groups can identify the presence of a superstructure which has a space group of $I\bar{4}$ and was reported for $Sr_{2-x}Ba_xCuO_2(CO_3)$ (x = 0) by Miyazaki *et al.*.[116] The alternative *P4/mmm* type structure is derived from that of $Sr_2CuO_2(CO_3)$ reported by Babu *et al.* where the origin is placed on a copper cation and the oxides within the carbonate groups have an occupancy of 0.25 on various sites.

Miyazaki *et al.* prepared the oxide carbonate series through either $BaCO_3$ or BaO_2 reacting with $SrCO_3$ and CuO in an alumina crucible and heated to 930 °C.[116] In the case of $x \leq$ 0.8 only BaO_2 was used as the only source of barium. IR spectroscopy showed that as the amount of barium increased the wavenumber value would decrease.[207] This is from barium having a greater reduced mass, μ value than strontium which decreases the wavenumber value. The magnetic structure of the $Sr_{2-x}Ba_xCuO_2(CO_3)$ $(0.5 \leq x \leq 2)$ series has also been studied and showed ordered local magnetic moments appearing at the Cu^{2+} sites.[119] As a result these compounds have been described as the parent compounds to a series of hole doped superconductors. The $Sr_{2-x}Ba_xCuO_2(CO_3)$ series is an example of how solid-solution oxide carbonates can be prepared "*ab initio*". It is therefore possible that by preparing the $Sr_{2-x}Ba_xCuO_3$ series first that these compounds can directly react with CO_2 towards forming the oxide carbonates.

$Ba_2Cu_{1.2}(CO_3)_{0.8}O_{2.42}$ prepared by Calestani *et al.* has been found to have a similar structure to $Sr_2CuO_2(CO_3)$ and $Ca_2CuO_2(CO_3)$, reported by Babu *et al.* and Kopnin *et al.*.[113, 80, 115] However, the main structural difference is that in the case of $Ba_2Cu_{1.2}(CO_3)_{0.8}O_{2.42}$ the carbon atoms share occupancy on the same crystallographic sites as the copper cations. This results is what has been described by Calestani *et al.* as carbocuprate groups.

3.5.2 Ca$_2$CuO$_2$(CO$_3$)

The oxide carbonate Ca$_2$CuO$_2$(CO$_3$) was prepared by Kopnin *et al.* in the form of single crystals.[115] This involved heating CaCO$_3$ and CuO with a flux reagent, AgO in a enclosed gold capsule. The reaction was carried out under a O$_2$/CO$_2$ gas mixture and at temperatures of 1300 °C and high pressures of 6 GPa. Ca$_2$CuO$_2$(CO$_3$) unlike the Sr$_{2-x}$Ba$_x$CuO$_2$(CO$_3$) (x = 0 – 2) series has only been reported with one type of crystal structure with that of *P4/mmm* which is similar to the model of Sr$_2$CuO$_2$(CO$_3$) reported by Babu *et al.*.[80] The oxygen atoms in the carbonate anions still have an occupancy of 0.25 each resulting in a disordered array.

Unlike the barium equivalent, there have been no reports of Sr$_{2-x}$Ca$_x$CuO$_2$(CO$_3$) solid-solutions. By forming Sr$_{2-x}$Ca$_x$CuO$_3$ first this maybe able to react directly with CO$_2$ in order to prepare a novel series of Sr$_{2-x}$Ca$_x$CuO$_2$(CO$_3$) compounds. The two possible *P4/mmm* and $I\overline{4}$ structures for the Sr$_2$CuO$_2$(CO$_3$) is shown previously in Figure 3.3 which the Sr$_{2-x}$Ca$_x$CuO$_2$(CO$_3$) series could adopt.

This project has investigated the preparation and direct reaction of the Sr$_{2-x}$A$_x$CuO$_3$ (A = Ba and Ca) series with CO$_2$. This has been aimed towards synthesis of potentially novel mixed anion carbonates. The reversibility of CO$_2$ incorporation has also been investigated in order to re-obtain the starting material over multiple cycles.

3.6 Experimental

3.6.1 Preparation and reaction of the Sr$_{2-x}$A$_x$CuO$_3$ (A = Ca and Ba) series with CO$_2$

The Sr$_{2-x}$A$_x$CuO$_3$ (A = Ca and Ba) series was prepared using a high temperature ceramic method with polycrystalline ACO$_3$ (A = Sr, Ba and Ca) (98.5% BDH GPR), and CuO (96.0% BDH GPR) reagents. These compounds were stored in an oven at approximately 100 °C to prevent moisture contamination. The reagents were mixed in a stoichiometric ratio to prepare 1g of product. This would then be dispersed with acetone to prepare a homogenous mixture.

Afterwards the mixture was then compressed into pellets of approximately 0.5 mm thickness. The reaction scheme (3.2) shows how the $Sr_{2-x}A_xCuO_3$ (A = Ca and Ba) series with x = 0–2 that can be prepared from stoichiometric quantities of ACO_3 (A = Ca and Ba) and CuO.

$$2\text{-x } SrCO_3 + x\, ACO_3 + CuO \rightarrow Sr_{2-x}A_xCuO_3 + 2\, CO_2 \qquad (3.2)$$
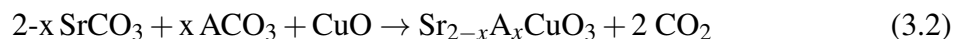
These mixture pellets were then placed into an aluminium crucible and inserted into a box/tubular furnace to be heated at 1000 °C for 14 hours in static air. Intermediate regrinding and reheating cycles were carried out until high purity (> 99%) products were achieved. These samples were then used for reacting with CO_2 gas. In the case of the $Sr_{2-x}Ba_xCuO_3$ (x < 0.5) series, compounds were prepared in a similar manner to the $Sr_{2-x}Ca_xCuO_3$ ($0 \leq x \leq 2$) compounds, except heating under O_2 gas was required. An O_2 atmosphere was needed due to the hydroscopic nature of BaO which could hydrate when exposed to a static air atmosphere.

Once a pure sample of $Sr_{2-x}A_xCuO_3$ (A = Ba and Ca) had been prepared, the next step was the reactions with CO_2 gas. As with Sr_2CuO_3, all reactions between the samples and CO_2 were carried out in-situ using TGA.

3.6.2 Charaterisation

3.6.2.1 Thermogravimetric analysis (TGA)

Thermogravimetric analysis (TGA) was carried out using a Metler Toledo TDA/DSC 1Star System which showed the sample mass changing at different temperatures and gases. CO_2, O_2 and air atmospheres were used. All gas flow rates were maintained at a value of 100 ml/min and the temperature ramp rate was at 100 °C/min. A standard reaction would involve inserting a single sample into the TGA furnace at room temperature to be exposed to the gaseous atmosphere before heating. Pre-weighted samples of $Sr_{2-x}A_xCuO_3$ (A = Ca, Ba) (50 mg) were placed into an alumina crucible then inserted into the TGA furnace chamber. In the case of $Sr_{2-x}Ca_xCuO_3$ ($0 \leq x \leq 2$) compounds, these samples were initially heated to 1000 °C under air to prevent decomposition towards undesired $Sr/CaCO_3$. Once the sample had reached 1000 °C it would be held for 2 minutes to reach equilibrium under air then the

gas flow would then be changed to pure CO_2. After a measured amount of time under CO_2 the gas was then switched back to air for the samples to cool to room temperature. In the case of the $Sr_{2-x}Ba_xCuO_3$ (x < 0.5) series O_2 was used instead of air. This acts to follow the preparation method used for the $Sr_{2-x}Ba_xCuO_3$ series. The overall change in mass of the sample was determined through subtracting the value at the start of the reaction, to that at the end of the reaction when the sample mass was allowed to reach equilibrium. This was to give a quantitative value of the amount of CO_2 utilised in the oxide towards the oxide carbonate. By monitoring the change in mass over time this also allowed the kinetics of the reaction to be studied.

3.7 Results and Discussion

3.7.1 Preparation of $Sr_{2-x}Ba_xCuO_2(CO_3)$ (0 < x < 0.5)

The $Sr_{2-x}Ba_xCuO_2(CO_3)$ ($0 \leq x \leq 2$) series, has already been reported by Armstrong and Edwards.[118] Samples were prepared through reacting $BaCO_3$, $SrCO_3$ and CuO under a CO_2/O_2 mixed atmosphere.[207] This method is similar to that used by Miyazaki *et al.* to prepare $Sr_2CuO_2(CO_3)$.[116] To the author's knowledge no attempt has been made towards directly reacting $Sr_{2-x}Ba_xCuO_3$ (x < 0.5) compounds with CO_2 to prepare oxide carbonates. As a result, this novel approach has been investigated in this work.

The incorporation of barium within the $Sr_{2-x}Ba_xCuO_3$ series for reacting with CO_2 has a number of advantages. As shown in Table 3.15, BaO groups have a greater ΔH_{rxn} for forming metal carbonates (-274 kJ/mol) than that of SrO (-234 kJ/mol).[122] The other advantage is that as Ba^{2+} has a larger ionic radii than Sr^{+2} therefore Ba^{2+}/Sr^{2+} substitution will increase the size of the anion vacancy and overall unit cell.

Synthesis of the $Sr_{2-x}Ba_xCuO_3$ (0 < x < 0.5) series was carried out using the same method as described by Adachi *et al.*.[217] This involved the reagents, ACO_3 (A = Sr and Ba) and CuO mixed together in stoichiometric quantities to prepare 1g of product and compressed into pellets, to be heated under an O_2 atmosphere at 1000 °C. Once prepared these solid-solution compounds could be investigated for reacting with CO_2 using the method of alternating gases,

designed in this work.

Preparation of the $Sr_{2-x}Ba_xCuO_3$ (x = 0.2, 0.3, 0.4 and 0.5) series showed only $Sr_{1.8}Ba_{0.2}CuO_3$ had been synthesised without any impurities. The PXRD pattern suggested that the oxide had been prepared however, no diffraction data on $Sr_{1.8}Ba_{0.2}CuO_3$ was available in the literature. The exact composition of the barium content was determined through Rietveld refinements, (Figure 3.27). The model was the diffraction data of Sr_2CuO_3 reported by Weller and Lines with barium added into the same occupied sites as the strontium.[88] Initially the barium content was set to one tenth of strontium. The refinement determined the barium occupancy as one-tenth of that of strontium as was aimed at during the synthesis.
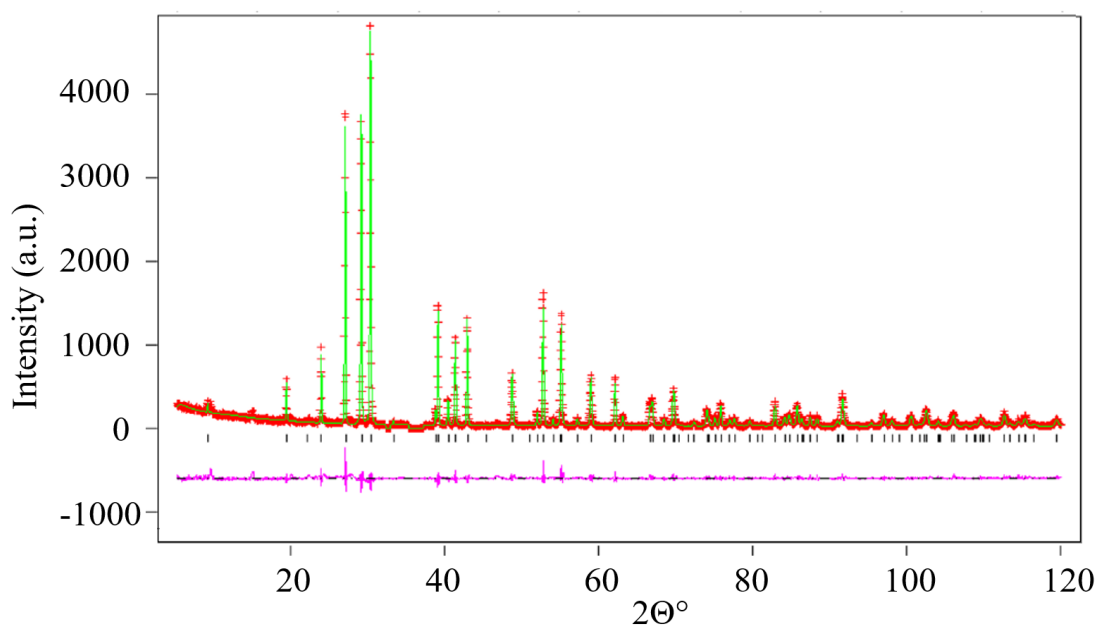
Figure 3.27: X-ray powder diffraction profile of $Sr_{1.8}Ba_{0.2}CuO_3$ showing the observed (red crosses), calculated (green) and difference (purple) patterns.

The R-values from the refinement were at R_{wp} = 14.2 % and R_p = 9.9 % with unit cell parameters at a = 12.7535(2) Å, b = 3.9327(1) Å, c = 3.5319(1) Å, V = 177.148(3) Å^3. $Sr_{1.8}Ba_{0.2}CuO_3$ was originally synthesised under a O_2 atmosphere. As a result, the alternating gases used were O_2 and CO_2, for the reaction towards the oxide carbonate.

3.7.1.1 Structural characterisation of $Sr_{2-x}Ba_xCuO_2(CO_3)$ (0 < x < 0.5)

Due to the Ba^{2+} cation having a greater ΔH_{rxn} for forming a metal carbonate than the Sr^{2+} cation, the first reaction under CO_2 was carried out for only 10 minutes. The reduced time was to observe if the formation of $Sr_{1.8}Ba_{0.2}CuO_2(CO_3)$ would occur faster compared to that of $Sr_2CuO_2(CO_3)$ at 15 minutes. This reaction also used the same temperature as for the preparation of $Sr_2CuO_2(CO_3)$ at 1000 °C under CO_2. The heating and cooling rates were also set to 100 °C/min, with the only difference being O_2 used instead of air. The results showed that although peaks potentially belonging to a $Sr_{2-x}Ba_xCuO_2(CO_3)$ phase were present, the pattern also indicated the presence of $SrCuO_2$ and $SrCO_3$ within the phase. As a result, different times were investigated such as 15 and 20 minutes under CO_2 gas. A comparison of the PXRD patterns of these samples were compared to one another within Figure 3.28. This comparison show the reactions under CO_2 for 10, 15 and 20 minutes. The TGA curve from the 15 minute reaction is shown in Figure 3.29. This curve shows the same trend as with Sr_2CuO_3 with the mass increasing only when CO_2 is introduced.
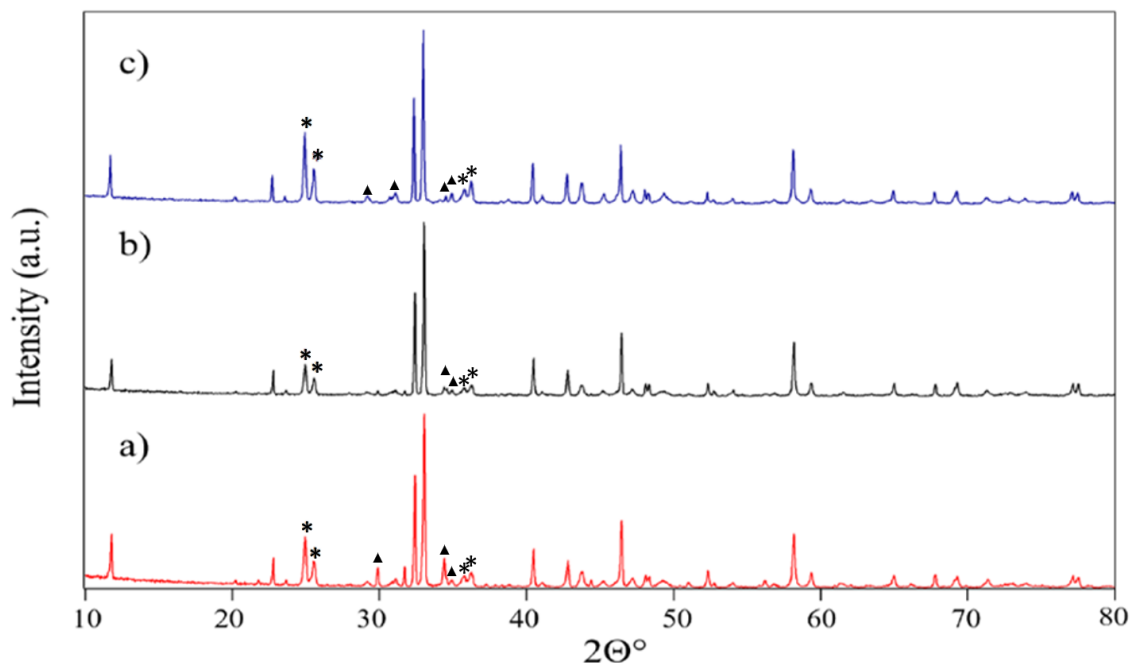
Figure 3.28: Comparison of PXRD patterns of $Sr_{1.8}Ba_{0.2}CuO_3$ under a) 10 minutes, b) 15 minutes and c) 20 minutes of CO_2 gas at 1000 °C. The (*) are the peaks belonging to $SrCO_3$ whilst the (▲) marked peaks belong to $SrCuO_2$.

148
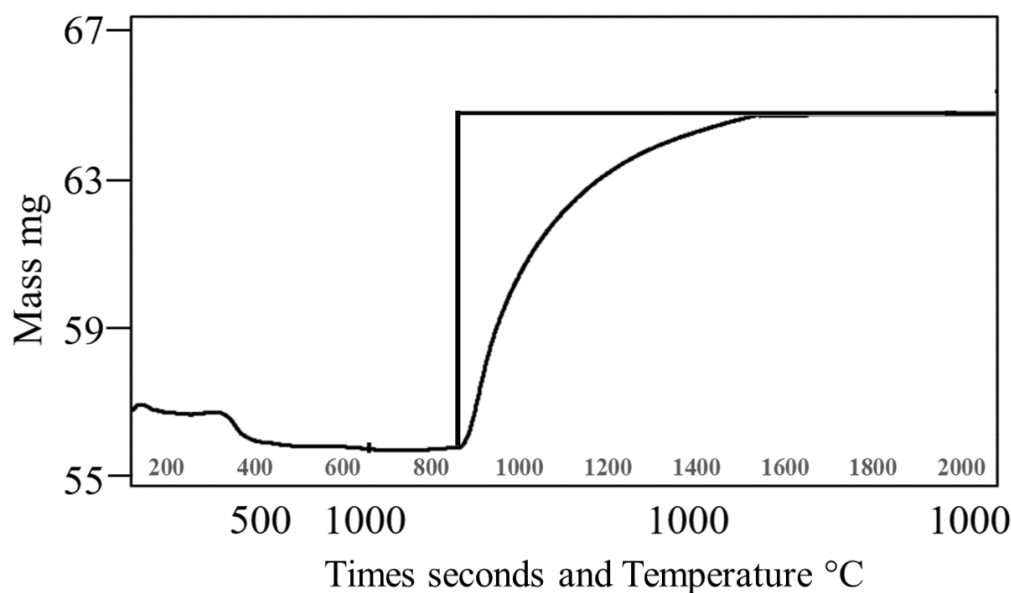
Figure 3.29: TGA curve of $Sr_{1.8}Ba_{0.2}CuO_3$ reacting under CO_2 for 15 minutes at 1000 °C.

The addition of barium into the starting compound showed no difference in the reaction time with 15 minutes under CO_2 still required for Sr_2CuO_3 to react with CO_2. This is potentially due to the reaction favouring complete decomposition of the mixed metal oxide structure towards the carbonates rather than forming a $Sr_{2-x}Ba_xCuO_2(CO_3)$ type phase. Occupancy of the barium in the oxide carbonate was determined through Rietveld refinements.

$Sr_{2-x}Ba_xCuO_2(CO_3)$ (x > 0.5) compounds were found to be tetragonal with the space group *P4/mmm*. This is the same type of structure as the $Sr_2CuO_2(CO_3)$ reported by Babu *et al.* and as a result this phase was used for refinements. Models of $SrCuO_2$ and $SrCO_3$ were used to refine and quantify these phases.[220, 221] A three-phase refinement (Figure 3.30) was carried out and showed fractional occupancy of barium had remained as one-tenth of strontium confirming $Sr_{1.8}Ba_{0.2}CuO_2(CO_3)$ had been prepared.
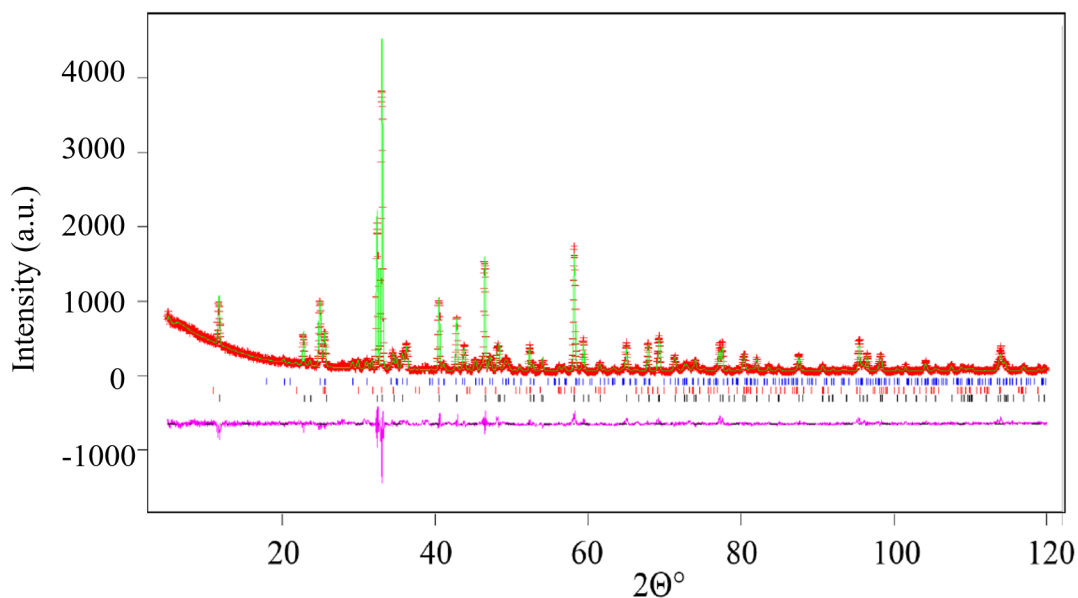
Figure 3.30: X-ray powder diffraction profile of $Sr_{1.8}Ba_{0.2}CuO_2(CO_3)$ showing the observed (red crosses), calculated (green) and difference (purple) patterns. The ticks represent $Sr_{1.8}Ba_{0.2}CuO_2(CO_3)$ (black), $SrCuO_2$ (red) and $SrCO_3$ (blue).

The lattice parameters were refined as a = 3.90924(5) Å, c = 7.53570(2) Å, V = 115.162(3) Å^3 and the R-values of R_{wp} = 11.3 % and R_p = 8.4 %. The structural information of $Sr_{1.8}Ba_{0.2}CuO_2(CO_3)$ has been shown in the appendix Table 8.4. The impurities within the sample were also confirmed as $SrCuO_2$ and $SrCO_3$, with the quantities of all three phases shown in Table 3.14. The oxide carbonate phase, $Sr_{1.8}Ba_{0.2}CuO_2(CO_3)$ showed that the amount of barium to strontium had remained within the oxide. This is also despite refinement of the other strontium containing phases which showed no barium present in those. It is possible that an additional barium based compound in present in the phase, but is unable to be detected via PXRD or Rietveld refinements.

Table 3.14: Quantities of $Sr_{1.8}Ba_{0.2}CuO_2(CO_3)$ with the other phases of $SrCO_3$ and $SrCuO_2$ within the sample.

Compound	Mass fraction %
$Sr_{1.8}Ba_{0.2}CuO_2(CO_3)$	66.1 ± 0.2
$SrCO_3$	29.2 ± 0.2
$SrCuO_2$	4.7 ± 0.1

A comparison of the unit cell parameters of $Sr_{1.8}Ba_{0.2}CuO_2(CO_3)$ to $Sr_2CuO_2(CO_3)$ (Table 3.15), show that as strontium is replaced by barium the unit cell increases in size. This will be a result of Ba^{2+} having a ionic radii of 1.38 (Å) compared to Sr^{2+} which has an ionic radii of 1.21 (Å).[219]

Table 3.15: Comparison of the unit cells parameters of $Sr_2CuO_2(CO_3)$ reported by Babu *et al.* to $Sr_{1.8}Ba_{0.2}CuO_2(CO_3)$.[80]

Compound	a(Å)	c(Å)	V(Å^3)
$Sr_2CuO_2(CO_3)$ (1)	3.9033(2)	7.4925(4)	114.153(16)
$Sr_{1.8}Ba_{0.2}CuO_2(CO_3)$ (2)	3.9092(3)	7.5350(1)	115.162(2)
Difference (1)-(2)	0.0103(3)	0.0248(1)	0.978(2)

The vibrational behaviour of the oxide carbonate was examined by FTIR spectroscopy. The ACO_3 (A = Sr, Ba and Ca) series has isostructural crystal structures to one another with the vibrational behaviour being affected by the A cation.[221] As barium has greater atomic mass to strontium its reduced mass, μ will also be greater reducing the wavenumber values of the carbonate groups compared to $SrCO_3$.[222] The vibrational frequencies in the IR spectrum have been reported from the IR spectrum of of $Sr_{1.8}Ba_{0.2}CuO_2(CO_3)$ are reported in Figure 3.31 with the wavenumber values compared to that of $Sr_2CuO_2(CO_3)$ in Table 3.16.
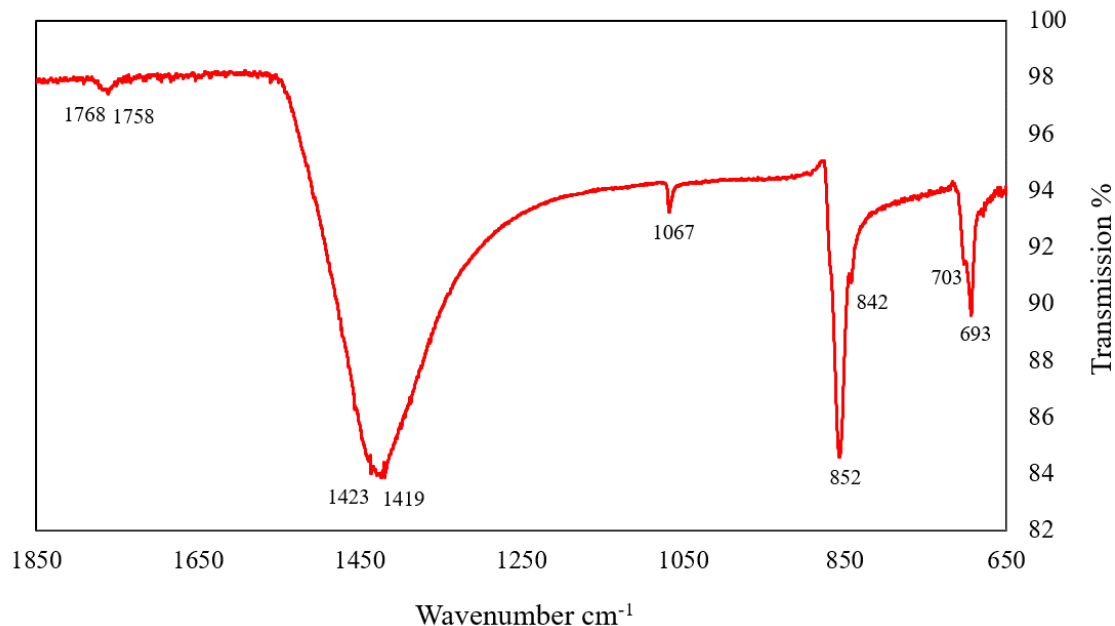
Figure 3.31: IR spectrum of $Sr_{1.8}Ba_{0.2}CuO_2(CO_3)$ with the vibrational frequency belonging to the carbonate groups shown.

Table 3.16: The values for the vibrational modes of $Sr_{1.8}Ba_{0.2}CuO_2(CO_3)$ compared to that of $Sr_2CuO_2(CO_3)$ reported within this project compared.

Vibrational mode cm^{-1}	$Sr_2CuO_2(CO_3)$ (1)	$Sr_{1.8}Ba_{0.2}CuO_2(CO_3)$ (2)	Difference (1) - (2)
Symmetric stretching v_1	1071	1067	4
Symmetric bending v_2	870	852	18
Asymmetric stretching v_3	1436	1423	13
Asymmetric stretching v_3'	1394	1419	-25
Asymmetric bending v_4	706	703	3
Asymmetric bending v_4'	698	693	5

The incorporation of barium into the oxide carbonate has shown a decrease in all of the vibrational frequencies, with the exception of the asymmetric stretching mode v_3'. Similar results were also observed and reported by Armstrong *et al.* for the $Sr_{2-x}Ba_xCuO_2(CO_3)$ $(0.5 \leq x \leq 1.5)$ series.[207] As with $Sr_2CuO_2(CO_3)$ this techniques shows limitations due to

the presence of another carbonate, $SrCO_3$ in the phase with both compounds contributing to the vibrational frequencies. The $Sr_{1.8}Ba_{0.2}CuO_2(CO_3)$ frequencies are generally lower than $Sr_2CuO_2(CO_3)$ indicating that a solid-solution mix with barium has been formed. The quantities of $Sr_{1.8}Ba_{0.2}CuO_2(CO_3)$ is also greater (66.1 ± 0.2 %) than those of $SrCO_3$ (29.2 ± 0.2 %). This makes the oxide carbonate the dominate phase and more likely to contribute to the vibrational frequencies detected.

As with Sr_2CuO_3, $Sr_{1.8}Ba_{0.2}CuO_3$ utilises CO_2 towards preparing $Sr_{1.8}Ba_{0.2}CuO_2(CO_3)$. The TGA curve results previously shown in Figure 3.26, show that the mass of $Sr_{1.8}Ba_{0.2}CuO_3$ only increasing when CO_2 is introduced at 1000 °C. This mass gain will be a result of CO_2 reacting within the oxide. CO_2 capturing capability of $Sr_{1.8}Ba_{0.2}CuO_3$ was determined as the average mass increased over the same reaction repeated several times along with an RMSD value from the uncertainties (Table 3.17).

Table 3.17: CO_2 capturing capacity of $Sr_{1.8}Ba_{0.2}CuO_3$ with uncertainties.

TGA curve	CO_2 capturing capacity mmol/g	Uncertainty mmol/g
1	4.233	0.004
2	3.761	0.004
3	3.982	0.004
Average	3.992	0.007

The overall CO_2 capturing capacity of $Sr_{1.8}Ba_{0.2}CuO_3$ has been found to be 3.99 ± 0.01 mmol/g. This is higher than that of Sr_2CuO_3 at 3.80 ± 0.01 mmol/g.

As with Sr_2CuO_3 the CO_2 capturing capability has also been determined using the mass % values of the phases produced from the reaction to coincide with the results from TGA. Table 3.14 shows the reaction between $Sr_{1.8}Ba_{0.2}CuO_3$ and CO_2 resulted in a mixed phase product consisting of 66.1 % of $Sr_{1.8}Ba_{0.2}CuO_2(CO_3)$, 29.2 % of $SrCO_3$ and 4.7 % of $SrCuO_2$. The TGA curve from this reaction showed that the mass of the end product was that of 65.071 mg. Using this value the mass %, mass of the phase and CO_2 mass content within each phase can be determined to calculate the amount of CO_2 captured. These values have been shown in Table 3.18.

Table 3.18: Overall mass and mass % of $Sr_{1.8}Ba_{0.2}CuO_2(CO_3)$ and $SrCO_3$ in product phase. Along with mass of CO_2 captured.

Phases	Mass %	Mass mg	CO_2 mass mg
$Sr_{1.8}Ba_{0.2}CuO_2(CO_3)$	66.1 %	43.434	5.607
$SrCO_3$	29.2 %	19.187	6.414

Based on the Rietveld refinement results the overall amount of CO_2 captured was that of 12.021 mg by 55.859 mg of $Sr_{1.8}Ba_{0.2}CuO_3$. These values were then used and determined a CO_2 capturing capability value of 4.91 ± 0.02 mmol/g. This value is greater than that calculated using just the mass difference from TGA results at 3.99 mmol/g. The difference in values could be due to the Rietveld refinement not determining barium in any other compounds despite the stiochiometric ratio indicating it should be either in other compounds, or in greater amounts in the oxide carbonate. The amount of barium will effect the molecular mass of each phase and will change the amount of CO_2 captured.

This value of 4.91 mmol/g along with that calculated by TGA, 3.99 mmol/g, is greater compared to the CO_2 capturing capability by Sr_2CuO_3 at 4.28 and 3.80 mmol/g. The reason for this can be attributed to the reaction producing higher quantities of $SrCO_3$ at 29.2 % compared to the reaction using Sr_2CuO_3 at 14.5 %. CO_2 makes up a greater amount of the molecular mass of $SrCO_3$ than $Sr_{1.8}Ba_{0.2}CuO_2(CO_3)$ which means more CO_2 has been captured and is present in the phase. This means more CO_2 is captured when $Sr_{1.8}Ba_{0.2}CuO_3$ is used.

3.7.1.2 Reaction kinetics of $Sr_{1.8}Ba_{0.2}CuO_3$ with CO_2

As with the direct reaction between Sr_2CuO_3 and CO_2 to produce $Sr_2CuO_2(CO_3)$, the kinetics for the reaction to prepare $Sr_{1.8}Ba_{0.2}CuO_2(CO_3)$ has also been studied using the same approach.

From the TGA curve of mass vs time the points where the mass is only increasing has been identified at 34.2331 mg (650 seconds) to 39.3593 mg (1450 seconds). During these points the mass of the sample increase by 5.1262 mg as CO_2 is being captured. These results showed

that for every 1 mg of CO_2 captured, 6.6781 mg of $Sr_{1.8}Ba_{0.2}CuO_3$ was consumed.

The rate of the reaction has been determined through the relationship between the concentration of $Sr_{1.8}Ba_{0.2}CuO_3$ vs time. Figure 3.32 shows three different graphs for concentration vs time, (1) moles of $Sr_{1.8}Ba_{0.2}CuO_3$ vs time seconds, (2) ln(moles) of $Sr_{1.8}Ba_{0.2}CuO_3$ vs time seconds, and (3) 1/(moles) of $Sr_{1.8}Ba_{0.2}CuO_3$vs time seconds.
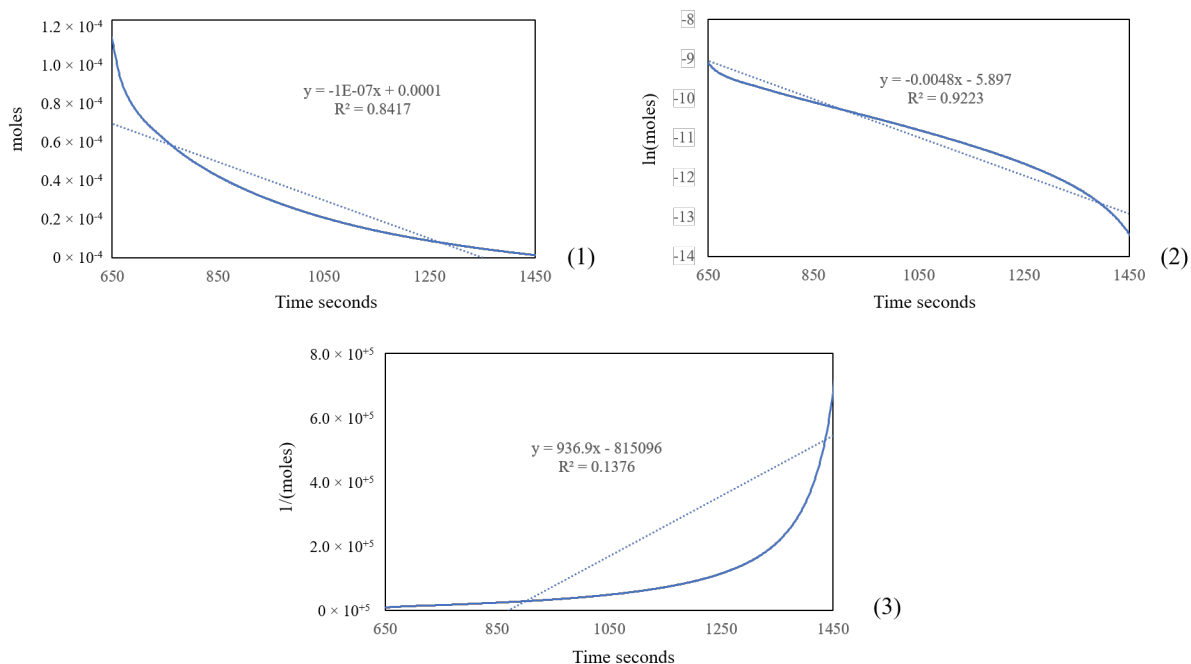
Figure 3.32: Three concentrations vs time graphs, (1) moles of $Sr_{1.8}Ba_{0.2}CuO_3$ vs time seconds, (2) ln(moles) of $Sr_{1.8}Ba_{0.2}CuO_3$ vs time seconds, and (3) 1/(moles) of $Sr_{1.8}Ba_{0.2}CuO_3$ vs time second. Equations of trendlines and R^2 are given for each.

As with Sr_2CuO_3 the trendline of ln(moles) of Sr_2CuO_3 vs time seconds graphs shows an R^2 value closest towards 1 indicating that the reaction is of 1st order. The rate constant has also been determined at 0.0048 S^{-1}. This value is higher than that for the reaction of Sr_2CuO_3 with CO_2 at 0.0045 S^{-1}. The cause of this will be due to the reaction involving $Sr_{1.8}Ba_{0.2}CuO_3$ capturing more CO_2 when forming the oxide carbonate and $SrCO_3$.

3.7.1.3 CO_2 extraction from $Sr_{1.8}Ba_{0.2}CuO_2(CO_3)$ under O_2

The extraction of CO_2 and the re-formation of the original oxide has also been investigated. $Sr_{1.8}Ba_{0.2}CuO_3$ was prepared under O_2, therefore only this gas was used for its re-formation from $Sr_{1.8}Ba_{0.2}CuO_2(CO_3)$.

$Sr_{1.8}Ba_{0.2}CuO_3$ was re-formed multiple times and as such was also reacted with CO_2 towards $Sr_{1.8}Ba_{0.2}CuO_2(CO_3)$ repeatedly. Figure 3.33 shows PXRD patterns for each time $Sr_{1.8}Ba_{0.2}CuO_2(CO_3)$ was re-formed. The oxide carbonate was found to be present alongside the $SrCuO_2$ and $SrCO_3$ as in the original reaction.
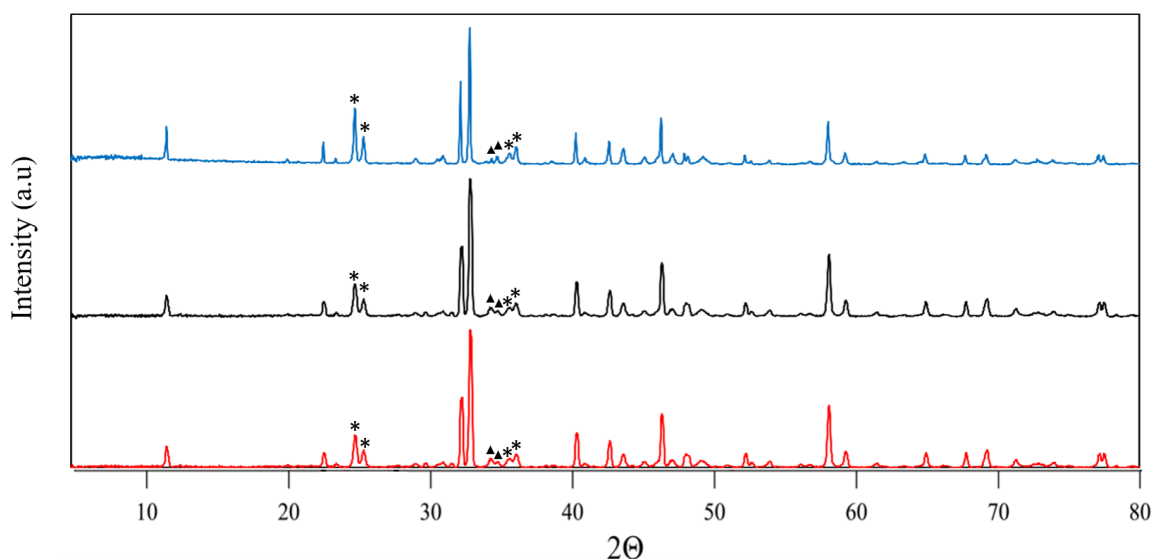
Figure 3.33: PXRD patterns of $Sr_{1.8}Ba_{0.2}CuO_2(CO_3)$ from the 1st (red), 2nd (black) and 3rd (blue) reactions of $Sr_{1.8}Ba_{0.2}CuO_3$, re-formed under O_2 with CO_2. The (*) peaks belong to $SrCO_3$ and (▲) peaks for $SrCuO_2$.

These reverse reactions show that it is possible to extract CO_2 from $Sr_{1.8}Ba_{0.2}CuO_2(CO_3)$ in order to re-form $Sr_{1.8}Ba_{0.2}CuO_3$. This can then be used for further reactions with CO_2 to repeatedly prepare the oxide carbonate. In the case of the 1st reverse reaction this showed a direct conversion to the $Sr_{1.8}Ba_{0.2}CuO_3$ phase under O_2. However, the 2nd and 3rd reverse reactions showed $SrCuO_2$ and $SrCO_3$ to also be present. The reason for the additional phases is potentially a result of the sintering of the sample's particles from repeated heating reactions and makes the reaction towards $Sr_{1.8}Ba_{0.2}CuO_3$ more difficult.[214]

After each reverse cycle the samples were analysed with PXRD to confirm their identity and Rietveld refinements were used to identify and quantify the phase(s) present. The refinements had the atomic coordinates of strontium and barium that were present were constrained and refined together. The identity and quantity of each phase from each reverse reaction has been shown in Table 3.18.

Table 3.19: Identity and quantity of end products from reverse reaction of $Sr_{1.8}Ba_{0.2}CuO_2(CO_3)$ towards $Sr_{1.8}Ba_{0.2}CuO_3$ under O_2.

Reverse reaction	Product phases
1	$Sr_{1.8}Ba_{0.2}CuO_3$ (100 %)
2	$Sr_{1.8}Ba_{0.2}CuO_3$ (94.8 %), $Sr_{1.8}Ba_{0.2}CuO_2(CO_3)$ (5.2 %)
3	$Sr_{1.8}Ba_{0.2}CuO_3$ (88.3 %), $SrCuO_2$ (9.0 %), $SrCO_3$ (2.7 %)

The phases reported from Rietveld refinement showed that despite the first reaction showing complete re-formation of the phase to $Sr_{1.8}Ba_{0.2}CuO_3$. That after each reverse reaction the re-formation of $Sr_{1.8}Ba_{0.2}CuO_3$ becomes less favourable.

3.7.2 Preparation of $Sr_{2-x}Ca_xCuO_2(CO_3)$ ($0 \leq x \leq 2$)

In the case of $Ca_2CuO_2(CO_3)$ this was prepared as single crystals at 1300 °C and 6 GPa of pressure using a flux agent (Ag_2O) whilst being sealed in a gold capsule.[115] To the author's knowledge no compounds have been reported within the solid-solution series of $Sr_{2-x}Ca_xCuO_2(CO_3)$ ($0 < x < 2$). The only known compound to have a similar structure is that of $Sr_{1.89}Ca_{1.11}(CuO_2)_2(CO_3)$ which was also prepared by Kopnin *et al.*, using a similar method as for $Ca_2CuO_2(CO_3)$.[115] In this structure copper-carbonate groups are present separating the Sr/CaO layers. The structure has also been reported to be similar to $Sr_2CuO_2(CO_3)$, with copper occupying carbon sites. The fractional occupancy of strontium and calcium is also different depending on the atomic site.

In this work, the $Sr_{2-x}Ca_xCuO_3$ ($0 \leq x \leq 2$) series of compounds has been investigated for reacting with CO_2 in order to prepare new materials, which can exist in the $Sr_{2-x}Ca_xCuO_2(CO_3)$ ($0 \leq x \leq 2$) series.

3.7.2.1 Structural Characterisation of $Sr_{2-x}Ca_xCuO_3$ ($0 \leq x \leq 2$)

The $Sr_{2-x}Ca_xCuO_3$ (x = 0, 0.5, 1.0 and 2.0) series was prepared using the same method as with the $Sr_{2-x}Ba_xCuO_3$ (x < 0.5) series. This involved the reagents being weighted to produce 1g of product and dispersed with one another to be compressed into pellets before heating. The $Sr_{2-x}Ca_xCuO_3$ (x = 0, 0.5, 1.0 and 2) compounds prepared resulted in dark brown polycrystalline samples. The identity of these samples were confirmed using PXRD analysis. Table 3.20 shows the unit cell parameters, anion vacancies (Å) and volume (Å^3) for all of these compounds.

Table 3.20: Structural data for $Sr_{2-x}Ca_xCuO_3$ (x = 0, 0.5, 1.0 and 2.0) series of compounds.[88, 223, 196]

Compound	a Å	b Å	c Å	V Å^3	Anion vacancy (Å)
Sr_2CuO_3	12.716(1)	3.916(4)	3.5032(3)	174.44(3)	3.5032(1)
$Sr_{1.5}Ca_{0.5}CuO_3$	12.596(1)	3.8787(5)	3.4425(4)	168.18(3)	3.4517(3)
$SrCaCuO_3$	12.48(1)	3.845(5)	3.388(4)	162.63(3)	3.3902(4)
Ca_2CuO_3	12.25(2)	3.789(8)	3.259(3)	150.87(3)	3.2490(10)

The incorporation of calcium into the sites occupied by strontium results in a decrease of the lattice parameters and unit cell volume. This is from the ionic radii of Ca^{2+} at 1.06 Å being smaller than that of Sr^{2+} at 1.21 Å. The anion vacancies present within the structure were also found to decrease as a result of the increased substitution quantities.

Once pure samples of the $Sr_{2-x}Ca_xCuO_3$ (x = 0, 0.5,1 and 2) series had been prepared the next step was the direct reactions with CO_2. As with Sr_2CuO_3 and $Sr_{1.8}Ba_{0.2}CuO_3$ the $Sr_{2-x}Ca_xCuO_3$ compounds were reacted with alternating gases of air and CO_2 at 1000 °C towards preparing the oxide carbonates.

3.7.2.2 Reaction of $Sr_{2-x}Ca_xCuO_3$ ($0 \leq x \leq 2$) compounds with CO_2

Ca_2CuO_3 was the first to react with CO_2 in the same way as with Sr_2CuO_3. This was aimed at preparing $Ca_2CuO_2(CO_3)$ which was reported by Kopnin*et al.*.[115] The 1st reaction under CO_2 lasted for 15 minutes and showed that Ca_2CuO_3 remained as the main phase with peaks belonging to $CaCO_3$ to also present.[199] The next reaction had the time under CO_2 increased from 15 to 60 minutes. This resulted as before in Ca_2CuO_3 alongside peaks belonging to $CaCO_3$ that had increased in intensity. The steady increase of $CaCO_3$ present from a longer time under CO_2 has been presented from a comparison of the PXRD patterns of these reactions in Figure 3.34.
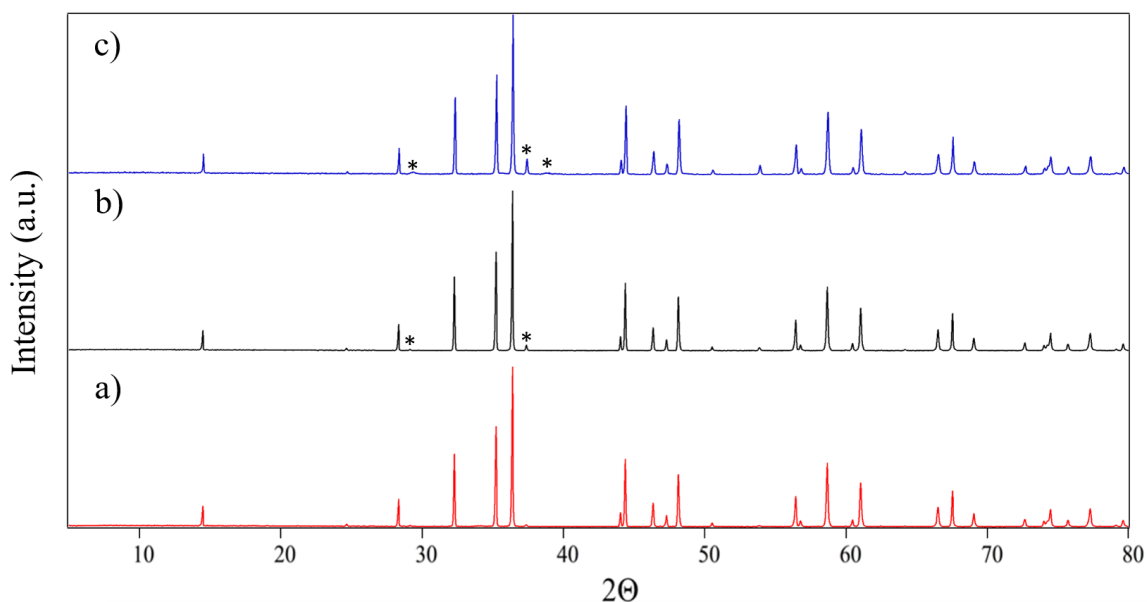
Figure 3.34: Comparison of PXRD patterns of a) Ca_2CuO_3 then b) 15 and c) 60 minutes under CO_2 reacting. The peaks marked (*) are those belonging to $CaCO_3$.

The inability for CO_2 to be incorporated within Ca_2CuO_3 is potentially a result of the anion vacancies being too small (3.25 Å) to accommodate CO_2 with its kinetic diameter of 3.30 Å. As a result, compounds within the $Sr_{2-x}Ca_xCuO_3$ ($0 \leq x \leq 2$) series with lower amounts of calcium have been investigated towards forming a $Sr_{2-x}Ca_xCuO_2(CO_3)$ compound.

$SrCaCuO_3$, a solid-solution containing 50:50, strontium and calcium was next investigated. The reaction times under CO_2 were 15, 60 and 90 minutes with the PXRD patterns from

each shown in Figure 3.35. However in each of the products formed multiple phase were present such as $Sr_2CuO_2(CO_3)$, $SrCuO_2$ and $SrCO_3$ type compounds. The amount of calcium is potentially the limiting factor for allowing CO_2 to enter and react within the structure to form a oxide carbonate. Therefore as calcium content increases the size of the anion vacancies decreases. This may increase the amount of energy required towards forming the oxide carbonate.
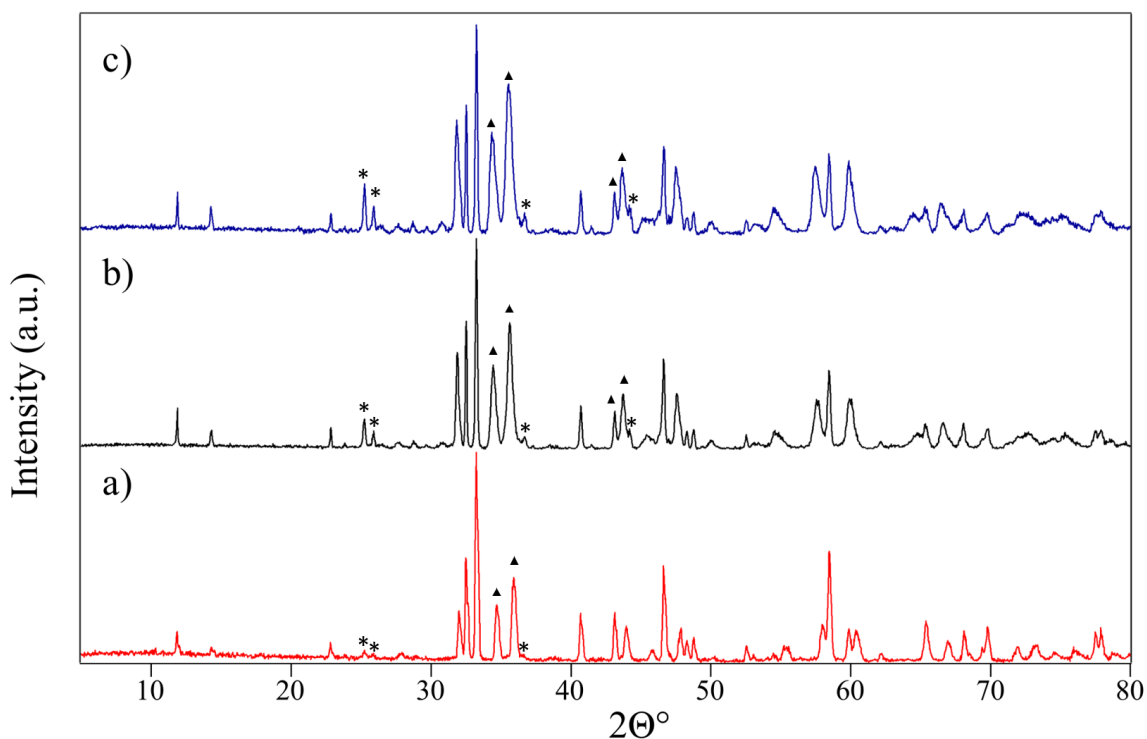
Figure 3.35: Comparison of PXRD patterns of $SrCaCuO_3$ reacting with CO_2 gas at different times, a) 90 minutes, b) 30 minutes and c) 15 minutes. Peaks belonging to $SrCO_3$ are labelled with (*) marks whilst (▲) are those belonging to $SrCuO_2$.

As the time under CO_2 increases the intensities of peaks belonging to phases such as $SrCuO_2$ and $SrCO_3$ would decrease. This is potentially due to the longer reaction time favouring the formation of the oxide carbonate.

$Sr_{1.5}Ca_{0.5}CuO_3$ was the next compound investigated with its calcium content lowered to one quarter. As with $SrCaCuO_3$, $Sr_{1.5}Ca_{0.5}CuO_3$ was exposed to 15, 60 and 90 minute reactions at 1000 °C under CO_2. The resulting PXRD patterns from each reactions have been presented in Figure 3.36. The PXRD patterns for the 15 and 60 minute reactions under CO_2 showed

that peaks belonging to $SrCuO_2$ and $SrCO_3$ were present within the sample. However peaks at approximately $2\theta \approx 32°$ indicated the presences of a "$Sr_2CuO_2(CO_3)$" type phase. The TGA curve for the 90 minute reaction between $Sr_{1.5}Ca_{0.5}CuO_3$ and CO_2 is shown in Figure 3.37.
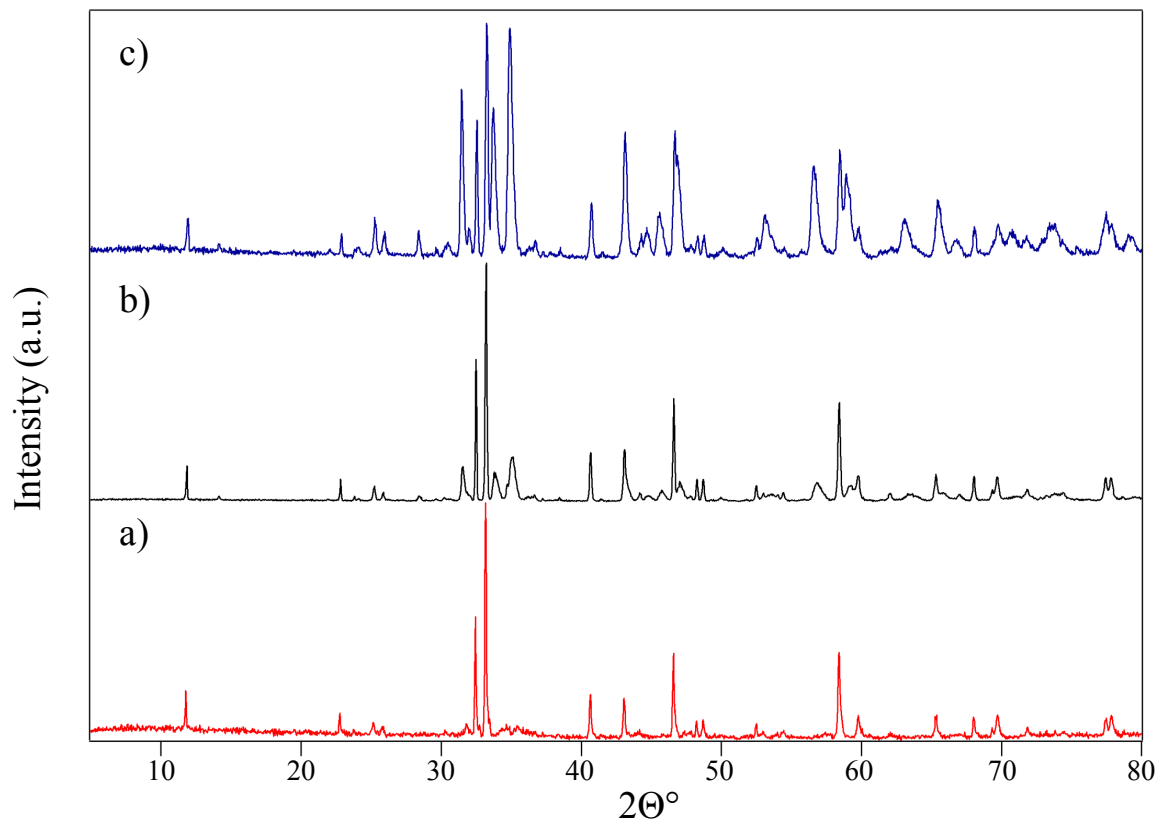
Figure 3.36: Comparison of PXRD patterns of $Sr_{1.5}Ca_{0.5}CuO_3$ reacting with CO_2 gas at different times, a) 90 minutes, b) 30 minutes and c) 15 minutes.
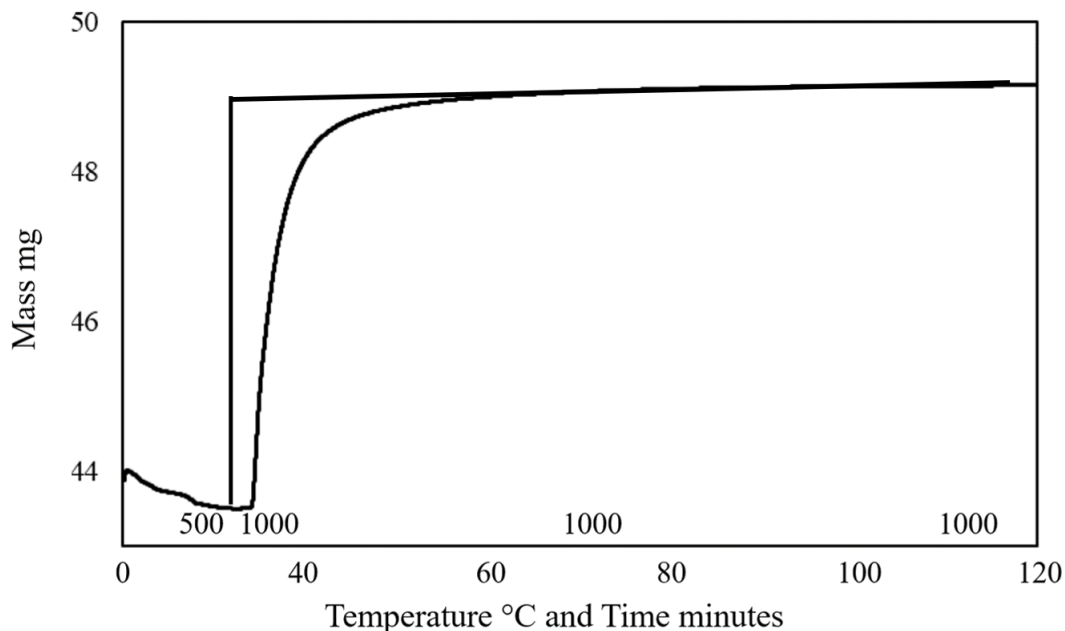
Figure 3.37: TGA curve of $Sr_{1.5}Ca_{0.5}CuO_3$ reacting with CO_2 for 90 minutes at 1000 $^\circ$C.

The PXRD pattern for the reaction under CO_2 for 90 minutes suggested that a $Sr_{2-x}Ca_xCuO_2(CO_3)$ type compound had been prepared. This sample was further analysed via a three-phase Rietveld refinement as $SrCO_3$ and $SrCaCuO_3$ were also present.[205, 196] In the refinements the model of $Sr_2CuO_2(CO_3)$ reported by Babu *et al.* was used for the oxide carbonate. This was due to the two end members of $Sr_2CuO_2(CO_3)$ and $Ca_2CuO_2(CO_3)$ having crystal structures which were similar to one another, both tetrahedral with a *P4/mmm* space group.[80, 115] The main difference however is that the strontium model will have copper set at the origin. It is proposed that "$Sr_{1.5}Ca_{0.5}CuO_2(CO_3)$" is closer towards the strontium compound and as a result this model was used for refinements. The calcium content was initially set at x = 0.5 as within the original oxide during the refinements.

For the refinement the background was modelled using the Cosine Fourier series with twelve terms. The multi-term Simpson's rule integration of the pseudo-Voigt was used in order to model the peaks shapes within for all phases.[203, 204] The parameters refined were: the cell parameters (*a, b, c*) and the scale factors for all three-phases. The U_{iso} and the atomic coordinates for the strontium and calcium were constrained with each other when refined. The Lorentzian anisotropic strain broadening was also refined as well. The fractional occupancy between the strontium and calcium was also refined within the oxide carbonate phase. The

162

refinement of the occupancies showed that the amount of calcium had been reduced from 25 % in $Sr_{1.5}Ca_{0.5}CuO_3$ to 12.5 % in the oxide carbonate. This gave the composition as $Sr_{1.75}Ca_{0.25}CuO_2(CO_3)$. The strontium and calcium occupancy of the $SrCaCuO_3$ secondary phase was also refined to be a 1:1 stoichiometry with the refinement pattern presented in Figure 3.38.
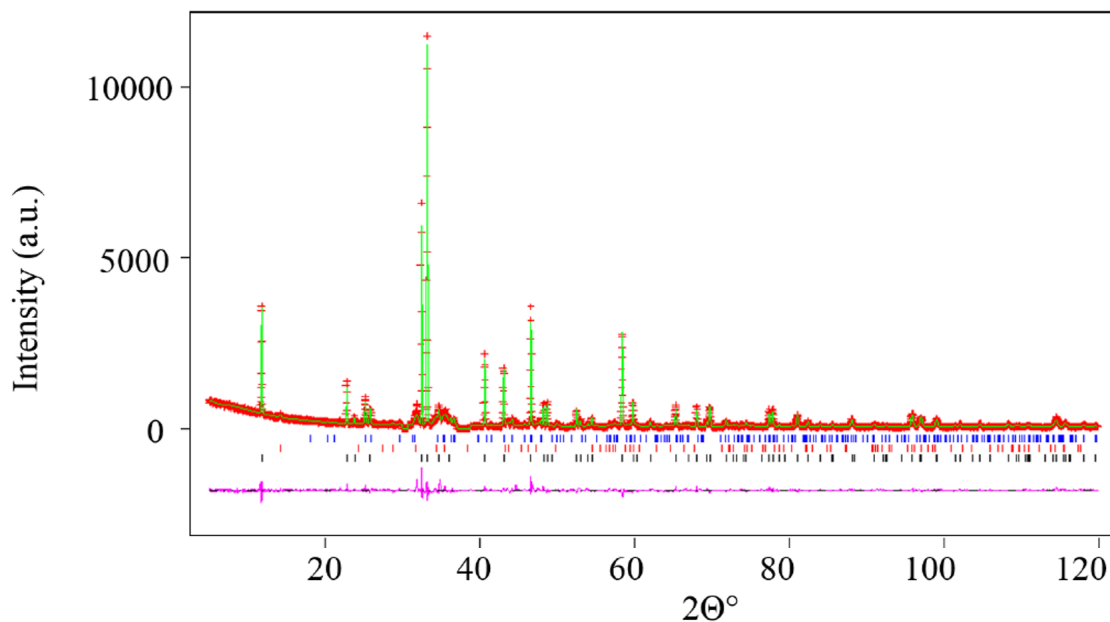
Figure 3.38: X-ray powder diffraction profiles of $Sr_{1.75}Ca_{0.25}CuO_2(CO_3)$ obtained from a 90 minute reaction of $Sr_{1.5}Ca_{0.5}CuO_2(CO_3)$ under CO_2. This shows the observed (red crosses), calculated (green) and difference (purple) patterns. The ticks represent $Sr_{1.75}Ca_{0.25}CuO_2(CO_3)$ (black), $SrCaCuO_3$ (red) and $SrCO_3$ (blue).

The R-values for this refinement were determined as R_{wp} = 12.9 % and R_p = 9.3. The structural data of the $Sr_{1.75}Ca_{0.25}CuO_2(CO_3)$ has also been presented in appendix, Table 8.5. The refinement showed the quantity of all phases as $Sr_{1.75}Ca_{0.25}CuO_2(CO_3)$ (70.5 $\pm$ 0.08 %), $SrCaCuO_3$ (20 $\pm$ 0.5 %) and $SrCO_3$ (9.5 $\pm$ 0.15 %).

As with the other oxide carbonates the CO_3 groups will have a disordered structure from the surrounding oxides of 0.25 occupancy. This refinement also has high U_{iso} values from the O2 and O3 atoms.

The loss of calcium from $Sr_{1.5}Ca_{0.5}CuO_3$ towards forming $Sr_{1.75}Ca_{0.25}CuO_2(CO_3)$ is likely

what also causes the formation of $SrCaCuO_3$. As seen with Ca_2CuO_3 and $SrCaCuO_3$ the incorporation of calcium for strontium causes the reaction to favour decomposition over forming an oxide carbonate. In the case of $Sr_{1.5}Ca_{0.5}CuO_3$ this resulted in not only $Sr_{1.75}Ca_{0.25}CuO_2(CO_3)$ but also $SrCaCuO_3$ and $SrCO_3$ being present. The unit cell parameters of $Sr_{1.75}Ca_{0.25}CuO_2(CO_3)$ have been compared to $Sr_2CuO_2(CO_3)$ showing the reduction from calcium substitution in Table 3.21.

Table 3.21: Comparison of the unit cells parameters of $Sr_2CuO_2(CO_3)$ reported by Babu *et al.* to $Sr_{1.75}Ca_{0.25}CuO_2(CO_3)$.[80]

Compound	a(Å)	c(Å)	V(Å^3)
$Sr_2CuO_2(CO_3)$ (1)	3.9033(2)	7.4925(4)	114.153(16)
$Sr_{1.75}Ca_{0.25}CuO_2(CO_3)$ (2)	3.8930(3)	7.4677(1)	113.175(2)
Difference (1)-(2)	0.0103(3)	0.0248(1)	0.978(2)

The result of partially substituting strontium for calcium sees a reduction within the unit cell parameters of the oxide carbonate phase. This is to be expected as the ionic radii of Ca^{2+}, is 0.15 (Å) smaller than that of Sr^{2+} cation. The reduction is of a scale below 0.1 (Å) for the unit cell parameters as only one eighth of the strontium was substituted by calcium.

The reaction of $Sr_{1.5}Ca_{0.5}CuO_3$ with CO_2 for 90 minutes has resulted in the formation of a novel oxide carbonate, $Sr_{1.75}Ca_{0.25}CuO_2(CO_3)$ along side other phases. The loss of calcium is attributed to the formation of $SrCaCuO_3$ present with the oxide carbonate. This time is also longer when compared to that for forming $Sr_2CuO_2(CO_3)$ which was only 15 minutes. This could be due to the change in size of Ca^{+2} to Sr^{+2} cations which reduce the size of the anion vacancies. Despite the impurities present, this is the first compound reported to exist within the $Sr_{2-x}Ca_xCuO_2(CO_3)$ series, This also highlights this novel approach of directly reacting CO_2 within compound with anion vacancies towards novel mixed anion materials.

The amount of CO_2 utilised by $Sr_{1.5}Ca_{0.5}CuO_3$ towards $Sr_{1.75}Ca_{0.25}CuO_2(CO_3)$ has also been determined. As with the previous compounds $Sr_{1.5}Ca_{0.5}CuO_3$ utilises the captured CO_2 in order to prepare an oxide carbonate. The TGA curve shows the amount of CO_2 which is captured by $Sr_{1.5}Ca_{0.25}CuO_3$ at 1000 °C. The amount of CO_2 captured was determined as

the average mass increase over a series of reactions with $Sr_{1.5}Ca_{0.5}CuO_3$ and CO_2, and the values have been presented in along with the RMSD Table 3.22.

Table 3.22: CO_2 capturing capacity of $Sr_{1.5}Ca_{0.5}CuO_3$ and uncertainties over a range of reactions

TGA curve	CO_2 capturing capacity mmol/g	Uncertainty mmol/g
1	2.912	0.003
2	2.811	0.003
3	2.839	0.003
Average	2.854	0.005

As with Sr_2CuO_3 the CO_2 capturing capability has also been determined using the mass % values of the phases produced from the reaction to coincide with the results from TGA. The reaction between $Sr_{1.5}Ca_{0.5}CuO_3$ and CO_2 resulted in a mixed phase product consisting of 70.5 % of $Sr_{1.75}Ca_{0.25}CuO_2(CO_3)$, 20.0 % of $SrCaCuO_3$ and 9.5 % of $SrCO_3$. The TGA curve from this reaction, Figure 3.36, showed that the mass of the end product was that of 49.051 mg. This value was used to determine the mass %, mass of the phase and CO_2 content for each phase to calculate he mass of CO_2 captured. These values have been shown in Table 3.23.

Table 3.23: Overall mass and mass % of $Sr_{1.8}Ba_{0.2}CuO_2(CO_3)$ and $SrCO_3$ in product phase. Along with mass of CO_2 captured.

Phases	Mass %	Mass mg	CO_2 mass mg
$Sr_{1.75}Ca_{0.25}CuO_2(CO_3)$	70.5 %	34.580	4.957
$SrCO_3$	9.5 %	4.660	1.558

Based on the Rietveld refinement results the overall amount of CO_2 captured was that of 6.5142 mg by 43.579 mg of $Sr_{1.5}Ca_{0.5}CuO_3$. These values were then used and determined a CO_2 capturing capability value of 3.40 $\pm$ 0.004 mmol/g. This value is greater than that calculated using just the mass difference from TGA results at 2.85 mmol/g.

This value of 3.40 mmol/g along with that calculated by TGA, 2.85 mmol/g, is lower that

that of the CO_2 capturing capability by Sr_2CuO_3 at 4.28 and 3.80 mmol/g. The reason for this can be attributed to fewer products being carbonate based. It has been found that with Sr_2CuO_3 that all products are carbonate based and hence more CO_2 has been captured. In the case of $Sr_{1.8}Ba_{0.2}CuO_3$ when this reacts with CO_2 that 29.2 % of the product as $SrCO_3$. This compound has more of its molecular mass contributed from CO_2 than the oxide carbonate. The reaction between $Sr_{1.5}Ca_{0.5}CuO_3$ and CO_2 results in the lowest amounts of $SrCO_3$ being produced. This means less CO_2 overall has been capture compared to the other mixed metal oxides

3.7.2.3   Reaction kinetics of $Sr_{1.5}Ca_{0.5}CuO_3$ with CO_2

As with the direct reaction between Sr_2CuO_3 and $Sr_{1.8}Ba_{0.2}CuO_2$ with CO_2 to produce their respective oxide carbonates, the kinetics for the reaction between $Sr_{1.5}Ca_{0.5}CuO_3$ and CO_2 has also been studied using the same methods.

From the TGA curve of mass vs time the points where the mass is only increasing has been identified at 43.5266 mg (850 seconds) to 49.1440 mg (4050 seconds). During these points the mass of the sample increased by 5.6174 mg as CO_2 is being captured and shows that for every 1 mg of CO_2 captured, 7.7485 mg of $Sr_{1.5}Ca_{0.5}CuO_3$ was consumed.

The rate of the reaction has been determined through the relationship between the concentration of $Sr_{1.5}Ca_{0.5}CuO_3$ vs time. Figure 3.39 shows three different graphs for concentration vs time, (1) moles of $Sr_{1.5}Ca_{0.5}CuO_3$ vs time seconds, (2) ln(moles) of $Sr_{1.5}Ca_{0.5}CuO_3$ vs time seconds, and (3) 1/(moles) of $Sr_{1.5}Ca_{0.5}CuO_3$ vs time seconds.

(1)

$y = -1 \times 10^{-8}x + 4 \times 10^{-5}$
$R^2 = 0.3308$

moles

Time seconds

(2)

$y = -0.0016x - 8.4424$
$R^2 = 0.8846$

ln(moles)

Time seconds

(3)

$y = 31459x - 7 \times 10^7$
$R^2 = 0.0474$

1/(moles)
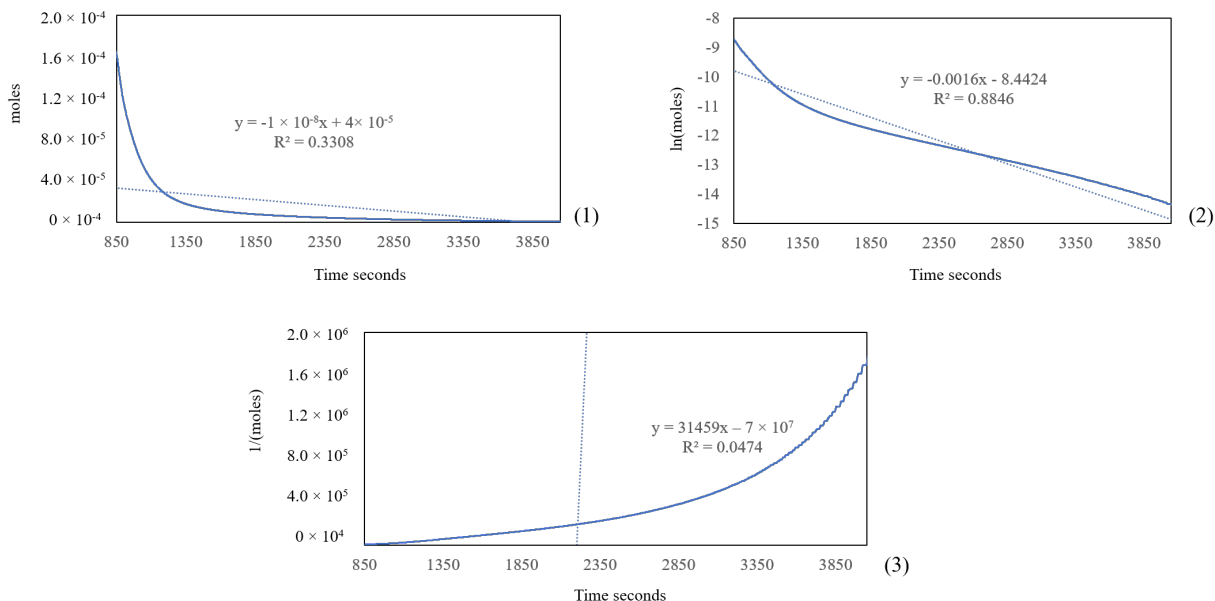
Time seconds

Figure 3.39: Three concentrations vs time graphs, (1) moles of $Sr_{1.5}Ca_{0.5}CuO_3$ vs time seconds, (2) ln(moles) of $Sr_{1.5}Ca_{0.5}CuO_3$ vs time seconds, and (3) 1/(moles) of $Sr_{1.5}Ca_{0.5}CuO_3$ vs time second. Equations of trendlines and R^2 are given for each.

As with Sr_2CuO_3 and $Sr_{1.8}Ba_{0.2}CuO_3$ the trendline of ln(moles) of $Sr_{1.5}Ca_{0.5}CuO_3$ vs time seconds graphs shows an R^2 value closest towards 1 and is the most linear. This shows that this reaction as with the others is of 1st order. The slope of the trendline shows the rate of the reaction at 0.0016 S^{-1}. This value is lower than that for the reactions of Sr_2CuO_3 and $Sr_{1.8}Ba_{0.2}CuO_3$ with CO_2 at 0.0045 and 0.0048 S^{-1} respectfully. The lower reaction rate is likely the cause of this reaction taking 90 minutes whereas the others only take 15 minutes. The incorporation of calcium into the strontium cuprate results in a lower reaction rate and slower reaction time compared to the full strontium equivalent.

3.7.2.4 Reversibility of $Sr_{2-x}Ca_xCuO_2(CO_3)$ series to re-form oxide precursor

3.7.2.4.1 CO_2 extraction from $Sr_{1.75}Ca_{0.25}CuO_2(CO_3)$ under Air

The extraction of CO_2 from $Sr_{1.75}Ca_{0.25}CuO_2(CO_3)$ to re-form $Sr_{1.5}Ca_{0.5}CuO_3$ has also been investigated. The re-formation of $Sr_{1.75}Ca_{0.25}CuO_2(CO_3)$ was carried out in tandem along-side the extraction reactions. The PXRD patterns (Figure 3.40) show that the 1st and 2nd

$Sr_{1.75}Ca_{0.25}CuO_2(CO_3)$ re-formation reactions have similar results. The 3rd reaction however, showed the peaks belonging to the $SrCO_3$ and $SrCuO_2$ phases increased in intensity.
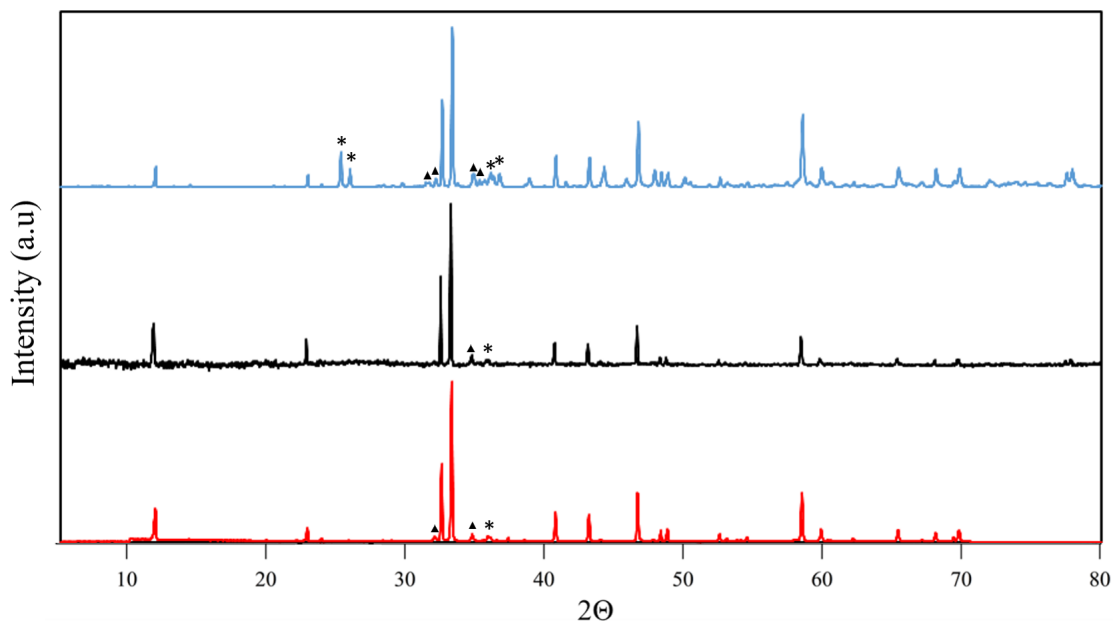
Figure 3.40: PXRD patterns of $Sr_{1.75}Ca_{0.25}CuO_2(CO_3)$ from the 1st (red), 2nd (black) and 3rd (blue) reactions of $Sr_{1.5}Ca_{0.5}CuO_3$, re-formed under air with CO_2. The (*) peaks belong to $SrCO_3$ and (▲) peaks for $SrCuO_2$.

This increase has been attributed to the starting phase from the 3rd reverse reaction showing a mixture of $Sr_{1.5}Ca_{0.5}CuO_3$, $SrCuO_2$ and $Sr_{1.75}Ca_{0.25}CuO_2(CO_3)$. As a carbonate and an oxide carbonate are already present, it is possible that the reaction under CO_2 for 90 minutes is favouring decomposition of the oxide carbonate giving $SrCO_3$. $SrCuO_2$ as a product does not react with CO_2 and as a result appears in the diffractogram alongside the oxide carbonate.

The 1st set of reverse reactions to re-form $Sr_{1.5}Ca_{0.5}CuO_3$ had $Sr_{1.75}Ca_{0.25}CuO_2(CO_3)$ heated under air, afterwards the sample was analysed using PXRD and Rietveld refinements. This was to confirm the identity of $Sr_{1.5}Ca_{0.5}CuO_3$, as well as any other phases. The fractional occupancy of the strontium and calcium was refined in each solid-solution to identify the phase composition. Refinement of the 1st reverse reaction under air (Figure 3.41) shows the different phases.
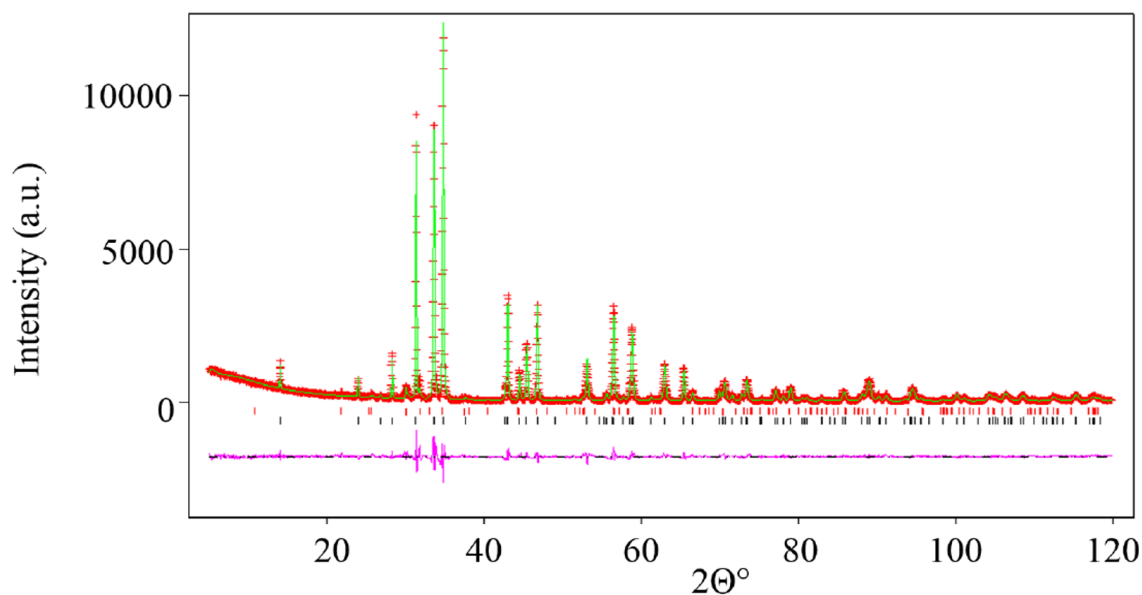
Figure 3.41: X-ray powder diffraction profiles of $Sr_{1.5}Ca_{0.5}CuO_3$ from 1st extraction of CO_2 from $Sr_{1.75}Ca_{0.25}CuO_2(CO_3)$ under air. This shows observed (red crosses), calculated (green) and difference (purple) patterns. Ticks belong to $Sr_{1.5}Ca_{0.5}CuO_3$ (black) and $SrCuO_2$ (red).

Despite the presence of $SrCuO_2$, the stoichiometry of the only other detected phase was still that of $Sr_{1.5}Ca_{0.5}CuO_3$. Attempts were made to include calcium within the refinement of $SrCuO_2$ phase however, none was detected. The reason for this is still unclear. The sample from the 2nd reverse cycle was then analysed showing $Sr_{1.5}Ca_{0.5}CuO_3$ alongside a $SrCuO_2$ phase. The refinement (Figures 3.42) however, determined that the secondary phase was a solid-state solution with the composition of $Sr_{0.58}Ca_{0.42}CuO_2$.
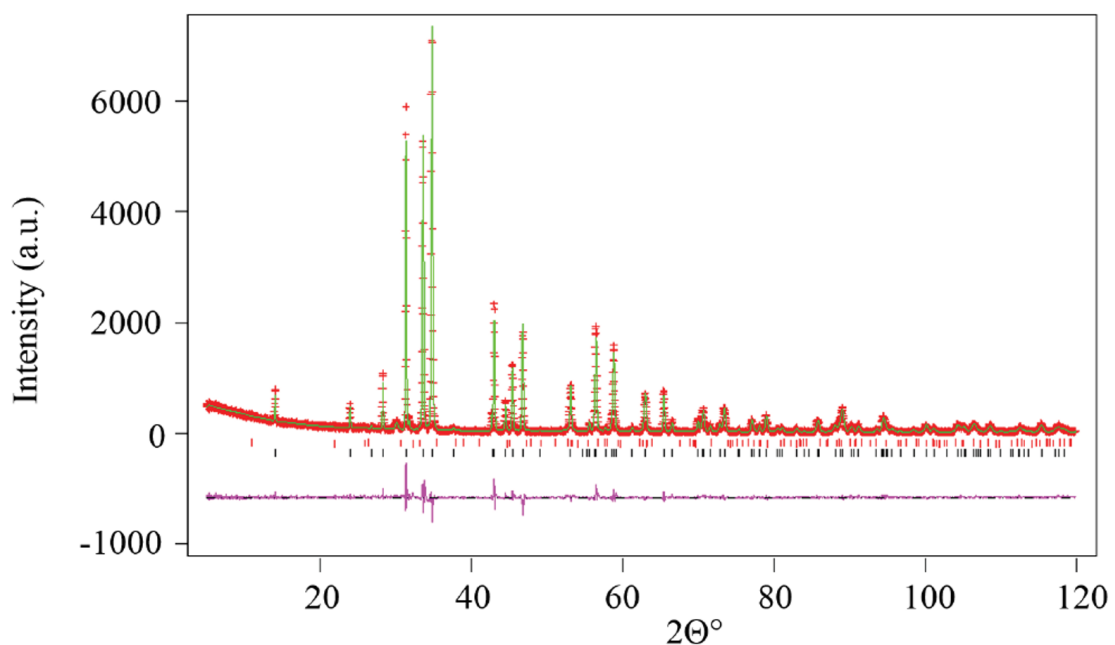
Figure 3.42: X-ray powder diffraction profiles of $Sr_{1.5}Ca_{0.5}CuO_3$ obtained from 2nd extraction of CO_2 from $Sr_{1.75}Ca_{0.25}CuO_2(CO_3)$ under air. This shows the observed (red crosses), calculated (green) and difference (purple) patterns. The ticks belong to $Sr_{1.5}Ca_{0.5}CuO_3$ (black) and $Sr_{0.58}Ca_{0.42}CuO_2$ (red).

The unit cell parameters of $Sr_{0.58}Ca_{0.42}CuO_2$ was also determined as ($a = 3.5470$, $b = 16.2722$ and $c = 3.8866$ Å). This showed a reduction in unit cell size as a result of calcium substitution compared to the values for $SrCuO_2$ at $a = 3.5766$, $b = 16.3354$ and $c = 3.9143$ Å.[220] The quantification of each different phases was also determined along with the R-values, and is shown within Table 3.24.

Table 3.24: Quantification of different phases, as well as R-values for the 1st and 2nd reverse reactions.

Reverse reaction	$Sr_{1.5}Ca_{0.5}CuO_3$ %	$SrCuO_2$ %	R_{wp} %	R_p %
1	95.9 ± 0.12	4.1 ± 0.04	12.54	8.31
Reverse reaction	$Sr_{1.5}Ca_{0.5}CuO_3$ %	$Sr_{0.58}Ca_{0.42}CuO_2$ %	R_{wp} %	R_p %
2	94.6 ± 0.26	5.4 ± 0.16	12.13	8.58

The 3rd reverse cycle showed peaks belonging to an oxide carbonate "$Sr_{2-x}Ca_xCuO_2(CO_3)$"

type phase present in the PXRD pattern. A three-phase refinement for this sample was carried out, Figure 3.43. This refinement had the background modelled using the Cosine Fourier series with twelve terms. The multi-term Simpson's rule integration of the pseudo-Voigt was used in order to model the peaks shapes within for all phases.[203, 204] The parameters refined were: the cell parameters (*a, b, c*) and the scale factors for all three-phases. The U_{iso} and the atomic coordinates for the strontium and calcium were constrained with each other when refined for each phase. The Lorentzian anisotropic strain broadening was also refined as well. The fractional occupancy between the strontium and calcium in all phases were also refined to determine the composition.
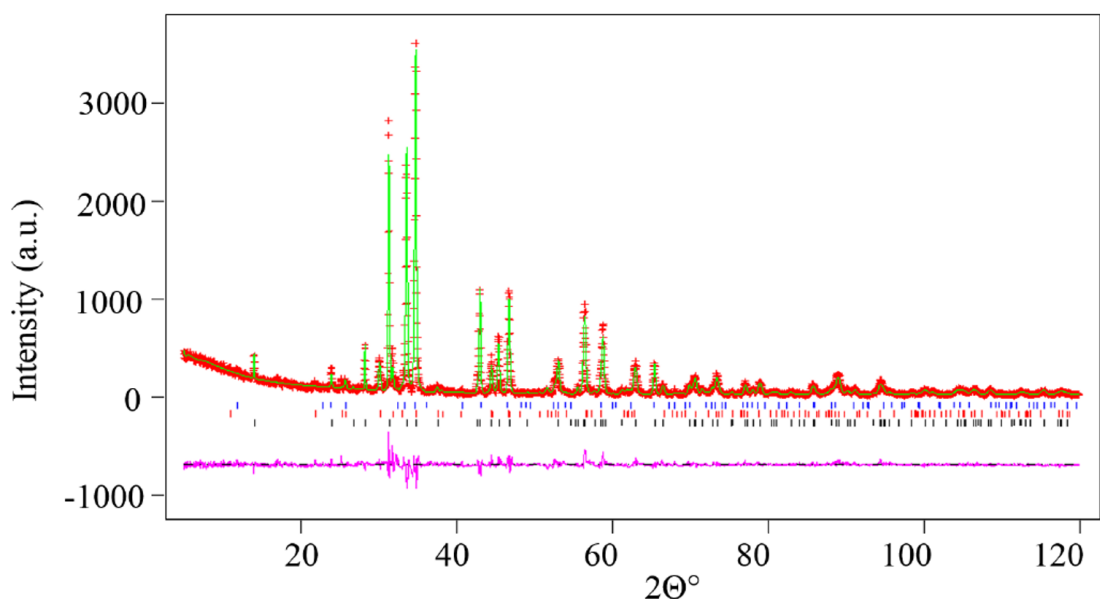
Figure 3.43: X-ray powder diffraction profiles of $Sr_{1.5}Ca_{0.5}CuO_3$ obtained from 3rd extraction of CO_2 from $Sr_{1.75}Ca_{0.25}CuO_2(CO_3)$ under air. This shows the observed (red crosses), calculated (green) and difference (purple) patterns. The tick belong to $Sr_{1.5}Ca_{0.5}CuO_3$ (black), $SrCuO_2$ (red) and $Sr_{1.75}Ca_{0.25}CuO_2(CO_3)$ (blue).

Rietveld refinements confirmed with PXRD the presence and quantification of $Sr_{1.5}Ca_{0.5}CuO_3$ (85.0 ± 0.13), $SrCuO_2$ (12.6 ± 0.20) and $Sr_{1.75}Ca_{0.25}CuO_2(CO_3)$ (2.4 ± 0.30). The R-values for the 3rd reverse cycle were also determined as, R_{wp} = 14.6 % and R_p = 10.2 %. These results also showed that after the 3rd reverse reaction an oxide carbonate phase will start to remain within the sample. It is possible that at this stage the repeated heating of the sample has

caused the particles themselves to be sintered. This may result in the reactivity of the sample changing making direct extraction of CO_2, and re-forming of $Sr_{1.5}Ca_{0.5}CuO_3$ more difficult. Despite this, reverse cycles under air were able to extract CO_2 from $Sr_{1.75}Ca_{0.25}CuO_2(CO_3)$ and have this react with the other phases to re-form $Sr_{1.5}Ca_{0.5}CuO_3$.

3.7.2.4.2 CO_2 extraction from $Sr_{1.75}Ca_{0.25}CuO_2(CO_3)$ under O_2

Extraction of CO_2 from $Sr_{1.75}Ca_{0.25}CuO_2(CO_3)$ to re-form $Sr_{1.5}Ca_{0.5}CuO_3$ has been investigated under pure O_2. The re-formation of the oxide carbonates has also been monitored from using each re-formed $Sr_{1.5}Ca_{0.5}CuO_3$ from the reverse reactions. The PXRD pattern of the re-formed $Sr_{1.75}Ca_{0.25}CuO_2(CO_3)$ is shown in Figure 3.44.
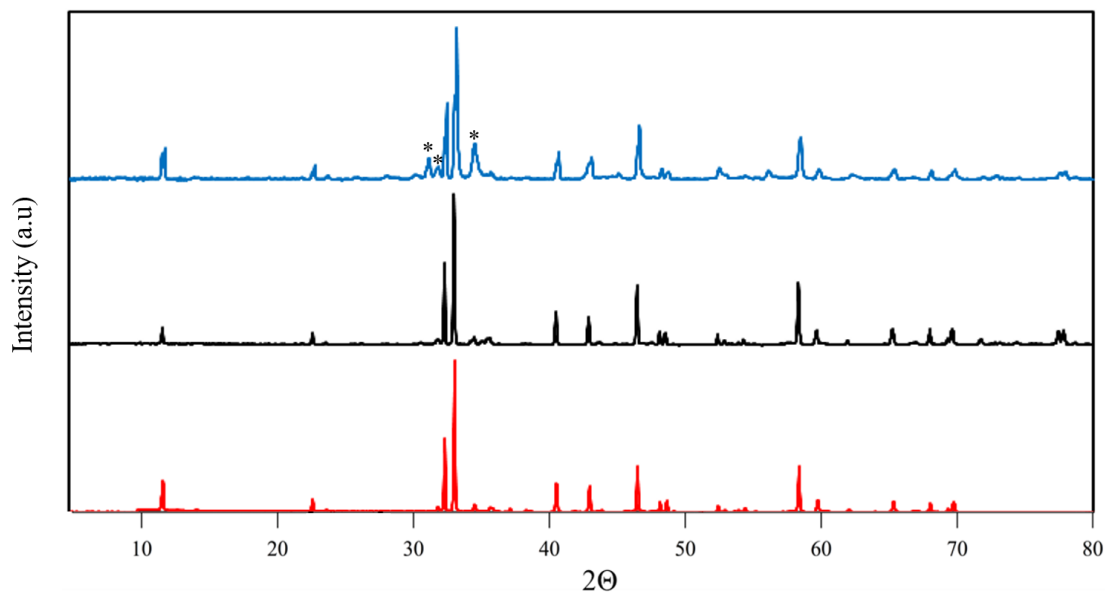
Figure 3.44: PXRD patterns of $Sr_{1.75}Ca_{0.25}CuO_2(CO_3)$ from the 1st (red), 2nd (black) and 3rd (blue) reactions of $Sr_{1.5}Ca_{0.5}CuO_3$, re-formed under O_2 with CO_2. Peaks highlighted (*) belong to unreatced $Sr_{1.5}Ca_{0.5}CuO_3$.

As with the reverse reactions under air. The PXRD patterns for the 1st and 2nd re-formation of $Sr_{1.75}Ca_{0.25}CuO_2(CO_3)$ showed similar results to one another. The 3rd reaction however, showed peaks belonging to unreacted $Sr_{1.5}Ca_{0.5}CuO_3$ that were present alongside the oxide carbonate.

PXRD patterns for the 1st and 2nd reverse reactions under O_2 showed $Sr_{1.5}Ca_{0.5}CuO_3$ had been re-formed with a $SrCuO_2$ type compound also present. Two-phase Rietveld refinements were carried out (Figures 3.45 and 3.46) to determine the quantity of each phase and the composition of $Sr_{1-x}Ca_xCuO_2$.
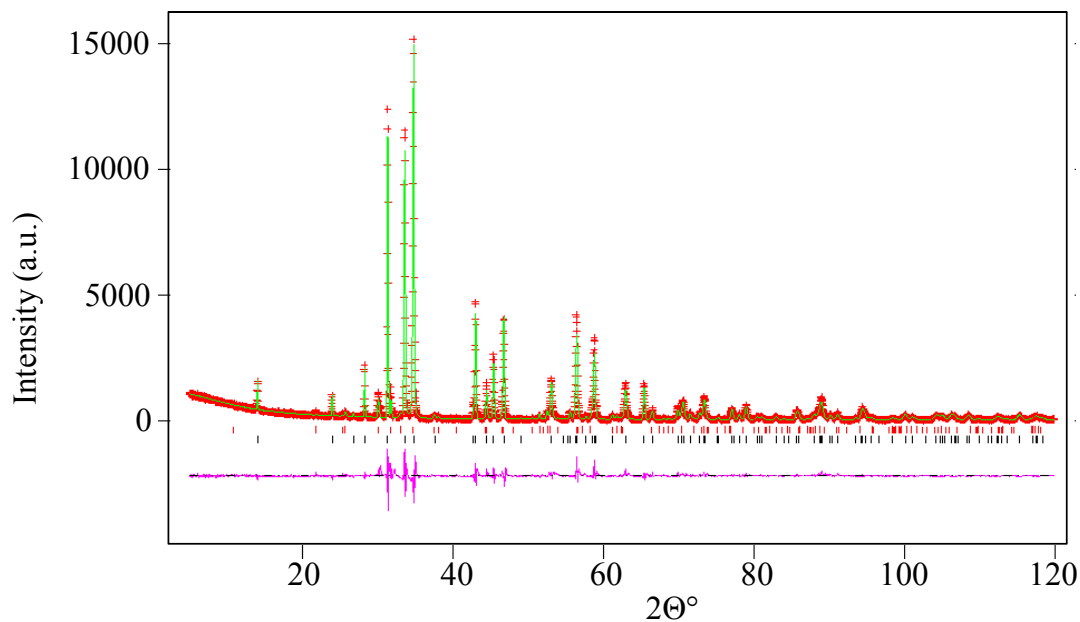
Figure 3.45: X-ray powder diffraction profiles of $Sr_{1.5}Ca_{0.5}CuO_3$ from 1st extraction of CO_2 from $Sr_{1.75}Ca_{0.25}CuO_2(CO_3)$ under O_2. This shows observed (red crosses), calculated (green) and difference (purple) patterns with ticks belonging to $Sr_{1.5}Ca_{0.5}CuO_3$ (black) and $Sr_{0.88}Ca_{0.12}CuO_2$ (red).
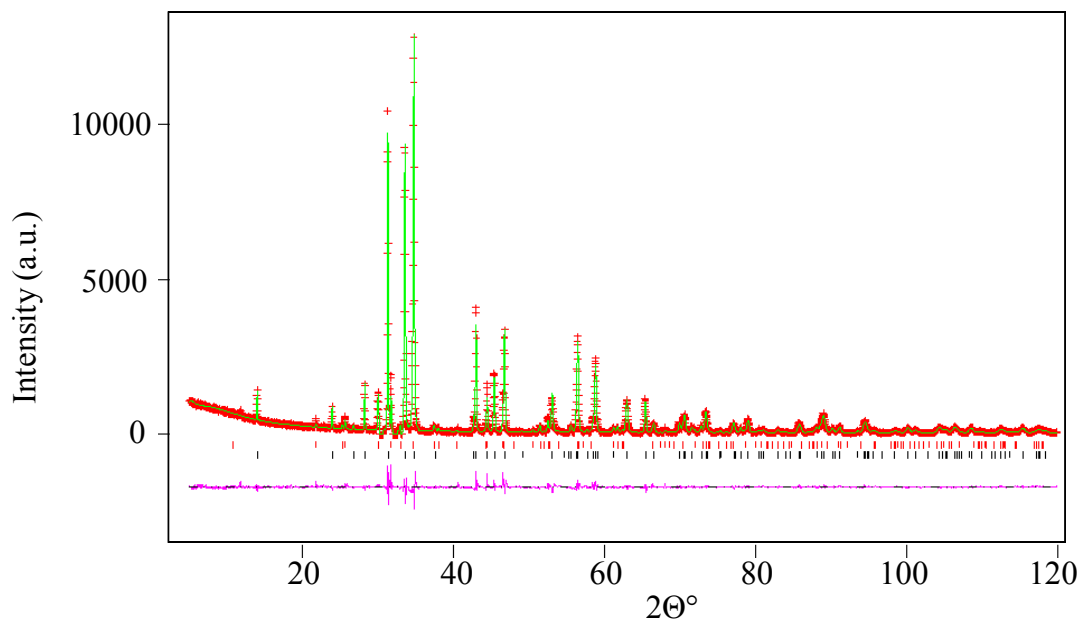
Figure 3.46: X-ray powder diffraction profiles of $Sr_{1.5}Ca_{0.5}CuO_3$ from 2nd extraction of CO_2 from $Sr_{1.75}Ca_{0.25}CuO_2(CO_3)$ under O_2. This shows observed (red crosses), calculated (green) and difference (purple) patterns. Ticks belong to $Sr_{1.5}Ca_{0.5}CuO_3$ (black) and $Sr_{0.82}Ca_{0.18}CuO_2$ (red).

The occupancy of strontium and calcium showed that $Sr_{1.5}Ca_{0.5}CuO_3$ had been prepared with $Sr_{0.88}Ca_{0.12}CuO_2$ from the 1st, and $Sr_{0.82}Ca_{0.18}CuO_2$ from the 2nd reverse reactions. The quantification of each phase, as well as the R-values from these refinements are presented in Table 3.25.

Table 3.25: Quantification of different phases, as well as R-values for the 1st and 2nd reverse reactions under O_2.

Reverse reaction	$Sr_{1.5}Ca_{0.5}CuO_3$ %	$Sr_{0.88}Ca_{0.12}CuO_2$ %	R_{wp}	R_p
1	92.5 ± 0.05	7.5 ± 0.02	14.33	9.84
Reverse reaction	$Sr_{1.5}Ca_{0.5}CuO_3$ %	$Sr_{0.82}Ca_{0.18}CuO_2$ %	R_{wp}	R_p
2	88.7 ± 0.07	11.3 ± 0.02	11.58	7.77

As seen with the reverse reactions under air, a mixture of re-formed $Sr_{1.5}Ca_{0.5}CuO_3$ and $Sr_{1-x}Ca_xCuO_2$ had been prepared. Despite the excess of O_2 a full re-formation of $Sr_{1.5}Ca_{0.5}CuO_3$ is not favoured, as other cuprate based compounds were also formed. Quantity of secondary

phases also increased under O_2 in comparison with that in air.

Analysis from the 3rd reverse reaction sample showed three phases present in the PXRD pattern. These phases were identified as $Sr_{1.75}Ca_{0.25}CuO_3$, $Sr_{0.85}Ca_{0.15}CuO_2$ and $Sr_2CuO_2(CO_3)$. The quantification of each phase, as well as the strontium and calcium compositions were determined with the refinement pattern shown in Figure 3.47. The initially phases used for the refinement were $Sr_{1.5}Ca_{0.5}CuO_3$ and $SrCuO_2$.[216,][220] When the occupancy of strontium and calcium were refined it showed the phases as $Sr_{1.75}Ca_{0.25}CuO_3$ and $Sr_{0.85}Ca_{0.15}CuO_2$, present alongside $Sr_2CuO_2(CO_3)$.
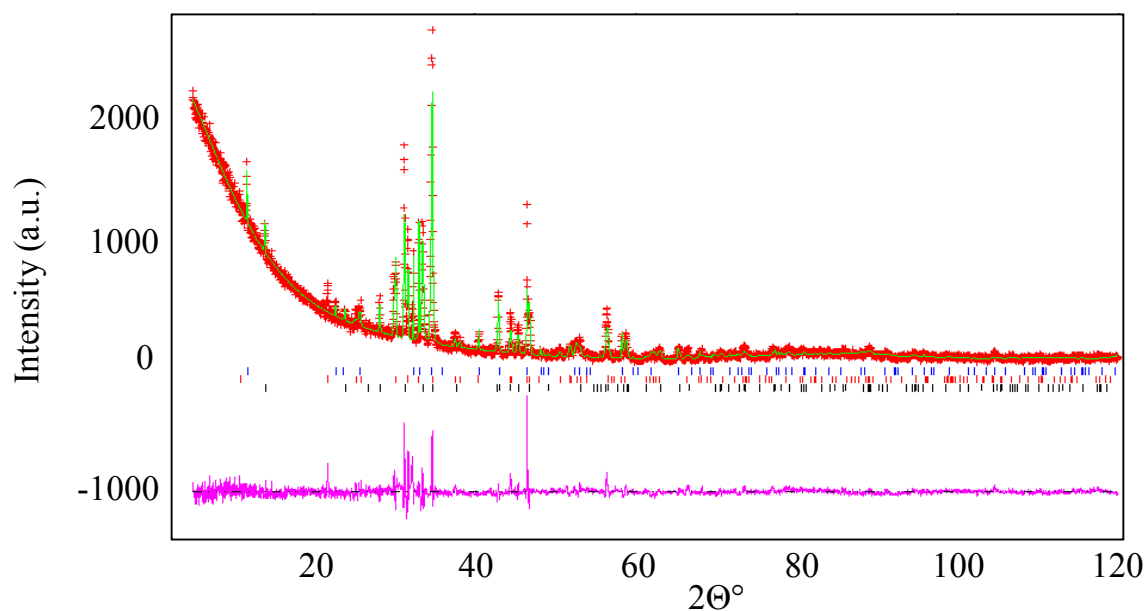
Figure 3.47: X-ray powder diffraction profiles of $Sr_{1.5}Ca_{0.5}CuO_3$ obtained from 3rd extraction of CO_2 from $Sr_{1.75}Ca_{0.25}CuO_2(CO_3)$ under O_2. This shows the observed (red crosses), calculated (green) and difference (purple) patterns. The tick belong to $Sr_{1.75}Ca_{0.25}CuO_3$ (black), $Sr_{0.85}Ca_{0.15}CuO_2$ (red) and $Sr_2CuO_2(CO_3)$ (blue).

Refinement of the 3rd reverse cycle sample calculated R-values of $R_{wp} = 9.7$ % and $R_p = 6.2$ %. It was found that the occupancy of calcium within $Sr_{1.5}Ca_{0.5}CuO_3$ had changed with the composition now being $Sr_{1.75}Ca_{0.25}CuO_3$ (52.11 $\pm$ 0.83) alongside $Sr_{0.75}Ca_{0.25}CuO_2$ (36.83 $\pm$ 0.42) and $Sr_2CuO_2(CO_3)$ (11.05 $\pm$ 0.68). The reverse reactions under O_2 were found to be less successful at driving the reaction towards re-forming $Sr_{1.75}Ca_{0.25}CuO_3$ than air. This has been assessed through comparing the quantities of $Sr_{1.5}Ca_{0.5}CuO_3$ prepared after the 1st

and 2nd reverse cycles under each gas in Table 3.26.

Table 3.26: A comparison of the quantities of $Sr_{1.5}Ca_{0.5}CuO_3$ prepared from the 1st and 2nd reverse cycles under air and O_2.

Reverse reaction 1	Air (1)	O_2 (2)	Difference (1) - (2)
$Sr_{1.5}Ca_{0.5}CuO_3$ (%)	94.6	92.5	2.1
Reverse reaction 2	Air (1)	O_2 (2)	Difference (1) -(2)
$Sr_{1.5}Ca_{0.5}CuO_3$ (%)	95.9	88.7	7.2

For the 3rd reverse cycles under O_2, $Sr_{1.75}Ca_{0.25}CuO_3$ was prepared at only 52.1% of the overall sample. This is compared to the 3rd reverse cycle under air with $Sr_{1.5}Ca_{0.5}CuO_3$ accounting for 85.1 %. These results show that in all reverse cycles, calcium is shared across different phases with the exception of the 1st under air. This was from the formation of $Sr_{1.5}Ca_{0.5}CuO_3$ alongside a $Sr_{1-x}Ca_xCuO_2$ phase. Synthesis of $Sr_{1-x}Ca_xCuO_2$ compounds can be carried out via reacting stoichiometric amounts of ACO_3 (A = Sr and Ca) and CuO between 800 - 1100 °C.[224–226] When $Sr_{1.75}Ca_{0.25}CuO_2(CO_3)$ is prepared $SrCaCuO_3$ and $SrCO_3$ are also present. It maybe that during the reverse cycles these multiple phases are reacting with one another giving $Sr_{1.75}Ca_{0.25}CuO_3$. The reverse reactions under O_2 has seen re-formation of $Sr_{1.5}Ca_{0.5}CuO_3$ to be less favoured compared to air with reasons unclear. This in turn has effected the reactivity for re-forming the oxide carbonate as well seen previously in Figure 3.42.

The incorporation of calcium in the precursor compound ($Sr_{1.5}Ca_{0.5}CuO_3$) to react with CO_2 has resulted in a change of reaction conditions when compared to Sr_2CuO_3. The incorporation reaction required heating $Sr_{1.5}Ca_{0.5}CuO_3$ under CO_2 for 90 as opposed to 15 minutes. In the case of the reverse reactions it has been found that under air or O_2 when attempting to extract CO_2 and re-form $Sr_{1.5}Ca_{0.5}CuO_3$, a secondary phase of $Sr_{1-x}Ca_xCuO_2$ is present. This maybe due to the fact that as $Sr_{1.75}Ca_{0.25}CuO_2(CO_3)$ is formed along side $SrCaCuO_3$ and $SrCO_3$. This has the reverse reactions favouring the preparation of $Sr_{1-x}Ca_xCuO_2$ compounds alongside $Sr_{1.5}Ca_{0.5}CuO_3$. It was also found that whilst under O_2 that Sr_2CuO_3 re-formation was slightly more favoured from the excess oxygen than compared to air. In the

case of $Sr_{1.5}Ca_{0.5}CuO_3$ the excess amount of O_2 made re-formation more difficult. Therefore for $Sr_{1.5}Ca_{0.5}CuO_3$ re-formation under air is the preferred gas type.

3.8 Conclusion

This part of the work presents a novel concept of anion vacancies present within solids being used to utilise CO_2 towards mixed anion compounds. A variety of A_2CuO_3 (A = Sr, Ca and Ba) compounds have been investigated to react with CO_2 towards novel oxide carbonates based on the formula $Sr_{2-x}A_xCuO_2(CO_3)$ (A = Ba and Ca). The $Sr_{2-x}Ca_xCuO_3$ ($0 \leq x \leq 2$) series was heated using an alternating gases process between air and CO_2, whilst the $Sr_{2-x}Ba_xCuO_3$ series required O_2 instead of air. In all reactions the starting compounds were heated to 1000 °C, then once at a stable temperature the gas was switched to CO_2. In the case of Sr_2CuO_3 and $Sr_{1.8}Ba_{0.2}CuO_3$ reactions under CO_2 required 15 minutes towards the desired oxide carbonate. $Sr_{1.5}Ca_{0.5}CuO_3$ however, required a longer reaction of 90 minutes.

The 1st set of reactions with Sr_2CuO_3 towards $Sr_2CuO_2(CO_3)$ acted as a case study of an alternating gases method to prepare desired compounds. This methodology was then applied towards formation of $Sr_{1.8}Ba_{0.2}CuO_2(CO_3)$ and $Sr_{1.5}Ca_{0.5}CuO_2(CO_3)$, which is to the author's knowledge the first compound to exist within the $Sr_{2-x}Ca_xCuO_2(CO_3)$ series.

Re-forming of the starting materials, Sr_2CuO_3, $Sr_{1.8}Ba_{0.2}CuO_3$ and $Sr_{1.5}Ca_{0.5}CuO_3$, has been studied under air and O_2 gas. These reverse reactions were carried out over multiple cycles to repeatedly insert and extract CO_2. This was possible for all compounds with degenerations occurring over time. In the case of Sr_2CuO_3 and $Sr_{1.8}Ba_{0.2}CuO_3$ reverse reactions under O_2 were found to be the most successful. This was not however in the case of $Sr_{1.5}Ca_{0.5}CuO_3$ where air proved to be more successful at removing CO_2 and re-forming the oxide.

Chapter 4

Direct reaction of $Sr_{2-x}Ba_xPdO_3$ (x = 0 – 2) and Ce_2MnN_3 with CO_2

4.1   Anion-deficient compounds for reacting with CO_2

This research project has studied the reaction of anion-deficient compounds for utilising CO_2, towards preparing complex inorganic materials. In particular the $Sr_{2-x}A_xCuO_3$, $0.5 \leq x \leq 2$ (A = Ba and Ca) series, described as anion-deficient equivalents of K_2NiF_4 have been studied (Chapter 3). This chapter describes the direct reaction of compounds isostructural to $Sr_{2-x}A_xCuO_3$, i.e $Sr_{2-x}A_xPdO_3$ (A = Ba) and Ce_2MnN_3 with CO_2.

4.1.1 $Sr_{2-x}Ba_xPdO_3$ (0 $\leq$ x $\leq$ 2)

The alkaline earth palladates Sr_2PdO_3 and Ba_2PdO_3, are classed as having one-dimensional crystal structures with chains of square planar corner-linked PdO_4. Both of these compounds have body centred orthorhombic crystal systems with an *Immm* space group. These palladates are isostructural to the cuprates Sr_2CuO_3 and Ca_2CuO_3, hence they have a Ln_2CuO_4-type structures which lack oxides along the *c* axis.[88, 196] The structures of the $Sr_{2-x}A_xCuO_3$ and $Ba_{2-x}Sr_xPdO_3$ are compared to one another in Figure 4.1.
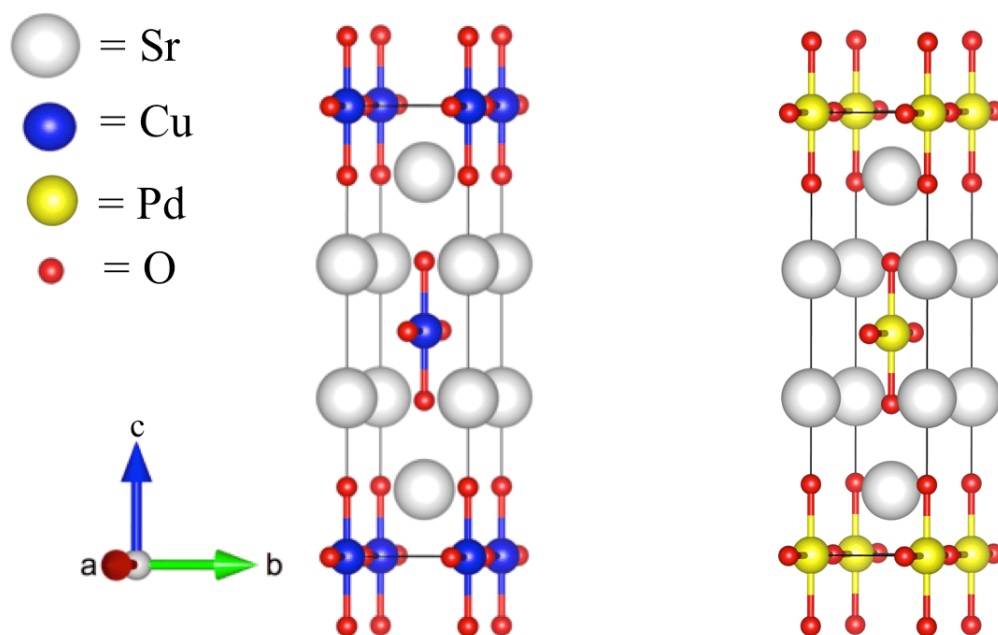
Figure 4.1: Structures of the $Sr_{2-x}A_xCuO_3$ (A = Ba and Ca) (left) and $Ba_{2-x}Sr_xPdO_3$ (right) series compared to one another showing their similarities.

Sr_2PdO_3 and Ba_2PdO_3 were originally reported by H. D. Wasel-Nielen and R Hopper*et al.* and Y. Laligant respectively.[227, 228] The unit cell parameters for each compound are presented within Table 4.1 (the values for Sr_2PdO_3 were also reported without errors).

Table 4.1: The unit cell parameters and space groups of Ba_2PdO_3 and Sr_2PdO_3.

Compound	Space group	$a(\text{Å})$	$b(\text{Å})$	$c(\text{Å})$	$V(\text{Å}^3)$
Ba$_2$PdO$_3$	*Immm*	3.8362(4)	4.080(5)	13.335(2)	208.72
Sr$_2$PdO$_3$	*Immm*	3.977	3.530	12.820	179.98

The complete replacement of strontium for barium within the palladate structure shows an expansion of the overall volume by almost 30 Å^3. This is due to the size difference of the Ba^{2+} ions (1.38 Å) compared to that of Sr^{2+} (1.21 Å), when both have a coordination number of 7.[219] Even through complete cation substitution of the strontium for barium, the palladate structure has been expanded without the crystal system and symmetry being changed. Baikie

179

et al. prepared the solid-state solution series of $Sr_{2-x}Ba_xPdO_3$ ($0.5 < x < 2$) by reacting stoichiometric quantities of $SrCO_3$ and $BaCO_3$ with PdO.[98, 99] These compounds were then used for anion insertion via fluorination to prepare the $Sr_{2-x}Ba_xPdO_2F_2$ series of compounds.

Cation substitution of the Pd sites has been carried out by Nagata *et al.* towards preparing the $Sr_2Pd_{1-x}A_xO_3$ (A = Cu and Co) series of compounds and studying the differences in the magnetic behaviour.[229] For each of these solid-state solutions, substitution of Pd with either Co or Cu showed no change towards the type of crystal structure.

In regards to the magnetic behaviour, the introduction of copper shows an increase in the magnetic moment and lowering of the magnetic resistance of Sr_2PdO_3 at a maximum of x = 0.2. Above this value the effective magnetic moment starts to decrease.[229]

Although palladium is limited within these compounds to a coordination state of 4, the presence of Ba-O groups can be beneficial for reacting with CO_2. The affinity of alkaline earth metal oxides, AO (A = Mg, Ca, Sr and Ba) to form carbonates increases when going down the series.[122] This is due to an increase in the basicity of the metal oxide group, which is attracted to the Lewis acidic CO_2. The ionic radii of Ba^{2+} is also larger than that of Sr^{2+} which could result in the crystal structure also allowing more CO_2 to be incorporated and to be reacted.[219]

Only 1 Ba-Pd oxide carbonate is known, $Ba_{11}Pd_{11}O_{20}(CO_3)_2$, and was reported by Crooks and Weller.[230] This was prepared by the direct reaction of $BaCO_3$ with PdO under a O_2/CO_2 gas mixture. This compound has also been described as having a "BaPdO_2" type structure, from the ratio between the cations and anions. In the crystal structure of $Ba_{11}Pd_{11}O_{20}(CO_3)_2$, palladium maintains its square planar coordination as in Ba_2PdO_3 with the carbonates having no coordination towards the palladium. Although distortion of the polyhedra is observed.

By taking into consideration that the $Sr_{2-x}Ba_xPdO_3$ series can accommodate additional anions as shown by Baikie *et al.*,[99] as well as the affinity for Ba-O groups to react and form $BaCO_3$, the $Sr_{2-x}Ba_xPdO_3$ series was investigated in reactions with CO_2, in the same way as the cuprate series with the aim at to prepare the proposed series of "$Sr_{2-x}Ba_xPdO_2(CO_3)$" compounds.

4.1.2 Ce_2MnN_3

Ce_2MnN_3 was first reported by Niewa *et al.*, and using PXRD methods was found to be isostructural to the $Sr_{2-x}Ca_xCuO_3$ and $Ba_{2-x}Sr_xPdO_3$ (x = 0 − 2) series of compounds.[102] In Ce_2MnN_3 the Mn cation is coordinated to 4 anions, forming a near square planar arrangement. These form corner linked linear chains that run along the crystal structure as shown in Figure 4.2. This same type of arrangement is also present for the copper and palladium sites in the cuprates, and palladates respectively. Niewa *et al.* however, reported that the MnN_4 polyhedra groups are not in an ideal square planar arrangement. This is due to the length of the Mn-$N_{bridging}$ bonds being 1.88 Å, whilst the Mn-$N_{terminal}$ bonds are 2.04 Å.
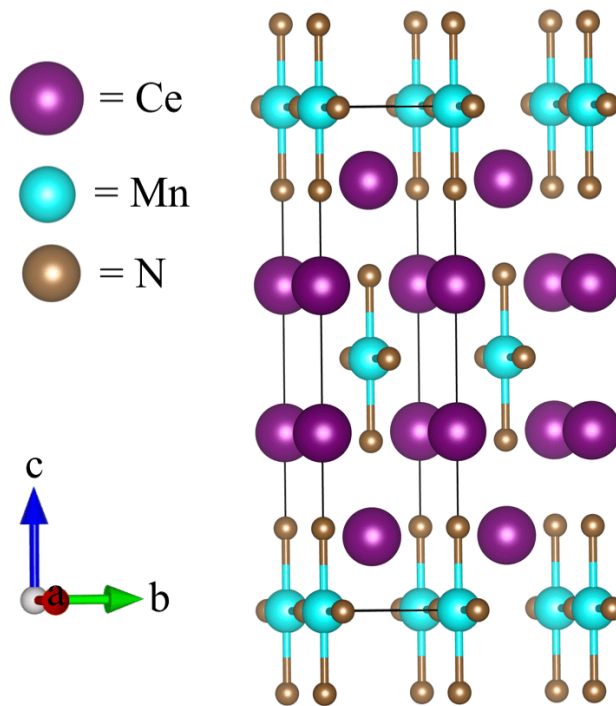
Figure 4.2: The unit cell structure of Ce_2MnN_3 showing bridging MnN_4 groups.

Ce_2MnN_3 is described as a one-dimensional anion-deficient K_2NiF_4-type ternary nitride. Ternary nitrides are defined as compounds which contain two different types of metals as well as the nitride anion N^{3-}. As for the oxidation state of the cations, cerium can potentially adopt either a 3+ or 4+ oxidation state. Investigations by Niewa *et al.* using Linear Muffin Tin Orbital (LMTO) theory and X-ray Adsorption Spectroscopy, (XAS) have indicated that Ce^{4+} is present within this compound resulting in the following charges, $Ce_2^{+4}Mn^{+1}N_3^{3-}$.

As a result of the similarities between Ce_2MnN_3 and the $Sr_{2-x}Ca_xCuO_3$ and $Ba_{2-x}Sr_xPdO_3$ (x = 0 – 2) series of compounds, anion incorporation has also been investigated. Headspith *et al.* were able to not only develop a novel route of preparing the mixed metal nitride, but was also able to insert fluorides within the structure to prepare the fluoride nitride compound $Ce_2MnN_3F_{2-\delta}$.[104] It was found that this anion-insertion resulted in the coordination number of Mn expanding from 4 to 6. This is similar to the coordination number of copper expanding within the cuprate series from F^- incorporation.[92]

The formation of $Ce_2MnN_3F_{2-\delta}$ was possible from the direct insertion of fluorides into the structure of Ce_2MnN_3 (Figure 4.3), via a solid-gas reaction with F_2 and a mixture of 10 % F_2 in N_2. A study of the structural refinement and magnetic moments showed that the coordination of Mn had expanded and the oxidation state had also changed, resulting in a suggested mixture of $Mn^{2/3+}$.
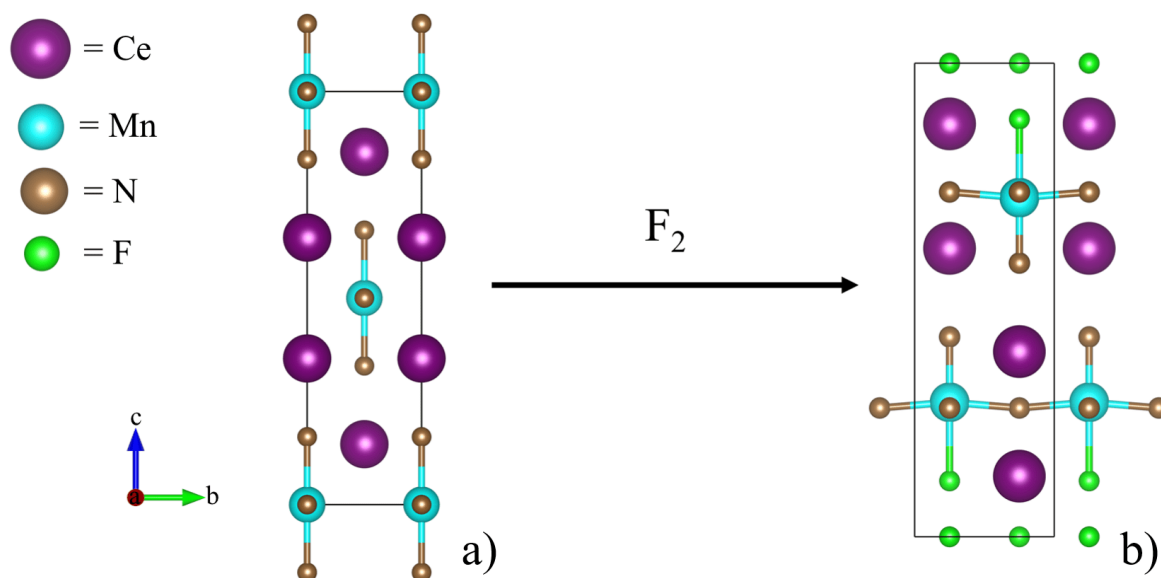
Figure 4.3: The crystal structure of a) Ce_2MnN_3 and b) $Ce_2MnN_3F_{2-\delta}$ formed from F^- incorporation.

This process of fluorination was also carried out in a similar manner used for Sr/Ca_2CuO_3 and Ba/Sr_2PdO_3 series via a solid-gas reaction. The difference however for Ce_2MnN_3, is that it involves only anion insertion of F^- and not substitution to form $Ce_2MnN_3F_{2-\delta}$.

Representations of the unit cells of Ce_2MnN_3 and Sr_2CuO_3 are presented in Figure 4.4, while

unit cell parameters are given in Table 4.2.[102, 88] Along the c-axis the B cations (Cu or Mn) are both coordinated to the anions (O or N) to form a square planar array. These SrO/CeN interlayers have also been described as having a NaCl, rock-salt type structure.
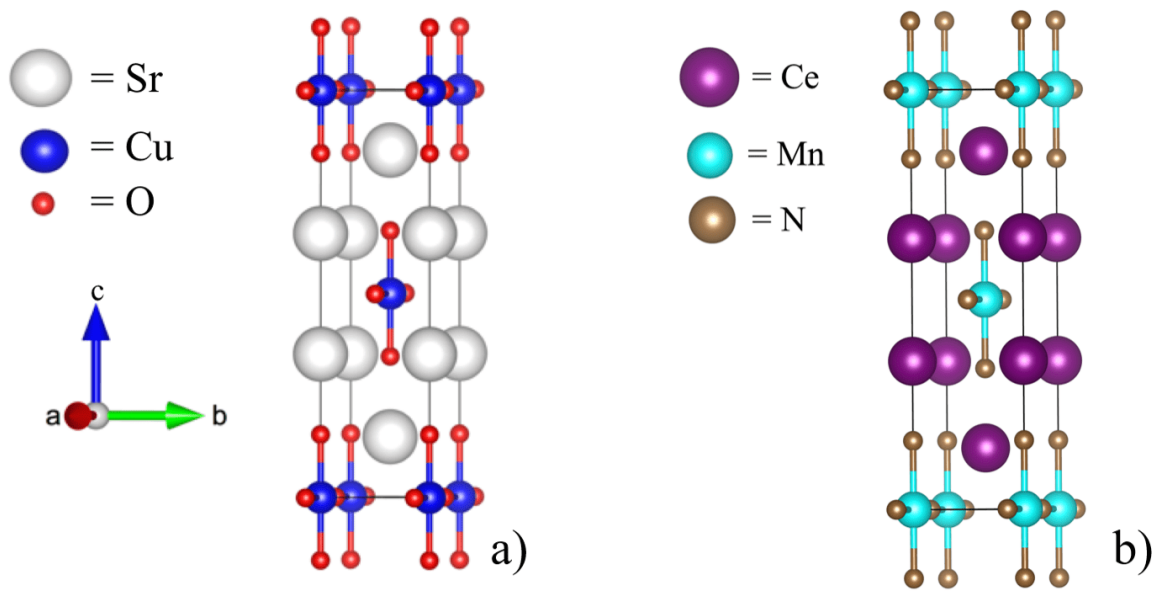
Figure 4.4: A comparison of the unit cell structures of a) Sr_2CuO_3 and b) Ce_2MnN_3 which are isostrucutral to one another.

Table 4.2: The unit cell parameters and cell volume of Sr_2CuO_3 and Ce_2MnN_3 along with their space groups.

Compound	Sr_2CuO_3 [88]	Ce_2MnN_3 [102]
a Å	3.9089(2)	3.7499(2)
b Å	3.4940(2)	3.445(2)
c Å	12.6910(7)	12.4601(9)
V Å^3	173.330(11)	160.9482(2)
Space group	*Immm*	*Immm*

Due to Ce_2MnN_3 being both isostructural to Sr_2CuO_3 and being able to incorporate additional anions within its structure ($Ce_2MnN_3F_{2-\delta}$), this compound has been investigated for reacting with CO_2 to prepare mixed anion compounds. It was shown that Mn could expand its

coordination number towards incorporating CO or alternatively NCO type groups as the existence of $Mn(NO)(CO)_4$ has also been reported.[231] The methodology of reacting Ce_2MnN_3 would follow the same procedure for Sr_2CuO_3 with alternating gases. However, nitrogen would be used instead of air, due to the oxygen sensitivity of Ce_2MnN_3.

For Ce_2MnN_3 reacting with CO_2, the type of end product must be considered. It is possible that at high temperatures CO_2 can react within the mixed metal nitride forming a cyanate (NCO^-) group within the structure. As mentioned previously, Ce_2MnN_3 has been found to have a similar anionic structure to that of the A_2CuO_3, (A = Sr, Ba and Ca) series. These alkaline earth metals have also been found to form an array of cyanate compounds in the form of $Sr(OCN)_2$, $Ba_3(O_3C_3N_3)_2$ and $Ca_3(C_6N_6O_6)$.[232–234] It is possible that Ce_2MnN_3 could react with CO_2 forming a novel $Ce_2MnN_{3-x}(NCO)_x$ series of compounds.

Metal carbide surfaces have also been able to capture CO_2. The series of MC (M = Ti, Zr, Hf, Nb, Ta, Mo) are able to react with CO_2 via the creation of M-O and C-C bonds.[235] The charge transfer of the CO_2 on to the surface also indicates activation is taking place. The bond angle and lengths of CO_2 are also shifted which makes the structure resemble that of a carbonate and makes it lose its original linear shape.

4.2 Experimental

4.2.1 Synthesis

The $Sr_{2-x}Ba_xPdO_3$ (x = 0, 0.5, 1 and 1.5) series was prepared via a high temperature ceramic method adapted from Baikie *et al.*.[99] This involved using polycrystalline reagents of $SrCO_3$ (98.5% BDH GPR), $BaCO_3$ (98.5% BDH GPR) and PdO (96.0% BDH GPR) which were also stored in a oven at approximately 100 °C to prevent moisture contamination. The reagents were weighted in stoichiometric ratios towards preparing 1g of product, and then placed in a mortar and mixed with a pestle until homogeneous. The synthesis was carried out following the reaction scheme in Equation 4.1:

$$2\text{-x SrCO}_3 + \text{x BaCO}_3 + \text{PdO} \rightarrow \text{Sr}_{2-x}\text{Ba}_x\text{PdO}_3 + 2\,\text{CO}_2 \qquad (4.1)$$
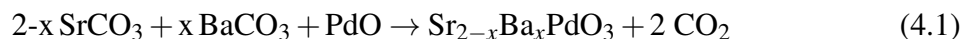
These reagents were then placed into an aluminia crucible and inserted into a box furnace for initial heating at 700 °C for 24 hours in air. This was to allow $SrCO_3$ and $BaCO_3$ to lose CO_2 and form SrO and BaO which could immediately react in-situ with PdO. The temperature of 700 °C was used as this is below that of 750 °C, which is the decomposition temperature of PdO to Pd metal. After this, a 2nd heating cycle was carried out at 1150 °C for 50 hours. The purity of the resulting compounds were confirmed with PXRD analysis. Once the purity and structure of the compounds were determined they were then used for reacting with CO_2 gas.

A pre-weighted sample of $Sr_{2-x}Ba_xPdO_3$ (x = 0 − 2), at approximately 50 mg was placed into an alumina crucible then inserted into the TGA furnace chamber. The samples were initially heated to 1000 °C under air to prevent decomposition into Ba/$SrCO_3$. The temperature was then maintained for 2 minutes to reach equilibrium before the gas flow was changed to pure CO_2. After a 15 minute isotherm at 1000 °C, the gas was then switched back to air for the sample to cool to room temperature.

The formation of Ce_2MnN_3 was carried out following the same experimental procedure outlined by Headspith et al..[104] A stoichiometric amount of Ce and Mn metal was measured to prepare a specific mass of product in an Ar filled glove box. This mixture was then placed into a alumina crucible and inserted into a quart tube with sealed taps before being removed from the glove box. The quartz tube was then placed into an upright furnace and connected to a nitrogen supply to prevent any oxygen contamination. The system was then flushed with nitrogen for several minutes and then heated to 900 °C to react for 36 hours. After the reaction the nitrogen filled tube was taken into the glove box for the sample to be prepared for analysis. A small amount of the sample was placed onto a zero-background Si crystal sample holder covered in a thin layer of paraffin oil for PXRD analysis. The oil covering the sample acts to prevent Ce_2MnN_3 reacting with oxygen and moisture in the atmosphere and to be transferred to the sample selector in the X-ray diffractometer for PXRD analysis. All scans were carried out from 2 to 80 ° however the peaks below 30 ° that belonged to the oil were removed.

Due to the air sensitivity of Ce_2MnN_3, nitrogen was used instead of air for the heating

and cooling steps to study the reaction of the compound with CO_2 at specific temperatures. Similarly to the method for Sr_2CuO_3, the sample was heated to a desired temperature (1000 °C) under nitrogen, allowed to reach equilibrium and then CO_2 was introduced for 15 minutes. The amount of sample used for each reaction was always weighted to approximately 40 mg for consistency.

The reaction process between the samples and CO_2 could be monitored using thermal gravimetric analysis, TGA. This allowed the change in the mass as CO_2 is reacting with the solid to be monitored. The heating and cooling rate used during the reactions was that of 100 °C/min, with the flow rate for all gases set to 100 ml/min.

4.2.2 Charaterisation

4.2.2.1 Thermogravimetric analysis (TGA)

Thermogravimetric analysis (TGA) was carried out using a Metler Toledo TDA/DSC 1Star System which showed the sample mass changing at different temperatures and gases. CO_2, N_2 and air atmospheres were used. All gas flow rates were maintained at a value of 100 ml/min and the temperature ramp rate was at 100 °C/min. A standard reaction would involve inserting a single sample into the TGA furnace at room temperature to be exposed to the gaseous atmosphere before heating. The overall change in mass of the sample was determined through subtracting the value at the start of the reaction, to that at the end of the reaction when the mass of the sample was allowed to reach equilibrium. This was to give a quantitative value of the amount of CO_2 utilised in the oxide or nitride.

4.3 Results and discussion

4.3.1 $Sr_{2-x}Ba_xPdO_3$ (x = 0 – 2) series

4.3.1.1 $Sr_{2-x}Ba_xPdO_3$ (x = 0 – 2) preparation

The synthesis of strontium palladate resulted in a dark brown polycrystalline product. The identity of the sample was confirmed using PXRD analysis with the pattern of Sr_2PdO_3, Figure 4.5 showing the synthesis of a single phase as being successful. This pattern was indexed to an orthorhombic cell with parameters $a = 3.9789(9)$ Å, $b = 3.531(1)$ Å and $c = 12.824(3)$ Å and a volume of 180.16 Å^3. These values were found to be in agreement with the cell reported by Muller and Roy with parameters of $a = 3.9700$ Å, $b = 3.5440$ Å, $c = 12.8400$ Å and a volume of 180.65 Å^3.[236]
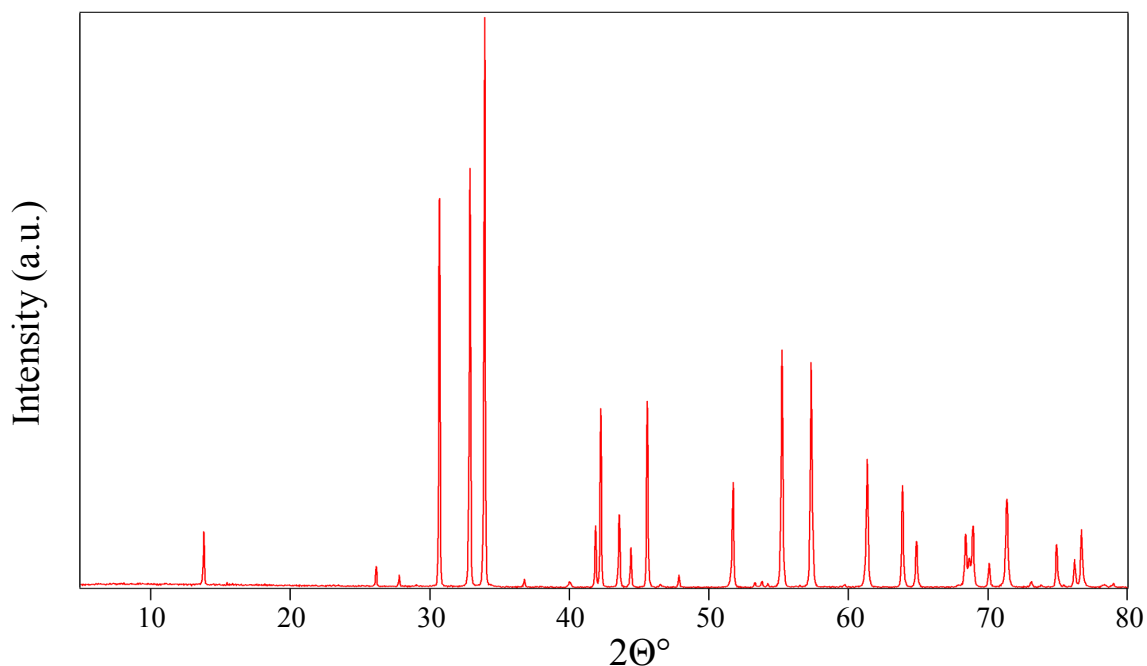
Figure 4.5: PXRD pattern of Sr_2PdO_3, used to confirm its identification.

The synthesis of the $Sr_{2-x}Ba_xPdO_3$ (x = 0 – 2) series was carried out using the same method as with Sr_2PdO_3 and Ba_2PdO_3. The PXRD patterns showed that the $Sr_{2-x}Ba_xPdO_3$ (x = 0, 0.3, 0.4 0.5 and 2) series had been prepared by using stoichiometric quantities of $BaCO_3$ and

$SrCO_3$. The following series of $Sr_{2-x}Ba_xPdO_3$ (x = 0.3, 0.4 and 0.5) have been prepared with the PXRD diffractogram in Figure 4.6.
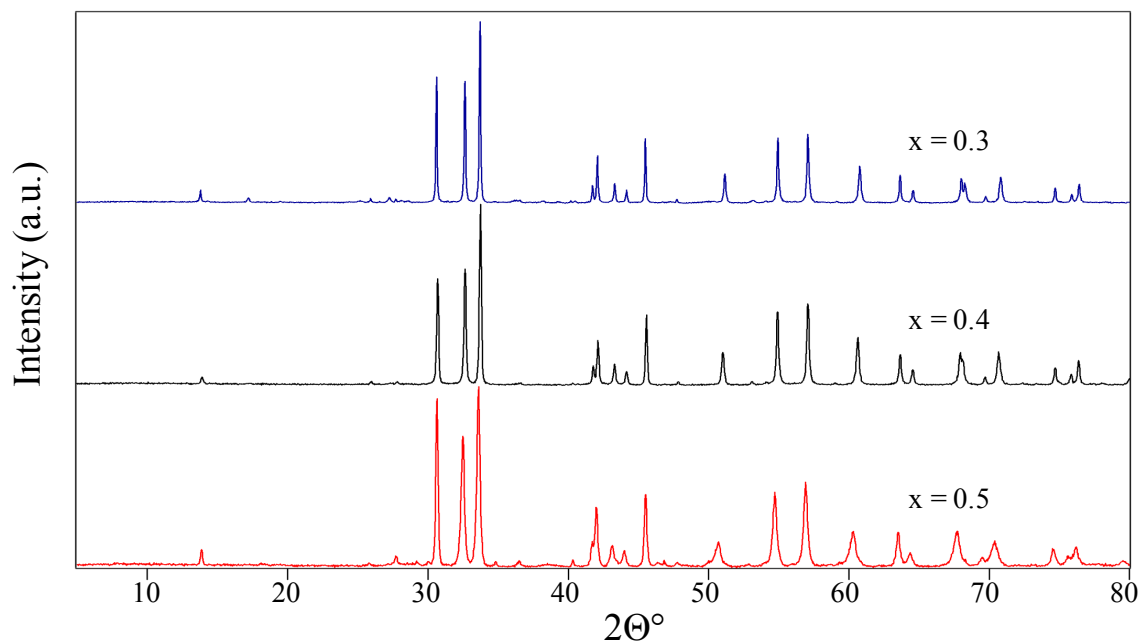
Figure 4.6: PXRD patterns of the $Sr_{2-x}Ba_xPdO_3$ series with x = 0.3, 0.4 and 0.5.

The increase in the barium content resulted in the unit cell of the crystal structure increasing along the series. The increasing unit cell parameters with the increased barium content is shown in Table 4.3. As with Sr_2PdO_3, the solid-solution compounds had their unit cells indexed using the model from Muller and Roy.[236]

Table 4.3: The lattice parameters of the $Sr_{2-x}Ba_xPdO_3$ (x = 0 − 2) series of compounds.

x	$a(\text{Å})$	$b(\text{Å})$	$c(\text{Å})$	$V(\text{Å}^3)$
0.0	3.979(1)	3.531(1)	12.824(3)	180.16
0.3	3.987(1)	3.569(1)	12.885(4)	183.35
0.4	3.985(3)	3.579(3)	12.890(8)	183.87
0.5	3.991(5)	3.601(5)	12.93(1)	185.81
2.0	3.822(2)	4.071(2)	13.288(6)	206.93

This series of compounds can be used to monitor and compare how the increase in barium

content affects the reactivity of the palladates towards CO_2.

The identity of the product was confirmed using PXRD analysis with the pattern (Figure 4.7), showing single phase Ba_2PdO_3. The pattern was indexed to an orthorhombic cell with parameters a = 4.071(2) Å, b = 3.822(2) Å and c = 13.288(6) Å and a volume of 206.93 Å^3. This is in good agreement with the cell reported by Laligant *et al.* with parameters a = 4.0804(5) Å, b = 3.8362(4) Å and c = 13.335(2) Å and volume = 208.72 Å^3.[228]
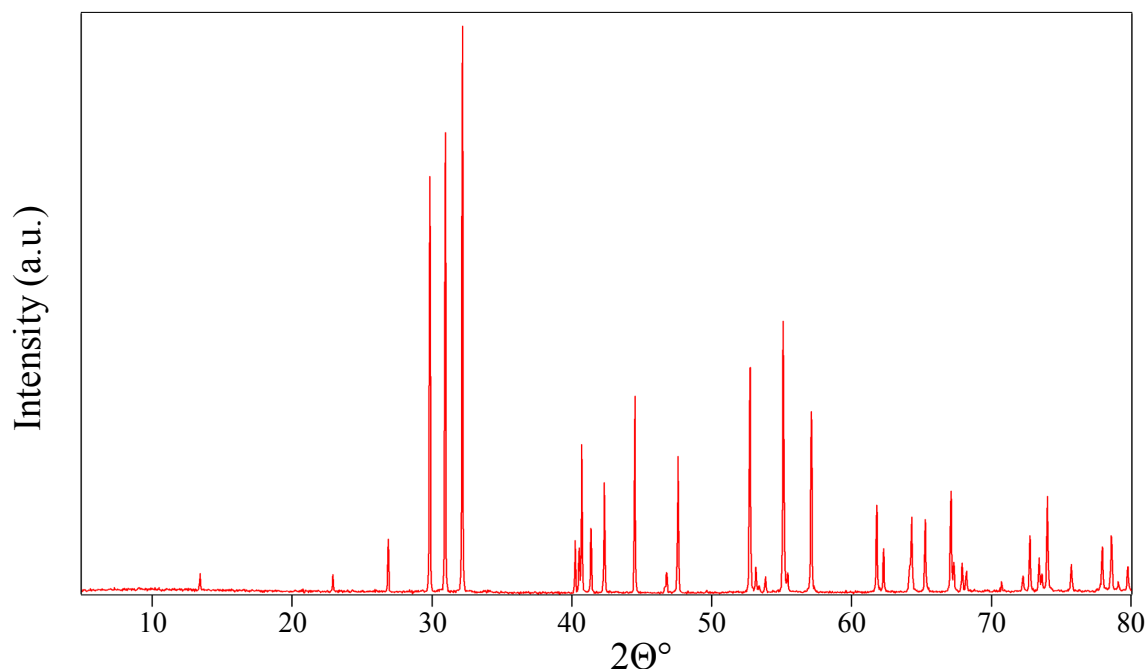
Figure 4.7: PXRD pattern of Ba_2PdO_3.

Once pure samples of the starting reagents had been prepared, the next step was to investigate their reactivity towards CO_2, as which was done with the cuprate series.

4.3.1.2 $Sr_{2-x}Ba_xPdO_3$ (x = 0 –2) reactions with CO_2

Using the same methodology as employed with the cuprate series, the samples of $Sr_{2-x}Ba_xCuO_3$ were reacted with CO_2 through alternating gases with air. Sr_2PdO_3 is isostructural to Sr_2CuO_3 with anion vacancies along the square planar PdO_4 chains. The purpose of these reactions was to investigate how changing the identity of the B cation (Pd for Cu) would affect the incorporation of CO_2.

The initial set of reactions were to determine the ideal conditions for Sr_2PdO_3 to react with CO_2 towards an oxide carbonate. The temperatures investigated were 700, 800 and 900 °C. The resulting PXRD patterns of these reactions show that Sr_2PdO_3 had decomposed to $SrCO_3$ and $SrPd_3O_4$.[237] A comparison of the PXRD patterns in Figure 4.8 shows that this process would start to occur at 700 °C when heated under CO_2. The amount of $SrCO_3$ would then increase at 800 °C, but was shown to decrease at 900 °C. The cause of this is potentially that at 900 °C the formation of $SrPd_3O_4$ is favoured with $SrCO_3$ reacting with PdO. The preparation of $SrPd_3O_4$ has been reported at temperatures of 900 °C when reacting $SrCO_3$ with PdO.[238]
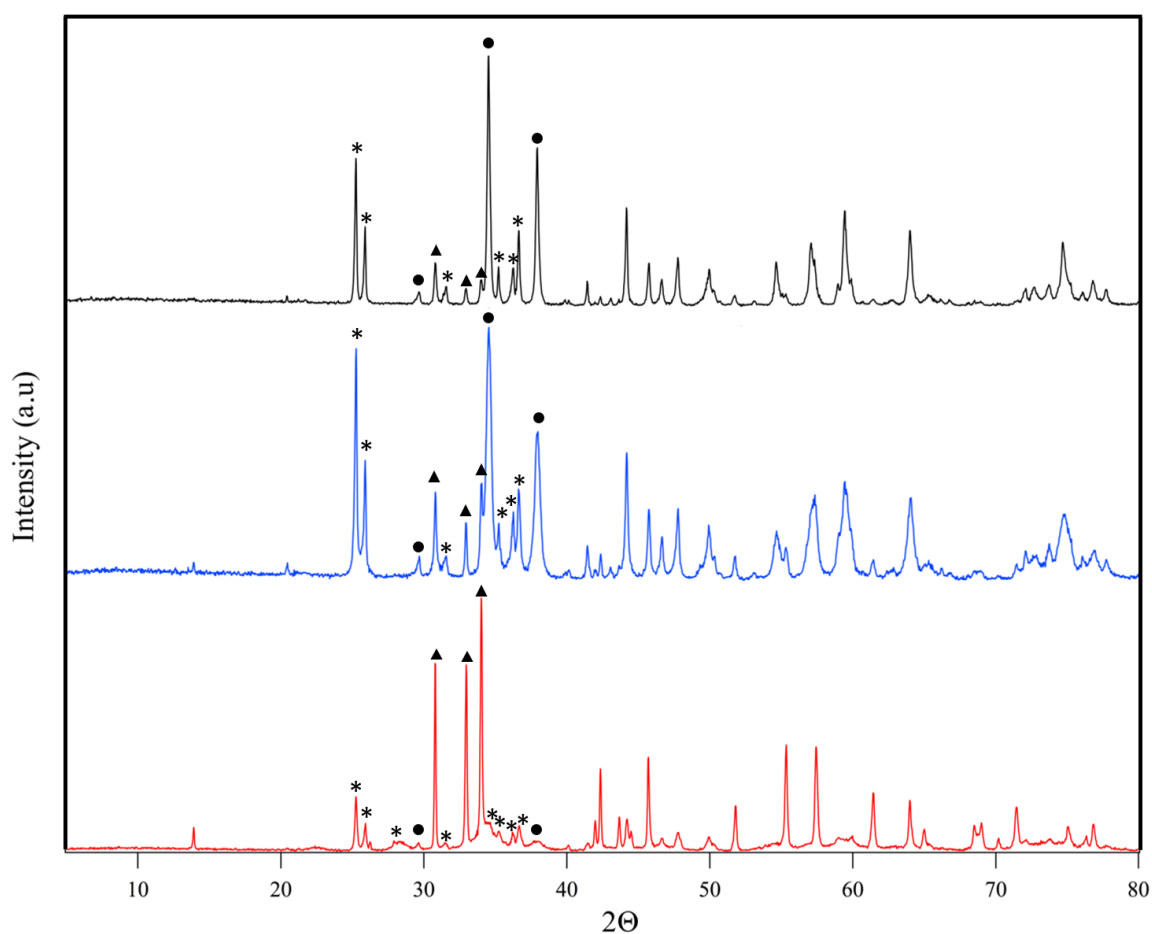
Figure 4.8: PXRD patterns of Sr_2PdO_3 heated under CO_2 at 700 °C (red) 800 °C (blue) and 900 °C (black). The peaks assigned are (*) $SrCO_3$, (▲) Sr_2PdO_3 and (●) $SrPd_3O_4$.

A temperature value of 1000 °C, the same temperature required for Sr_2CuO_3 to react with

CO_2 and form $Sr_2CuO_2(CO_3)$ was then investigated. The TGA curve showed no gain in mass from the reaction at 1000 °C. The sample was then analysed using PXRD (Figure 4.9) and compared to the pattern of Sr_2PdO_3 before the reaction with CO_2 and showed no signs of any structural changes.
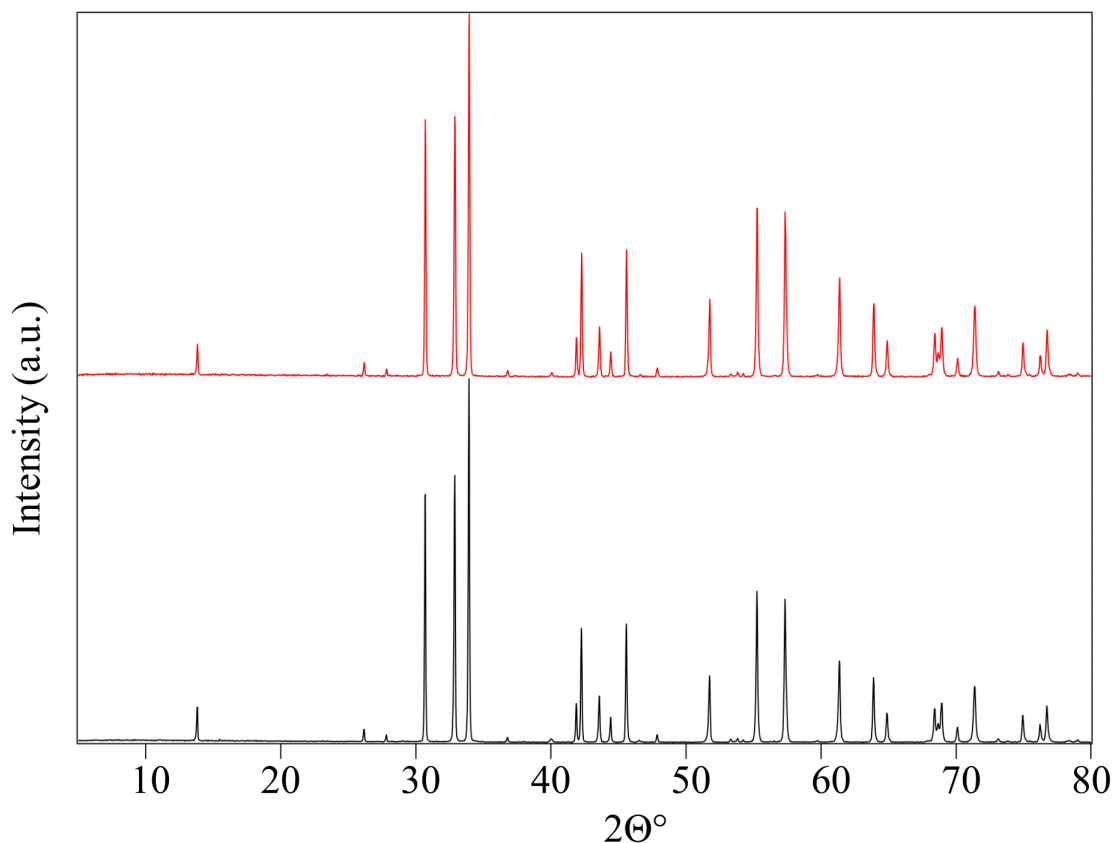
Figure 4.9: PXRD patterns of Sr_2PdO_3 (black) before and after (red) being heated under CO_2 at 1000 °C.

The use of FTIR spectroscopy confirmed the presence of $SrCO_3$ within the phase, with the spectrum shown in Figure 4.10.[130, 222, 239] Taking into accountant that this phase was not detected with PXRD, it is possible that $SrCO_3$ has been formed on the surface of the solid from the exposure to CO_2.
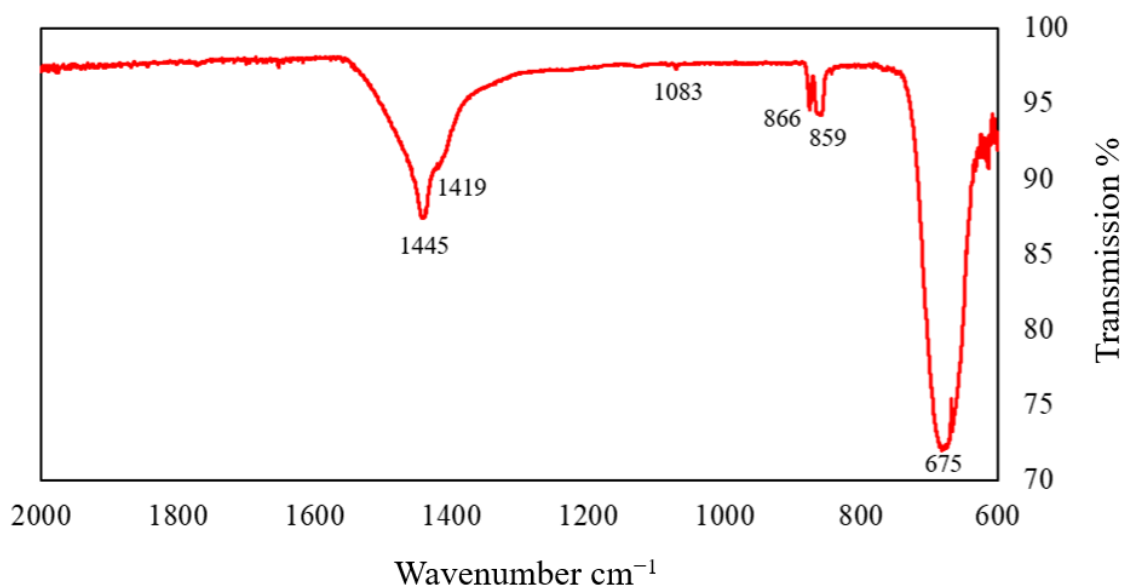
Figure 4.10: FTIR spectrum of Sr_2PdO_3 after reacting with CO_2 at 1000 °C.

The labeled peaks in the FTIR spectrum indicate that $SrCO_3$ is present when compared to the frequency values as reported by Krishnamurti.[222] There are however differences such as splitting observed for the symmetric bending at 866 and 859 cm^{-1}. It also appears that the asymmetric bending modes have combined into one band in the spectrum at 675 cm^{-1}. The PXRD results showed that Sr_2PdO_3 can either decompose under CO_2, below 1000 °C to form $SrCO_3$ and $SrPd_3O_4$. Or alternatively at 1000 °C have low reactivity towards CO_2. The TGA curve data confirms this hypothesis as below the maximum temperature (1000 °C) the mass of the sample increases under CO_2 as $SrCO_3$ is forming, whilst at 1000 °C no overall increase is observed at this temperature. The use of FTIR spectroscopy shows the presence of $(CO_3)^{2-}$, but this is likely only on the surface of Sr_2PdO_3 and not in the bulk.

Following these results the next step was to substitute strontium for barium within the palladates to see if any change in reactivity towards CO_2 happens. The expansion of the unit cell through barium incorporation, as well as the greater affinity of Ba-O to react with CO_2 could improve the reactivity of the palladate series of compounds. This series of compounds have previously been found to incorporate additional anions by Baikie *et al.* towards preparing the oxyfluoride series, $Sr_{2-x}Ba_xPdO_2F_2$.[99]

$Sr_{1.7}Ba_{0.3}PdO_3$ was the first compound to be investigated. This has the lowest amount of

barium content and its PXRD pattern (Figure 4.11) showed that no changes in structure had occurred from the reaction with CO_2. A comparison of the unit cell parameters of compounds before and after the reaction showed no overall change in values.
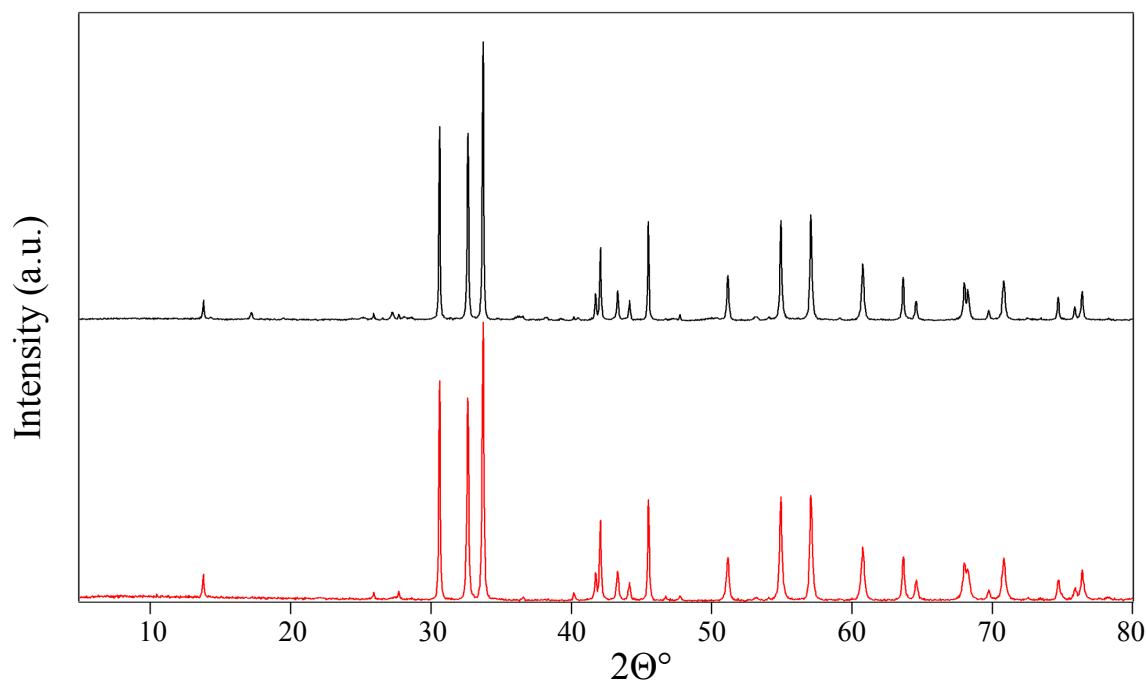
Figure 4.11: PXRD pattern of $Sr_{1.7}Ba_{0.3}PdO_3$ before (red) and after (black) being heated under CO_2 at 1000 °C.

$Sr_{1.6}Ba_{0.4}PdO_3$ was next to be investigated in reaction with CO_2. The comparison of the PXRD pattern in Figure 4.12 from before and after the reaction showed that no other phases had been formed. However, a comparison of the unit cell parameters in Table 4.4 do show a slight increase in values.
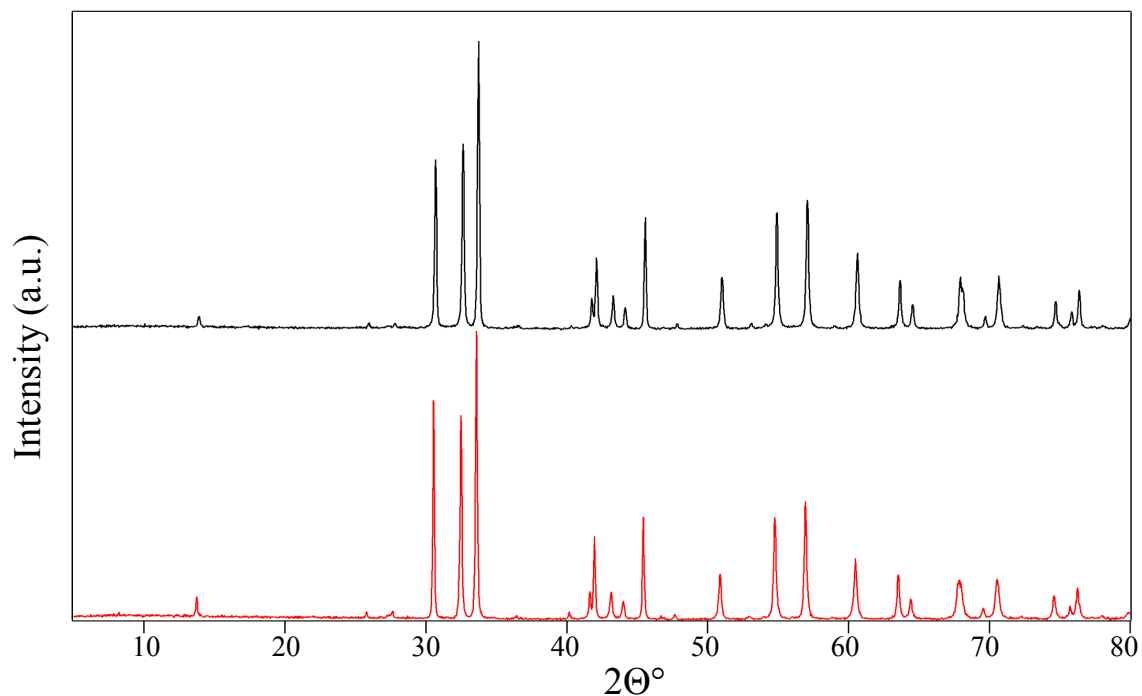
Figure 4.12: PXRD pattern of $Sr_{1.6}Ba_{0.4}PdO_3$ before and after being heated under CO_2 at 1000 °C.

Table 4.4: The cell parameters and unit volume of $Sr_{1.6}Ba_{0.4}PdO_3$ before and after being exposed to CO_2 at 1000 °C.

	Initial (1)	After CO_2 reaction (2)
a Å	3.985 ± 0.003	3.993 ± 0.004
b Å	3.579 ± 0.003	3.587 ± 0.001
c Å	12.890 ± 0.008	12.916 ± 0.004
Volume Å^3	183.87 ± 0.01	185.00 ± 0.01

$Sr_{1.5}Ba_{0.5}PdO_3$, which had a quarter of strontium replaced by barium was then investigated. It was found that at this barium content, decomposition towards Ba/SrCO$_3$ at 1000 °C started to take place. The PXRD pattern in Figure 4.13 showed that along with the $Sr_{1.5}Ba_{0.5}PdO_3$ phase, $BaCO_3$ had also been formed.
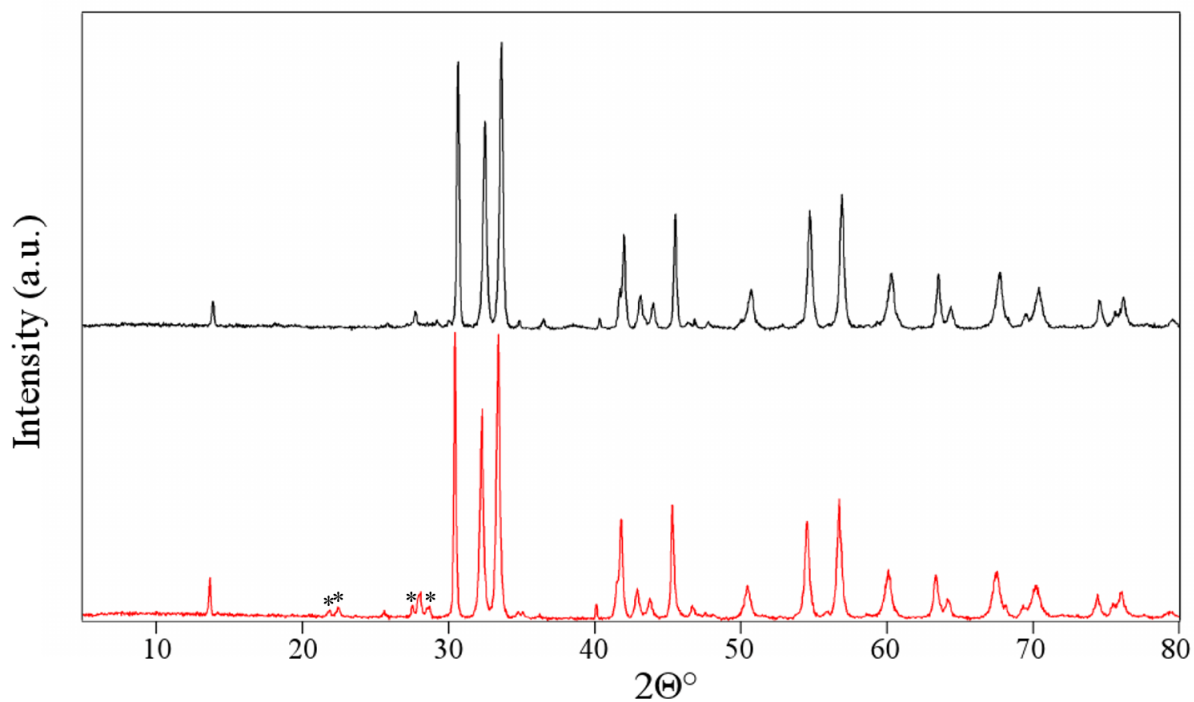
Figure 4.13: PXRD pattern of $Sr_{1.5}Ba_{0.5}PdO_3$ before (black) and after (red) being heated under CO_2 at 1000 °C. (*) peaks indicate $BaCO_3$.

A comparison of the unit cell parameters before and after the reaction with CO_2 is presented in Table 4.5. The data showed that a decrease in values had occurred from the reaction. This has been proposed to be a result of BaO being removed from the palladate structure in the form of $BaCO_3$.

Table 4.5: The cell parameters and unit volume of $Sr_{1.5}Ba_{0.5}PdO_3$ before and after being exposed to CO_2 at 1000 °C.

	Initial (1)	After CO_2 reaction (2)
a Å	3.991 ± 0.005	4.008 ± 0.001
b Å	3.601 ± 0.005	3.52 ± 0.01
c Å	12.93 ± 0.01	12.70 ± 0.03
V Å^3	185.81 ± 0.01	179.35 ± 0.03

All solid-state solutions after reacting with CO_2 were analysed using FTIR spectroscopy to

detect any carbonates (Figure 4.14). The spectra for x = 0.3 and 0.4 showed similar results to that of Sr_2PdO_3 after reaction with CO_2. This included the symmetric bending modes splitting (875, 874 and 858 cm^{-1}), and the asymmetric modes being merged into one peak shown at 652 and 645 cm^{-1}. These two spectra, however, show no signs of the symmetric stretching mode which should appear at approximately 1110 cm^{-1}. It is possible that this vibrational mode shows too little intensity to be detected via this method.

In the case of $Sr_{1.5}Ba_{0.5}PdO_3$ the IR spectrum shows two peaks belonging to symmetric stretching modes (1117 and 1083 cm^{-1}) and a symmetric bending mode of 874 cm^{-1}. There is however, only one asymmetric stretching mode at 1394 cm^{-1}. It is possible in this case that the other asymmetric stretching mode peaks have merged into one, making the individual identification of each vibration difficult. The values for the vibrational frequencies in this spectrum are also more closely related to those reported for $BaCO_3$ than $SrCO_3$.[222] It is expected that the wavenumber values for $BaCO_3$ will be lower than those for $SrCO_3$. This is due to the increased reduced mass, μ of barium compared to that of strontium. As discussed in Chapter 1, Equation 1.14 the greater the reduced mass value then the lower the wavenumber value. This also correlates with the presence of $BaCO_3$ in the PXRD pattern (Figure 4.13).
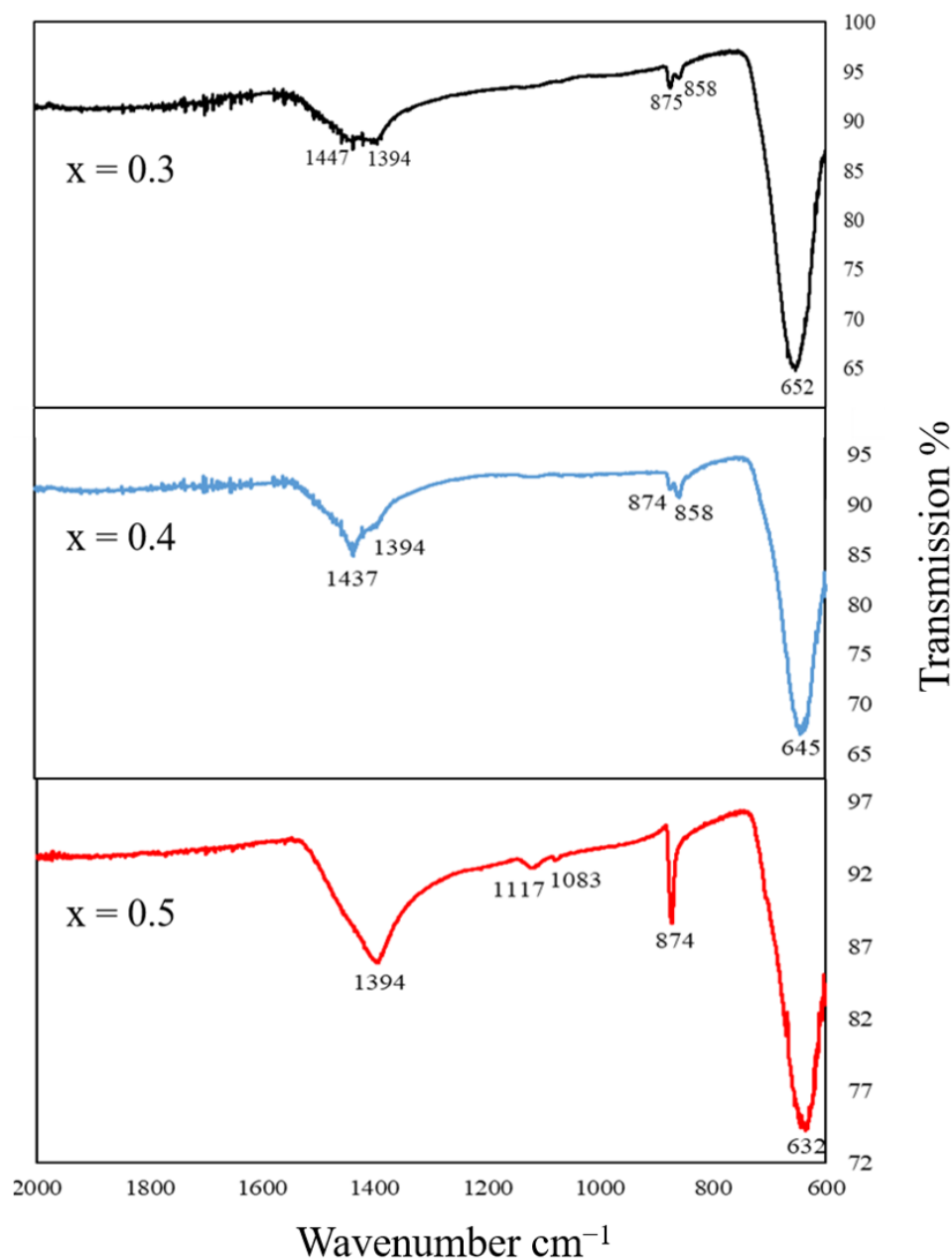
Figure 4.14: FTIR spectra of all the $Sr_{2-x}Ba_xPdO_3$ (x = 0.3, 0.4 and 0.5) compounds after reacting with CO_2.

The $Sr_{2-x}Ba_xPdO_3$ (x = 0.3, 0.4 and 0.5) series has been investigated for direct reactions with CO_2 at 1000 °C. The PXRD results showed that only when x = 0.5 a carbonate phase was present along with the palladate compound. Using FTIR spectroscopy it was found that carbonate groups were present, likely on the palladates surface. This however, made the analysis difficult as only certain vibrational peaks could be detected. What can be seen

from these results however, is that as the content of barium increases, so does the reactivity towards CO_2. This is to be expected when Ba-O has a greater affinity towards CO_2, and that the larger barium ionic radii will increase the size of the unit cell volume. The next palladate investigated for reacting with CO_2 was that of the all barium compound Ba_2PdO_3.

Ba_2PdO_3 has the largest unit cell volume compared to the other palladates (Table 4.2). The change in mass of the sample as it reacts with CO_2 is shown via the TGA curve, Figure 4.15.
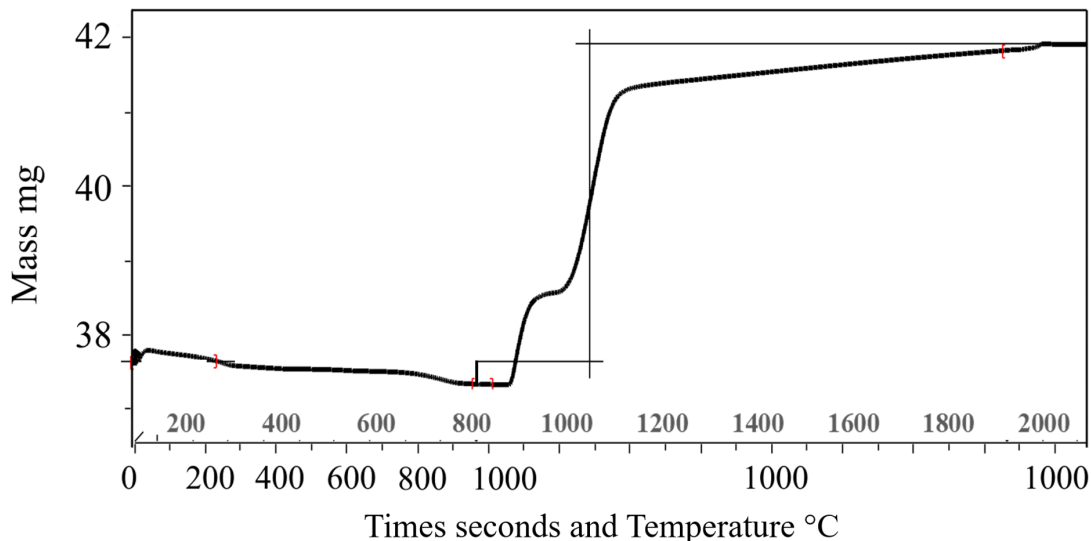
Figure 4.15: TGA curve of Ba_2PdO_3 being heated under CO_2 at 1000 °C.

The TGA curve shows the sample's mass would only increase when CO_2 was introduced at 1000 °C. The overall mass increase from the reaction with CO_2 was found to be approximately 11% of the original value. Along the curve the mass would plateau before increasing again. This could be from the loss of oxygen as a result of the formation of Pd metal. This phase will not form a carbonate and will not utilise any of the CO_2.

The resulting sample when analysed by PXRD showed a pattern (Figure 4.16) containing a mixed phase of $Ba_{11}Pd_{11}O_{20}(CO_3)_2$, $BaCO_3$ and Pd metal. The reaction of Ba_2PdO_3 under CO_2 not only resulted in a mixed metal oxide carbonate, but also the formation of $BaCO_3$ and the reduction of Pd^{2+} to palladium metal. To determine the quantity of each phase, a three phase Rietveld refinement was carried out. The refinement pattern and quantification values are presented in Figure 4.17 and Table 4.6.
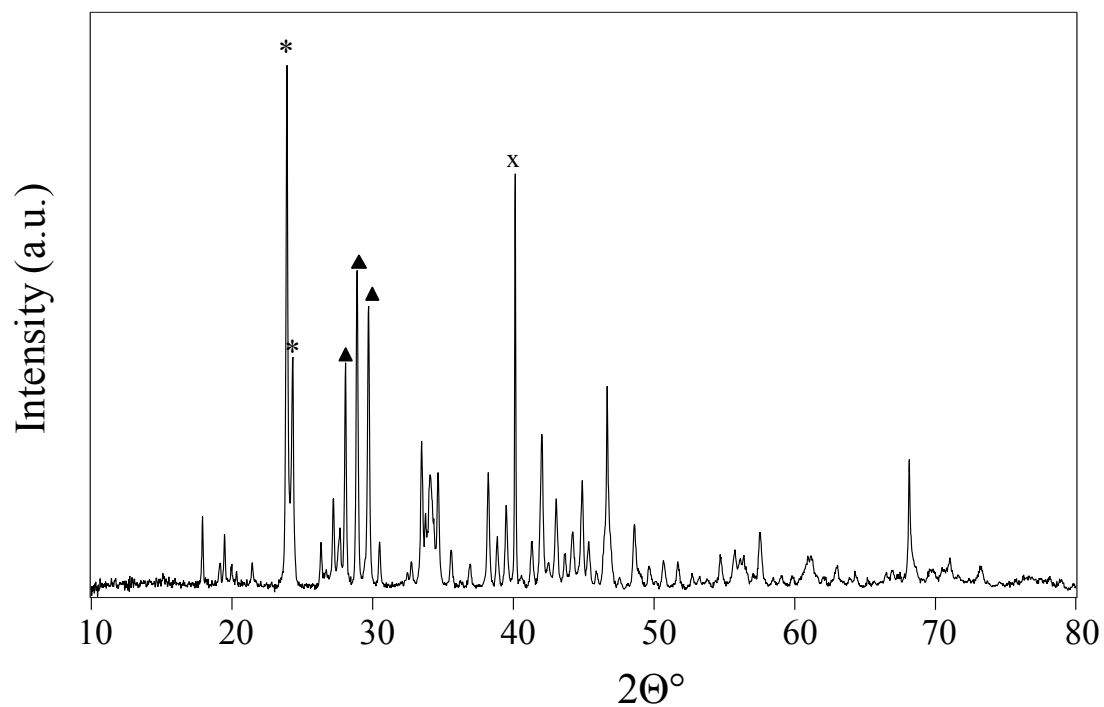
Figure 4.16: PXRD of Ba_2PdO_3, after reacting with CO_2 showing a mixed phase of $Ba_{11}Pd_{11}O_{20}(CO_3)_2$ (▲) and 'BaCO$_3$ (*) and Pd (X) metal.
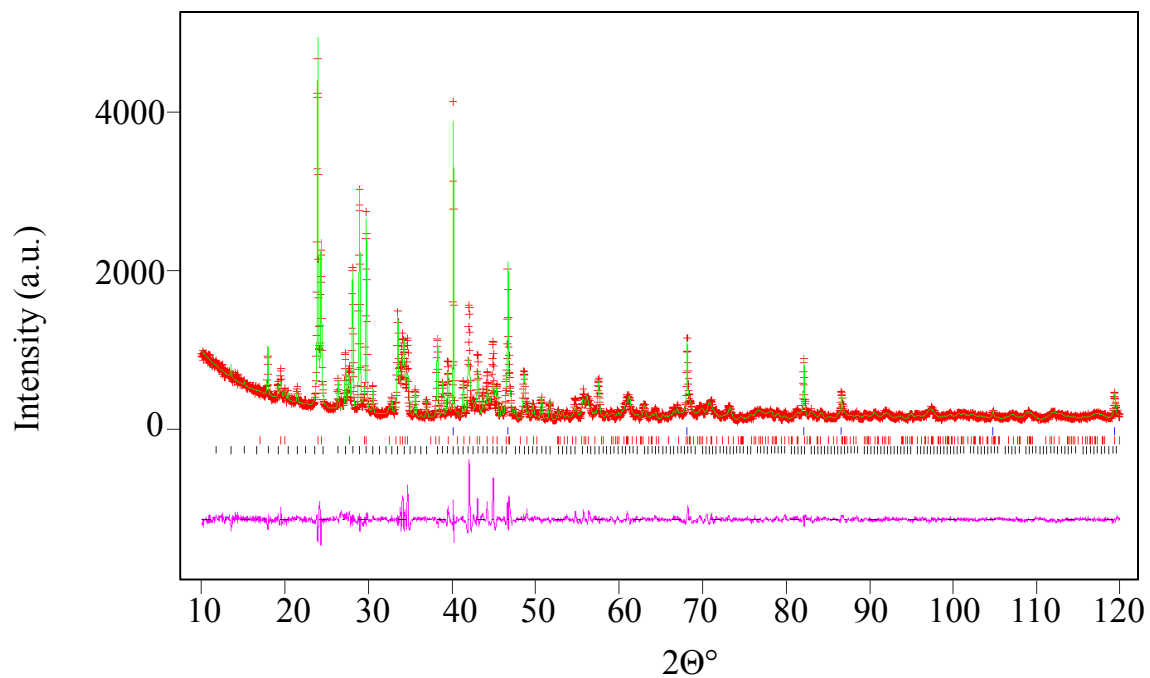
Figure 4.17: Rietveld refinement pattern of Ba_2PdO_3 after reacting with CO_2. This shows the observed(red crosses), calculated (green) and difference (purple) patterns. The ticks belong to $Ba_{11}Pd_{11}O_{20}(CO_3)_2$ (black), $BaCO_3$ (red) and Pd metal (blue).

Table 4.6: Refinement of the quantification of the multiple phases from Ba_2PdO_3 reacting with CO_2. The values of R_{wp} = 11.4 and χ^2 = 3.981 were reported from the refinement.

Phase	Weight fraction %	Error %
$Ba_{11}Pd_{11}O_{20}(CO_3)_2$	50	0.44
$BaCO_3$	42	0.31
Pd metal	8	0.16

The Rietveld refinement showed the quantification of each phase as $Ba_{11}Pd_{11}O_{20}(CO_3)_2$ (50 %), $BaCO_3$ (42 %) and Pd metal (8 %) weight fractions.[230, 221, 240] The sample was then analysed by FTIR to confirm the presence of carbonates (Figure 4.18). The peaks and wavenumber values match those reported by Crooks and Weller for the oxide carbonate phase as well as those reported of $BaCO_3$.[130]
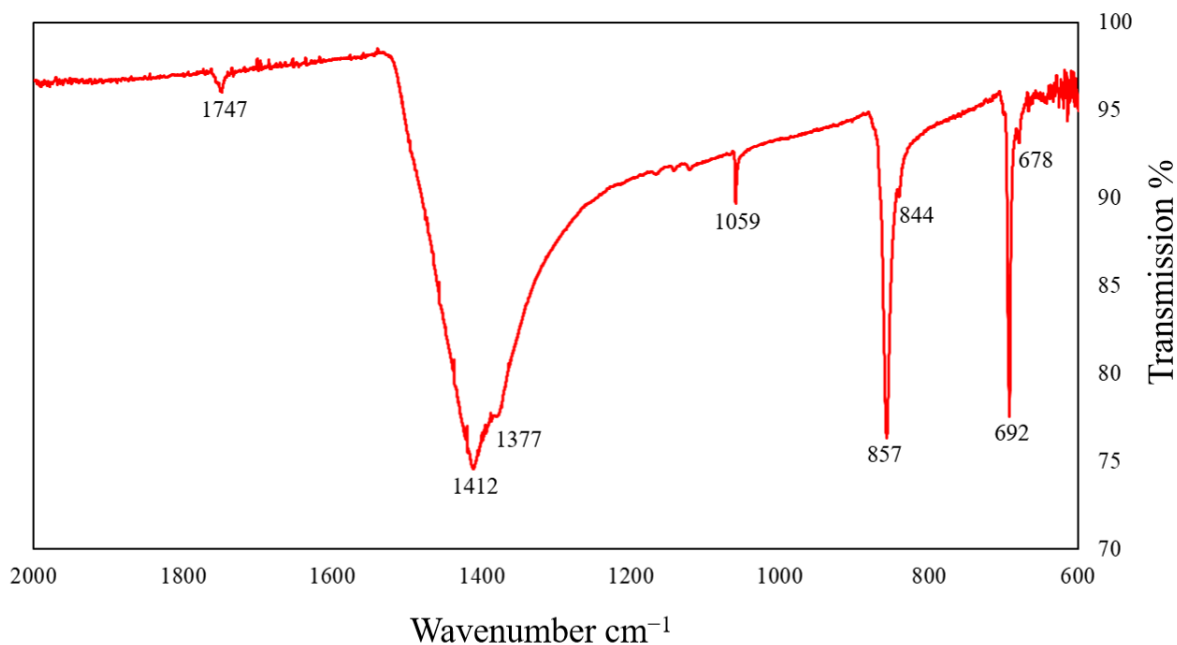
Figure 4.18: FTIR spectrum of $Ba_{11}Pd_{11}O_{20}(CO_3)_2$ and $BaCO_3$ mixture.

To summarise, the $Sr_{2-x}Ba_xPdO_3$ (x = 0 − 2) series of compounds have been investigated for reacting with CO_2 towards preparing mixed anion compounds. A synthetic procedure of having these compounds react with CO_2 gas at specific temperatures was employed as this was used for reactions with the cuprate series, $Sr_{2-x}A_xCuO_3$ (A = Ba and Ca) towards preparing

oxide carbonates. It has been found that compounds of $Sr_{2-x}Ba_xPdO_3$ ($x < 0.5$) have shown no reactivity towards CO_2 at 1000 °C. When this temperature is decreased, or the amount of Ba increased, the end result (decomposition) takes place, resulting in $Sr/BaCO_3$ and Pd metal being formed. $Ba_{11}Pd_{11}O_{20}(CO_3)$ was an oxide carbonate prepared from Ba_2PdO_3, and was present with secondary phases, $BaCO_3$ and Pd metal.

It is proposed that the reason for this inability to react and form an oxide carbonate of general formula $Sr_{2-x}Ba_xPdO_2(CO_3)$ as in the case of the cuprate compounds, is the Pd cation. In the $Sr_{2-x}Ba_xCuO_2(CO_3)$ and $Ca_2CuO_2(CO_3)$ series of compounds it has been found that ACO_3 (A = Sr, Ba and Ca) like groups are arranged between CuO_2 planes in this arrangement that the carbonate groups are being coordinated to the copper. Pd possibly, is unable to expand its coordination within these types of solid compounds. In the case of $Ba_{11}Pd_{11}O_{20}(CO_3)_2$, the crystal structure shows a carbonate located close towards the PdO type groups, but no coordination is observed as shown in Figure 4.19.[230]
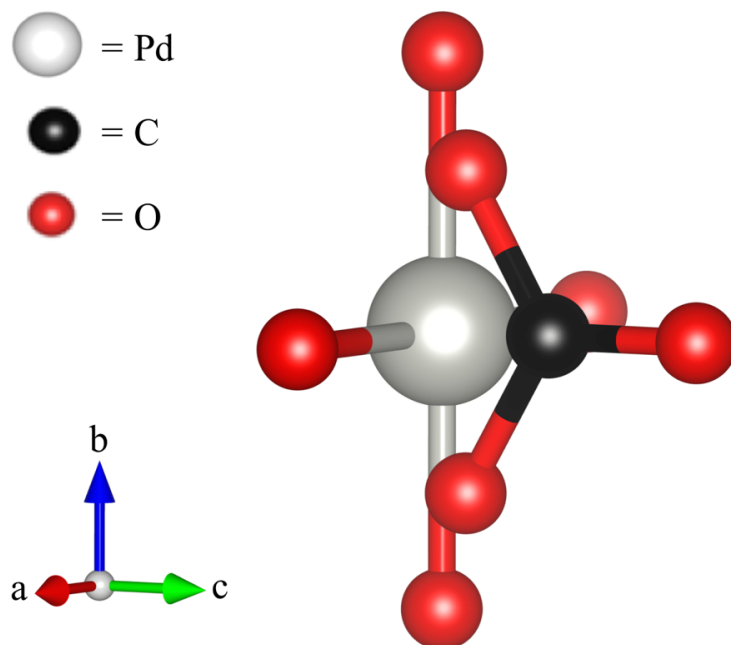
Figure 4.19: Strucutre of square planar PdO_4 groups with CO_3 a top within the crystal structure of $Ba_{11}Pd_{11}O_{20}(CO_3)_2$.

In this arrangement the carbonates show no coordination towards the Pd^{2+} cations. Also present within $Ba_{11}Pd_{11}O_{20}(CO_3)_2$ are groups of $Pd_{18}O_{24}$ cages with Pd_6O_{12} rings alongside barium ions with carbonate groups.

4.3.2 Ce_2MnN_3

4.3.2.1 Ce_2MnN_3 preparation

A sample of Ce_2MnN_3 was confirmed using PXRD (Figure 4.20) to contain a mixed phase of the mixed metal nitride along with CeO_2. This was taken into accountant when the sample was used for reacting with CO_2. Due to the oxygen and moisture sensitivity of Ce_2MnN_3, a thin layer of paraffin oil was placed over the sample during analysis to prevent reactions with oxygen. As a result the pattern starts from 30 $2\theta°$ to exclude the peaks from the oil.
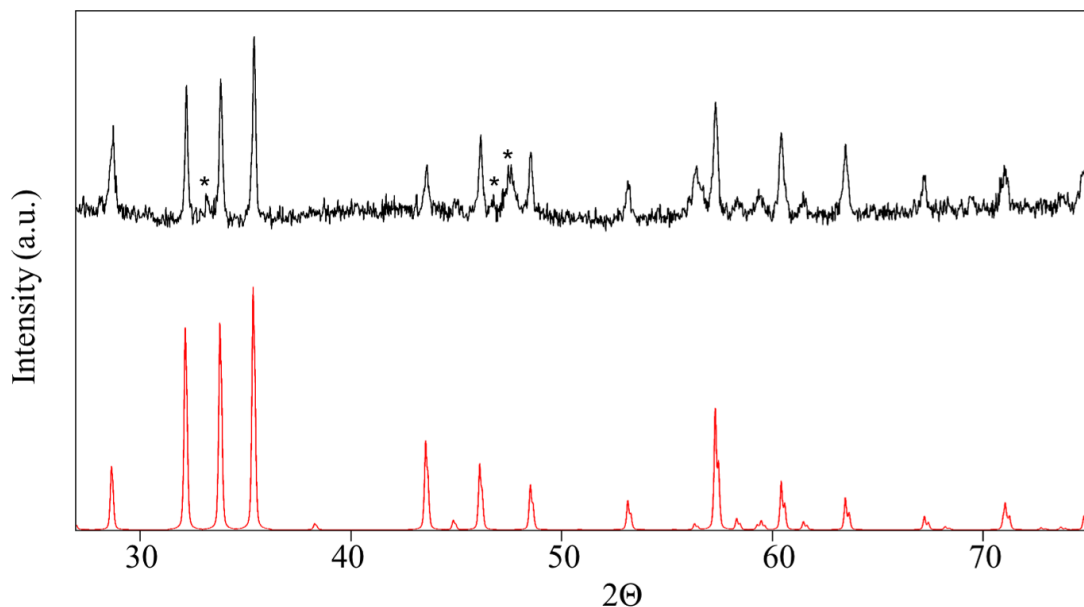
Figure 4.20: A comparison of the PXRD patterns of Ce_2MnN_3 containing CeO_2 (*) used for reacting with CO_2, to that of a pattern of Ce_2MnN_3 reported by Niewa *et al.* [102]

The peaks belonging to Ce_2MnN_3 were indexed to an orthorhombic unit cell with parameters of a = 3.751(2) Å, b = 3.444(2) Å and c = 12.446(9) Å. This was in agreement with the cell reported by Niewa *et al.* with parameters a = 3.749(9) Å, b = 3.444(5) Å and c = 12.460(1) Å. [102] Taking the purity into consideration, this sample was used for reactions with CO_2 gas.

4.3.2.2 Ce$_2$MnN$_3$ reactions with CO$_2$

Initially Ce$_2$MnN$_3$ was heated to 1000 °C in pure CO$_2$ gas with the TGA curve shown in Figure 4.21. This was to identify at what temperatures the mass of the sample would change, and to indicate when the reaction with CO$_2$ was occurring. The TGA curve showed an increase in mass starting at approximately 350 °C and continued steadily up until 750 °C. After this point a decrease in mass was observed until plateauing at 1000 °C.
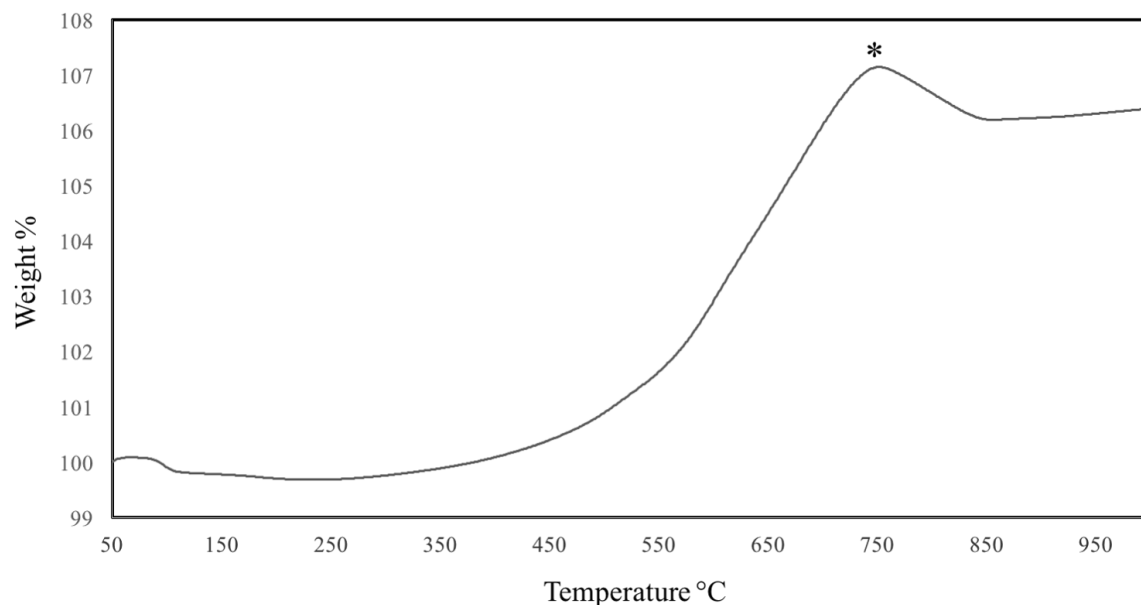
Figure 4.21: TGA curve showing the mass gain as Ce$_2$MnN$_3$ is heated to 1000 °C under pure CO$_2$ gas. The point at (*) represents the highest mass point at 750 °C.

The increase in mass was found to be over 6.5%, and was measured from the difference between the first and final points on the TGA curve. As the highest point was at 750 °C a TGA analysis at this temperature was carried out separately and is shown in Figure 4.22. Afterwards the resulting sample was then placed onto a zero-background Si-crystal holder covered in paraffin oil for PXRD analysis. A mixture of CeO$_2$ with MnO$_2$ was observed from the pattern shown in Figure 4.21. The reported pattern of CeO$_2$ by Nakamatsu *et al.* was used to identify these phase among the background peaks.[241]
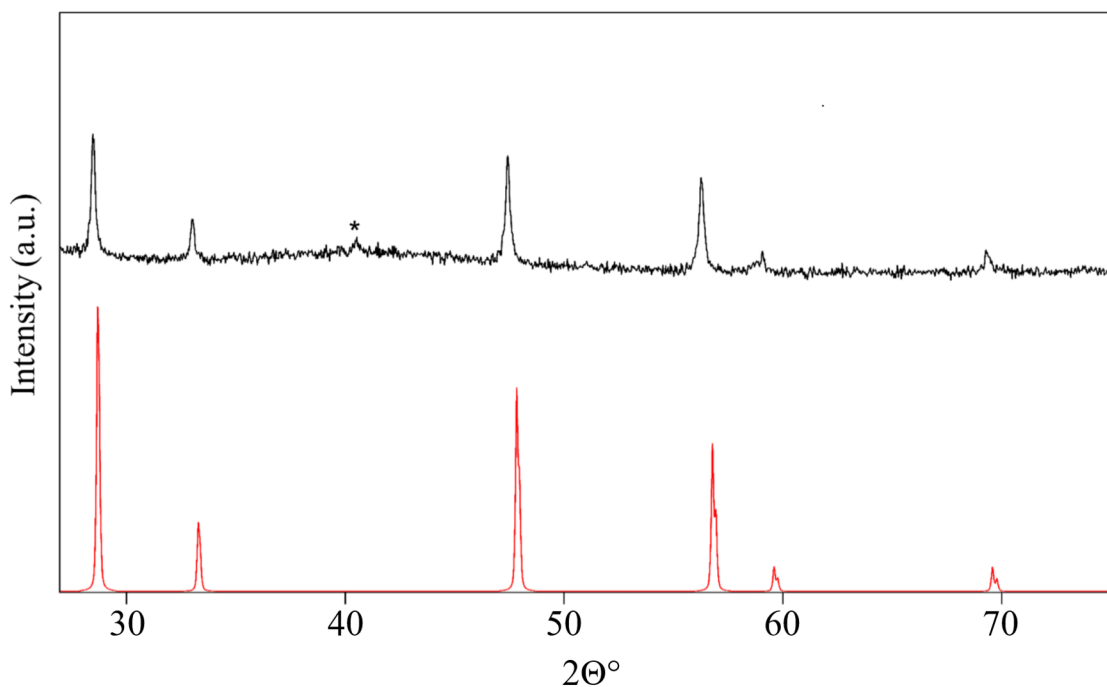
Figure 4.22: PXRD pattern of CeO_2 and MnO_2 (*) (black) formed from Ce_2MnN_3 reacting with CO_2 at 1000 °C and CeO_2 (red).

The results from the reaction showed only CeO_2 and MnO_2 to be present. The formation of CeO_2 implies the presence of O_2. However, care was taken to avoid any air/moisture contamination. Hence oxygen must have been generated during the reaction. This is proposed to be a result of CO_2 splitting into CO and O_2 in the presence of Ce_2MnN_3, as the affinity for Ce to be oxidised and form CeO_2 would have resulted in the dissociation of $Ce_2^{4+}Mn^{1+}N_3^{3-}$. Some non-oxide solids have been found to split CO_2 into CO and $\frac{1}{2} O_2$.[242, 243]

The next reaction involved using alternating gases for Ce_2MnN_3 to react with CO_2 at a specific temperature. This followed the same methodology as with Sr_2CuO_3 except nitrogen was used instead of air. Initially Ce_2MnN_3 was reacted with CO_2 at 350 °C for 15 minutes. The sample was then analysed with the resulting PXRD pattern (Figure 4.23) showing that CeO_2 was beginning to form but peaks belonging to Ce_2MnN_3 were still present.
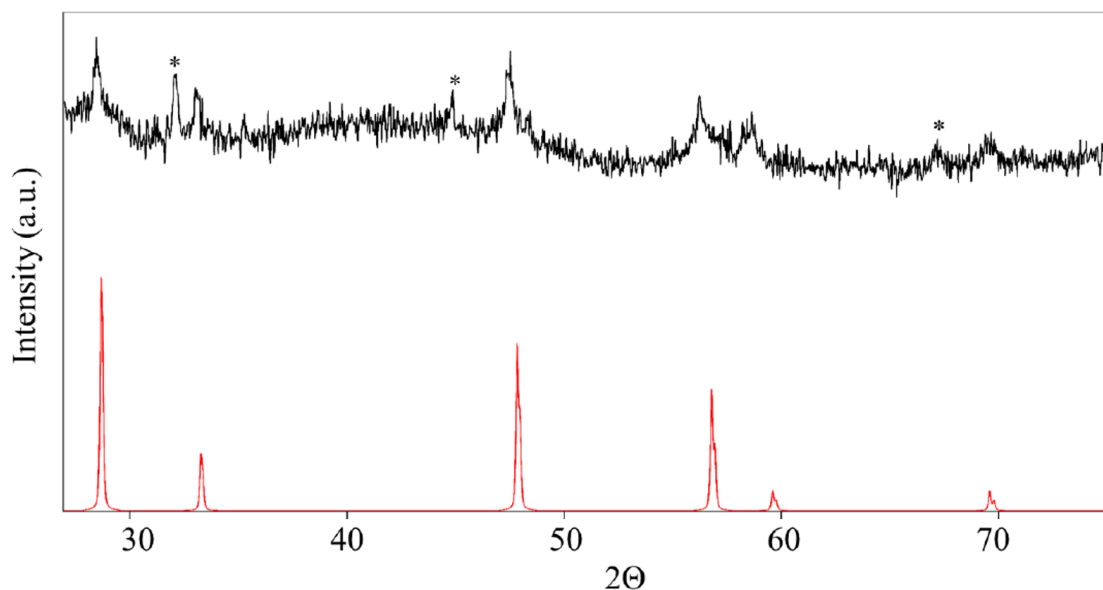
Figure 4.23: PXRD pattern from reaction at 350 °C with CO_2 showing CeO_2 being formed and (*) peaks belonging to Ce_2MnN_3. The is compared to the pattern of CeO_2 (red).[241]

Ce_2MnN_3 was then heated to 750 °C (Figure 4.24). It was at this temperature the sample's mass increased the most, Figure 4.20. The sample mass was found to initially decrease due to the loss of moisture that would have come from moving the sample from the glovebox to the TGA furnace. This decrease in mass however, stopped when CO_2 was introduce and an increase of nearly 20% of the original mass was observed. The PXRD pattern (Figure 4.25) from the reaction at 750 °C, showed that a mixed phase of CeO_2 and MnO_2 had been formed. As with the previous reaction with CO_2, a reported pattern of CeO_2 was compared to that of the sample.
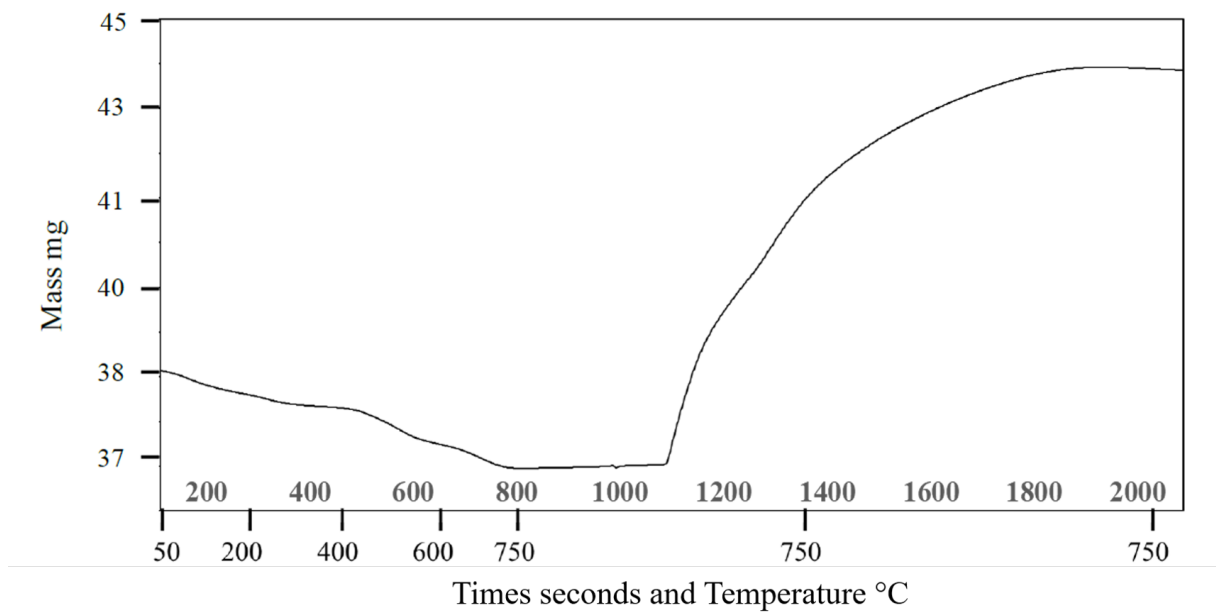
Figure 4.24: TGA curve of Ce_2MnN_3 heated to 750 °C in nitrogen then maintained at this temperature for 15 minutes under CO_2, then cooled to room temperature under nitrogen.
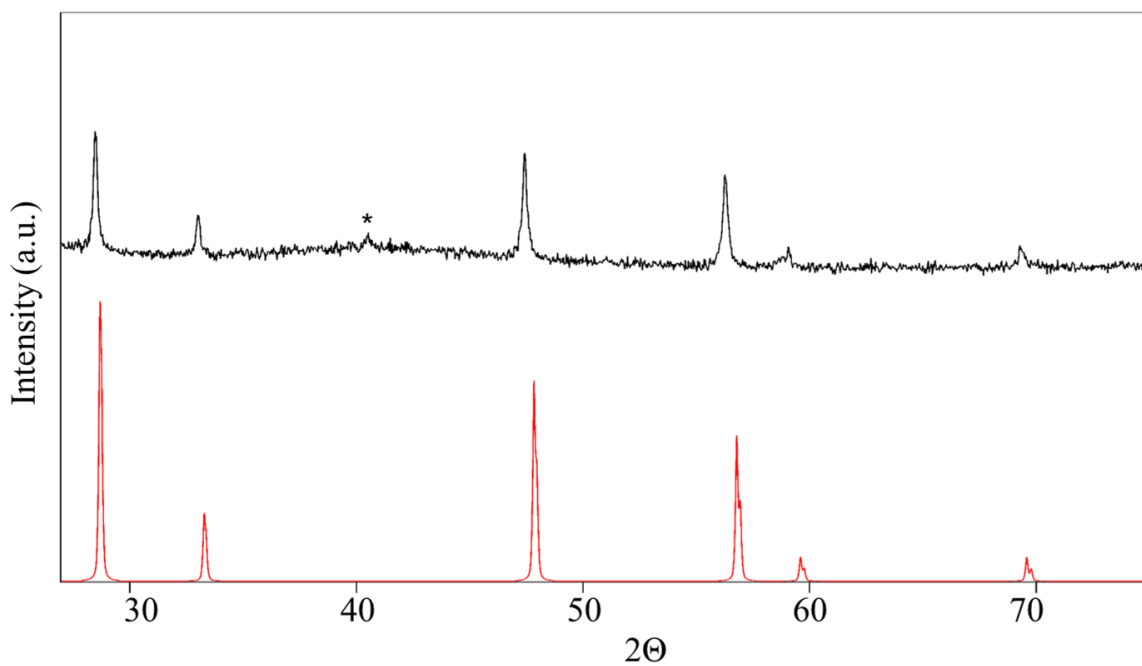
Figure 4.25: PXRD patterns showing CeO_2 and MnO_2 (*) being formed from Ce_2MnN_3 reacting with CO_2 at 750 °C (black) compared to that of a reported pattern of CeO_2 (red).

These results showed that even by heating Ce_2MnN_3 under specific temperatures and gases

206

CeO_2 would still be the primary product. It is proposed that the increase in mass observed is a result of Ce_2MnN_3 splitting CO_2 to provide CO and O_2, which reacts with the mixed metal nitride to form CeO_2 along with MnO_2. In the case of the formation of CeO_2 an anion exchange is taking place as for every one Ce cation three N^{3-} will be exchanged for six O^{2-} as shown in Equation 4.2. This may accountant for the increase in mass observed.

$$Ce_2MnN_3 + CO_2 \rightarrow 2CeO_2 + MnO_2 + nCO + 3NO_x \tag{4.2}$$
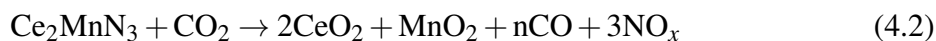
The thermal decomposition of CO_2 has been previously explored by Lietzke and Mullins over a range of different temperatures and pressures.[244] This thermodynamic study found that 1 mole of pure CO_2 gas would decompose at 100 atm and 632 °C to prepare 10^{-9} moles of CO. Equations 4.3 and 4.4 shows two potential dissociation reactions that CO_2 can undergo. This needs to be considered when reacting compounds with CO_2 at high temperatures as a certain amount of the CO_2 may decompose into CO and oxygen.

$$CO_2 \rightarrow CO + \frac{1}{2}O_2 \tag{4.3}$$

$$CO_2 \rightarrow C + O_2 \tag{4.4}$$

The decomposition reaction of CO_2 has been investigated by oxide based compounds.[245] CO_2 splitting has also however, been found to occur over non-oxide based compounds. In the field of photocatalysis non-oxide based compounds have been used for splitting CO_2 along with H_2 towards preparing hydrocarbons. Kuhl *et al.* showed that copper metal can be used to reduce CO_2 via electrochemical methods.[242] The reaction of CO_2 over metal surfaces has also been explored using theoretical DFT methods by Liu *et al.*.[246] This study showed that CO_2 reacts differently over metal compounds to form metal oxides. In the case of metal oxides, the CO_2 forms a chemical bond which results in a surface carbonate being formed. When metals are used however, the CO_2 dissociates into CO and O on the surface. The CO molecule is then desorbed with the O being retained.

Graphitic carbon nitride (g-C_3N_4) has also been investigated by Goettmann *et al.* for splitting

CO_2 towards preparing hydrocarbons.[243] This study provides a potential mechanism which has CO_2 being bonded to the edges of g-C_3N_4 via a N-C bond. From this CO_2 can be split to have an oxide removed for reacting with a organic molecule, in this case benzene to form phenol. It is possible that a similar reaction is occurring in the case of Ce_2MnN_3. CO_2 could be attracted to the nitride groups with the oxide removed towards reacting with Ce and Mn forming the respective oxides. The CO could then be free to then be released.

In the terms of CO_2 reactions, CeO_2 has been used for a variety of different purposes. This has varied from being a support on Fe_2O_3 for splitting CO_2 to prepare CO.[247, 248] To being used as a catalyst to utilise CO_2 towards preparing other organic compounds.[249, 250] This shows the possibilities of cerium based compounds for reacting with CO_2. It also shows that the Ce-N groups in Ce_2MnN_3 might behave in a similar way to the oxides.

The work into Ce_2MnN_3 reacting with CO_2 has not only provided insight into how CO_2 can be split under different conditions, it has also highlighted the importance of the anions as well as the cations within compounds for reacting with CO_2. It was found in this work that in the case of $Sr_{2-x}A_xCuO_3$ that the oxides are reacting with CO_2 to form carbonate groups towards the oxide carbonates, $Sr_{2-x}A_xCuO_2(CO_3)$. As a similar reaction does not occur for metal nitrides, it is proposed here that CO_2 splits into either CO and $\frac{1}{2}O_2$, or C and O_2 in the presence of Ce_2MnN_3. This has been seen at temperatures above 350 °C in the formation of CeO_2 alongside MnO_2. In order to determine which of these reactions could be occurring, future work could involve using TGA-MS to monitor the presence of CO and O_2. Also the residue sample could be studied using electron microscopy techniques to determine the presence of surface carbon.

In the case of studying the formation of $Sr_2CuO_2(CO_3)$ an understanding into how CO_2 will react is important. The potential of CO_2 splitting when reacting in the presence of Ce_2MnN_3 may need further study. This could result in an alternative route for CO_2 splitting to provide CO, which is used for further reactions such as Fischer-Tropsch towards preparing hydrocarbon products.[251,252]

4.4 Conclusion

The reaction of anion deficient compounds such as the $Sr_{2-x}Ba_xPdO_3$ series as well as Ce_2MnN_3, with CO_2 have been investigated. This was aimed at attempting to prepare a series of novel mixed anion carbonates from filling the anion vacancies present.

The results have found that in the case of $Sr_{2-x}Ba_xPdO_3$ that CO_2 would not react within the bulk of the material for $x < 0.5$, but surface $Sr/BaCO_3$ is proposed to be present based on the results from FTIR spectroscopy. When $x \geq 0.5$ decomposition took place which resulted in $Sr/BaCO_3$ being formed. The cause of this has been contributed to Pd being unable to expand its coordination state in the same way Cu can and is unable to form a stable $Sr_2PdO_2(CO_3)$ type structure. Previous work into anion substitution within palladates have found that additional anions can be located within the interstitial sites of the crystal structure without expanding the coordination of palladium such as with the $Sr_{2-x}Ba_xPdO_2F_2$ series. It however, has been found that when Ba_2PdO_3 ($x = 2$) reacts with CO_2 to prepare $Ba_{11}Pd_{11}O_{20}(CO_3)_2$ alongside $BaCO_3$ and Pd metal. In this structure the carbonates are not coordinated to the Pd cations which, maintains its original square planar arrangement.

In the case of Ce_2MnN_3, this was found to decompose into CeO_2 and MnO_2 when reacting with CO_2 gas at temperatures exceeding 350 °C. Ce_2MnN_3 despite being isostrucutral to Sr_2CuO_3, and being able to accommodate additional anions ($Ce_2MnN_3F_{2-\delta}$), is still incapable of forming mixed anion compounds with CO_2. The reason for this is proposed to be a result of CO_2 splitting in the presence of the mixed metal nitride to provide an O_2 atmosphere above 300 °C.

Both of these types studies highlight what properties are required for anion-deficient compounds to react with CO_2 towards preparing complex inorganic solids. Reactions with the palladate series showed that in order to form a carbonate within these types of structures, a B cation which can expand its coordination number is required. The reaction with Ce_2MnN_3 showed that not only does the anion need to be able to react with CO_2 towards forming a stable anionic group. This study also shows that the thermal behaviour of CO_2 under certain conditions and with compounds also needs to be considered.

Chapter 5

Computational study of Sr_2CuO_3 reacting with CO_2 towards $Sr_2CuO_2(CO_3)$

5.1 Reaction of CO_2 with alkali metal oxides to form metal carbonates

A variety of solid materials are able to react with CO_2 toward the formation of metal carbonates in particular alkaline earth metal oxides AO (A = Mg, Ca and Sr).[13, 214] These reactions have also been found to be reversible so that CO_2 can be removed and the original oxide reformed and reused. This PhD project has investigated compounds with the formula A_2BO_3, (A = Sr, Ca and Ba, B = Cu and Pd) that have anion vacancies and alkaline earth metals. These compounds have been directed towards utilising CO_2 for preparing complex mixed anion materials. In these compounds it has been proposed that CO_2 enters through the anion vacancies and reacts with AO groups within the crystal structure to form a carbonate. This not only results in the formation of ACO_3 groups but also in the change of the overall structure.

The direct reaction of these compounds with CO_2 has been studied using DFT methods. This has been focused on exploring the novel reaction of CO_2 with Sr_2CuO_3 to produce $Sr_2CuO_2(CO_3)$. This study aims to not only show how the carbonate groups are being formed, it is also to provide a model on how the structure of Sr_2CuO_3 changes when reacting with

CO_2 towards $Sr_2CuO_2(CO_3)$. Previous work with Sr_2CuO_3 on anion insertion has found that the anion vacancies can be filled to form mixed anion compounds.[90, 92]

In this chapter, initial studies have been carried out on the known reactions of CO_2 on AO (A = Ba, Ca and Sr) surfaces. As well as on the bulk reaction of CO_2 reacting within SrO towards $SrCO_3$. This study was to not only determine the surface adsorption energy, but also to understand the formation of the surface carbonate. This would then lead on to develop a computational methodology to determine the enthalpy of reaction, ΔH_{rxn} and vibrational frequencies of carbonates in the bulk phase. Once an accurately performing method was developed this would be applied to study the novel reaction of CO_2 within the bulk of Sr_2CuO_3 towards $Sr_2CuO_2(CO_3)$. In this reaction the ΔH_{rxn} value is a combination of structural rearrangement, $\Delta H_{structure}$ and carbonate formation, $\Delta H_{carbonate}$ enthalpies.

5.2 Computational Methodology

The theoretical modeling of the interaction between CO_2 and the AO (A = Ca, Sr and Ba) surfaces was carried out using the ORCA suite of programs (version 3.0.3).[193] The Perdew-Burke-Ernzerhof (PBE) exchange correlation functional was used with a resolution of identity approximation for the Coulomb interactions.[177, 253] The valence electrons were represented with a triple zeta valence polarised def2-TZVP basis set along with a compatible def2-TZVP/J auxiliary basis set.[254, 255] The TightOpt criteria implemented in ORCA was used to stop the geometry optimization at a total energy change of $1 < 10^{-6}$ Eh, respectively. Dispersion forces for each system were included using the Becke-Johnson damping D3BJ method.[256]

A surface model of the AO (A = Ba, Ca and Sr) oxides were prepared using the first top two layers of the reported crystal structures.[257–259] In all cases the metal oxides have a NaCl type structure. A CO_2 molecule would be placed over the metal oxide and allowed to optimise towards forming a carbonate.

Bulk reactions for SrO and Sr_2CuO_3 involved periodic calculations that were performed within the *ab inito* program CP2K.[194] The exchange-correlation energy was calculated us-

ing the E_{xc} functionals PBE and TPSS, along with revised version revTPSS and a PBE type functional for solid systems PBEsol.[177–180] The valence electrons were represented using the DZVP-MOLOPT-SR-GTH basis set, a plane wave cutoff energy of 360 Ry, and the core-electrons with the GTH pseudopotentials.[254, 260] The Broyden-Fletcher-Goldfarb-Shanno, BFGS algorithm was used to optimise each system.[261]

The bulk reactions for SrO involved a supercell of the oxide with unit cell parameters of 2×2×2 and all atoms free to optimise. The SrO groups would only be repeated within the b direction. CO_2 was initially positioned within the supercell and was allowed to optimise forming groups of $SrCO_3$.

In the case of Sr_2CuO_3 fractional coordinates were used to represent all models. The first step involved changing the atomic coordinates and the unit cell parameters of those of Sr_2CuO_3 to those of $Sr_2CuO_2(CO_3)$. This would result in a $Sr_2CuO_2(CO_3)$ type structure with CO_2 groups removed, Sr_2CuO_2-O. This model would also have oxides positioned in the c direction to react with CO_2. This structural rearrangement was carried out using the reported coordinates and unit cell parameters of Sr_2CuO_3 reported by Weller and Lines and $Sr_2CuO_2(CO_3)$, Nakata *et al.*.[88, 117] The energy difference from these structures would provide an enthalpy for structural rearrangement, $\Delta H_{structure}$, as well as a possible step by step structural procedure. In the case of $\Delta H_{carbonate}$, CO_2 molecules were repeated through symmetry and positioned over the SrO groups in the Sr_2CuO_2-O model. These would then be optimised towards forming carbonates. In order to reduce computational time and complexity only the atoms within CO_2 and selected oxides in Sr_2CuO_3 were free to be optimised with the Sr, Cu and other O atoms constrained.

All calculations were performed on the high-performance computer (HPC), Viper, at the University of Hull.

5.2.1 Determination of the enthalpy of reactions ΔH_{rxn}

The reaction of CO_2 with a variety of compounds towards forming carbonates has been investigated on both the surface and in the bulk phase. All models have CO_2 free to optimise with an oxide towards a carbonate. In order to study the carbonate formation, as well as

the structural rearrangement in the case of $Sr_2CuO_2(CO_3)$, a thermodynamic model has been used to calculate enthalpy values.

The enthalpy of reaction, ΔH_{rxn}, was determined as the difference from the total energy of the reactants to that of the products. Equations 5.1 shows how the ΔH_{rxn} can be determined for the formation of $SrCO_3$.

$$\Delta H_{rxn} = \Delta H_f(SrCO_3) - \Delta H_f(SrO + CO_2) \tag{5.1}$$

In the case of $Sr_2CuO_2(CO_3)$ the ΔH_{rxn} is composed of the enthalpy of structural rearrange-ment $\Delta H_{structure}$ and carbonate formation, $\Delta H_{carbonate}$. For these calculations Sr_2CuO_2-O represents a structure between Sr_2CuO_3 and $Sr_2CuO_2(CO_3)$ that has CO_2 inserted to optimise into the oxide carbonate. Equations 5.2 to 5.5 show how these values can be determined. The $\Delta H_{carbonate}$ value for a single carbonate is determined from the overall $\Delta H_{carbonate}$ divided by two. This is a result of the $Sr_2CuO_2(CO_3)$ model having a number of formula units, $Z = 2$. As a result two sets of CO_2 inserted to form into carbonates during the optimisation of the system.

$$\Delta H_{rxn} = \Delta H_{structure} + \Delta H_{carbonate} \tag{5.2}$$

$$\Delta H_{rxn} = \Delta H_f(Sr_2CuO_2(CO_3)) - \Delta H_f(Sr_2CuO_3 + CO_2) \tag{5.3}$$

$$\Delta H_{carbonate} = \Delta H_f(Sr_2CuO_2(CO_3)) - \Delta H_f(Sr_2CuO_2 - O + CO_2) \tag{5.4}$$

$$\Delta H_{structure} = \Delta H_f(Sr_2CuO_2 - O) - \Delta H_f(Sr_2CuO_3) \tag{5.5}$$

To understand how the enthalpy values are determined at different reaction phases. A Born-Haber diagram of SrO_s formation has been displayed in Figure 5.1. This shows the different thermodynamics process present during a reaction. Of particular interest is the enthalpy of formation, ΔH_f.
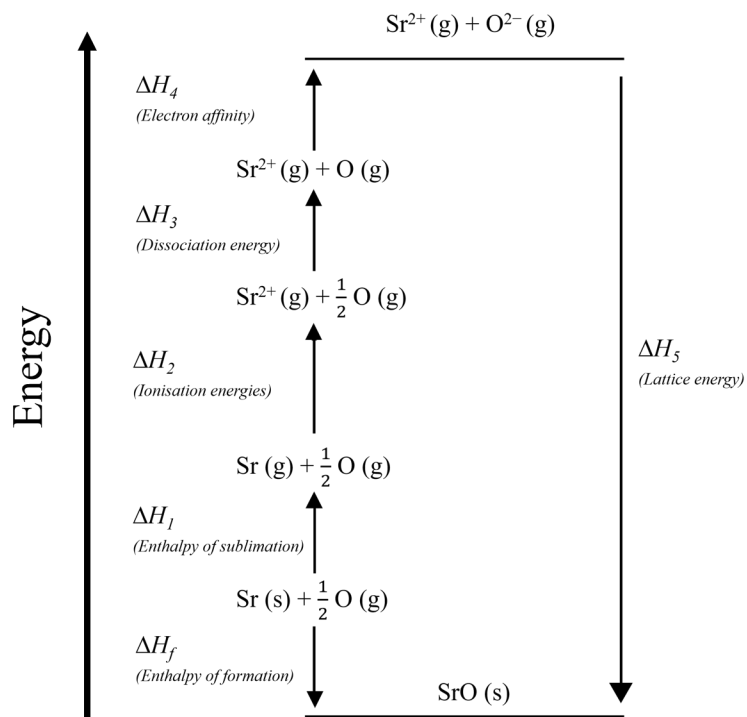
Figure 5.1: A Born-Haber diagram showing the different thermodynamics steps towards the enthalpy of formation, ΔH_f of $SrO_{(S)}$ from $Sr_{(S)}$ and $O_{2(g)}$.

In the case of surface reactions, the bond length and angles were measured and compared to experimental values. This along with the surface adsorption energy was used to verify the accuracy of calculating surface carbonates. For the bulk reactions towards $SrCO_3$ and $Sr_2CuO_2(CO_3)$ the vibrational frequencies of the carbonate groups were also determined and compared to experimental results. This was an additional way to assess the accuracy of the methodology.

5.3 Results and Discussion

5.3.1 Surface reaction of AO (A = Ca, Sr and Ba) compounds with CO_2

The reaction of CO_2 into the anion vacancies of Sr_2CuO_3 has been proposed to occur between the SrO groups towards forming a carbonate. This with the overall structural rearrangement results in the formation of $Sr_2CuO_2(CO_3)$. Initial calculations focused on the reaction of

CO_2 over a surface cluster of alkaline earth metal oxides, AO (A = Ca, Sr and Ba). This was to provide an understanding of the carbonate formation, and also verify the computational method for determining adsorption energies. Figure 5.2 shows a representation of the AO surface consisting of 18 atoms prepared from the original AO crystal structure.
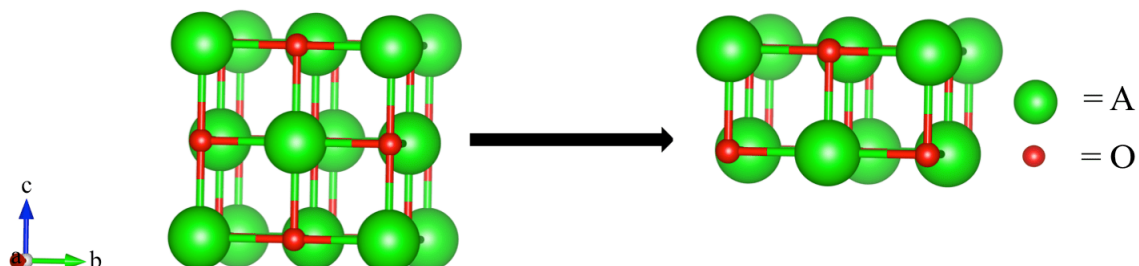
Figure 5.2: The crystal structure of a AO compound (A = Ca, Sr and Ba) is on the left, with the reduced cluster on the right.

CO_2 was relaxed over an oxide group on the AO surface to form into a carbonate. An example of the structure before and after optimisation, showing the carbonate formation is represented in Figure 5.3. The adsorption energy from the carbonate forming on the surface can be determined and compared to reported values. This was used to assess the computational methods accuracy. The adsorption energy was determined as the difference between the optimised CO_2 and cluster energy separately to that of the surface-carbonate end product. The surface-carbonate structure is shown in Figure 5.4 which also shows how the bond length and angles can be measured.
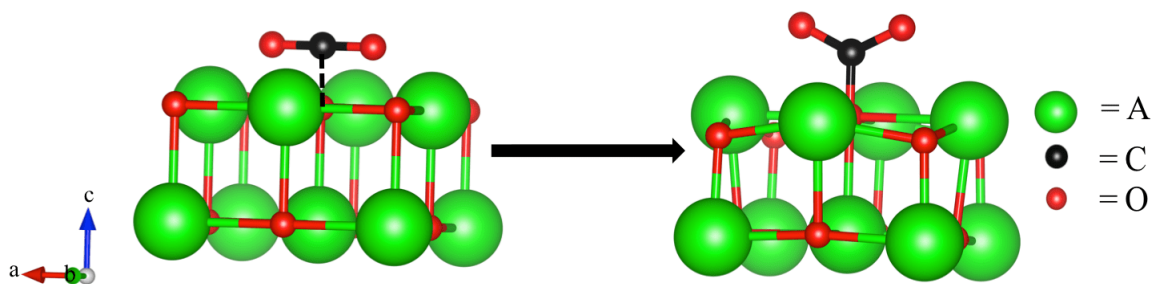
Figure 5.3: The crystal structure of the AO compounds (A = Ca, Sr and Ba) with CO_2 above on the left, with the optimised surface carbonate on the cluster on the right.
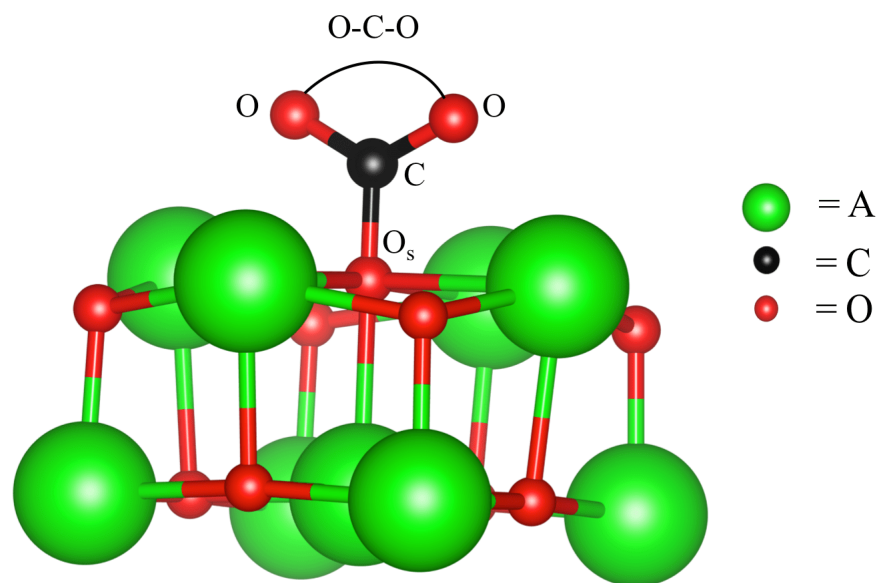
Figure 5.4: The optimised carbonate on the AO (A = Ca, Sr and Ba) cluster. The areas where the O-C-O $^\circ$ angles and C-O$_S$ bond lengths are measures are shown.

Each of the AO (Ca, Sr and Ba) surfaces have been investigated in reaction with CO_2 to form the carbonate ion coordinated to the A cation. In each case the starting distance between the carbon within CO_2 and an oxide on the surface cluster has been set according to values reported by either Schneider[262] or Karlsen et $al.$, Table 5.1.[263] CO_2 over the cluster and the overall system would be optimised to its lowest energy state. This would then result in a carbonate forming on top of the surface. A comparison of the differences in surface adsorption energy values, as well as bond lengths and angles for $SrCO_3$ to computational values reported by Schneider and Karlsen et $al.$ is reported in Tables 5.2 and 5.3.[262, 263]

Table 5.1: The C-O$_s$ bond lengths for carbonates formed on top AO (A = Ca, Sr and Ba) surfaces reported by Schneider[262] and Karlsen et $al.$.[263]

Compound	C-O$_s$, Å(Schneider)	C-O$_s$,Å(Karlsen)
CaO	1.384	1.49
SrO	1.370	1.46
BaO	1.358	1.44

Table 5.2: The carbon-oxide bonds, angles and surface adsorption energy calculated for SrO compared to computational values reported by Schneider.[262]

Values	Schneider (1)	Calculated values (2)	Difference (1) - (2)
O_s-C distance Å	1.37	1.392	-0.022
C-O distance Å	1.276	1.267	0.009
O-C-O angle °	127.5	127.0	0.5
Adsorption energy kJ mol^{-1}	-188.1	-163.0	-25.1

Table 5.3: The carbon-oxide bonds, angles and surface adsorption energy calculated for SrO compared to computational values reported by Karlsen *et al.*.[263]

Values	Karlsen(1)	Calculated values (2)	Difference (1) - (2)
O_s-C distance Å	1.46	1.392	-0.068
C-O distance Å	1.24	1.267	-0.027
O-C-O angle °	132.0	127.0	5.0
Adsorption energy kJ mol^{-1}	-123.0	-163.0	40

In the case of $SrCO_3$, the differences in adsorption energy value is between 40 to -25 kJ/mol in comparison to those reported within the literature. The bond length and angles for the carbonates are also in close agreement. Results reported by Schneider appear to be in closer agreement to those calculated in this project compared to those determined by Karlsen *et al.*. This same methodology was then applied for the CaO and BaO systems, Tables 5.4 to 5.7.

Table 5.4: The carbon-oxide bonds, angles and adsorption energy calculated for CaO compared to the values reported by Schneider.[262]

Values	Schneider (1)	Calculated values (2)	Difference (1) - (2)
O_s-C distance Å	1.384	1.413	-0.029
C-O distance Å	1.270	1.262	0.008
O-C-O angle°	129.1	128.6	0.5
Adsorption energy kJ mol^{-1}	-129.7	-124.0	-5.7

Table 5.5: The carbon-oxide bonds, angles and adsorption energy calculated for CaO compared to the values reported by Karlsen *et al.*.[263]

Values	Karlsen(1)	Calculated values (2)	Difference (1) - (2)
O_s-C distance Å	1.490	1.412	0.078
C-O distance Å	1.230	1.262	-0.032
O-C-O angle °	134.0	128.6	5.6
Adsorption energy kJ mol^{-1}	-87.0	-124.0	37

Table 5.6: The carbon-oxide bonds, angles and adsorption energy calculated for BaO compared to the values reported by Schneider.[262]

Values	Schneider (1)	Calculated values (2)	Difference (1) - (2)
O_s-C distance Å	1.358	1.374	-0.018
C-O distance Å	1.282	1.272	0.010
O-C-O angle °	126.0	125.6	0.4
Adsorption energy kJ mol^{-1}	-225.9	-192.6	-33.3

Table 5.7: The carbon-oxide bonds, angles and adsorption energy calculated for BaO compared to the values reported by Karlsen *et al.*.[263]

Values	Karlsen(1)	Calculated values (2)	Difference (1) - (2)
O_s-C distance Å	1.44	1.37	0.07
C-O distance Å	1.24	1.27	-0.03
O-C-O angle°	130.4	125.6	4.8
Adsorption energy kJ mol^{-1}	-158.2	-192.6	34.4

The investigation into how CO_2 forms into a carbonate over each metal oxide surface has shown various trends. Firstly in each case the initial distance of the CO_2 to the surface oxide (C-O_s distance) does not effect the adsorption energy outcome. This is likely due to CO_2 being free as it is optimising without constraints and able to form a carbonate. When comparing the adsorption energy values and carbonate structure (bonds and angles), the calculated values are in greater agreement with computational values reported by Schneider than those by Karlsen *et al.*, with Tables 5.8 and 5.9 showing the differences in surface adsorption energy values.

Table 5.8: The difference in adsorption energy (kJ mol^{-1}) values on the AO (A = Sr, Ca and Ba) calculated to those reported by Schneider.[262]

Metal oxide surface	Schneider (1)	Calculated values (2)	Difference (1) - (2)
SrO	-188.1	-163.0	-25.1
CaO	-129.7	-124.0	-5.7
BaO	-225.9	-192.6	-33.3

Table 5.9: The difference in adsorption energy (kJ mol^{-1}) values on the AO (A = Sr, Ca and Ba) calculated to those reported by Karlsen *et al.*.[263]

Metal oxide surface	Karlsen (1)	Calculated values (2)	Difference (1) - (2)
SrO	-123.0	-163.0	40.0
CaO	-87.0	-124.0	37.0
BaO	-158.2	-192.6	34.4

Also of note is that the adsorption energy values calculated for all systems were lower than those reported by Schneider, and greater than those determined by Karlsen *et al.*.[262, 263]

The difference in values compared to those reported by Schneider and Karlsen *et al.* could be attributed to the different computational methods. Schneider used a periodic supercell with plane wave DFT within the Vienna *ab initio* simulation package (VASP) code program.[264] This software allows DFT calculations to be carried out specifically for solid state materials, and can therefore be applied to metal-oxide systems. Schneider also looked at layers of SrO in a periodic supercell for optimising with CO_2. This is very different to the model carried out in this project that uses isolated cluster layers.

In the case of programs both Orca and VASP are able to use DFT methods to study clusters of solids. Orca was the only one of these programs available and as a result was used within this project. In the terms of the functionals both PBE and PW91, which Schneider used, belong to the class of generalized gradient approximations (GGA), which rely on the electron density and gradient.[175] PBE itself is in fact based upon PW91 but is simplified to allow the functional to be used for studying a wider variety of properties. This does make standard PBE less accurate compared to PW91 at a cost of allowing this to be used across a variety of applications. In response to this a resolution of identity, RI correction is used along side PBE. This accountants for the treatment of the two-electron Coulomb repulsion integrals and the response of an electron in an external field.[253]

In the case of Karlsen *et al.* the Gaussian98 software package was used. This operates via an embedded cluster model through embedding *ab initio* mode potentials (EAIMP) along with the B3LYP functional and Dunning D95V basis sets. The hybrid functional, B3LYP itself

incorporates exact Hartree-Fock exchange energy along with exchange-correlation obtained from other functionals.[176] This differs to the likes of PBE which has been used within this study, which is a purely *ab initio* functional requiring no empirical values. The limits of B3LYP is that as it is tailored using empirical values for calculating accurate results. That it may only work well for systems that it has been specifically suited to. This means that B3LYP can have limitations for studying large scale systems and surfaces as it no longer approaches the ground uniform electron gas limit.[265]

In summary, the formation of a carbonate atop the AO (A = Ca, Sr and Ba) surfaces has been carried out using DFT methods within the software package Orca. This was done using a surface layer cluster approach to provide a "simplistic" case study of determining the adsorption energy and carbonate structure. The values for adsorption energies varied from the literature by -5.7 to 50 kJ mol^{-1} depending on the type of surface. If the differences in values reported by Schneider are used this gives an uncertainty average of $\pm$ 21.4 kJ mol^{-1} which is lower than using values by Karlsen *et al.* at $\pm$ 37.1 kJ mol^{-1}. The next step after the surface reactions was to study the bulk formation of $SrCO_3$ from SrO and CO_2.

5.3.2 Reaction of CO_2 within the bulk towards $SrCO_3$ and $Sr_2CuO_2CO_3$

5.3.2.1 Reaction of CO_2 with SrO

Following the AO (A = Ba, Sr and Ca) surface reactions, the next step was the reaction of CO_2 within the bulk of SrO. This was to provide a thermodynamic study for $SrCO_3$ formation by determining the enthalpy of reaction, ΔH_{rxn} within the bulk phase. This methodology when developed and refined would then be applied for the reaction of Sr_2CuO_3 with CO_2 towards $Sr_2CuO_2(CO_3)$.

The crystal structure of $SrCO_3$ reported by Villiers was used to construct a model of SrO groups by removing the CO_2 atoms.[221] Through a backward approach this provided a representation of SrO groups within the $SrCO_3$ unit cell. The bond lengths in the SrO groups were also set to match those reported for the crystal structure of SrO.[266] To determine the ΔH_{rxn}, similar methods have been used as with those reported by Duan *et al.* and Zhang *et*

al..[267, 268] This involves all atoms being free to optimise and being in a supercell, 2×2×2 of the original SrCO$_3$ unit cell parameters.

The purpose of a supercell is to provide adequate space for the atoms during optimisation, and to prevent undesired interactions taking place from adjacent periodically repeated unit cells. In the 2×2×2 cell only in the *b* direction were the groups of SrO and CO$_2$ repeated. This meant there was a total of 8 groups of SrCO$_3$ within the unit cell after optimisation. This was double the amount of groups reported in the crystal structure of SrCO$_3$ which only had 4. The additional groups of SrCO$_3$ were included so that the system would behave as a crystalline solid and avoid the risk of groups behaving like isolated molecular SrCO$_3$. The overall supercell had 8 CO$_2$ molecules and SrO groups optimised towards 8 SrCO$_3$ with the step by step process shown in Figure 5.5.
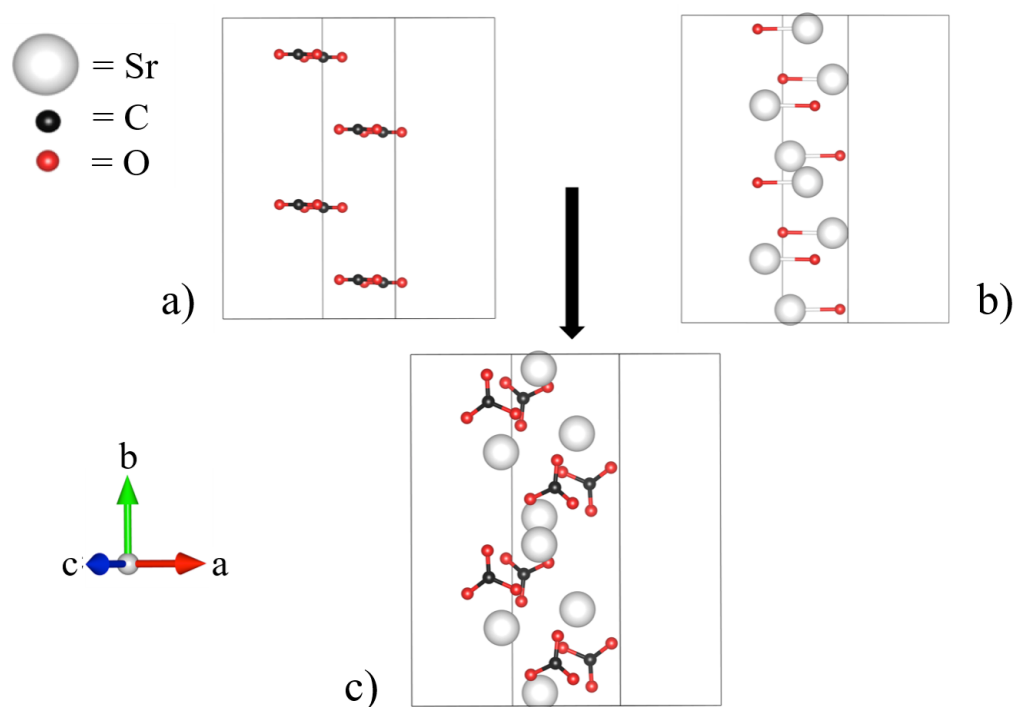
Figure 5.5: The structures of 8SrO groups, a), 8CO$_2$ molecules b) which have been optimised and resulted in formation of the 8SrCO$_3$ groups, c).

The ΔH_{rxn} was determined from the difference between optimised SrCO$_3$ from that of the SrO and CO$_2$ groups using Equation 5.1. As the calculation resulted in 8SrCO$_3$ groups the overall change in the energy was the ΔH_{rxn} average for single SrCO$_3$ formation. Using the

same methodology four different exchange-correlation, E_{xc} functionals were employed for calculating this reaction. These functionals were PBE, PBEsol, TPSS and revTPSS which were also used for studying similar reactions by Zhang *et al.*.[268]

In order to determine an accurate value for the ΔH_{rxn}, corrections have been applied to account for the zero-point energy, U_{ZPE} as well as the rotational, translation, $U_{trans+rot}$ and vibrational contributions, U_{vib}. The determination of these corrections have been discussed in Chapter 2.

The vibrational frequencies were calculated for each of the optimised structures. This was to first confirm that the structures had been optimised to the lowest energy state. This would result in all positive frequencies. Secondly to use the vibrational frequencies for determining the U_{ZPE} and U_{vib} energy corrections. The vibrational frequencies were determined using the same parameters as with the optimisation calculations. In each $SrCO_3$ group 5 atoms were free to be optimised. This when using the 3N-6 rule would mean 9 frequencies would be reported. However, for this study only the frequencies belonging to the carbonate groups, 6 in total, were used and compared to experimental values. The calculated vibrational frequencies for the carbonate groups have been presented in Tables 5.10 to 5.13 and compared to experimental values reported by Krishnamurti to asses the methods level of accuracy.[222]

Table 5.10: The harmonic frequencies of $SrCO_3$ calculated using the PBE functional compared to experimental values determined by Krishnamurti using Raman spectroscopy.[222]

Vibrational frequency cm^{-1}	PBE functional (1)	Literature (2)	Difference (1) - (2)
Symmetric stretching ν_1	1015	1074	-59
Symmetric bending ν_2	856	855	1
Asymmetric stretching ν_3	1569	1447	122
Asymmetric stretching ν_3'	1283	1438	-150
Asymmetric bending ν_4	798	711	87
Asymmetric bending ν_4'	753	701	52
RMSD	N/A	N/A	92

Table 5.11: The harmonic frequencies of $SrCO_3$ calculated using the PBEsol functional compared to experimental values determined by Krishnamurti using Raman spectroscopy.[222]

Vibrational frequency cm^{-1}	PBEsol functional (1)	Literature (2)	Difference (1) - (2)
Symmetric stretching v_1	988	1074	-86
Symmetric bending v_2	825	855	-30
Asymmetric stretching v_3	1595	1447	148
Asymmetric stretching v_3'	1302	1438	-136
Asymmetric bending v_4	702	711	-9
Asymmetric bending v_4'	662	701	-39
RMSD	N/A	N/A	90

Table 5.12: The harmonic frequencies of $SrCO_3$ calculated using the TPSS functional compared to experimental values determined by Krishnamurti using Raman spectroscopy.[222]

Vibrational frequency cm^{-1}	TPSS functional (1)	Literature (2)	Difference (1) - (2)
Symmetric stretching v_1	892	1074	-182
Symmetric bending v_2	799	855	-56
Asymmetric stretching v_3	1470	1447	23
Asymmetric stretching v_3'	1174	1438	-264
Asymmetric bending v_4	678	711	-33
Asymmetric bending v_4'	642	701	-59
RMSD	N/A	N/A	136

Table 5.13: The harmonic frequencies of $SrCO_3$ calculated using the revTPSS functional compared to experimental values determined by Krishnamurti using Raman spectroscopy.[222]

Vibrational frequency cm^{-1}	revTPSS functional (1)	Literature (2)	Difference (1) - (2)
Symmetric stretching ν_1	900	1074	-174
Symmetric bending ν_2	798	855	-57
Asymmetric stretching ν_3	1481	1447	34
Asymmetric stretching ν_3'	1186	1438	-252
Asymmetric bending ν_4	675	711	-36
Asymmetric bending ν_4'	640	701	-61
RMSD	N/A	N/A	131

The comparison values for the different E_{xc} functionals show that the asymmetric stretching ν_3 and ν_3' had the highest level of difference ranging from 122 to 264 cm^{-1}. The computational vibrations behave harmonically, this means that the degenerating of the chemical bonds as they are being stretched and compressed is not considered. The asymmetric stretching mode ν_3 shows for the carbonates one of the C-O bonds being stretched and extended. This is from both the oxygen and carbon being moved further away from each other as shown in Figure 1.31. This will result in weaker bond strength and lower wavenumber values. When PBE and PBEsol where used, the computational vibrations showed the calculated ν_3 values to be greater than experimental ones. This will be a result of the computational methods not accounting for the chemical bonds weakening as they are being stretched. The ν_3' values calculated however, were found to be lower than the experimental values. This could be due to this vibration showing two of the C-O bonds decreasing whilst the other is increasing. It is possible that PBE and PBEsol underestimate the bond strength increasing as the carbon and oxygens are being pushed closer together.

In the case of TPSS and revTPSS the ν_3' frequencies show the largest difference with values lower than experimental ones by up to 264 cm^{-1}. This could be due to how the method accounts for two sets of C-O bonds being compressed whilst the other is being stretched. As with the PBE based methods this could be due to the method being unable to account for how

the strength of the C-O bonds increase as they are being reduced in length. The symmetric stretching v_1 frequency results in all C-O bonds being stretched at once. The calculated values were also found to be lower than experimental ones by approximately 180 cm^{-1}. This could be due to TPSS and revTPSS overestimating how weak the chemical bonds become when they are being stretched from the vibrations.

Using the vibrational frequencies and thermal corrections the zero-point energy U_{ZPE}, and the vibrational contribution U_{vib} could be determined. In the case of just the CO_2 molecules the translation and rotational $U_{trans+rot}$ contributions as well as the ideal gas identity, $PV = RT$ were included. When determining the correction values the temperature was set to the same value as the experimental ΔH_{rxn} results at 298.5 K and 1 atm pressure.[122] Using these values, the ΔH_{rxn} for $SrCO_3$ was determined using the different functionals and has been compared to the experimental values in Table 5.14.

Table 5.14: The enthalpy of reaction ΔH_{rxn} values calculated using the different functionals. All ΔH_{rxn} values are reported in kJ/mol at 298.5 K and 1 atm.

Functional	Overall ΔH_{rxn}	ΔH_{rxn} per CO_2	Difference to exp. (-234.6 kJ/mol[122])
PBE	-1473.5	-184.2	50.4
PBEsol	-1715.3	-214.3	20.2
TPSS	-875.1	-109.4	125.2
revTPSS	-965.0	-120.6	114.0

The resulting ΔH_{rxn} values show PBEsol to be the most accurate of the fucntionals used, with a difference towards experimental values at 8.6 %. This is followed by PBE at 21.5 %, revTPSS (48.6 %) and TPSS (53.4 %). The relative performance of these functionals are similar to those reported by Zhang *et al.* with absolute relative mean errors at 31.8 %, 16.3 %, 115.5 % and 171.6 % for PBE, PBEsol, TPSS and revTPSS respectively.[268] The only major difference is that the errors between calculated and experimental values in this project are lower than those reported by Zhang *et al.*.[268] This maybe due to the different models used in this project to represent the formation of $SrCO_3$. It could also be a result of the type of reactions being studied. Zhang *et al.* calculated the reactions of AO + CO_2 = ACO_3

and $A(OH)_2 + CO_2 = ACO_3 + H_2O$ (A = Mn, Ni, Zn and Cd), all transition metals forming transition metal carbonates.[268] None of the reactions studied by Zhang *et al.* are the same as those within this project that focuses on alkaline earth metal based compounds. Despite this however, the general trend remains the same with PBEsol being the most accurate followed by PBE and finally TPSS and revTPSS.

Using the reaction of SrO and CO_2 towards $SrCO_3$ in the bulk phase as a case study. This was to firstly devise a methodology for studying bulk carbonate formation reactions, and secondly, to compare the accuracy of four different types of E_{xc} functionals (PBE, PBEsol, TPSS and revTPSS). The accuracy of these functionals was determined through calculating the ΔH_{rxn} and vibrational frequencies of $SrCO_3$, compared to experimental results. This type of study for the known reaction of $SrCO_3$ formation is imperative as no experimental data for the ΔH_{rxn} between CO_2 and Sr_2CuO_3 with $Sr_2CuO_2(CO_3)$ as a product is available. Table 5.15 shows the RMSD for each of these functionals for the ΔH_{rxn} and vibrational values.

Table 5.15: Difference of calculated ΔH_{rxn} values to experimental, as well as RMSD for the vibrational frequencies for the $SrCO_3$ groups.

Functional	ΔH_{rxn} % difference	Vibrational frequencies RMSD cm^{-1}
PBE	21.5	92
PBEsol	8.6	90
TPSS	53.4	136
revTPSS	48.6	131

PBEsol was able to calculate an ΔH_{rxn} value and vibrational frequencies for $SrCO_3$ closest to experimental results. This suggests that in determining the ΔH_{rxn} for the novel reaction of Sr_2CuO_3 with CO_2 towards $Sr_2CuO_2(CO_3)$, that this type of functional is the most likely to calculate the most accurate set of results.

5.3.2.2 Reaction of CO_2 with Sr_2CuO_3

Sr_2CuO_3 directly reacting with CO_2 with the formation of $Sr_2CuO_2(CO_3)$ has been investigated using computational methods via periodic calculations. In order to study this reaction two aspects had to be considered, a) the structural rearrangement of Sr_2CuO_3 reacting with CO_2 giving $Sr_2CuO_2(CO_3$ b) the carbonate formation within the structure. Both of these have been investigated through a thermodynamic model of the overall reaction.

Theoretical modeling of the reaction was designed to be as accurate as possible. In this the initial structure of Sr_2CuO_3, reported by Weller and Lines was used as the starting point.[88] In the case of $Sr_2CuO_2(CO_3)$ the crystal structure reported at temperatures of over 300 °C by Nakata *et al.* was used.[117] It is proposed that this will be the structure the oxide carbonate will adopt as it is formed from Sr_2CuO_3 reacting with CO_2 at 1000 °C. This choice in structure acts to make the theoretical model as accurate as possible. The structures of Sr_2CuO_3 and $Sr_2CuO_2(CO_3)$ for the calculations are shown in Figure 5.6.
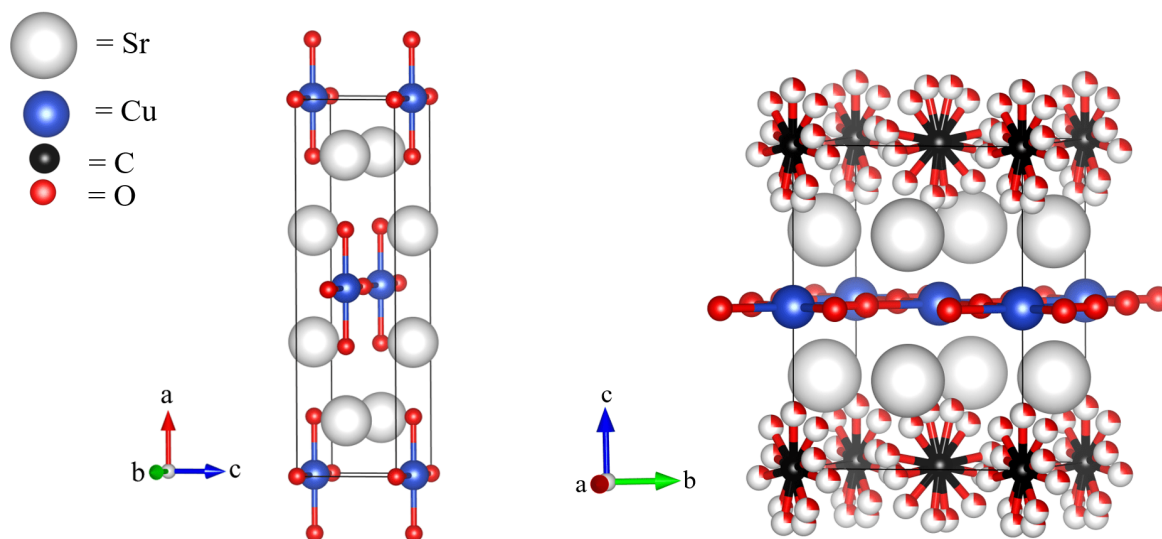
Figure 5.6: Structural Sr_2CuO_3 (left) and the high temperature (> 300°C) structure of $Sr_2CuO_2(CO_3)$ (right).[88, 117]

In the terms of structural rearrangement one of the important factors to consider is that the same number of atoms are maintained. Using the Wyckoff sites for Sr_2CuO_3 reported by Weller and Lines it was found that this unit cell contains 12 atoms in total, 4Sr, 2Cu and

6O.[88] This gives an overall composition of $Sr_4Cu_2O_6$ from the formula units per cell Z, being equal to 2. $Sr_2CuO_2(CO_3)$ reported by Nakata et $al.$ was also found to have Z = 2, $Sr_4Cu_2O_4(CO_3)_2$.[117] This shows that during the structural changes 2 equivalents of CO_2 were needed to be inserted into Sr_2CuO_3 to optimise towards $Sr_2CuO_2(CO_3)$.

As seen from Figure 5.6, one of the structural changes is from the oxides within the CuO_4 groups which results in oxides being released. This rearrangement has been found to occur in examples of anion substitution with $Sr_{2-x}A_xCuO_3$ (A = Ba and Ca) compounds as reported by Francesconi et $al.$ for the incorporation of F^- anions to give $Sr_{2-x}A_xCuO_2F_{2+\delta}$, Figure 5.7.[93]
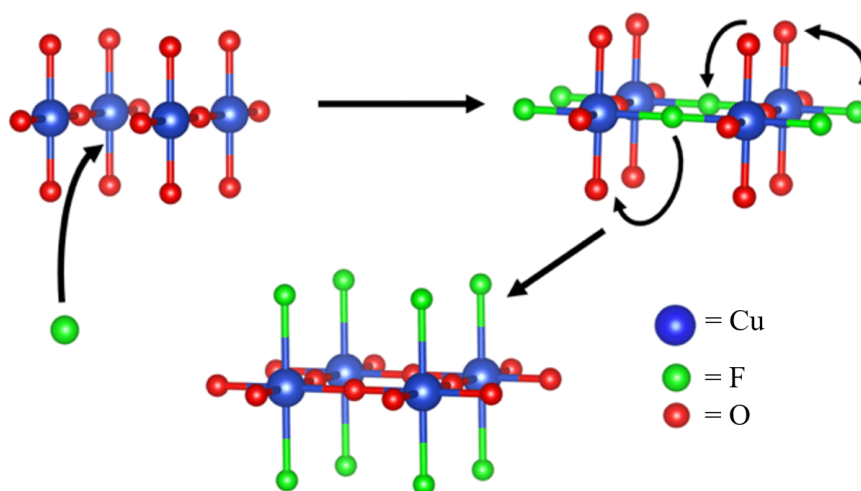
Figure 5.7: Structural rearrangement of Sr_2CuO_3 from the incorporation of F^- anions to form CuO_2 planes within $Sr_2CuO_2F_{2+\delta}$.

It is proposed that the reaction of $Sr_2CuO_3 + CO_2 = Sr_2CuO_2(CO_3)$ follows a similar structural rearrangement. In this case an oxide from the rearranged CuO_2 groups is made available to react with CO_2 towards forming a carbonate. As a result, the direct reaction between Sr_2CuO_3 and CO_2 has been treated as an overall anion incorporation rather than substitution reaction.

Using the structures of Sr_2CuO_3 and $Sr_2CuO_2(CO_3)$ as starting and end points a step by step structural rearrangement process was proposed. Figure 5.8 shows Sr_2CuO_3 alongside a structure which has the coordinates and unit cell parameters of $Sr_2CuO_2(CO_3)$ minus CO_2 in the form of Sr_2CuO_2-O.
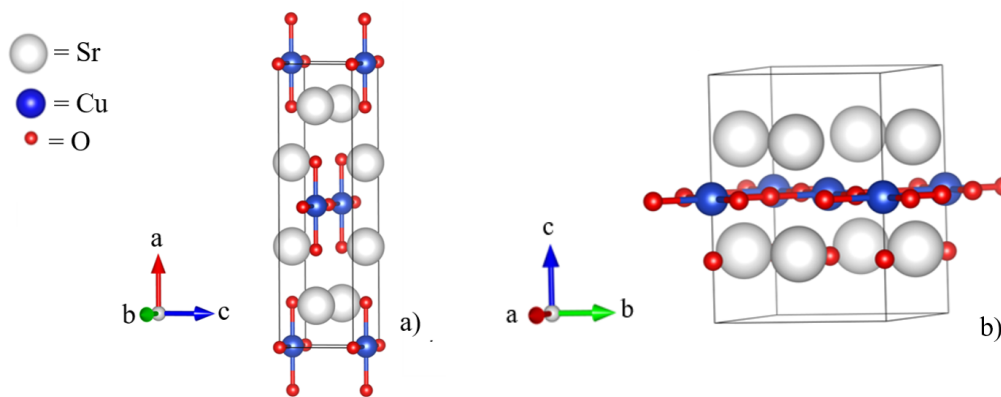
Figure 5.8: Structures of a) Sr_2CuO_3 and b) Sr_2CuO_2-O.

The contribution from each atom is shown in Table 5.16. This is to highlight that the overall formula, $Sr_4Cu_2O_6$ has been maintained with the same number of atoms remaining constant.

Table 5.16: Contribution of each atom to the overall unit cell formula for Sr_2CuO_3 and Sr_2CuO_2-O.

Atoms	Sr_2CuO_3	Sr_2CuO_2-O
Sr	$1/2 \times 8 = 4$	$1/2 \times 8 = 4$
Cu	$1/2 \times 2 + 1/4 \times 4 = 2$	$1 + 1/4 \times 4 = 2$
O	$1/8 \times 8 + 1/2 \times 8 + 1 = 6$	$1 \times 5 + 1/4 \times 4 = 6$

The next step was to have a structure of Sr_2CuO_2-O with two CO_2 groups inserted and repeated through symmetry. As with the $SrCO_3$ model these can be optimised over specific SrO sites that are repeated through the periodic unit cells towards forming carbonates. These different structures are shown in Figure 5.9.
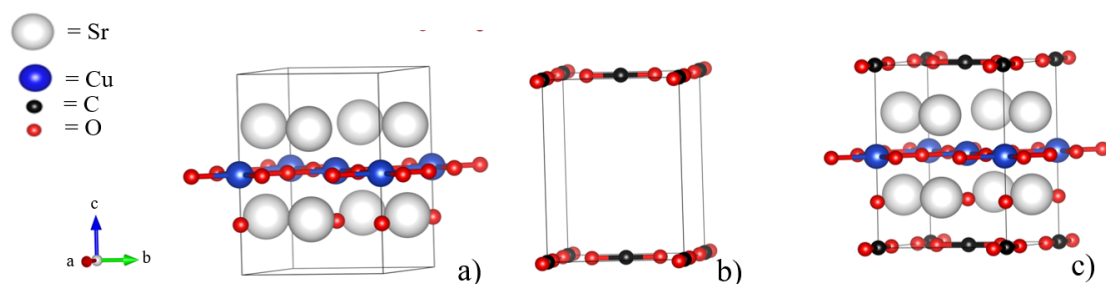
Figure 5.9: Structures of a) Sr_2CuO_2-O, b) CO_2 and c) Sr_2CuO_2-O with CO_2. These all have the unit cell parameters of $a = b = 5.54364$ Å and $c = 7.53823$ Å with α, β and $\gamma = 90\,^\circ$.

The optimised energy values from the structure of Sr_2CuO_3 in Figure 5.8 as well as those from Figure 5.9 were used to calculate the $\Delta H_{structure}$ and $\Delta H_{carbonate}$. In the case of Sr_2CuO_3 two types of oxides from the structure can be freed from the structural rearrangement in Figure 5.7. The freed oxide can then be used to react directly with CO_2 towards forming the carbonate groups. The different oxides that could be freed from the structural rearrangement have been investigated to provide an in-depth understanding of the structural rearrangement and overall reaction pathway. The two types of oxides which could be freed are shown in Figure 5.10.
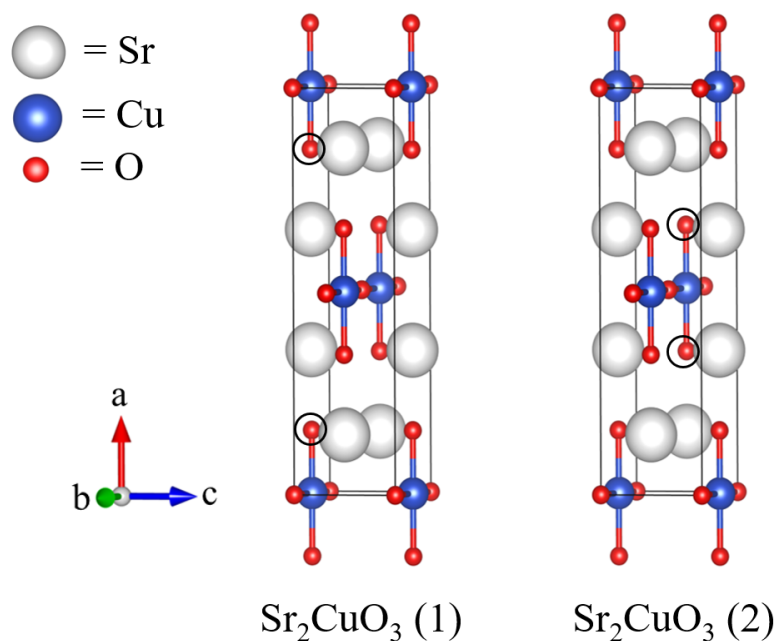
Figure 5.10: The two different oxide groups highlighted with the black circles. These could each be used to form a carbonate in the structure of $Sr_2CuO_2(CO_3)$.

As a result, the optimised energy value for Sr_2CuO_3 has been determined using the different oxides, 1) at (0.1547, 0.5000, 0.0000) and (0.8453 0.5000 0.0000), and 2) at (0.6547, 0.0000, 0.5000) and (0.3453 0.0000 0.5000). The difference in the type of oxide used only effects the ΔH_{rxn} and $\Delta H_{structure}$.

The previous study with $SrCO_3$ showed that PBE and PBEsol calculated ΔH_{rxn} values with the greatest levels of accuracy towards experimental results. This level of performance when compared to TPSS and revTPSS was also reported by Duan *et al.* when they studied $SrCO_3$ formation.[267] As a result, only these functionals were used for studying the bulk formation of the oxide carbonate. The optimised structure of $Sr_2CuO_2(CO_3)$ is shown in Figure 5.11 which displays how the carbonate groups were determined with one at the origin and the other in the *c*-axis corners that are repeated through symmetry.
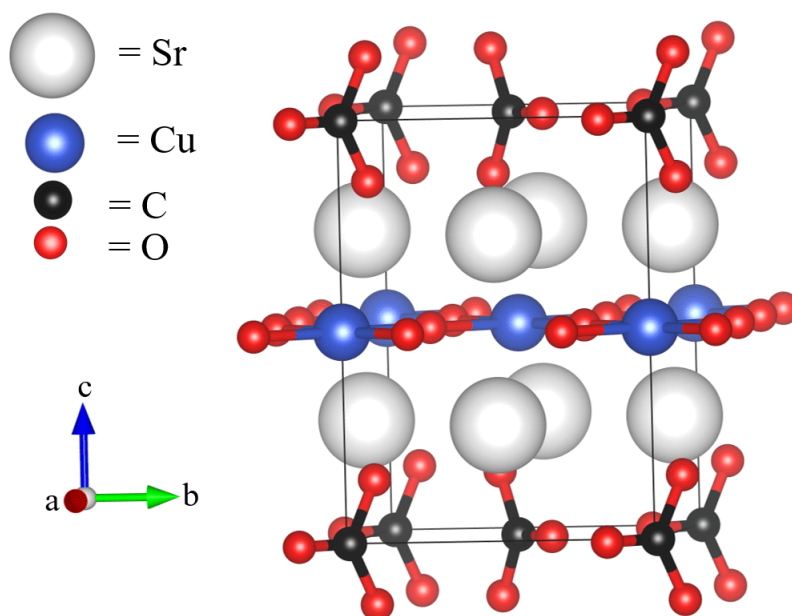
Figure 5.11: Optimised $Sr_2CuO_2(CO_3)$ type structure from Sr_2CuO_2-O optimising with CO_2.

The vibrational frequencies of these groups were used and compared to those of $Sr_2CuO_2(CO_3)$ reported by Armstrong et al..[207] The overall average frequencies calculated using PBE and PBEsol for the two sets of carbonates in $Sr_2CuO_2(CO_3)$ are reported in Tables 5.17 and 5.18. Table 5.19 shows the RMSD values for the calculated results towards both those reported by Armstrong et al..[207] as well as experimental values reported in this project.

Table 5.17: The harmonic frequencies of $Sr_2CuO_2(CO_3)$ calculated using PBE compared to experimental values determined by Armstrong et al..[207]

Vibrational frequency cm^{-1}	PBE functional (1)	Literature (2)	Difference (1) - (2)
Symmetric stretching ν_1	1119	1072	47
Symmetric bending ν_2	867	858	9
Asymmetric stretching ν_3	1462	1449	13
Asymmetric stretching ν_3'	1437	1412	-25
Asymmetric bending ν_4	819	704	115
Asymmetric bending ν_4'	726	699	27
RMSD	N/A	N/A	53

Table 5.18: The harmonic frequencies of $Sr_2CuO_2(CO_3)$ calculated using PBEsol compared to experimental values determined by Armstrong *et al.*.[207]

Vibrational frequency cm^{-1}	PBEsol functional (1)	Literature (2)	Difference (1) - (2)
Symmetric stretching ν_1	1067	1072	-5
Symmetric bending ν_2	831	858	-27
Asymmetric stretching ν_3	1466	1449	17
Asymmetric stretching ν_3'	1432	1412	20
Asymmetric bending ν_4	675	704	-29
Asymmetric bending ν_4'	657	699	-42
RMSD	N/A	N/A	26

Table 5.19: RMSD values for the harmonic frequencies of $Sr_2CuO_2(CO_3)$ calculated by PBE and PBEsol compared to values reproted by experimental values calculated by Armstrong *et al.*.[207] and within this project.

E_{xc} functional	Literature	Experimental
PBE	53	56
PBEsol	26	33

By assessing their performances, PBE and PBEsol are able to calculate average vibrational frequencies with RMSD values of 53 and 26 cm^{-1} respectively. Attempts at reducing the RMSD values have also been discussed using scaling factors within Chapter 6.

As with the $SrCO_3$ calculations the vibrational frequencies for all of the different structures have been used to determine the thermal corrections of U_{ZPE} and U_{vib}. In the case of just the CO_2 molecules the translation and rotational $U_{trans+rot}$ contribution and the ideal gas identity, $PV = RT$ were also included. These corrections were then applied to the optimised energies for calculating the various enthalpy values. Using Equations 5.2 to 5.5 the results from the two different functionals have been presented in Table 5.20. This also includes values for the two different oxides that could be used from Sr_2CuO_3.

Table 5.20: The ΔH_{rxn}, $\Delta H_{carbonate}$, single $\Delta H_{carbonate}$ and $\Delta H_{structure}$ reported in kJ/mol determined for the reaction of Sr_2CuO_3 and CO_2 towards $Sr_2CuO_2(CO_3)$.

Value	PBE	PBEsol
ΔH_{rxn} (1)	-1635.5	-1732.1
ΔH_{rxn} (2)	-1635.2	-1731.8
$\Delta H_{carbonate}$	-1040.0	-1089.7
Single $\Delta H_{carbonate}$	-520.0	-544.9
$\Delta H_{structure}$ (1)	-595.3	-642.4
$\Delta H_{structure}$ (2)	-595.0	-642.3

For the different starting oxides from Sr_2CuO_3, the enthalpy values show there to be a difference of approximately 0.3 kJ/mol for PBE, with PBEsol only showing a difference of 0.1 kJ/mol. These values could be a result of rounding up errors when considering the optimised energy values for each structure. Overall this does show that the type of starting oxide has a minimal effect on the overall values.

In the case of $\Delta H_{carbonate}$, PBE and PBEsol calculated values of -520.0 and -544.9 kJ/mol respectively. This shows that the $\Delta H_{carbonate}$ for a singular carbonate in $Sr_2CuO_2(CO_3)$ is over twice that for $SrCO_3$ determined both experimentally (-234.6 kJ/mol) as well as those within this project (PBE = -184.2 kJ/mol and PBEsol = -214.4 kJ/mol). The reason for the higher $\Delta H_{carbonate}$ values could be attributed to the carbonates being coordinated to the Cu cations. Miyazaki *et al.* reported that Cu expands its coordination number from a square planar polyhedral to a distorted octahedra in $Sr_2CuO_2(CO_3)$ in the presence of carbonates.[116] This has also been found to occur during the formation of other similar mixed anion compounds such as $Sr_2CuO_2F_{2+\delta}$ and $Sr_2CuO_{3+\delta}$.[93,92] By additionally coordinating to the Cu cations this could also make the reaction more favourable to form carbonates compared to just SrO groups reacting with CO_2 towards $SrCO_3$.

This series of calculations has also provided the opportunity to study and determine an enthalpy value for structural rearrangement, $\Delta H_{structure}$. The formation of $Sr_2CuO_2(CO_3)$ results in all atomic positions changing as well as the crystal system going from an orthorhom-

bic to tetragonal system. The $\Delta H_{structure}$ values are negative showing this to be as with the carbonate formation an exothermic reaction. Figure 5.12 shows a Born-Haber cycle of the reaction that displays how the ΔH_{rxn}, $\Delta H_{carbonate}$ and $\Delta H_{structure}$ were determined. The Born-Haber cycle has the initial structures of each model before being optimised. The difference in optimised energies are then used to determine the enthalpy values.
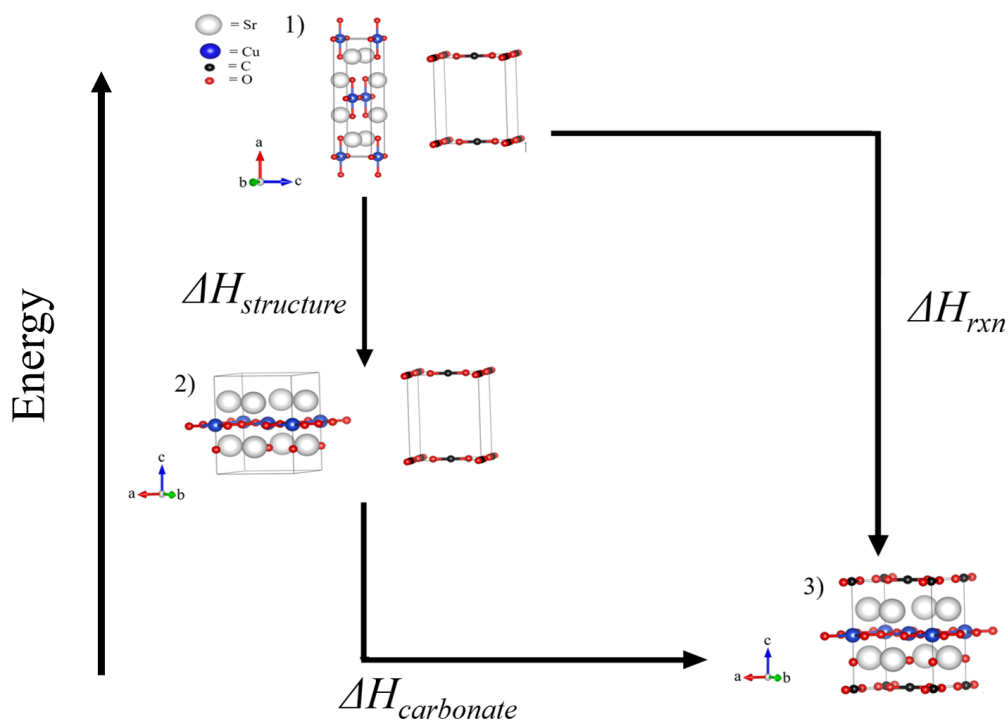
Figure 5.12: Born-Haber diagram showing the different stages of the overall reaction. 1) Sr_2CuO_3 with separate CO_2, 2) Sr_2CuO_2-O with separate CO_2 and 3) Sr_2CuO_2-O with inserted CO_2 with the enthalpies that are calculated shown.

For each of the enthalpy values, ΔH_{rxn} is calculated as the overall difference from optimised Sr_2CuO_3 and separate CO_2 from that of optimised Sr_2CuO_2-O with inserted CO_2. $\Delta H_{structure}$ is the difference between optimised Sr_2CuO_3 and Sr_2CuO_2-O. $\Delta H_{carbonate}$ is the difference of optimised Sr_2CuO_2-O and separate CO_2 from that of optimised Sr_2CuO_2-O with inserted CO_2. These values act to show that the exothermic overall reaction consists of structural rearrangement, $\Delta H_{structure}$ followed by carbonate formation, $\Delta H_{carbonate}$. Through measuring a heat flow vs temperature curve for a standard reaction of Sr_2CuO_3 with CO_2 towards $Sr_2CuO_2(CO_3)$ via TGA, Figure 5.13. The has been used to verify the thermodynamic be-

haviour of the reaction.
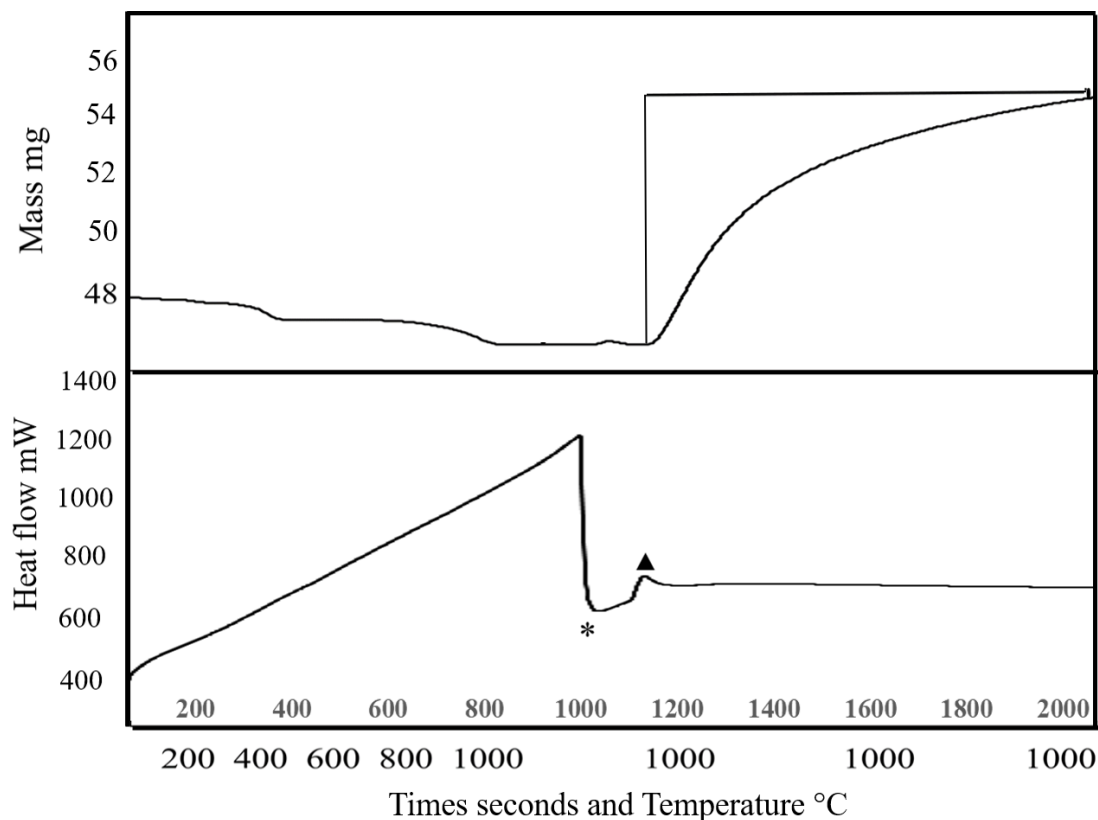
Figure 5.13: TGA curve of Sr_2CuO_3 reacting with CO_2 towards $Sr_2CuO_2(CO_3)$. Upper curve, mass against temperature, bottom curve, heat flow against temperature. The (*) marked peak shows a fall in the heat flow as a result of the temperature no longer rising. The (▲) peaks indicates heat being released from the reaction.

The upward peak (▲) shows an increase in the heat flow when CO_2 is introduced into the system. This will be from the formation of $Sr_2CuO_2(CO_3)$ taking place and indicates that it is an exothermic process. This is also the same point at which the mass of the sample increases. It is proposed that at this point structural rearrangement towards a Sr_2CuO_2-O type structure is occurring which allows CO_2 to react with SrO groups towards $Sr_2CuO_2(CO_3)$. After this peak the heat flow then plateaus for the rest of the reaction. This maybe due to no further reactions taking place.

The novel direct reaction of $Sr_2CuO_3 + CO_2 = Sr_2CuO_2(CO_3)$ has through theoretical calculations and experimental TGA data been proposed to be a overall two step exothermic

reaction. It is proposed that the reaction occurs via a two step procedure of structural rearrangement followed by carbonate formation. The limitations of the experimental process is that TGA is unable to determine enthalpy values from the peaks in the heat flow curve. This is from having no way to subtract the heat flow of the sample holder so only the heat flow curve of Sr_2CuO_3 reacting with CO_2 can be recorded. This type of experiment would require differential scanning calorimetry, DSC methods.[156, 269]

The direct synthesis of $Sr_2CuO_2(CO_3)$ from Sr_2CuO_3 and CO_2 showed that this reaction can result in side decomposition forming $SrCO_3$. As a result, the reaction was designed to be carried out at only 1000 °C for 15 minutes to reduce this occurring. It is only under these conditions that the structural rearrangement reaction can occur which is essential to avoid decomposition of the structure. This can then be followed by carbonation formation to lead towards $Sr_2CuO_2(CO_3)$.

5.4   Conclusion

Through a computational method the novel reaction between CO_2 and Sr_2CuO_3 towards $Sr_2CuO_2(CO_3)$, developed experimentally has been studied. This reaction is proposed to be a result of Sr_2CuO_3 going through structural rearrangement to allow the availability of SrO group for reacting CO_2 towards forming carbonates leading to $Sr_2CuO_2(CO_3)$.

Initial studies looked into the adsorption of CO_2 towards carbonates on AO (A = Ca, Sr and Ba) surfaces. This was then followed by bulk reactions between SrO and CO_2 towards $SrCO_3$. These acted as case studies to understand the carbonate formation process, as well as to verify a methodology for studying reactions within bulk phase. The formation of bulk $SrCO_3$ showed of the E_{xc} functionals that PBEsol would calculate a ΔH_{rxn} value with the lowest level of error at 8.6%, as well as vibrational frequencies with the lowest RMSD value.

Similar theoretical methods were then used to study the formation of $Sr_2CuO_2(CO_3)$ from Sr_2CuO_3 and CO_2. The enthalpy values calculated using PBEsol were, ΔH_{rxn} = -1732.1, $\Delta H_{structure}$ = -642.3 and $\Delta H_{carbonate}$ -544.9 kJ/mol. Using these results it is proposed that this is a exothermic reaction that consists of structural rearrangement followed by carbonate

formation. Experimental TGA results also indicated an exothermic reaction taking place between Sr_2CuO_3 and CO_2 at 1000 °C. The work in this project acts to provide an insight into determining the possible thermodynamics behavior and and structural changes that are occurring during novel chemical reactions. This also acts as an example on how theoretical methods could provide an in-depth study of a novel reaction that would be difficult via purely experimental methods.

Chapter 6

Scaling Factors for Vibrational Frequencies of $SrCO_3$ and $Sr_2CuO_2(CO_3)$

6.1   Vibrational behaviour of metal carbonate compounds

Some of the most abundant minerals and compounds are based on alkaline and alkaline earth metal carbonates. These take a variety of different forms such as Limestone ($CaCO_3$), Magnesite ($MgCO_3$) and Natrite (Na_2CO_3). As discussed in previous chapters, metal oxide based materials have been investigated for reacting with CO_2 towards metal carbonates. The reaction itself is via the basic $M\text{-}O^-$ groups being strongly attracted to CO_2 which is Lewis acidic in behaviour.[54, 123] Schneider studied how acidic gases such as CO_2 can react on the surface of alkaline earth metal oxides forming into a carbonate using DFT methods.[262] This work also showed how the shift in electron density from the solid acts to chemisorb the CO_2 onto the surface.

The different reaction processes of CO_2 can be monitored via vibrational frequencies. Examples of these types studies include CO_2 capture and reactions with heterogenous catalysts.[85, 270] During a chemical reaction, bonds will be broken, created or altered as a result of the shift in electron densities. Vibrational analysis can be used to monitor these changes from the conformation of a molecule or compound at each point of a reaction.

This PhD project has studied the direct reaction of CO_2 and Sr_2CuO_3 towards forming $Sr_2CuO_2(CO_3)$ through experimental and computational methods. This reaction has been proposed to be a result of the mixed metal oxide initially going through a structural rearrangement process. This results in SrO groups being made available to react with CO_2 towards forming carbonates leading towards $Sr_2CuO_2(CO_3)$. Using DFT methods the structural rearrangement and thermodynamics of the reaction has been discussed in Chapter 5 through determining the enthalpy of reaction, ΔH_{rxn}. The work discussed in this chapter is on using scaling factors to reduce the difference between calculated harmonic frequencies to experimental anharmonic ones. The effect of scaled vibrational frequencies on the enthalpy values for $SrCO_3$ formation has also been discussed.

6.2 Computational methodology

Periodic calculations were carried out within the *ab inito* program CP2K.[194] In the case of the $SrCO_3$ formation calculations, this had all atoms free to optimise and vibrate. For $Sr_2CuO_2(CO_3)$ only the atoms in CO_2 and selected oxides from Sr_2CuO_3 were free with all others constrained. The E_{xc} functionals used were the same as those used for determining the enthalpy values discussed in Chapter 5; PBE, PBEsol, TPSS and revTPSS.[177–180] The valence electrons were represented using the DZVP-MOLOPT-SR-GTH basis sets, a plane wave cutoff energy of 360 Ry, and the core-electrons with the Goedecker-Teter-Hutter GTH pseudopotentials for the core electrons.[254, 260] The optimisation of these systems were also carried out using the Broyden-Fletcher-Goldfarb-Shanno, BFGS algorithm.[261] All calculations were at T = 0 K.

6.2.1 Optimisation and vibrational calculations

Many of the compounds studied had their crystal structural information obtained from the inorganic crystal structural database, ICSD.[221] This provided reported positions of each atom within the solid. Using this information each compound was optimised to its lowest energy and most stable state. The optimisation of a compound has the electronic structure being altered until it reaches a specific level of convergence. This is based on a self consistent field

(SCF) methods which for these calculations has a value of 1×10^{-7} atomic units. Once the structure had reached convergence it would be in its lowest energy state. All compounds were first optimised before the vibrational frequencies were determined.

Once the ACO_3 (A = Sr, Ba and Ca) series and $Sr_2CuO_2(CO_3)$ were optimised to their lowest energy most stable state. CP2K was used to calculate the harmonic frequencies. These calculations used the reduced mass of the molecule μ and force constant k of the bonds when vibrating. The k is obtained via a second-order derivatives of the electronic energy with respect to the nuclear coordinates. This is described more in-depth in Chapter 2.

All types of calculations were carried out using the high-performance computer (HPC), Viper, at the University of Hull.

6.2.2 Scaling factors

Vibrational frequencies determined using *ab initio* methods can contain systematic errors resulting in differences towards experimental values. These can be caused from the harmonic treatment of the chemical bonds as they are vibrating. This generally results in calculated harmonic frequencies being greater than experimental anharmonic ones.[271] This is due to computational methods not considering the chemical bonds degenerating as they are vibrating. One of the ways to compensate for the differences towards experimental values is through using scaling factors on calculated harmonic results.[272, 273] Specific scaling factors have been designed for the different types of theory/basis-set combinations. Scaling factors are determined as the ratio difference between the experimental and computational frequencies. This ratio can then be used as a mathematical function to decrease the difference as shown in Equation 6.1, ν the anharmonic vibrational frequency, ω the harmonic vibrational frequency and s as the scaling factor.[274]

$$\nu = \omega s \tag{6.1}$$

A least-squares procedure with a data set of vibrational frequencies is used to determine linear scaling factors as shown in Equation 6.2.

$$s = \sum \omega_i v_i / \omega_i^2 \tag{6.2}$$

A scaling factors ability to decrease the difference between harmonic and anhamronic results is assessed by the RMSD value. This is through comparing the RMSD before and after applying the scaling factors to the vibrational frequencies.

Linear scaling factors can be unsuitable in cases where the difference between calculated and experiment values don't follow a linear trend. As a result, alternative methods have been designed for non-linear trends. Yoshisa *et al.* reported a Wavenumber-linear scaling, WLS method to accountant for the non-linear frequency differences.[275] This is through a comparison of the multiplied calculated and experimental frequencies v_i/ω_i, over the calculated ones, ω_i. This comparison can be used to produce an equation of a trendline as shown in Equation 6.3, a the slope and b the intercept. This can provide a WLS scaling factor to improve the comparison between calculated and experimental results, Equation 6.4.

$$v_i / \omega_i = a\omega_i + b \tag{6.3}$$

$$v_i = a\omega_i^2 + b\omega_i \tag{6.4}$$

Another type of approach was proposed by Sibaev and Crittenden using quadratic scaling methods.[276] This had the difference between the computational and experimental values, Δ_{anh} shown in Equation 6.5, compared to the calculated frequencies. This can then be rearranged to produce a quadratic scaling factor, Equation 6.6, to decrease the difference between calculated and experimental result.

$$\Delta_{anh} = \omega_i - v_i \tag{6.5}$$

$$v_i = \omega_i - a\omega_i^2 - b\omega_i \tag{6.6}$$

Another route towards quadratic scaling factors is through applying a polynomial trendline for the experimental results compared to the calculated ones. This can produce a quadratic scaling factor that is approximately the same as those determined using the previous two methods. This has been applied within this study as an improvement to the scaling factors purely determined through a linear approach.

Scaling factors were determined using the vibrational frequencies from the ACO_3 (A = Sr, Ba and Ca) series of compounds. This provided 18 data points in total for each functional. The equation of the line for the plotted data points was determined with a set intercept for both linear and quadratic factors. The scaling factors would then be applied to the frequencies of bulk $SrCO_3$ and $Sr_2CuO_2(CO_3)$.

6.3 Results and Discussion

6.3.1 Scaling factors for vibrational analysis of $SrCO_3$

6.3.1.1 Vibrational frequencies of ACO_3 (A = Ca, Ba and Sr) compounds

The ACO_3 (A = Sr, Ca and Ba) series reported by Villiers show the same type of structure with 4 sets of ACO_3 groups in a orthorhombic crystal system, Figure 6.1.[221]
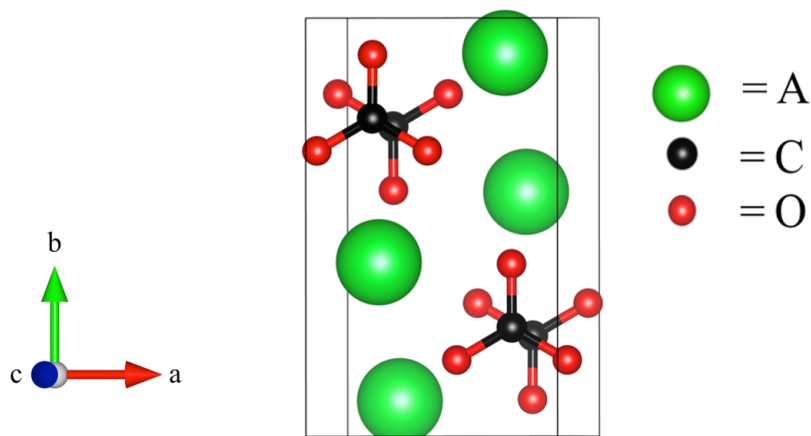
Figure 6.1: Crystal structure the ACO_3 (A = Sr, Ba and Ca) series.

The harmonic frequencies from each optimised ACO_3 compound has been calculated using each of the E_{xc} functionals. These values were then compared to those reported experimentally by Krishnamurti with the RMSD determined and shown in Tables 6.1-4.[222]

Table 6.1: The calculated harmonic frequencies of ACO_3 (A = Sr, Ba and Ca) compared to the experimental values (cm^{-1}) with the differences and RMSD presented using PBE.

Compounds	Frequencies	Experimental (1)	Theoretical (2)	(1) - (2)
$SrCO_3$	Symmetric stretching v_1	1074	1176	-102
	Symmetric bending v_2	855	902	-47
	Asymmetric stretching v_3	1447	1521	-74
	Asymmetric stretching v_3'	1438	1472	-34
	Asymmetric bending v_4	711	831	-120
	Asymmetric bending v_4'	701	822	-121
RMSD	N/A	N/A	N/A	90
$BaCO_3$	Symmetric stretching v_1	1061	1107	-46
	Symmetric bending v_2	852	886	-34
	Asymmetric stretching v_3	1421	1486	-50
	Asymmetric stretching v_3'	1409	1426	-17
	Asymmetric bending v_4	699	806	-107
	Asymmetric bending v_4'	691	789	-98
RMSD	N/A	N/A	N/A	67
$CaCO_3$	Symmetric stretching v_1	1086	1131	-45
	Symmetric bending v_2	854	907	-53
	Asymmetric stretching v_3	1463	1513	-50
	Symmetric stretching v_3'	1415	1461	-46
	Asymmetric bending v_4	716	808	-92
	Asymmetric bending v_4'	707	760	-53
RMSD	N/A	N/A	N/A	59

Table 6.2: The calculated harmonic frequencies of ACO_3 (A = Sr, Ba and Ca) compared to the experimental frequencies (cm^{-1}) with the differences and RMSD presented using PBEsol.

Compounds	Frequencies	Experimental (1)	Theoretical (2)	(1) - (2)
$SrCO_3$	Symmetric stretching ν_1	1074	1076	-2
	Symmetric bending ν_2	855	818	37
	Asymmetric stretching ν_3	1447	1512	-65
	Asymmetric stretching ν_3'	1438	1447	-9
	Asymmetric bending ν_4	711	718	-7
	Asymmetric bending ν_4'	701	662	27
RMSD	N/A	N/A	N/A	33
$BaCO_3$	Symmetric stretching ν_1	1061	1074	-13
	Symmetric bending ν_2	852	854	-2
	Asymmetric stretching ν_3	1421	1490	-69
	Asymmetric stretching ν_3'	1409	1438	-29
	Asymmetric bending ν_4	699	688	11
	Asymmetric bending ν_4'	691	654	27
RMSD	N/A	N/A	N/A	33
$CaCO_3$	Symmetric stretching ν_1	1086	1076	10
	Symmetric bending ν_2	854	820	-34
	Asymmetric stretching ν_3	1463	1531	-68
	Asymmetric Stretching ν_3'	1415	1426	-11
	Asymmetric bending ν_4	716	732	-16
	Asymmetric bending ν_4'	707	657	32
RMSD	N/A	N/A	N/A	35

Table 6.3: The calculated harmonic frequencies of ACO_3 (A = Sr, Ba and Ca) compared to the experimental frequencies (cm^{-1}) with the differences and RMSD presented using TPSS.

Compounds	Frequencies	Experimental (1)	Theoretical (2)	(1) - (2)
$SrCO_3$	Symmetric stretching ν_1	1074	1035	39
	Symmetric bending ν_2	855	820	35
	Asymmetric stretching ν_3	1447	1429	18
	Asymmetric stretching ν_3'	1438	1363	75
	Asymmetric bending ν_4	711	720	-9
	Asymmetric bending ν_4'	701	673	27
RMSD	N/A	N/A	N/A	40
$BaCO_3$	Symmetric stretching ν_1	1061	1023	38
	Symmetric bending ν_2	852	820	32
	Asymmetric stretching ν_3	1421	1403	18
	Asymmetric stretching ν_3'	1409	1341	68
	Asymmetric bending ν_4	699	706	-7
	Asymmetric bending ν_4'	691	674	17
RMSD	N/A	N/A	N/A	35
$CaCO_3$	Symmetric stretching ν_1	1086	1044	42
	Symmetric bending ν_2	854	820	34
	Asymmetric stretching ν_3	1463	1450	13
	Asymmetric stretching ν_3'	1415	1363	52
	Asymmetric bending ν_4	716	726	-10
	Asymmetric bending ν_4'	707	677	30
RMSD	N/A	N/A	N/A	34

Table 6.4: The calculated harmonic frequencies of ACO_3 (A = Sr, Ba and Ca) compared to the experimental frequencies (cm^{-1}) with the differences and RMSD presented using revTPSS.

Compounds	Frequencies	Experimental (1)	Theoretical (2)	(1) - (2)
$SrCO_3$	Symmetric stretching ν_1	1074	1040	34
	Symmetric bending ν_2	855	816	39
	Asymmetric stretching ν_3	1447	1440	7
	Asymmetric stretching ν_3'	1438	1371	67
	Asymmetric bending ν_4	711	711	0
	Asymmetric bending ν_4'	701	676	25
RMSD	N/A	N/A	N/A	36
$BaCO_3$	Symmetric stretching ν_1	1061	1025	36
	Symmetric bending ν_2	852	817	35
	Asymmetric stretching ν_3	1421	1411	10
	Asymmetric stretching ν_3'	1409	1359	50
	Asymmetric bending ν_4	699	701	-2
	Asymmetric bending ν_4'	691	672	19
RMSD	N/A	N/A	N/A	30
$CaCO_3$	Symmetric stretching ν_1	1086	1046	40
	Symmetric bending ν_2	854	817	37
	Asymmetric stretching ν_3	1463	1456	7
	Asymmetric stretching ν_3'	1415	1372	43
	Asymmetric bending ν_4	716	723	-7
	Asymmetric bending ν_4'	707	671	36
RMSD	N/A	N/A	N/A	32

The accuracy of each functional for calculating the vibrational behaviour can be assessed from the RMSD values. In the case of $SrCO_3$, PBEsol shows the lowest value followed by revTPSS, TPSS and PBE. The RMSD values for just the $SrCO_3$ calculations using each functional have been presented in Table 6.5.

Table 6.5: The RMSD values for the vibrational frequencies of $SrCO_3$ determined using each functional.

Functional	RMSD (cm^{-1})
PBE	90
PBEsol	33
TPSS	40
revTPSS	36

In the case of PBE and PBEsol the majority of calculated frequencies were found to be greater compared to experimental values. This is to be expected for harmonic frequencies that don't account for chemical bonds weakening as they are vibrating. However, this trend is not observed when TPSS and revTPSS were used, Tables 6.3 and 6.4, which showed these frequencies as generally being lower than experimental values. As all other parameters were maintained this will be a result of the different functionals used to describe the electronic interactions.

The performance of each functional to calculate the vibrational frequencies of $SrCO_3$ is the most important within this project. Table 6.5 shows that PBEsol calculates frequencies closest towards experimental values with the lowest RMSD of 33 cm^{-1}. As discussed in Chapter 5 this functional has also calculated an ΔH_{rxn} value, -214.3 kJ/mol which is the closets to the experimental value of -234.6 kJ/mol for $SrCO_3$.[122] The largest difference found in the vibrational frequencies was in the asymmetric stretching v^3 mode with an overestimation of 65 cm^{-1}. As stated previously these vibrations behave harmonically, which do not account for the bonds weakening as they are being stretched. This overestimation is seen for all stretching modes for PBEsol. The symmetric and one of the asymmetric bending modes show an underestimation between 20-40 cm^{-1}. This difference could be a result of how the bonds of each carbonate group are bending next to one another within the crystal structure.

The vibrational frequencies of $SrCO_3$ formed from SrO optimising with CO_2 in the $2\times2\times2$ unit cell, were calculated using each functional. These were compared to the experimental frequencies of $SrCO_3$ in Tables 6.6-9. A comparison of the RMSD values for the $1\times1\times1$ and

$2\times2\times2$ unit cells in Table 6.10 shows that the frequencies calculated in the $1\times1\times1$ unit cell are closest towards experimental values.

Table 6.6: Comparison of the experimental harmonic frequencies for $SrCO_3$ to those determined by the PBE functional for the $2\times2\times2$ (2) unit cells.

Vibrational frequency cm^{-1}	Experimental (1)	$2\times2\times2$ (2)	Difference (1) - (2)
Symmetric stretching ν_1	1074	1015	59
Symmetric bending ν_2	855	856	-1
Asymmetric stretching ν_3	1447	1569	-122
Asymmetric stretching ν_3'	1438	1283	155
Asymmetric bending ν_4	711	798	-87
Asymmetric bending ν_4'	701	753	-52
RMSD	N/A	N/A	92

Table 6.7: Comparison of the experimental harmonic frequencies for $SrCO_3$ to those determined by the PBEsol functional for the $2\times2\times2$ (2) unit cells.

Vibrational frequency cm^{-1}	Experimental (1)	$2\times2\times2$ (2)	Difference (1) - (2)
Symmetric stretching ν_1	1074	988	86
Symmetric bending ν_2	855	825	30
Asymmetric stretching ν_3	1447	1595	-148
Asymmetric stretching ν_3'	1438	1302	136
Asymmetric bending ν_4	711	702	9
Asymmetric bending ν_4'	701	701	0
RMSD	N/A	N/A	90

Table 6.8: Comparison of the experimental harmonic frequencies for $SrCO_3$ to those determined by the TPSS functional for the $2\times2\times2$ (2) unit cells.

Vibrational frequency cm^{-1}	Experimental (1)	$2\times2\times2$ (2)	Difference (1) - (2)
Symmetric stretching ν_1	1074	892	182
Symmetric bending ν_2	855	799	56
Asymmetric stretching ν_3	1447	1470	-23
Asymmetric stretching ν_3'	1438	1174	264
Asymmetric bending ν_4	711	678	33
Asymmetric bending ν_4'	701	642	59
RMSD	N/A	N/A	136

Table 6.9: Comparison of the experimental harmonic frequencies for $SrCO_3$ to those determined by the revTPSS functional for the $2\times2\times2$ (2) unit cells.

Vibrational frequency cm^{-1}	Experimental (1)	$2\times2\times2$ (2)	Difference (1) - (2)
Symmetric stretching ν_1	1074	900	-174
Symmetric bending ν_2	855	798	57
Asymmetric stretching ν_3	1447	1481	-34
Asymmetric stretching ν_3'	1438	1186	252
Asymmetric bending ν_4	711	675	-36
Asymmetric bending ν_4'	701	640	61
RMSD	N/A	N/A	131

Table 6.10: The RMSD (cm^{-1}) values for the vibrational frequencies of SrCO$_3$ determined using each functional for the 1×1×1 and 2×2×2 unit cells.

Functional	1×1×1	2×2×2
PBE	90	92
PBEsol	33	90
TPSS	40	136
revTPSS	36	131

The reason for the vibrational frequencies in the 1×1×1 unit cell being closer towards the experimental values is likely due to these systems using the original atomic positions reported by Villiers.[221] These calculations also show that PBEsol reports vibrational frequencies closest towards experimental values in all cases studied. This verifies the accuracy of PBEsol for studying these systems as the vibrational frequencies have an effect on the overall ΔH_{rxn} values.

6.3.1.2   Vibrational frequencies of carbonate groups in Sr$_2$CuO$_2$(CO$_3$)

Vibrational frequencies for the carbonate groups in Sr$_2$CuO$_2$(CO$_3$) were carried out in a similar way to bulk SrCO$_3$. The main difference was that in the oxide carbonate only two groups of carbonates that were repeated through symmetry and allowed to optimise. Based on the performance of each different functional only PBE and PBEsol were used for these calculations. This was based on the poor performance of TPSS and revTPSS for the SrCO$_3$ ΔH_{rxn} and vibrational calculations. The RMSD values for the vibrational frequencies for Sr$_2$CuO$_2$(CO$_3$) using PBE and PBEsol were 53 and 26 cm^{-1} respectfully and are shown in Tables 6.11 and 6.12.

Table 6.11: The harmonic frequencies of the $SrCO_3$ groups in $Sr_2CuO_2(CO_3)$ calculated using PBE and compared to experimental values determined by Armstrong *et al.*.[207]

Vibrational frequency cm^{-1}	PBE functional (1)	Literature (2)	Difference (1) - (2)
Symmetric stretching ν_1	1119	1072	47
Symmetric bending ν_2	867	858	9
Asymmetric stretching ν_3	1462	1449	13
Asymmetric stretching ν_3'	1437	1412	-25
Asymmetric bending ν_4	819	704	115
Asymmetric bending ν_4'	726	699	27
RMSD	N/A	N/A	53

Table 6.12: The harmonic frequencies of the $SrCO_3$ groups in $Sr_2CuO_2(CO_3)$ calculated using PBEsol and compared to experimental values determined by Armstrong *et al.*.[207]

Vibrational frequency cm^{-1}	PBEsol functional (1)	Literature (2)	Difference (1) - (2)
Symmetric stretching ν_1	1067	1072	-5
Symmetric bending ν_2	831	858	-27
Asymmetric stretching ν_3	1466	1449	17
Asymmetric stretching ν_3'	1432	1412	20
Asymmetric bending ν_4	675	704	-29
Asymmetric bending ν_4'	657	699	-42
RMSD	N/A	N/A	26

Using the difference ratio between the experimentally reported ACO_3 frequencies to calculated ones, scaling factors have been determined. These can then be used to decrease the difference between harmonic frequencies in bulk $SrCO_3$ and in $Sr_2CuO_2(CO_3)$ to the respective experimental values.

6.3.2 Vibrational scaling factors for harmonic frequencies

The vibrational frequencies of the ACO_3 (A = Sr, Ca and Ba) series, bulk $SrCO_3$ and $Sr_2CuO_2(CO_3)$ calculated using DFT methods have shown RMSD values ranging from 26 to 136 cm^{-1}. In order to compensate for the differences, vibrational scaling factors have been determined using the data points from the ACO_3 series. This is to reduce the difference between calculated and experimental frequencies without having to use more computationally expensive anharmonic methods.

6.3.2.1 Linear scaling

Initially a linear scaling factor was determined and used for the vibrational frequencies. Various examples exist where scaling factors have been determined using a linear trend of the calculated and experimental frequencies to them be applied to improve the difference in values.[276, 277] By comparing the harmonic frequencies of the ACO_3 (A = Sr, Ba and Ca) series to experimental values, a linear trend has been plotted to determine a scaling factor for each functional. An example of a linear plot for determining a scaling factor using values calculated by PBEsol is shown in Figure 6.2. The equation of the line (y) and R^2 for each functional is been presented in Table 6.13.
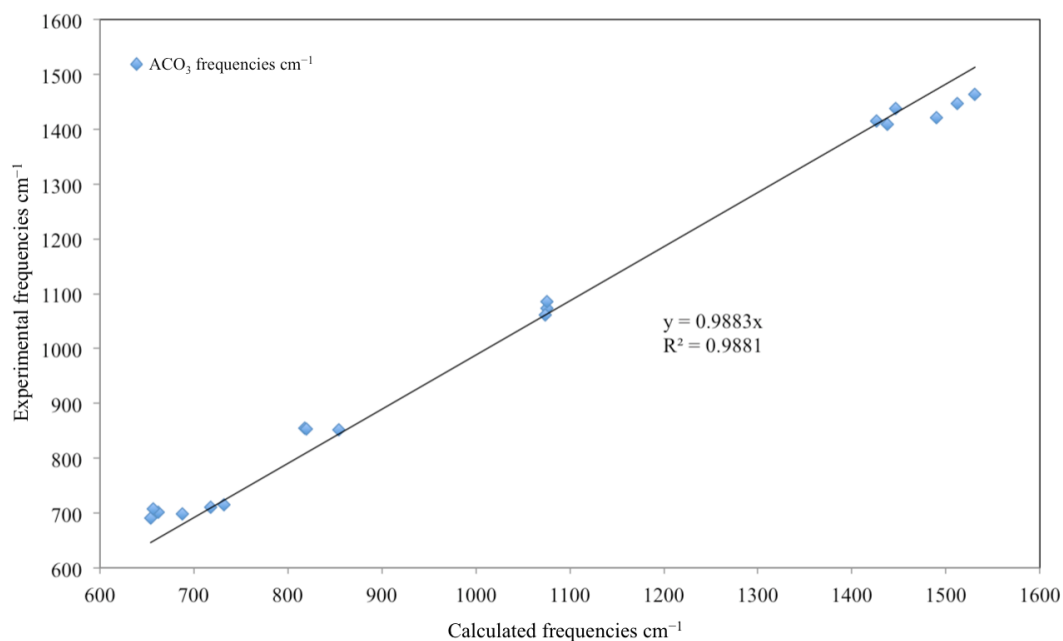
Figure 6.2: Theoretical and experimental frequencies obtained for ACO_3 (A = Sr, Ca and Ba) compounds compared using a linear trend method for results determined using PBEsol.

Table 6.13: The equation of line (y) and R^2 values for each functional using a linear trend.

Functional	Equation of the line (y)	R^2 value
PBE	0.9466x	0.9817
PBEsol	0.9883x	0.9898
TPSS	1.0289x	0.9956
revTPSS	1.0254x	0.9961

As expected the scaling factors for PBE and PBEsol are below 1 to decrease the calculated values. This is to expected as the results in Table 6.1 and 6.2 show the harmonic values to be greater than the anharmonic ones. The TPSS and revTPSS scaling factors are greater and designed to increase the calculated values to make them closer to experimental. This is again expected from the results reported in Table 6.2 and 6.3. These scaling factors have also been compared to those reported for PBE, TPSS and revTPSS in Table 6.14.[278–280] In the case of PBEsol no vibrational scaling factor has been previously reported to the author's knowledge.

Table 6.14: The scaling factors for the functional both calculated within the project alogn with those previously reported.

Method	Scaling factor calculated	Scaling factor literature
PBE	0.9466x	1.026x
PBEsol	0.9883x	N/A
TPSS	1.0289x	0.996x
revTPSS	1.0254x	1.012x

The largest difference is seen for the PBE scaling factors. This has the literature value > 1 whilst that reported in this project is < 1 at 0.9466. This is likely due to the difference in the relationship between calculated and experimental frequencies. Those reported by Alecu are for values where the frequencies are generally lower than the anharmonic ones.[278] In this project however, the calculated frequencies for the ACO_3 series are as expected greater than experimental ones. For TPSS this is in reverse as the literature scaling factor is < 1. The scaling factors for revTPSS are in the closets agreement.

Both the scaling factors determined in this projected and those reported in the literature were applied to the calculated frequencies for bulk $SrCO_3$, Table 6.15. The calculated scaling factors showed an increase in the RMSD for PBE and PBEsol functionals whereas for TPSS and revTPSS showed a decreased. This is likely due to the difference for PBE and PBEsol following a less linear trend than for TPSS and revTPSS.

When the scaling factors from the literature were used it was found that the RMSD value would increases compared to calculated scaling factors for TPSS and revTPSS. This is potentially a result of the calculated scaling factors being determined using the data sets from the ACO_3 series which is similar to the bulk $SrCO_3$ system. The literature scaling factors were determined from an array of different molecules rather than solid carbonates.

Table 6.15: RMSD values cm^{-1} for the vibrational frequencies of the carbonate groups within SrCO$_3$ with linear scaling factor determined both within this project, and sources from the literature.

Functional	Unscaled	Calculated scaled factors	Literature scaled factors
PBE	92	108	100
PBEsol	90	94	N/A
TPSS	136	119	139
revTPSS	131	116	125

For SrCO$_3$, TPSS and revTPSS methods calculate frequencies which follow a reasonably linear trend. Also PBE does show all the calculated frequencies as being higher to the experimental, whilst TPSS and revTPSS show the majority of calculated values being lower. The increase in RMSD for PBEsol is potentially a result of the linear scaling factor used being too simplistic for the differences between experimental and calculated frequencies that don't follow a linear trend as seen in Table 6.2. One example is that of the asymmetric stretching modes ν_3 and ν_3' have one being greater to experimental values and the other being lower.

The RMSD values for Sr$_2$CuO$_2$(CO$_3$), were found to increase for both PBE and PBEsol when linear scaling factors were used, Table 6.16. This maybe a result of the difference between the vibrational behaviour of the ACO$_3$ groups to those in Sr$_2$CuO$_2$(CO$_3$). Another possibility is that the linear scaling method is too simplistic. Despite the vibrational frequencies behaving harmonically some are lower than experimental. This is particularly seen for frequencies calculated by PBEsol in Table 6.12.

Table 6.16: RMSD values cm^{-1} for the vibrational frequencies of the carbonate groups within Sr$_2$CuO$_2$(CO$_3$) before and after linear scaling.

Functional	Unscaled	Linear scaled
PBE	39	50
PBEsol	26	30

The next set of calculations involved using a polynomial trend for the data sets to determine quadratic scaling factors. This is a more accurate approach which will take into consideration that the difference between experimental and computational frequencies does not follow a linear trend.[276]

6.3.2.2 Quadratic scaling

In order to lower the RMSD for calculated vibrational frequencies in bulk $SrCO_3$ and $Sr_2CuO_2(CO_3)$, linear scaling factors were used. Although this type of approach was able to reduce the difference between experimental frequencies for TPSS and revTPSS in bulk $SrCO_3$. In the case of PBE and PBEsol the RMSD actually increased. This was also seen for the vibrational calculations using PBE and PBEsol for $Sr_2CuO_2(CO_3)$. As a result, a polynomial trend for the data points was applied to determine a quadratic scaling factor. Figure 6.3 shows an example of a polynomial trend between the Δ_{anh} and calculated frequencies. The equation of the line is determined and used to calculate the quadratic scaling factor and uses data points determined using PBEsol.
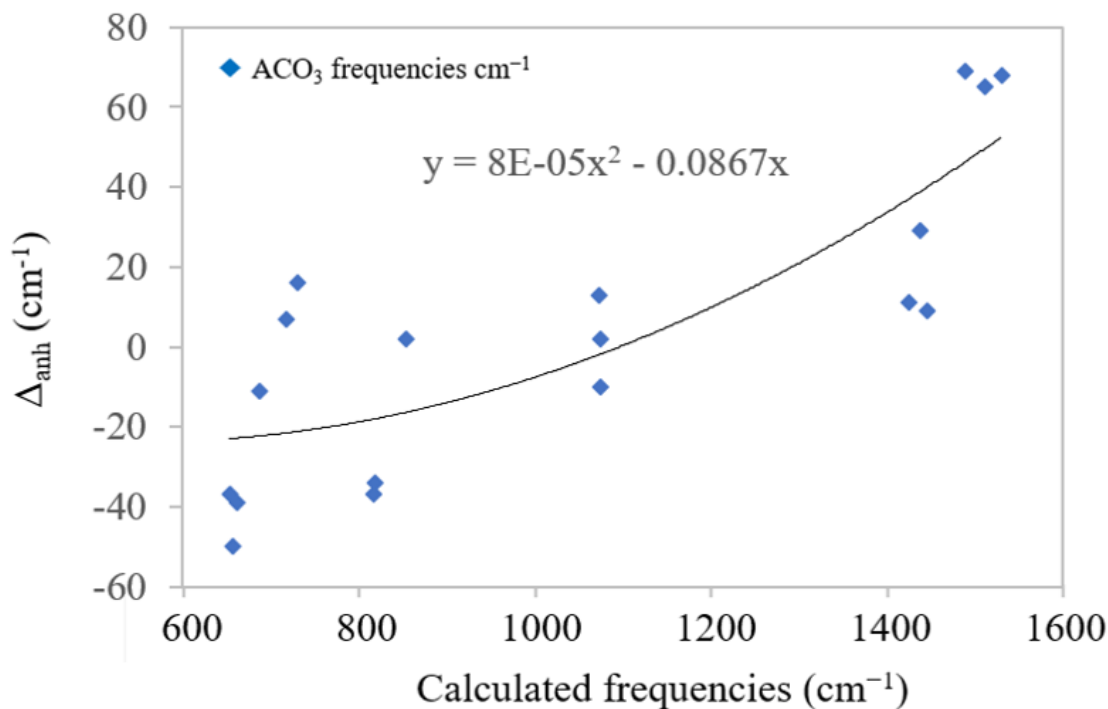
Figure 6.3: Δ_{anh} compared to the computational frequencies for the ACO_3 (A = Sr, Ca and Ba) compounds determined using PBEsol and compared using a polynomial trend.

For calculating the scaling factor Equations 6.7 to 6.9 were used with $\omega_i = x$. This same value for the scaling factor was also determined using a polynomial trend for the comparison between the experimental and calculated frequencies in Figure 6.4.

$$v_i - x = -8x10^{-5}x^2 - (-0.0867x) \tag{6.7}$$

$$v_i = x - 8x10^{-5}x^2 - (-0.0867x) \tag{6.8}$$

$$v_i = -8x10^{-5}x^2 + 1.0867x \tag{6.9}$$
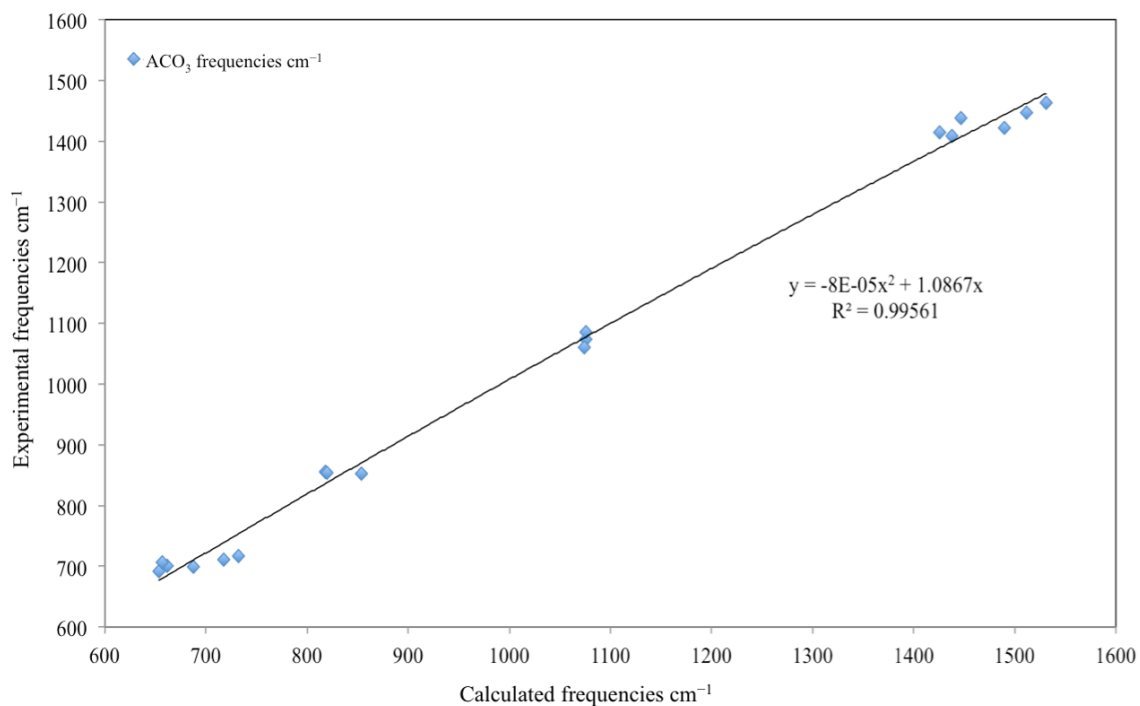
Figure 6.4: Theoretical and experimental frequencies obtained for ACO_3 (A = Sr, Ca and Ba) compounds compared using a polynomial trend for results determined using PBEsol.

Quadratic scaling factors have been found to out perform that of linear models and reduce the chances of over correcting data.[276] This type of approach is also needed for cases where the difference between calculated and experimental values do not follow a linear trend. The

equation of the line (y) and R^2 for each functional used to determine the scaling factor have been presented in Table 6.17.

Table 6.17: The equation of line (y) and R^2 values using a polynomial trend.

Functional	Equation of the line (y)	R^2 value
PBE	$9 \times 10^{-5}x^2 + 0.8279x$	0.9914
PBEsol	$-8 \times 10^{-5}x^2 + 1.0868x$	0.9956
TPSS	$-1 \times 10^{-6}x^2 + 1.0273x$	0.9956
revTPSS	$-2 \times 10^{-5}x^2 + 1.0437x$	0.9963

Using the equation of the line (y) a quadratic scaling factor was determined and applied to the vibrational frequencies for each functional. The non-scaled as well as linear and quadratically scaled RMSD values have been presented in Table 6.18 for bulk $SrCO_3$ and Table 6.19 for $Sr_2CuO_2(CO_3)$.

Table 6.18: RMSD values cm^{-1} for the vibrational frequencies of the carbonate groups within $SrCO_3$ unscaled, liner and quadratically scaled.

Functional	Original RMSD	Linearly scaled	Quadratically scaled
PBE	92	108	119
PBEsol	90	94	81
TPSS	136	119	120
revTPSS	131	116	116

Table 6.19: RMSD values cm^{-1} for the vibrational frequencies of the carbonate groups within $Sr_2CuO_2(CO_3)$ unscaled, liner and quadratically scaled.

Functional	Original RMSD	Linearly scaled	Quadratically scaled
PBE	39	50	48
PBEsol	26	30	17

In the case of bulk $SrCO_3$ quadratically scaled values show a decrease in the RMSD compared to unscaled values for all functionals except PBE. This is potentially a result of the quadratic scaling factor over compensating the frequencies and making them lower increasing the RMSD. Using a quadratic scaling factor the RMSD for PBEsol decreased from 90 to 81 cm^{-1}. This is the lowest RMSD value of all the functional used for bulk $SrCO_3$. This method was also found to calculate an ΔH_{rxn} for SrO reacting with CO_2 towards $SrCO_3$ with the greatest level of accuracy.

The quadratically scaled frequencies for $Sr_2CuO_2(CO_3)$ showed an increase in RMSD for PBE (39 to 48 cm^{-1}). However, in the case of PBEsol, quadratic scaling increased the frequency values making them closer to experimental results and lowering the RMSD from 26 to 17 cm^{-1}. Overall this shows that PBEsol calculates vibrational frequencies and an ΔH_{rxn} value closest towards those reported for $SrCO_3$.

The effect of linearly and quadratically scaled vibrational frequencies on the ΔH_{rxn} for $SrCO_3$ and $Sr_2CuO_2(CO_3)$ has also been discussed. By using the scaling factors on the vibrational frequencies the U_{ZPE} and U_{vib} corrections will be changed. The effect of these scaled frequencies on the ΔH_{rxn} for $SrCO_3$ and $Sr_2CuO_2(CO_3)$ are shown in Tables 6.21 and 6.22.

Table 6.20: ΔH_{rxn} values reported in kJ/mol for formation of SrO_3 in the 2×2×2 unit cell.

Functional	Original	Linear	Quadratic
PBE	-184.2	-185.9	-187.4
PBEsol	-214.3	-215.6	-214.6
TPSS	-109.4	-109.9	-110.2
revTPSS	-120.6	-121.4	-121.1

Table 6.21: ΔH_{rxn} values reported in kJ/mol for $Sr_2CuO_2(CO_3)$ formation from Sr_2CuO_3 and CO_2.

Functional	Original	Linear	Quadratic
PBE	-1635.5	-1636.3	-1635.0
PBEsol	-1731.9	-1732.1	-1730.4

In the case of $SrCO_3$ scaling factors act to slightly improve the calculated ΔH_{rxn} results to the experimental value of -234.6 kJ/mol. This improvements however is minimal with the highest value being being from quadratic scaling for PBE by 3.2 kJ/mol. Currently there is no known reported ΔH_{rxn} value for $Sr_2CuO_2(CO_3)$ from Sr_2CuO_3 and CO_2. Thus, assessing how the scaled frequencies affect the accuracy of the method for calculating the reaction enthalpy is difficult. The results do however show that the scaling frequencies effect the original enthalpy values by around 2 kJ/mol. This as with $SrCO_3$ shows that these scaled frequencies have little overall influence on the enthalpy values compared to unscaled values.

6.4   Conclusion

The vibrational frequencies of the ACO_3 (A = Sr, Ba and Ca) series has been determined using the same functionals as used for the enthalpy calculations in Chapter 5. Linear and quadratic scaling factors were determined from these values and used to reduce the difference between calculated and experimental frequencies for $SrCO_3$ and $Sr_2CuO_2(CO_3)$.

Linear scaling factors were found to only improve the vibrational frequencies determined by TPSS and revTPSS for $SrCO_3$. The RMSD for all the other studies were found to increase. This has been proposed as a result, of the differences between calculated and experimental frequencies not following a linear trend. It was however found that the calculated linear scaling factors performed better for reducing the RMSD than those reported in the literature for each functional.

Quadratic scaling was found to decrease the RMSD values for all functionals except PBE in

both systems compared to unscaled values. In the case of $Sr_2CuO_2(CO_3)$ quadratic scaling was applied and resulted in the lowest RMSD when using PBEsol, whilst increasing that for PBE. This reinforces the reliability of PBEsol for studying these types of systems as this method also calculated enthalpy values closest towards experimental results for $SrCO_3$, as well as having the lowest RMSD for the vibrational frequencies.

Both scaling methods were studied for their effect on the ΔH_{rxn} for $SrCO_3$ and $Sr_2CuO_2(CO_3)$. Although these were able to reduce the difference towards experimental results for $SrCO_3$. This level of improvement varied with the highest value being 3.2 kJ/mol using quadratic scaling for PBE. In the case of $Sr_2CuO_2(CO_3)$, changes in the enthalpy values from scaled frequencies only resulted in differences that were below 2 kJ/mol. Therefore, although scaling factors can improve the difference between calculated and experimental frequencies, their overall effect on the enthalpy values is limited.

Chapter 7

Overall Conclusion

Traditionally, research in carbon capture and storage/utilisation materials has focused on several types of approaches. Two of these include either using simple metal oxides, AO (A = Sr, Ca and Ba) for the chemisorbption of CO_2 forming metal carbonates ACO_3 or porous materials, such as zeolites and MOFs, that have pores to store CO_2 through physisorbtion.[55, 199, 208, 214, 281] This PhD has focused on combining these principles into one class of material towards utilising CO_2 to prepare complex mixed anion solids.

Compounds with the general composition A_2BX_3 (A = Sr, Ba, Ca and Ce, B = Cu, Pd and Mn, X = O and N) have been investigated for direct reaction with CO_2 towards mixed anion carbonates. These compounds show one-dimensional structures with anion vacancies that have been previously exploited for anion insertion. In particular F^- and Cl^- have been used to prepare mixed anion fluorides and chlorides.[92, 93, 282] The incorporation of additional fluoride anions can result in changing the chemical properties as seen with $Sr_2CuO_2F_{2+\delta}$, which behaves as a high temperature superconductor. These vacancies can be described as being similar to pores within zeolites and MOFs. Some of these compounds also contain alkaline earth metal (Sr, Ba and Ca) oxides that can react with CO_2 forming metal carbonates. As a result, compounds with anion vacancies in their crystal structure were investigated for their ability to insert and react with CO_2. These compounds also contain alkaline earth metal (Sr, Ca and Ba) oxides with high tendency to react and form metal carbonates.

The series of compounds investigated in this project were $Sr_{2-x}A_xCuO_3$ (A = Ca and Ba),

$Sr_{2-x}Ba_xPdO_3$ (x = 0 – 2) and Ce_2MnN_3.

Sr_2CuO_3 has a one-dimensional structure with chains of corner-linked CuO_4 square planar groups along the [001] direction inter layered by Sr^{2+} cations. It has been described as a anion-deficient K_2NiF_4 type structure. The $Sr_{2-x}A_xCuO_3$ (A = Ca and Ba) series, derived from isovalent substitution of Sr^{2+} has also showing the same type of crystal structure.

An alternating gases approach was used so the $Sr_{2-x}A_xCuO_3$ (A = Ca and Ba) series could react directly with CO_2 at 1000 °C. Through these reactions the formation of $Sr_2CuO_2(CO_3)$, $Sr_{1.8}Ba_{0.2}CuO_2(CO_3)$ and $Sr_{1.75}Ca_{0.25}CuO_2(CO_3)$ was possible. By heating the starting oxides in air and swapping it with CO_2 at the reaction temperature decomposition towards ACO_3 (A = Sr, Ba and Ca) was mostly avoided. The isovalent substitution of strontium for barium and calcium was carried out to assess how these changes would affect the reactivity of the compounds towards binding to CO_2. $Sr_{1.75}Ca_{0.25}CuO_2(CO_3)$ was prepared from $Sr_{1.5}Ca_{0.5}CuO_2$ using the same method as $Sr_2CuO_2(CO_3)$ but with the time under CO_2 increased from 15 to 90 minutes. The longer reaction time maybe due to Ca^{2+} having a smaller ionic radii than Sr^{2+} causing smaller anion vacancies.[122, 219] In the case of Ba^{2+}, despite having a larger ionic radii and a stronger affinity for reacting with CO_2, the time required to form $Sr_{1.8}Ba_{0.2}CuO_2(CO_3)$ was the same as that for $Sr_2CuO_2(CO_3)$.

The quantity of CO_2 utilised when forming the oxide carbonates was also determined for each of the mixed metal oxides. The CO_2 capturing capability was determined from both the change in mass observed through TGA and from the mass % of the products formed via Rietveld refinements. This gave values for Sr_2CuO_3 (3.80 ± 0.01 mmol/g), $Sr_{1.8}Ba_{0.2}CuO_3$ (3.99 ± 0.01 mmol/g) and $Sr_{1.5}Ca_{0.5}CuO_3$ (2.85 ± 0.01 mmol/g) from the TGA results, and values of 4.28 ± 0.01 mmol/g, 4.91 ± 0.02 mmol/g and 3.40 ± 0.004 mmol/g for the mass % respectively. These values are a result of the different phases being present from the reaction with CO_2. In the case of $Sr_{1.8}Ba_{0.2}CuO_3$ greater amounts of $SrCO_3$ was prepared from the reaction with CO_2 than with Sr_2CuO_3. As for $Sr_{1.5}Ca_{0.5}CuO_3$, reactions with CO_2 resulted in less carbonate based products such as $SrCO_3$ than Sr_2CuO_3.

The kinetics of the reaction were also determined using the TGA results that showed that change in mass over time. It was found that the reactions of Sr_2CuO_3, $Sr_{1.8}Ba_{0.2}CuO_3$ and $Sr_{1.5}Ca_{0.5}CuO_3$ with CO_2 were all 1st order reactions. The rate of reactions k were also de-

termined at 0.0045, 0.0048 and 0.0016 S^{-1} respectively. This follows the same trend with the CO_2 capturing capability, as the incorporation of barium increases the CO_2 capturing reactivity compared to the original strontium equivalent, whist calcium incorporation decreases the reactivity.

The extraction of CO_2 and repeatable reversibility was also investigated under O_2 and air respectively. The results showed that the original compounds could be re-formed in either gas over multiple cycles.

Reactions of the $Sr_{2-x}Ba_xPdO_3$ (x = 0 − 2) series with CO_2 found that below 1000 °C decomposition would take place forming $SrCO_3$ alongside either PdO or $SrPd_3O_4$. At 1000 °C it was found that Sr_2PdO_3 would not react with CO_2 even though FTIR spectroscopy indicated the possible presence of surface $SrCO_3$. As the content of barium increased in the starting material it was also found that the amount of Sr/$BaCO_3$ present from after the reaction with CO_2 also increased. Ba_2PdO_3 was found to react with CO_2 producing $Ba_{11}Pd_{11}O_{20}(CO_3)_2$ alongside $BaCO_3$ and Pd metal. This highlights the importance of the nature of the B cations, in particular their ability to expand their coordination number for incorporating carbonates.

Ce_2MnN_3 when reacted with CO_2 found that the mixed metal nitride would react to give CeO_2 and MnO_2. This is proposed to be a result of CO_2 actually splitting in the presence of Ce_2MnN_3 between 350 to 1000 °C providing a O_2 atmosphere that reacts with Ce_2MnN_3 towards forming oxides. This acts as an example on how the X anion identity affects the reactivity with CO_2. It also provides a potential novel route for CO_2 splitting using mixed metal nitrides.

A computational approach was developed using density functional theory, DFT methods to understand the thermodynamics of the reaction, $Sr_2CuO_3 + CO_2 = Sr_2CuO_2(CO_3)$. Initial case studies were carried out for formation of $SrCO_3$ from SrO and CO_2 on the surface and in the bulk. These case studies were used to develop a methodology for understanding carbonate formation, as well as to asses the accuracy of different computational methods for determining the enthalpy of reactions, ΔH_{rxn}. The exchange correction functional PBEsol was found to be the most accurate for calculating the ΔH_{rxn} and vibrational frequencies compared to experimental values. As a result, this was method was used to study the novel reaction, $Sr_2CuO_3 + CO_2 = Sr_2CuO_2(CO_3)$.

The structural changes of Sr_2CuO_3 towards $Sr_2CuO_2(CO_3)$ upon CO_2 insertion was investigated alongside the reaction enthalpy. A proposed model of the structural rearrangement had the atomic positions and unit cell parameters in Sr_2CuO_3 changed to that of $Sr_2CuO_2(CO_3)$ with CO_2 removed in the form of Sr_2CuO_2-O.[88, 117] This possible structural rearrangement provided SrO groups that were optimised with CO_2 forming carbonates leading to the overall formation of $Sr_2CuO_2(CO_3)$. This structural rearrangement results in an oxides being freed to react with CO_2 give carbonate groups. This shows that the reaction could be considered as being that of anion incorporation rather than substitution.

Using this approach the overall reaction enthalpy, ΔH_{rxn} was determined as the sum of the enthalpy of structural rearrangement $\Delta H_{structure}$ and carbonate formation $\Delta H_{carbonate}$. This shows the overall reaction as an exothermic process that agrees in line with experimental TGA results from a heat flow vs temperature curve.

This study provides a possible explanation into why an alternating gases approach was needed. It is proposed that only when Sr_2CuO_3 reacts with CO_2 at 1000 °C that an initial structural rearrangement step can occur towards forming a "Sr_2CuO_2-O" type structure. This can then be followed by carbonate formation within the structure leading towards the desired $Sr_2CuO_2(CO_3)$. This has also provided an opportunity to identify different possible reaction steps that are occurring using a computational method that would be difficult via an experimental approach.

Scaling factors were found to reduce the difference between calculated and experimental vibrational frequencies. The linear scaling factors determined in the project were also generally found to reduce the RMSD values more than those reported in the literature for certain functionals used.[279, 280] The effect of scaled frequencies on the ΔH_{rxn} for $SrCO_3$ showed an improvement of approximately 3 kJ/mol towards experimental values. In the case of $Sr_2CuO_2(CO_3)$ scaled frequencies showed to only change values compared to unscaled by 2 kJ/mol.

Overall this work demonstrates the reactivity of various anion deficient mixed metal compounds with CO_2 towards preparing complex inorganic solids. Through an alternating gases approach the $Sr_{2-x}A_xCuO_3$ (A = Ca and Ba) cuprate series has been found to react with CO_2 within the anion vacancies at specific temperatures. This results in the controlled synthesis

of $Sr_{2-x}A_xCuO_2(CO_3)$ compounds. It has also been found that this reaction can be reversed up to 3 times resulting in a novel way to prepare the original oxides. Computational DFT methods have show a proposed model for this reaction through a thermodynamics study. This consists of a two step process with structural rearrangement followed by carbonate formation. The vibrational behaviour of the carbonate groups have also been investigated with scaling factors to decrease the difference between calculated and experimental values. The effects of scaled frequencies on the enthalpy values has also been discussed.

Reaction of the $Sr_{2-x}Ba_xPdO_3$ series showed how the B cation needs to expand its coordination number for reacting with CO_2. The work with Ce_2MnN_3 highlighted the importance of the X anions to react for forming stable anionic groups to form mixed anion compounds.

Chapter 8

Appendix

Table 8.1: The structural information of $Sr_2CuO_2(CO_3)$ Babu *et al.*.[80]

Atom	x	y	z	site occupancy	B
Sr	0.5000	0.5000	0.2283	1	0.65
Cu	0.0000	0.0000	0.0000	1	0.52
C	0.0000	0.0000	0.5000	1	0.66
O(1)	0.0000	0.5000	0.0000	1	0.78
O(2)	0.3340	0.0000	0.5000	0.25	310.564
O(3)	0.8620	0.5000	0.6460	0.25	307.932

Table 8.2: The structural information of $Sr_2CuO_2(CO_3)$ Miyazaki *et al.*.[116]

Atom	x	y	z	site occupancy	B
Sr(1)	0.0000	0.0000	0.1140	1	0.65
Sr(2)	0.0000	0.0000	0.3860	1	0.65
Sr(3)	0.0000	0.5000	0.1042	1	0.65
Sr(4)	0.5000	0.0000	0.3810	1	0.65
Cu	0.2530	0.2480	-0.0010	1	0.34
C	0.2420	0.2490	0.2490	1	0.79
O(1)	0.2508	-0.0030	0.0100	1	0.43
O(2)	0.2520	0.0030	0.4960	1	0.43
O(3)	0.1590	0.7420	0.1830	1	0.25
O(4)	0.4160	0.7400	0.2450	1	3.3
O(5)	0.2340	0.2970	0.1682	1	3.3

Table 8.3: Structural data of $Sr_2CuO_2(CO_3)$ obtained from PXRD analysis and Rietveld refinements using the model by Babu *et al.*.[80]

Atom	x	y	z	Multiplicity	Occupancy	Uiso
Sr1	0.5	0.5	0.22705(4)	2	1	0.00927
Cu1	0	0	0	1	1	0.00411
C1	0	0	0.5	1	1	0.00028
O1	0	0.5	0	2	1	0.01121
O2	0.34747(6)	0	0.5	4	0.25	0.01417
O3	0.84321(4)	0	0.64463(9)	8	0.25	0.01417

Table 8.4: Refined structural data of prepared $Sr_{1.8}Ba_{0.2}CuO_2(CO_3)$.

Atom	x	y	z	Multiplicity	Occupancy	Uiso
Sr1	0.5	0.5	0.2292(7)	2	0.9	0.00283
Cu1	0	0	0	1	1	0.00027
C1	0	0	0.5	1	1	0.01900
O1	0	0.5	0	2	1	0.00527
O2	0.3894(3)	0	0.5	4	0.25	0.01308
O3	0.8662(4)	0	0.6330(1)	8	0.25	0.01308
Ba1	0.5	0.5	0.2292(7)	2	0.1	0.00283

Table 8.5: Structural data of $Sr_{1.75}Ca_{0.25}CuO_2(CO_3)$ prepared.

Atom	x	y	z	Multiplicity	Occupancy	Uiso
Sr1	0.5	0.5	0.2272(1)	2	0.875	0.01029
Cu1	0	0	0	1	1	0.01619
C1	0	0	0.5	1	1	0.00867
O1	0	0.5	0	2	1	0.02834
O2	0.3426(4)	0	0.5	4	0.25	0.05421
O3	0.8389(6)	0	0.6488(5)	8	0.25	0.05421
Ca1	0.5	0.5	0.2272(1)	2	0.125	0.01029

Bibliography

[1] P. Nejat, F. Jomehzadeh, M. Taheri, M. Gohari and M. Majid, *Renew. Sust. Energ. Rev.*, 2015, **43**, 843.

[2] J. G. Olivier, G. Janssens-Maenhout, M. Muntean and J. A. Peters, *Trends in global CO$_2$ emissions: 2014 Report*, PBL Netherlands Environmental Assessment Agency, The Hague, 2014.

[3] M. Poliakoff, W. Leither and E. S. Streng, *Faraday Discuss.*, 2015, **183**, 9.

[4] R. B. Jackson, C. L. Quere, R. M. Andrew, J. G. Canadell, G. P. Peters, J. Roy and L. Wu, *Environ. Res. Lett.*, 2017, **12**, 110202.

[5] M. Hasib-ur rahman, M. Siaj and F. Larachi, *Chem. Eng. Process*, 2010, **49**, 313.

[6] M. Aresta, A. Dibenedetto and A. Antonella, *Chem. Rev.*, 2014, **144**, 1709.

[7] S. Eloneva, E.-M. Puheloinen, J. Kanerva, A. Ekroos, R. Zevenhoven and C.-J. Fogelholm, *J. Clean. Prod.*, 2010, **18**, 1833.

[8] M. Aresta, E. Quaranta, I. Tommasi, P. Giannoccaro and A. Ciccarse, *Chim. Ital.*, 1995, **125**, 509.

[9] M. Aresta and I. Tommasi, *Energ. Convers. Manage.*, 1997, **38**, S373.

[10] A. Samanta, A. Zhao, G. K. H. Shimizu, P. Sarkar and R. Gupta, *Ind. Eng. Chem. Res.*, 2012, **51**, 1438.

[11] J. Abanades, E. Rubin and E. Anthony, *Ind. Eng. Chem. Res.*, 2004, **43**, 3462.

[12] G. T. Rochelle, *Science.*, 2009, **325**, 1652.

[13] D. D'Alessandro, B. Smit and J. Long, *Angew. Chem. Int. Ed.*, 2010, **49**, 6058.

[14] R. Zevenhoven, J. Fagerlund and J.-K. Songok, *Greenhouse Gases Sci and Technol.*, 2011, **1**, 48.

[15] A. B. Rao and E. S. Rubin, *Environ. Sci. & Technol.*, 2002, **36**, 4467.

[16] F. A. Chowdhury, H. Okabe, S. Shimizu, M. Onoda and Y. Fujioka, *Energy Procedia*, 2009, **1**, 1241.

[17] N. MacDowell, N. Florin, A. Buchard, J. Hallett, A. Galindo, G. Jackson, C. S. Adjiman, C. K. Williams, W. N. Shan and P. Fernnell, *Energy Environ. Sci.*, 2010, **3**, 1645.

[18] H. Hikita, S. Asai, Y. Katsu, I. S. Y. and S. Ikuno, *AIChE. J.*, 1979, **25**, 793.

[19] E. Sada, H. Kumuzawa and M. Butt, *Can. J. Chem. Eng.*, 1976, **54**, 421.

[20] S. S. Laddha and P. V. Danckwerts, *Chem. Eng. Sci.*, 1981, **36**, 479.

[21] D. E. Penny and T. J. Ritter, *J. Chem. Soc. Faraday Trans. 1*, 1983, **79**, 2103.

[22] R. Shao and A. Stangeland, *Amines Used in CO_2 Capture - Health and Environmental Impacts*, The bellona foundation technical report, 2009.

[23] K. Resnik, *Int. J. Environ. Technol. Manage.*, 2004, **4**, 89.

[24] J. Čejka, A. Corma and S. Zones, *Zeolites and Catalysis: Synthesis, Reactions and Applications*, Wiley-VCH, New York USA, 2010.

[25] S. J. Chen, M. Zhu, Y. Fu, Y. X. Huang, Z. C. Tao and W. L. Li, *Appl. Energy*, 2017, **191**, 87.

[26] I. G. B. N. Makertihartha, P. T. Dharmawijaya, M. Zunita and I. G. Wenten, *AIP Conference Proceeding*, 2017, **1818**, 020074.

[27] R. Xu, W. Pang, J. Yu, Q. Huo and J. Chen, *Chemistry of Zeolites and Related Porous Materials: Synthesis and Structure*, Wiley, Clementi Singapore, 2007.

[28] A. W. Chester and E. G. Derouane, *Zeolite Characterization and Catalysis: A Tutorial*, Springer, New York, 2009.

[29] E. Gallei and G. Stumpf, *J. Colloid. Interf. Sci.*, 1976, **55**, 415.

[30] Z. Yong, V. Mata and A. Rodrigues, *Sep. Purif. Technol.*, 2002, **26**, 195.

[31] Q. Wang, J. Luo, Z. Zhong and A. Borgna, *Energy Environ. Sci.*, 2011, **4**, 42.

[32] J. R. Li, R. J. Kuppler and H. C. Zhou, *Chem. Soc. Rev*, 2009, **38**, 1477.

[33] Y. Lee, D. Liu, D. Seoung, Z. Liu, C. Kao and T. Vogt, *J. Am. Chem. Soc.*, 2011, **133**, 1674.

[34] P. E. Riley and K. Seff, *Inorg. Chem.*, 1974, **13**, 1355.

[35] X. Xu, C. Song, J. M. Andresen, B. G. Miller and A. W. Scaroni, *Microporous. Mesoporous. Mater.*, 2003, **62**, 29.

[36] P. J. E. Harlick and A. Sayari, *Ind. Eng. Chem. Res.*, 2006, **45**, 3248.

[37] K. T. Chue, J. N. Kim, Y. U. Yoo, S. H. Cho and R. T. Yang, *Ind. Eng. Chem. Res.*, 1995, **34**, 591.

[38] A. Auroux and A. Gervasini, *J. Phys. Chem.*, 1990, **94**, 6371.

[39] E. Mostafavi, M. H. Sedghkerdar and N. Mahinpey, *Ind. Eng. Chem. Res.*, 2013, **52**, 4725.

[40] Y. Duan and D. C. Sorescu, *J. Chem. Phys.*, 2010, **133**, 074508.

[41] L. Li, X. Wen, X. Fu, F. Wang, N. Zhao, F. Xiao, W. Wei and Y. Sun, *Energy Fuels*, 2010, **24**, 5773.

[42] G. V. Colombo and E. S. Mills, *Chem. Eng. Prog. Symp. Ser.*, 1966, **62**, 89.

[43] J. Blamey, E. Anthony, J. Wang and l. P. Fennel, *Prog. Energ. Combust.*, 2010, **36**, 260.

[44] Z. Skoufaa, A. Antzaraa, E. Heracleousb and A. A. Lemonidoua, *Energy Procedia*, 2016, **86**, 171.

[45] B. Dou, C. Wang, Y. Song, H. Chem, B. Jiang, M. Yang and Y. Xu, *Renew. Sust. Energ. Rev.*, 2016, **53**, 536.

[46] Z. S. Li, N. S. Cai, Y. Huang and H. J. Han, *Energy Fuels*, 2005, **19**, 1447.

[47] L. Y. Li, D. L. King, Z. M. Nie, X. S. Li and C. Howard, *Energy Fuels*, 2010, **24**, 3698.

[48] B. Feng, H. An and E. Tan, *Energy. Fuels.*, 2007, **21**, 426.

[49] J. Wang, L. Huang, R. Yang, Z. Zhang, J. Wu, Y. Gao, Q. Wang, D. O'Hare and Z. Zhong, *Energy Environ. Sci.*, 2014, **7**, 3478.

[50] X. Zhao, G. Ji, W. Liu, W. He, E. J. Anthony and M. Zhao, *Chem. Eng. J.*, 2018, **332**, 216.

[51] A. T. Vu, Y. Park, P. R. Jeon and C.-H. Lee, *Chemical Engineering Journal*, 2014, **258**, 254.

[52] V. Hiremath, R. Shavi and J.-G. Seo, *J. Colloid Interface Sci.*, 2017, **498**, 55.

[53] S. Lee, H. Chae, S. Lee, B. Choi, C. Yi, J. B. Lee, C. Ryu and J. C. Kim, *Environ. Sci. Technol.*, 2008, **42**, 2736.

[54] L. K. G. Bhatta, S. Seetharamu, D. C. Madhusoodana, O. Sharon and V. Krishna, *J. Clean. Prod.*, 2015, **103**, 171.

[55] F. Miccio, A. N. Murri and E. Landi, *Ind. Eng. Chem. Res.*, 2016, **55**, 6696.

[56] S. Kumar and S. K. Saxena, *Mater. Renew. Sustain. Energy*, 2014, **3**, 1.

[57] K. Nakagawa and T. J. Ohashi, *J. Electrochem. Soc.*, 1998, **145**, 1344.

[58] K. Essaki, K. Nakagawa, M. Kato and H. Uemoto, *J. Chem. Eng. Jpn.*, 2004, **37**, 772.

[59] H. Pfeiffer, C. Vazquez, V. H. Lara and P. Bosch, *Chem. Mater.*, 2007, **19**, 922.

[60] T. Zhao, M. Ronning and D. Chen, *Chem. Mater.*, 2007, **19**, 3294.

[61] T. Ishihara, *Perovskite Oxide for Solid Oxide Fuel Cells*, Springer, New York USA, 2009.

[62] R. Buttner and E. Maslen, *Acta Crystallogr. C.*, 1988, **44**, 1707.

[63] R. M. Hazen, *Scientific American,*, 1988, **258**, 74.

[64] J. S. Zhou and J. B. Goodenough, *Phys. Rev. Lett.*, 2005, **94**, 065501.

[65] V. M. Goldschmidt, *Naturwissenschaften*, 1926, **14**, 14.

[66] F. S. Galasso, *Perovskites and High Tc Superconductors*, Gordon and Breach, New York, 1990.

[67] D. R. Lide, *Handbook of Chemistry and Physics*, CRC Press, Boca Raton, FL, 1999.

[68] K. Wang, C. Liu, P. Du, L. Chen, J. Zhu, A. Karim and X. Gong, *Organic Electronics.*, 2015, **21**, 19.

[69] S. Zhong, Y. Sun, H. Xin, C. Yang, L. Chen and X. Li, *Chem. Eng. J.*, 2015, **275**, 351.

[70] A. Mawdsley, J. Tallon and M. Presland, *Physica C.*, 1992, **190**, 437.

[71] S. N. Ruddlesden and P. Popper, *Acta Crystallogr.*, 1957, **10**, 538.

[72] S. N. Ruddlesden and P. Popper, *Acta Crystallogr.*, 1958, **11**, 54.

[73] S. Yeh, S. Wu, C. S. Lee and Y. Wang, *Acta Crystallogr. B.*, 1993, **49**, 806.

[74] D. Babel and E. Herdtweck, *Z. Anorg. Allg. Chem.*, 1982, **487**, 75.

[75] H. Shaked, P. M. Keane, J. C. Rodriguez, F. F. Owen, R. L. Hitterman and J. D. Jorgensen, *Crystal Structures of the High-Tc Superconducting Copper-Oxides*, Elsevier Science B.V., Illinois,, 1994.

[76] I. B. Sharma and S. D., *Bull. Mater. Sci.*, 1998, **21**, 262.

[77] J. F. Bringley, S. S. Trail and B. A. Scott, *J. Solid State Chem.*, 1990, **86**, 310.

[78] B. H. Chen, *J. Solid State Chem.*, 1996, **125**, 63.

[79] R. D. Shannon and C. T. Prewitt, *Acta Crystallogr. Sect. B.*, 1969, **25**, 925.

[80] T. Narendra Babu, D. Fish and C. Greaves, *J. Mater. Chem.*, 1991, **1**, 677.

[81] B. Raveau, M. Hervieu, D. Pelloquin, C. Michel and R. Retoux, *Z. Anorg. Allg. Chem.*, 2005, **631**, 1831.

[82] G. Tobias, D. Beltran Porter, O. I. Lebedev, G. van Tendeloo, J. Rodriguez Carvajal and A. Fuertes, *Inorg. Chem.*, 2004, **43**, 810.

[83] K. Yamaura, Q. Huang, J. W. Lynn, R. W. Erwin and R. J. Cava, *J. Solid State Chem.*, 2000, **152**, 374.

[84] C. S. Knee and M. T. Weller, *J. Solid State Chem.*, 2002, **168**, 1.

[85] J. M. D. Tascon and L. G. Tejuca, *J. Chem. Soc., Faraday Trans. 1.*, 1981, **77**, 591.

[86] C. Galven, J. Fourquet, E. Suard, M. Crosnier-Lopez and F. Le Berre, *Dalton Trans.*, 2010, **39**, 4191.

[87] M. T. Dunstan, W. Liu, A. F. Pavan, J. A. Kimpton, C. D. Ling, S. A. Scott, J. S. Dennis and C. P. Grey, *Chem. Mater.*, 2013, **25**, 4881.

[88] M. T. Weller and D. R. Lines, *J. Solid State Chem.*, 1989, **82**, 21.

[89] P. R. Slater, J. P. Hodges, M. G. Francesconi, P. P. Edwards, C. Greaves, I. Gameson and M. Slaski, *Physica C.*, 1995, **253**, 16.

[90] C. Greaves and M. G. Francesconi, *Curr. Opin. Solid St. M.*, 1998, **3**, 132.

[91] B. V. Beznosikov and K. S. Aleksandrov, *Crystallogr. Rep.*, 2000, **45**, 792.

[92] M. AI-Mamouri, P. P. Edwards, C. Greaves and M. Slaski, *Nature (London).*, 1994, **369**, 382.

[93] M. G. Francesconi, P. R. Slater, J. P. Hodges, C. Greaves, P. P. Edwards, M. Al-Mamouri and M. Slaski, *J. Solid. State Chem.*, 1998, **135**, 17.

[94] J. Kissick, C. Greaves, P. Edwards, V. Cherkashenko, E. Kurmaev, E. Bartkowski and M. Neumann, *Phys. Rev. B.*, 1997, **56**, 2831.

[95] C. Greaves, J. L. Kissick, M. G. Francesconi, L. D. Aikens and L. J. Gillie, *J. Mater. Chem.*, 1999, **9**, 111.

[96] Z. Hiroi, M. Takano, M. Azuma and Y. Takeda, *Nature*, 1993, **364**, 315.

[97] M. Al-Mamouri, P. Edwards, C. Greaves, P. Slater and M. Slaski, *J. Mater. Chem.*, 1995, **5**, 913.

[98] T. Baikie, E. L. Dixon, J. F. Rooms, N. A. Young and M. G. Francesconi, *Chem. Comm.*, 2003, **0**, 1580.

[99] T. Baikie, N. A. Young and M. G. Francesconi, *Prog. Solid State Chem.*, 2007, **35**, 265.

[100] F. A. Cotton and G. Wilkinson, *Advanced Inorganic Chemistry A comprehensive text,*, Interscience, 1971, vol. 3rd ed.

[101] M. J. Winter, *d-Block Chemistry*, Oxford Science Publications, 2015.

[102] R. Niewa, G. V. Vajenine, F. J. Disalvo, H. Luo and W. B. Yelon, *Z. Naturforsch.*, 1998, **53**, 63.

[103] S. Broll and W. Jeitschko, *Z. Naturforsch., B: Chem. Sci.*, 1995, **50**, 905.

[104] D. A. Headspith, E. Sullivan, C. Greaves and M. G. Francesconi, *Dalton. Trans.*, 2009, **42**, 9273.

[105] H. Takahashi, K. Igawa, K. Arii, Y. Kamihara, H. M. and H. Hosono, *Nature*, 2008, **453**, 376.

[106] C. De Cruz, Q. Huang, J. W. Lynn, J. Li, W. R. Ii, J. L. Zarestky, H. A. Mook, G. F. Chen, J. L. Luo, N. L. Wang and P. Dai, *Nature*, 2008, **453**, 899.

[107] M. Jansen and H. P. Letschert, *Nature*, 2000, **404**, 1999.

[108] K. Maeda and K. Domen, *J. Chem. Phys.*, 2007, **111**, 7851.

[109] H. Gupta and L.-S. Fan, *Ind. & Eng. Chem. Res.*, 2002, **41**, 4035.

[110] Y. Breard, M. C., M. Hervieu, A. Ducouret, M. Nguyen, F. Studer, A. Maignan and B. Raveau, *Chem. Mater.*, 2001, **13**, 2423.

[111] Y. Breard, C. Michel, F. Maignan, A. Studer and B. Raveau, *Chem. Mater.*, 2003, **15**, 1273.

[112] A. Demont, D. Pelloquin, H. S., Y. Breard, J. Howling, M. Y. and A. Maignan, *J. Solid State Chem.*, 2011, **184**, 1655.

[113] G. Calestani, F. C. Matacotta, A. Migliori, P. Nozar, L. Righi and K. A. Thomas, *Physica C.*, 1996, **261**, 38.

[114] A. Lappas, K. Prassides, A. R. Armstrong and P. P. Edwards, *Inorg. Chem.*, 1993, **32**, 383.

[115] E. M. Kopnin, A. T. Matveev, P. S. Salamakha, A. Sato and E. Takayama-Muromachi, *Physica C.*, 2003, **384**, 163.

[116] Y. Miyazaki, H. Yamane, T. Kajitani, T. Oku, K. Hiraga, Y. Morii, K. Fuchizaki, S. Funahashi and T. Hirai, *Physica C.*, 1992, **191**, 434.

[117] H. Nakata, J. Akimitsu, S. Katano, T. Minami, N. Ogita and M. Udagawa, *Physica C.*, 1995, **255**, 157.

[118] A. R. Armstrong and P. P. Edwards, *J. Solid State Chem.*, 1992, **98**, 432.

[119] K. Kinoshita and T. Yamada, *Nature*, 1992, **357**, 313.

[120] S. M. Kazakov, E. V. Antipov, C. Chaillout, J. J. Caponi, M. Brunner, J. L. Tholence and M. Marezio, *Physica C.*, 1995, **253**, 401.

[121] O. Cheung and H. Hedin, *RSC Adv.*, 2014, **4**, 14480.

[122] *CRC Handbook of Chemistry and Physics*, ed. R. Weast, The Chemical Rubber Co., 18901 Cranwood Parkway, Cleveland, Ohio, 1971.

[123] H. Flood and T. Furland, *Acta Chem. Scand.*, 1947, **1**, 592.

[124] C. H. Yu, C. H. Huang and C. S. Tan, *Aerosol and Air Quality Research*, 2012, **12**, 745.

[125] H. Tsuji, A. Okamura-Yoshida, T. Shishido and H. Hattori, *Langmuir*, 2003, **19**, 8793.

[126] F. Carey and R. Giuliano, *Organic Chemistry*, McGraw-Hill Education, 2016.

[127] J. Tan and K. S. Chan, *Understanding Advanced Physical Inorganic Chemistry*, World Scientific, 2011.

[128] P. Atkins, J. de Paula and R. Friedman, *Physical Chemistry, Quanta, Matter, and Change*, OUP Oxford, 2014.

[129] P. Atkins and J. de Paula, *Elements of Physical Chemistry*, OUP Oxford, 5th edn., 2009.

[130] M. Jacox, *NIST Chemistry WebBook*, P. J. Linstrom, and W. G. Mallard,, National Institute of Standards and Technology, Gaithersburg MD, 2016, p. NIST Standard Reference Database Number 69.

[131] H. Pfnür, D. Menzel, F. Hoffmann, A. Ortega and A. Bradshaw, *Surf. Sci.*, 1980, **93**, 431.

[132] N. Nijem and Y. J. Chabal, *Comment. Inorg. Chem.*, 2014, **34**, 78.

[133] A. Chedin, *J. Mol. Spectrosc.*, 1979, **76**, 430.

[134] M. Donahue, E. Botonjic-Sehic, D. Wells and C. Brown, *Am. Pharmaceut. Rev.*, 2011, **14**, 104.

[135] V. Rodriguez-Garcia, S. Hirata, K. Yagi, K. Hirao, T. Taketsugu, S. I. and M. Tasumi, *J. Chem. Phys.*, 2007, **126**, 124303.

[136] E. Fermi, *Z. Physic.*, 1931, **71**, 250.

[137] B. E. Scheetz and W. B. White, *Am. Mineral.*, 1977, **62**, 36.

[138] L. E. Smart and E. Moore, *Solid State Chemistry An Introduction*, CRC Taylor Francis, 2005.

[139] L.-l. Ooi, *Principles of X-ray Crystallography*, Oxford University Press, 2010.

[140] Z. Ullah, S. Atiq and S. Naseem, *J. Sci. Res.*, 2013, **5**, 235.

[141] W. L. Bragg, *Proc. Cambridge Philos. Soc.*, 1913, **17**, 43.

[142] C. G. Barkla, *Phil. Trans. R. Soc. Lond. A*, 1905, **204**, 467.

[143] W. Friedrich, P. Knipping and M. Laue, *Ann. Phys.*, 1913, **346**, 971.

[144] A. West, *Solid State Chemistry and its Applications*, Wiley, 2014.

[145] M. T. Weller, *Inorganic Materials Chemistry*, Oxford University Press, 1994.

[146] C. Bong, H. Chen and F. Wu, *J. Appl. Cryst.*, 1999, **32**, 168.

[147] B. Fultz and J. M. Howe, *Transmission Electron Microscopy and Diffractometry of Materials*, Springer, 2013.

[148] R. G. Narasimha, V. Sastry, M. H. Gopala Krishana, V. Seshagiri and T. Radhakrishnan, *Powder Diffr.*, 1996, **11**, 200.

[149] L. Brügemann and K. E. G. Ekkehard, *Nucl. Instrum. Methods Phys. Res., Sect. A.*, 2004, **531**, 292.

[150] R. E. Dinnebier and S. J. L. Billinge, *Powder Diffraction: Theory and Practice*, RSC Publishing, 2009.

[151] R. A. Young, *The Rietveld Method*, Oxford Science Publications, 1993.

[152] A. C. Larson and R. B. V. Dreele, *General structure analysis system (GSAS)*, Los alamos national laboratory report laur technical report, 2004.

[153] R. Tilley, *Crystals and Crystal Structures*, John Wiley Sons Ltd, 2006.

[154] B. H. Toby, *J. Appl. Cryst.*, 2001, **34**, 210.

[155] O. Koshy, L. Subramanian and S. Thomas, *Thermal and Rheological Measurement Techniques for Nanomaterials Characterization*, Elsevier, 2017.

[156] M. Wagner, *Thermal Analysis in Practice*, Hanser, 2018.

[157] C. Janke, M. S. Duyar, M. Hoskins and R. Farrauto, *Appl. Catal., B.*, 2014, **152**, 184.

[158] I. Corazzari, R. Nistico, F. Turci, M. G. Faga, F. Franzoso, F. Tabasso and G. Magnacca, *Polym. Degrad. Stab.*, 2015, **112**, 1.

[159] Z. Yong, V. Mata and A. E. Rodrigues, *Sep. Purif. Technol.*, 2002, **26**, 195.

[160] J. Brown, *Molecular Spectroscopy*, Oxford Science Publications, Oxford UK, 1996.

[161] R. L. Brooks, in *Vibrations and Rotations of Diatomic Molecules*, Springer New York, New York, NY, 2013, p. 139.

[162] E. Schrödinger, *Phys. Rev.*, 1926, **28**, 1049.

[163] E. Lewars, *Computational Chemistry Introduction to the Theory and Applications of Molecular and Quantum Mechanics*, Springer US, USA, 2003.

[164] E. Lewars, *Computational Chemistry*, Springer Netherlands, Massachusetts USA, 2011.

[165] M. Born and R. Oppenheimer, *Ann. Phys.*, 1927, **84**, 457.

[166] P. Hohenberg and W. Kohn, *Phys. Rev. B.*, 1964, **136**, 864.

[167] W. Kohn and L. J. Sham, *Phys. Rev.*, 1965, **140**, A1133.

[168] D. R. Hartree, *Math. Proc. Cambridge*, 1928, **24**, 89.

[169] V. A. Fock, *Z. Phys.*, 1930, **61**, 126.

[170] J. C. Slater, *Phys. Rev.*, 1930, **210**, 35.

[171] V. Sahni, *The Hohenberg-Kohn Theorems and Kohn-Sham Density Functional Theory*, Springer, 2004.

[172] S. Kurth and J. P. Perdew, *Int. J. Quantum. Chem.*, 2000, **77**, 814.

[173] J. P. Perdew and K. Schmidt, *AIP. Con. Proc.*, 2001, **57**, 1.

[174] R. O. Jones and O. Gunnarsson, *Rev. Mod. Phys.*, 1989, **61**, 689.

[175] J. P. Perdew, K. Burke and Y. Wang, *Phys. Rev. B.*, 1996, **54**, 533.

[176] A. D. Becke, *J. Chem. Phys.*, 1993, **98**, 5648.

[177] J. P. Pedrew, K. Burke and M. Ernzerhof, *Phys. Rev. Letter.*, 1996, **77**, 3865.

[178] J. P. Perdew, A. Ruzsinszky, G. I. Csonka, O. A. Vydrov, G. E. Scuseria, L. A. Constantin, X. Zhou and K. Burke, *Phys. Rev. Lett.*, 2008, **100**, 136406.

[179] J. Tao, J. P. Perdew, V. N. Staroverov and G. E. Scuseria, *Phys. Rev. Letter.*, 2003, **91**, 146401.

[180] J. P. Perdew, A. Ruzsinszky, G. I. Csonka, L. A. Constantin and J. Sun, *Phys. Rev. Lett.*, 2009, **103**, 026403.

[181] M. Ropo, K. Koko and L. Vitos, *Phys. Rev. B.*, 2008, **77**, 195445.

[182] Y. Zhao and G. D. Truhlar, *J. Chem. Phys.*, 2008, **128**, 184109.

[183] V. N. Staroverov, G. E. Scuseria, J. Tao and J. P. Perdew, *Phys. Rev. B*, 2004, **69**, 075102.

[184] J. Tao, J. P. Perdew, L. M. Almeida, C. Fiolhais and S. Kum-mel, *Phys. Rev. B*, 2008, **77**, 245107.

[185] F. R. Burden and R. M. Wilson, *Adv. Phys.*, 1972, **21**, 825.

[186] R. Alrichs and P. R. Taylor, *J. Chim. Phys*, 1981, **78**, 315.

[187] S. Huzinaga, *Com. Phys. Rep.*, 1985, **2**, 279.

[188] J. C. Philips, *Phys. Rev.*, 1958, **112**, 685.

[189] J. C. Philips and L. Kleinman, *Phys. Rev.*, 1959, **116**, 287.

[190] L. Kleinman and J. C. Philips, *Phys. Rev.*, 1960, **118**, 287.

[191] A. Einstein and O. Stern, *Annalen der Physik.*, 1913, **345**, 551.

[192] P. Pulay, *Modern Theoretical Chemistry*, Plenum, 1977.

[193] F. Neese, *WIREs Comput Mol Sc*, 2011, **2**, 73.

[194] J. VandeVondele, M. Krack, F. Mohamed, M. Parrinello, T. Chassaing and J. Hutter, *Comp. Phys. Comm.*, 2005, **167**, 103.

[195] G. Lippert, J. Hutter and M. Parrinello, *Mol. Phys.*, 1997, **92**, 477.

[196] D. R. Lines, M. T. Weller, D. B. Currie and D. M. Ogborne, *Mater. Res. Bull.*, 1991, **26**, 323.

[197] T. Ami, M. K. Crawford, R. L. Harlow, Z. R. Wang, D. C. Johnston, Q. Huang and R. W. Erwin, *Phys. Rev. B*, 1995, **51**, 5994.

[198] W. Wong-Ng, J. Kaduk, Q. Huang, L. Espinal, L. Li and J. Burress, *Microporous. Mesoporous. Mater.*, 2013, **172**, 95.

[199] J. Urmos, S. K. Sharma and F. T. Mackenzie, *Am. Mineral.*, 1991, **76**, 641.

[200] G. Juhasz, Z. Homonnay, K. Nomura, T. Hayakawa and A. Hamakawa, S. amd Vertes, *Solid State Ionics*, 2001, **139**, 219.

[201] Z. Homonnay, K. Nomura, G. Juhasz, M. Gal, K. Solymos, S. Hamakawa, T. Hayakawa and A. Vertes, *Chem. Mater.*, 2002, **14**, 1127.

[202] *HighScore Plus (3.0e (3.0.5))*, Panalytical technical report, 2012.

[203] C. J. Howard, *J. Appl. Crystallogr.*, 1982, **15**, 615.

[204] P. Thompson, D. E. Cox and J. B. Hastings, *J. Appl. Crystallogr.*, 1987, **20**, 79.

[205] S. M. Antao and I. Hassan, *Can. Mineral.*, 2009, **47**, 1245.

[206] S. Alikhanzadeh-Arani, M. Salavati-Niasari and F. Davar, *High Temp. Mater. Proc.*, 2013, **32**, 1.

[207] A. R. Armstrong, H. S. Obhi and P. P. Edwards, *J. Solid State Chem.*, 1993, **106**, 120.

[208] P. J. E. Harlick and F. H. Tezel, *Microporous Mesoporous Mater.*, 2004, **76**, 71.

[209] S. Liu, X. Zhang, J. Li, N. Zhao, W. Wei and Y. Sun, *Catal. Commun.*, 2008, **9**, 1527.

[210] R. A. Khatri, S. S. C. Chuang, Y. Soong and M. Gray, *Energy Fuels*, 2006, **20**, 1514.

[211] M. K. Ram Reddy, Z. P. Xu, G. Q. M. Lu and J. C. Diniz da Costa, *Ind. Eng. Chem. Res.*, 2006, **45**, 7504.

[212] C. Galven, J. Fourquet, E. Suard, M. Crosnier-Lopez and F. Berrea, *Dalton Trans.*, 2010, **39**, 4191.

[213] Y. Wang, B. A. Scott, B.-H. Chen and D. Walker, *Physica C: Superconductivity*, 1997, **275**, 52 – 64.

[214] G. S. Grasa and J. C. Abanades, *Ind. Eng. Chem. Res.*, 2006, **45**, 8846.

[215] N. Ohashi, H. Imagawa, T. Tsurumi and F. Fukunaga, *Physica C.*, 1997, **278**, 71.

[216] C. Krueger, W. Reichelt, A. Almes, U. Koenig, H. Oppermann and H. Scheler, *J. Solid State Chem.*, 1992, **96**, 67.

[217] S. Adachi, T. Tatsuki, T. Sugano, A. Tokiwa-Yamamoto and K. Tanabe, *Physica C: Superconductivity*, 2000, **334**, 87 – 94.

[218] K. Wong-Ng, K. L. Davis and R. S. Roth, *J. Am. Cer. Soc.*, 1988, **71**, 64.

[219] R. D. Shannon, *Acta Cryst.*, 1976, **A32**, 751.

[220] M. Heinau, J. R. Baumann, B. Nick, M. Hartweg and L. Walz, *Z. Kristallogr.*, 1994, **209**, 418.

[221] J. P. R. de Villiers, *Am. Mineral.*, 1971, **56**, 758.

[222] D. Krishnamurti, *The Raman spectra of aragonite, strontianite and witherite.*, Indian Academy of Sciences., 1960.

[223] I. Y. Sazeev and L. F. Grigor'eva, *Zhurnal Prikladnoi Khimii*, 1998, **71**, 20.

[224] H. Shaked, Y. Shimakawa, B. A. Hunter, P. G. Radaelli, B. Dabrowski, R. L. Hitterman, J. D. Jorgensen, P. D. Han, D. A. Payne, S. Kikkawa, G. Er and F. Kanamaru, *Phys. Rev. B*, 1994, **50**, 12752.

[225] N. Ohashi, I. Imagawa, T. Tsurumi and O. Fukunaga, *Physica C.*, 1997, **278**, 71.

[226] T. M. Gambardella, B. Domenges and B. Raveau, *Mater. Res. Bull.*, 1992, **27**, 629.

[227] H. D. Wasel-Nielen and R. Hopper, *Z. Anorg. Allg. Chem.*, 1970, **375**, 209.

[228] Y. Laligant, A. L. Bail, G. Ferey, M. Hervieu, B. Raveau, A. Wilkinson and A. K. Cheetham, *Eur. J. Sol. State Inor.*, 1988, **25**, 237.

[229] Y. Nagata, T. Taniguchi, G. Tanaka, M. Satho and H. Samata, *J. Alloys Compd.*, 2002, **346**, 50.

[230] R. J. Crooks and M. T. Weller, *J. Solid State Chem.*, 1997, **128**, 220.

[231] B. A. Frenz, J. H. Enemark and J. A. Ibers, *Inorg. Chem.*, 1969, **8**, 1288.

[232] S. Pagano, G. Montana, C. Wickleder and W. Schnick, *Chem. Eur. J.*, 2009, **15**, 6186.

[233] M. Kalmutzki, M. Stroebele, H. Bettinger and J. Meyer, *Eur. J. Inorg. Chem.*, 2014, **15**, 2536.

[234] M. Kalmutzki, M. Stroebele, F. Wackenhut, A. Meixner and J. Meyer, *Angew. Chem. Int. Ed.*, 2014, **53**, 14260.

[235] C. Kunkel, V. F. and F. Illas, *Energy Environ. Sci.*, 2016, **9**, 141.

[236] O. Muller and R. Roy, *Adv. Chem. Sr*, 1971, **98**, 28.

[237] H. D. Wisel-Nielen and R. Hoppe, *Z Anorg. Allg. Chem.*, 1970, **375**, 209.

[238] T. C. Ozawa, A. Matsushita, Y. Hidaka, T. Taniguchi, S. Mizusaki, Y. Nagata, Y. Noro and H. Samata, *J. Alloys Compd.*, 2008, **448**, 77.

[239] S. M. Teleb, D. E. Nassar and E. M. Nour, *Bull. Mater. Sci.*, 2004, **27**, 483.

[240] E. A. Owen and E. L. Yates, *Philos. Mag.*, 1933, **15**, 472.

[241] H. Nakamatsu, T. Mukoyama and H. Adachi, *Chem. Phys. Lett.*, 1995, **247**, 168.

[242] K. P. Kuhl, E. R. Cave, D. N. Abram and T. F. Jaramillo, *Energy Environ. Sci.*, 2012, **5**, 7050.

[243] F. Goettmann, A. Thomas and M. Antoniett, *Angew. Chem. Int. Ed.*, 2007, **46**, 2717.

[244] M. H. Lietzke and C. Mullins, *J. Inorg Nucl. Chem.*, 1981, **43**, 1769.

[245] H. C. Shin and S. C. Choi, *Chem. Mater.*, 2001, **13**, 1238.

[246] T. Liu, C. Cundari and A. K. Wilson, *J. Phys. Chem. C.*, 2012, **116**, 5681.

[247] V. V. Galvita, H. Poelman, V. Bliznuk, C. Detavernier and G. B. Marin, *Ind. Eng. Chem. Res.*, 2013, **52**, 8416.

[248] Q. Jiang, G. Zhou, Z. Jiang and C. Li, *Sol. Energy*, 2014, **99**, 55.

[249] T. Masazumi, I. Kazuki, N. Yoshinao and T. Keiichi, *J. Cata.*, 2016, **343**, 75.

[250] H. Liu, X. Zou, X. Wang, X. Lu and W. Ding, *J. Nat. Gas Chem.*, 2012, **21**, 703.

[251] F. Fischer and H. Trpsch, *Brennstoff-Chem.*, 1926, **7**, 97.

[252] F. Fischer and H. Trpsch, *Brennstoff-Chem.*, 1930, **11**, 489.

[253] M. Feyereisen, G. Fitzgerald and A. Komornicki, *Chem. Phys. Lett.*, 1993, **208**, 359.

[254] J. VandeVondele and J. Hutter, *J. Chem. Phys.*, 2007, **127**, 114105.

[255] K. Eichkorn, F. Weigend, O. Treutler and R. Ahlrichs, *Theoretical Chemistry Accounts*, 1997, **97**, 119.

[256] S. Grimme, S. Antony, J. Ehrlich and H. Krieg, *J. Chem. Phys.*, 2010, **132**, 154104.

[257] J. Bashir, R. T. H. Khan, N. M. Butt and G. Heger, *Powder Diffr.*, 2002, **17**, 222.

[258] Q. Huang, O. Chmaissem, J. J. Caponi, C. Chaillout, M. Marezio, J. L. Tholence and A. Santoro, *Physica C, Superconductivity*, 1994, **227**, 1.

[259] W. Gerlach, *Zeitschrift fuer Physik*, 1922, **9**, 184.

[260] S. Goedecker, M. Teter and J. Hutter, *Phys. Rev. B.*, 1996, **54**, 1703.

[261] J. Head and M. Zerner, *Chem. Phys. Lett.*, 1985, **122**, 264.

[262] W. F. Schneider, *J. Phys. Chem. B*, 2004, **108**, 273.

[263] E. J. Karlsen, M. A. Nygren and L. G. M. Pettersson, *J. Phys. Chem. B*, 2003, **107**, 7795.

[264] G. Kresse and J. Furthmüller, *Comput. Mater. Sci.*, 1996, **6**, 15.

[265] A. Stroppa and G. Kresse, *New Journal of Physics*, 2008, **10**, 063020.

[266] J. Bashir, R. T. H. Khan, N. M. Butt and G. Heger, *Powder Diffr.*, 2002, **17**, 222.

[267] Y. Duan, B. Zhang, D. C. Sorescu, K. J. Johnson, E. H. Majzoub and D. R. Luebke, *J. Phys. Condens. Mater.*, 2012, **24**, 325501.

[268] B. Zhang, Y. Duan and K. Johnson, *J. Chem. Phys.*, 2012, **136**, 64516.

[269] S. Loganathan, R. B. Valapa, R. K. Mishra, G. Pugazhenthi and S. Thomas, *Thermal and Rheological Measurement Techniques for Nanomaterials Characterization*, Elsevier, 2017.

[270] K. R. McCrea and G. A. Somorjai, *J. Mol. Catal. A: Chem.*, 2000, **163**, 43.

[271] G. M. Barrow, *Introduction to Molecular Spectroscopy*, McGraw-Hill, New York, NY, USA, 1962.

[272] P. Sinha, S. E. Boesch, C. Gu, R. A. Wheeler and A. K. Wilson, *J. Phys. Chem. A*, 2004, **108**, 9213.

[273] M. D. Halls, J. Velkovski and H. B. Schlegel, *Theor. Chem. Acc.*, 2001, **105**, 413.

[274] *Scaling factors for ab initio vibrational frequencies: comparison of uncertainty models for quantified prediction*, `https://hal.archives-ouvertes.fr/hal-00349953/document`, (accessed March 2019).

[275] H. Yoshida, K. Takeda, A. Okamura, J.and Ehara and H. Matsuura, *J. Phys. Chem. A*, 2002, **106**, 3580.

[276] M. Sibaev and D. L. Crittenden, *J. Phys. Chem. A*, 2015, **119**, 13107.

[277] D. M. Benoit, B. Madebene, I. Ulusoy, L. Mancera, Y. Scribano and S. Chulkov, *Beilstein J. Nanotechnol.*, 2011, **2**, 427.

[278] I. M. Alecu, unpublished, 2011.

[279] I. M. Alecu, J. Zheng and D. G. Zhao, *J. Chem. Theory Comput.*, 2010, **6**, 2872.

[280] H. Yu, J. Zheng and D. G. Truhlar, unpublished, 2015.

[281] J. Liu, P. K. Thallapally, B. P. McGrail, D. R. Brown and J. Liu, *Chem. Soc. Rev.*, 2012, **41**, 2308.

[282] L. L. Miller, X. L. Wang, S. X. Wang, C. Stassis, D. C. Johnston, J. Faber and C.-K. Loong, *Phys. Rev. B*, 1990, **41**, 1921.